

Ages and Origins of Calcite and Opal in the Exploratory Studies Facility Tunnel, Yucca Mountain, Nevada

By James B. Paces, Leonid A. Neymark, Brian D. Marshall,
Joseph F. Whelan, and Zell E. Peterman

U.S. GEOLOGICAL SURVEY

Water-Resources Investigations Report 01-4049

Prepared in cooperation with the
NEVADA OPERATIONS OFFICE,
U.S. DEPARTMENT OF ENERGY, under
Interagency Agreement DE-AI08-97NV12033

Denver, Colorado
2001

U.S. DEPARTMENT OF THE INTERIOR
GALE A. NORTON, Secretary

U.S. GEOLOGICAL SURVEY
Charles G. Groat, Director

The use of firm, trade, and brand names in this report is for identification purposes only and does not constitute endorsement by the U.S. Geological Survey.

For additional information write to:
Chief, Yucca Mountain Project Branch
U.S. Geological Survey
Box 25046, Mail Stop 421
Denver Federal Center
Denver, CO 80225-0046

Copies of this report can be purchased
from:

U.S. Geological Survey
Information Services
Box 25286
Denver Federal Center
Denver, CO 80225-0286

CONTENTS

Abstract.....	1
Introduction.....	2
Purpose and Scope.....	3
Geologic Setting.....	4
Hydrogeologic Setting.....	4
Analytical Techniques.....	5
Morphology of Calcite and Silica Deposits.....	7
Locations of Calcite and Silica in the Rock Mass.....	8
Fracture Coatings.....	8
Lithophysal Cavity Coatings.....	11
Textures.....	11
Paragenesis.....	17
Radiocarbon and $^{230}\text{Th}/\text{U}$ Ages of Calcite and Opal.....	19
Radiocarbon Data.....	19
Sampling Methods.....	20
Distribution of Radiocarbon Ages.....	20
Uranium-Series Disequilibrium Methods and Data.....	23
Sampling Procedures.....	24
Uranium and Thorium Isotopes and $^{230}\text{Th}/\text{U}$ Ages.....	24
Distribution of Initial $^{234}\text{U}/^{238}\text{U}$ and Correlation with Age.....	29
Carbon, Oxygen, and Strontium Isotopes.....	33
Carbon and Oxygen Isotopes in Unsaturated-Zone Calcite.....	34
Oxygen Isotopes in Unsaturated-Zone Silica Phases.....	39
Strontium Isotopes in Unsaturated-Zone Calcite.....	40
Correlation Between Strontium, Carbon, and Oxygen Isotopes.....	43
Interpretation of Ages.....	46
Conceptual Models of Deposition.....	46
Numerical Model of Continuous Deposition.....	47
Discordance Between Isotopic Systems.....	52
Constraints on Depositional Processes from Geochronology.....	52
Origin and Composition of Fracture Water and Mechanisms of Mineral Deposition.....	56
Origins of Fracture Water.....	56
Isotopic Compositions Associated with a Meteoric Water Source.....	57
Isotopic Compositions Associated with a Saturated-Zone Water Source.....	60
Hydrochemistry of Fracture Water.....	61
Modification of $^{234}\text{U}/^{238}\text{U}$ Activity Ratios in Fracture Water.....	63
Mechanisms of Unsaturated-Zone Fracture Flow and Mineral Deposition.....	65
Long-Term Thermal and Isotopic Evolution of Fracture Water.....	67
Thermal Evolution.....	67
Long-Term Isotopic Variations.....	69
Variations in Quaternary Moisture.....	70
Implications for Percolation Flux.....	71
Summary and Conclusions.....	73
References.....	75
Appendix.....	83
Appendix 1. Radiocarbon data for subsamples of unsaturated-zone calcite from the Exploratory Studies Facility tunnel, Yucca Mountain, Nevada, and procedural blanks.....	85
Appendix 2a. Description of subsamples of unsaturated-zone calcite and opal analyzed for uranium and thorium isotopes from the Exploratory Studies Facility tunnel, Yucca Mountain, Nevada.....	87
Appendix 2b. Uranium-series disequilibrium data for subsamples of unsaturated-zone calcite and opal from the Exploratory Studies Facility tunnel, Yucca Mountain, Nevada.....	90
Appendix 3. Strontium, carbon, and oxygen isotope data for subsamples of unsaturated-zone calcite from the Exploratory Studies Facility tunnel, Yucca Mountain, Nevada.....	94

FIGURES

1. Generalized geologic map and cross section of Yucca Mountain, Nevada	3
2. Map showing location of the Exploratory Studies Facility tunnel, Yucca Mountain, Nevada	9
3. Log showing location of mineral coating samples and samples used for isotopic analyses, Exploratory Studies Facility tunnel, Yucca Mountain, Nevada	10
4-8. Photographs showing:	
4. Calcite and opal deposits from the floors of lithophysal cavities in the Exploratory Studies Facility tunnel, Yucca Mountain, Nevada	12
5. Calcite blades with minor opal from the floor of a lithophysal cavity and geochronological results for calcite and opal subsamples, Exploratory Studies Facility tunnel, Yucca Mountain, Nevada	13
6. Secondary electron image of the outer growth surface from a fracture coating and geochronological results from calcite and opal subsamples, Exploratory Studies Facility tunnel, Yucca Mountain, Nevada	14
7. Secondary electron images of a single blade of calcite and opal at successively greater magnification, Exploratory Studies Facility tunnel, Yucca Mountain, Nevada	15
8. Secondary electron image of the outer surface of a mineral coating after removal of calcite with dilute hydrochloric acid leaching, Exploratory Studies Facility tunnel, Yucca Mountain, Nevada	16
9. Schematic illustration showing typical mineral sequences coating (A) lithophysal cavity floors, and (B) steeply dipping fracture surfaces	18
10. Histograms showing distribution of radiocarbon and uranium-series disequilibrium ages for subsamples of calcite and opal from the Exploratory Studies Facility tunnel, Yucca Mountain, Nevada	21
11. Graph showing uncorrected radiocarbon ages for subsamples of calcite relative to distance from the north portal of the Exploratory Studies Facility tunnel, Yucca Mountain, Nevada	22
12. Graph showing uranium and thorium concentrations for subsamples of calcite and opal from the Exploratory Studies Facility tunnel, Yucca Mountain, Nevada	25
13. Uranium-series disequilibrium evolution diagram showing data for calcite and opal from the Exploratory Studies Facility tunnel, Yucca Mountain, Nevada	26
14-20. Graphs showing:	
14. Conventional thorium-230/uranium ages for subsamples of calcite and opal relative to distance from the north portal of the Exploratory Studies Facility tunnel, Yucca Mountain, Nevada	28
15. Uranium concentrations and measured uranium-234/uranium-238 activity ratios in saturated-zone ground water, perched water, and runoff in the vicinity of Yucca Mountain, Nevada	31
16. Initial uranium-234/uranium-238 activity ratios for subsamples of calcite and opal relative to distance from the north portal of the Exploratory Studies Facility tunnel, Yucca Mountain, Nevada	32
17. Initial uranium-234/uranium-238 activity ratios and conventional thorium-230/uranium ages for subsamples of calcite and opal from the Exploratory Studies Facility tunnel, Yucca Mountain, Nevada	33
18. Carbon and oxygen isotope compositions of subsamples of calcite relative to distance from the north portal of the Exploratory Studies Facility tunnel, Yucca Mountain, Nevada	35
19. Stable carbon and oxygen isotope compositions of subsamples of unsaturated-zone calcite from drill core at Yucca Mountain, Nevada	36
20. Isotopic compositions of carbon and oxygen in subsamples of calcite from the Exploratory Studies Facility tunnel, Yucca Mountain, Nevada	37
21. Photographs of cross sections of two mineral coatings from the Exploratory Studies Facility tunnel, Yucca Mountain, Nevada, showing the scale of microsampling and the results of stable carbon and oxygen isotope analyses	38
22. Histograms showing distribution of delta carbon-13 values for calcite microsamples classified by relative microstratigraphic position from the Exploratory Studies Facility tunnel, Yucca Mountain, Nevada	39
23. Histograms showing distribution of delta oxygen-18 values for subsamples of unsaturated-zone chalcedony, quartz, and opal from drill core and the Exploratory Studies Facility tunnel at Yucca Mountain, Nevada	40
24. Graph showing strontium isotope compositions of calcite subsamples from drill core and the Exploratory Studies Facility tunnel at Yucca Mountain, Nevada, as a function of depth relative to the water table	42
25. Graphs showing strontium isotope compositions (A) and concentrations (B) for subsamples of calcite classified by relative microstratigraphic position from the Exploratory Studies Facility tunnel, Yucca Mountain, Nevada	43

26. Photograph of sample HD2065 mineral coating from the Exploratory Studies Facility tunnel, Yucca Mountain, Nevada, showing calcite subsample locations and plot showing strontium isotope compositions and concentrations relative to microstratigraphic position.....	44
27. Photograph of sample HD2019 mineral coating from the Exploratory Studies Facility tunnel, Yucca Mountain, Nevada, showing calcite subsample locations and plot showing strontium isotope compositions and concentrations relative to microstratigraphic position.....	45
28. Graphs showing relations among carbon, oxygen, and strontium isotope composition and reciprocal strontium concentration for subsamples of calcite from the Exploratory Studies Facility tunnel, Yucca Mountain, Nevada ...	46
29. Conceptual models of episodic/instantaneous and continuous mineral deposition	47
30-36. Graphs showing:	
30. Model thorium-230/uranium-238 and uranium-234/uranium-238 activity ratios in a hypothetical 1-millimeter-thick mineral coating formed under conditions of continuous deposition over the last million years.....	50
31. Relation between subsample thickness and conventional thorium-230/uranium calculated from isotopic ratios in hypothetical minerals formed under conditions of continuous deposition at slow growth rates.....	51
32. Uranium-series disequilibrium evolution diagram showing comparisons between isotopic compositions of hypothetical minerals formed under conditions of continuous and instantaneous deposition.....	53
33. Conventional thorium-230/uranium age and initial uranium-234/uranium-238 activity ratios for subsamples of calcite and opal from the Exploratory Studies Facility tunnel, Yucca Mountain, Nevada, along with trends expected for continuous deposition, instantaneous deposition, and mixing between two components with different ages	54
34. Relations between the true average ages of hypothetical minerals formed under conditions of continuous deposition and the conventionally calculated ages based on the isotopic compositions of oldest to youngest materials within a subsample for geochronometers with different decay constants	55
35. Oxygen isotope composition of water in equilibrium with calcite at various temperatures compared to (A) the ranges of surface and shallow unsaturated-zone temperatures and oxygen isotope compositions of precipitation expected during the Pleistocene, and (B) the ranges of present-day ground-water temperatures and oxygen isotope compositions.....	59
36. Calcite and chalcedony saturation indices for perched water, runoff, and saturated-zone ground water from Yucca Mountain, Nevada	62
37. Schematic cross section showing uranium isotope compositions of water, calcite, and opal, Yucca Mountain, Nevada.....	64

TABLES

1. Comparison of carbon-14 (^{14}C) and thorium-230/uranium ($^{230}\text{Th}/\text{U}$) ages determined on outer surface subsamples from the same sample, Exploratory Studies Facility tunnel, Yucca Mountain, Nevada	30
2. Comparison of effects for instantaneous and continuous depositional models	56

CONVERSION FACTORS, ABBREVIATIONS, AND VERTICAL DATUM

Multiply	By	To obtain
millimeter (mm)	3.937×10^{-2}	inch
centimeter (cm)	3.937×10^{-1}	inch
meter (m)	3.281	foot
kilometer (km)	6.214×10^{-1}	mile
square centimeter (cm ²)	0.1550	square inch
millimeter per year (mm/yr)	3.937×10^{-2}	inch per year
gram (g)	3.527×10^{-2}	ounce
kilogram (kg)	2.205	pound, avoirdupois

Temperature can be converted to degrees Celsius (°C) or degrees Fahrenheit (°F) by the formulas:

$$^{\circ}\text{F} = 1.8 \text{ }^{\circ}\text{C} + 32$$

$$^{\circ}\text{C} = (^{\circ}\text{F} - 32) / 1.8$$

Additional abbreviations

micrometer (μm), 10⁻⁶ meter
 nanometer (nm), 10⁻⁹ meter
 milligram (mg), 10⁻³ gram
 microgram (μg), 10⁻⁶ gram
 nanogram (ng), 10⁻⁹ gram
 picogram (pg), 10⁻¹² gram
 microgram per gram (μg/g)
 milligram per liter (mg/L), part per million (for dilute water)
 microgram per liter (μg/L), part per billion (for dilute water)
 k.y., thousands of years
 ka, kilo-annum, thousands of years before present
 m.y., millions of years
 Ma, Mega-annum, millions of years before present

Isotopic notation: Oxygen-18 (¹⁸O) and carbon-13 (¹³C) are reported using delta (δ) notation in units of parts per thousand (per mil). Delta notation (δ¹⁸O or δ¹³C) represents the relative difference between ¹⁸O/¹⁶O or ¹³C/¹²C measured for a sample and a standard value, or $\delta = 1,000((R_{\text{sample}} - R_{\text{standard}}) / R_{\text{standard}})$, where R is either the ¹⁸O/¹⁶O or ¹³C/¹²C ratio. The standards are Vienna Standard Mean Ocean Water (VSMOW) for δ¹⁸O and Vienna Pee Dee belemnite (VPDB) for δ¹³C.

Sea level: In this report, "sea level" refers to the National Geodetic Vertical Datum of 1929 (NGVD of 1929)—a geodetic datum derived from a general adjustment of the first-order level nets of both the United States and Canada, formerly called "Sea Level Datum of 1929."

Ages and Origins of Calcite and Opal in the Exploratory Studies Facility Tunnel, Yucca Mountain, Nevada

By James B. Paces, Leonid A. Neymark, Brian D. Marshall, Joseph F. Whelan, and Zell E. Peterman

Abstract

Deposits of calcite and opal are present as coatings on open fractures and lithophysal cavities in unsaturated-zone tuffs at Yucca Mountain, Nevada, site of a potential high-level radioactive waste repository. Outermost layers of calcite and opal have radiocarbon ages of 16,000 to 44,000 years before present and thorium-230/uranium ages of 28,000 to more than 500,000 years before present. These ages are young relative to the 13-million-year age of the host rocks. Multiple subsamples from the same outer layer typically show a range of ages with youngest ages from the thinnest subsamples. Initial uranium-234/uranium-238 activity ratios between 1 and 9.5 show a distinct negative correlation with thorium-230/uranium age and are greater than 4 for all but one sample younger than 100,000 years before present. These data, along with micrometer-scale layering and distinctive crystal morphologies, are interpreted to indicate that deposits formed very slowly from water films migrating through open cavities. Exchanges of carbon dioxide and water vapor probably took place between downward-migrating liquids and upward-migrating gases at low rates, resulting in oversaturation of mineral constituents at crystal extremities and more or less continuous deposition of very thin layers. Therefore, subsamples represent mixtures of older and younger layers on a scale finer than sampling techniques can resolve. Slow, long-term rates of deposition (less than about 5 millimeters of mineral per million

years) are inferred from subsamples of outermost calcite and opal. These growth rates are similar to those calculated assuming that total coating thicknesses of 10 to 40 millimeters accumulated over 12 million years.

Calcite has a wide range of delta carbon-13 values from about -8.2 to 8.5 per mil and delta oxygen-18 values from about 10 to 21 per mil. Systematic microsampling across individual mineral coatings indicates basal (older) calcite tends to have the largest delta carbon-13 values and smallest delta oxygen-18 values compared to calcite from intermediate and outer positions. Basal calcite has relatively small strontium-87/strontium-86 ratios, between 0.7105 and 0.7120, that are similar to the initial isotopic compositions of the strontium-rich tuff units, whereas outer calcite has more radiogenic strontium-87/strontium-86 ratios between 0.7115 and 0.7127. Isotopic compositions of strontium, oxygen, and carbon in the outer (youngest) unsaturated-zone calcite are coincident with those measured in Yucca Mountain calcrete, which formed by pedogenic processes.

The physical and isotopic data from calcite and opal indicate that they formed from solutions of meteoric origin percolating through a limited network of connected fracture pathways in the unsaturated zone rather than by inundation from ascending ground water originating in the saturated zone. Mineral assemblages, textures, and distributions within the unsaturated zone are distinctly different from those deposited below the water table at Yucca Mountain. The calcite

and opal typically are present only on footwall surfaces of a small fraction of fractures and only on floors of a small fraction of lithophysal cavities. The similarities in the carbon, oxygen, and strontium isotopic compositions between fracture calcite and soil-zone calcite, as well as the gradation of textures from detritus-rich micrite in the soil to detritus-free spar 10 to 30 meters below the surface, also support a genetic link between the two depositional environments. Older deposits contain oxygen isotope compositions that indicate elevated temperatures of mineral formation during the early stages of deposition; however, in the youngest deposits these values are consistent with deposition under geothermal gradients similar to modern conditions. Correlations between mineral ages and varying Pleistocene climate conditions are not apparent from the current data. Cumulative evidence from calcite and opal deposits indicates that the growth of minerals within the fracture network at the potential repository horizon has remained relatively uniform over long periods of time, implying a relatively stable hydrologic environment in the lower part of the Yucca Mountain unsaturated zone.

INTRODUCTION

Yucca Mountain, located in southern Nevada, is being considered as a potential site for isolating high-level radioactive waste produced in the United States from the accessible environment for thousands to hundreds of thousands of years (U.S. Department of Energy, 1998; Office of Civilian Radioactive Waste Management, 2000; Hanks and others, 1999). Positive attributes of the site include a thick unsaturated zone (UZ) and a semiarid climate, which together are likely to limit the amount of water that could contact the waste packages. Although the amount of water currently percolating through the mountain is too small to measure directly, it still is an important aspect of site characterization. A substantial proportion of the UZ water is likely to percolate through connected fractures in the welded tuffs that form the potential repository block rather than through the low-permeability matrix. However, water flowing in UZ fractures has

not yet been observed because of the inherent difficulties in confirming the presence of very small water fluxes in areas disturbed by borehole and tunnel construction. Therefore, the distribution, amount, and composition of fracture flow through the potential repository block must be evaluated by indirect methods.

In addition to the problem of collecting information on present-day fracture flow, the long half-lives of many of the radioactive isotopes in the waste require that estimates of the amounts of UZ fracture water must be relevant to a range of possible future climate conditions. Future climate at Yucca Mountain will most likely be within the range of conditions experienced in the last 500 thousand years (k.y.) on the basis of the cyclic nature of climate variation throughout the Quaternary Period (Winograd and others, 1992). Although fracture water of Pleistocene and older age may no longer be present in the UZ, a partial record of flow remains in the form of mineral deposits (dominantly calcite and opal) in fractures and cavities.

Calcite (CaCO_3) and opal ($\text{SiO}_2 \cdot n\text{H}_2\text{O}$), present as coatings in fractures and lithophysal cavities, represent direct evidence of past fracture flow at the site of deposition. The isotopic compositions of these minerals are related to the compositions of the water from which they formed, thus providing indirect estimates of the isotopic compositions of past fracture water. This information can be used to evaluate the sources of past fracture water and provide constraints on the hydrologic conditions in flowing fractures. The minerals also incorporate small amounts of natural radioactive isotopes that can be used to estimate ages of deposition, allowing the inferred information to be interpreted in a framework meaningful to the time scale of radioactive waste isolation. Therefore, information on the origins of percolating water, the mechanisms of mineral deposition and inferences on the nature of fracture flow, and the response of percolation to changes in climate can be determined by examining the growth history and isotopic compositions of these minerals at the potential repository. The U.S. Geological Survey (USGS), in cooperation with the U.S. Department of Energy under Interagency Agreement Number DE-AI08-97NV12033, studied fracture minerals in Yucca Mountain to provide this information.

Purpose and Scope

This report provides ages and isotopic compositions of UZ fracture minerals from Yucca Mountain that can be used to better understand UZ fracture flow over the last 500 k.y. Mineral samples used for this study were collected from the Exploratory Studies Facility (ESF), a tunnel as much as 300 meters (m)

below the surface, that partly intersects the potential repository horizon (fig. 1). Physical aspects of the mineral coatings are described and used to interpret the location of percolation pathways and mechanisms of mineral deposition from percolating water. Radio-carbon and uranium-thorium isotope data are used to calculate ages of outermost parts of the mineral coatings and estimate a time framework for the overall

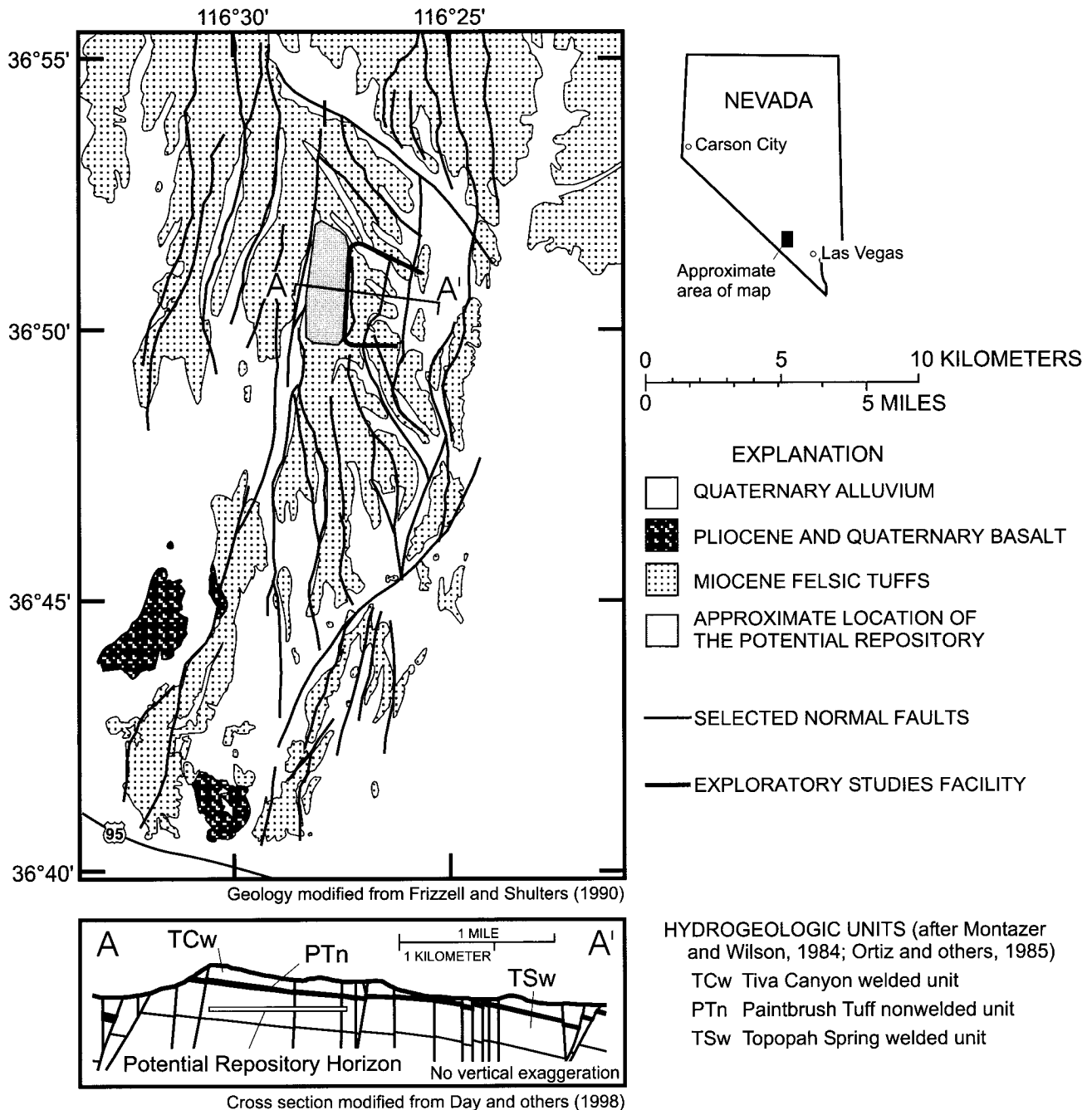


Figure 1. Generalized geologic map and cross section of Yucca Mountain, Nevada.

history of mineral precipitation from fracture solutions. Isotopic compositions of carbon, oxygen, and strontium in calcite are used to constrain the source of fracture water from infiltrating solutions. Despite the long-term uniformity of mineral growth rates, variations in the isotopic compositions of mineral coatings indicate that the composition of infiltration and temperature of mineral formation changed over time. Geochronological and isotopic data are used to interpret the mechanisms and processes of mineral deposition from fracture flow, and the response of deep percolation to estimated changes in climate at the surface.

Although conditions of water flow and mineral deposition in the felsic tuffs of Yucca Mountain are not geologically unique, mineralogical, geochemical, or isotopic studies of the genesis of similar deposits appear to be limited. Speleothem deposits in karstic limestone terranes also can form in an unsaturated environment. However, major differences in rock types, water fluxes, hydrochemistry, and deposition rates between the two different settings make the comparisons difficult at best and may provide a very misleading context in which to evaluate the Yucca Mountain calcite and opal deposits. Therefore, interpretations presented in this report primarily are based on observations made in the ESF tunnel and analytical data from the ESF samples. Data presented in this report were obtained by the USGS between late 1995 and mid-1996.

Geologic Setting

Yucca Mountain is located 145 kilometers (km) northwest of Las Vegas, Nevada (fig. 1), in the southwestern Nevada volcanic field (Christiansen and others, 1977). It is composed of a 1- to 3-km-thick sequence of thick, welded ash-flow tuffs interlayered with thinner, nonwelded air-fall and ash-flow tuffs that erupted about 13 million years before present (Ma) (Sawyer and others, 1994, table 3). High-angle normal faults have disrupted the originally flat-lying strata and created a series of north-trending structural blocks tilted so that beds dip 5 to 10 degrees to the east (Scott and Bonk, 1984; Carr and others, 1986). Faults, shears, and cooling joints in welded tuffs form a network of fractures that may provide pathways for water movement through the rock mass.

In the central Yucca Mountain area, the UZ is composed principally of Tertiary rocks of the Paintbrush Group and Calico Hills Formation. These rocks include, in descending order, the Tiva Canyon Tuff, Yucca Mountain Tuff, Pah Canyon Tuff, Topopah Spring Tuff, and Calico Hills Formation (Buesch and others, 1996). The Tiva Canyon and Topopah Spring Tuffs are thick, tabular, regionally extensive ignimbrites consisting mostly of densely welded quartz latite to high-silica rhyolite. In contrast, the Yucca Mountain and Pah Canyon Tuffs are thin, lenticular, and more localized ignimbrites and volcanic ashes that are mostly nonwelded in the central Yucca Mountain area. Other localized nonwelded volcanic ash units also are present along with the Yucca Mountain and Pah Canyon Tuffs between the two major tuffs in the Paintbrush Group. The underlying Calico Hills Formation consists mostly of nonwelded and bedded tuffs that have been variously altered (0- to 75-percent replacement) to zeolites (Levy, 1991; Bish and Chipera, 1989; Broxton and others, 1987, 1993).

Hydrogeologic Setting

In addition to informal lithostratigraphic subdivisions (Buesch and others, 1996), the tuffs at Yucca Mountain have been grouped into informal hydrogeologic and thermal/mechanical units based on their physical properties (Montazer and Wilson, 1984; Ortiz and others, 1985). Moderately to densely welded units of the Tiva Canyon Tuff (TCw hydrogeologic unit) and Topopah Spring Tuff (TSw hydrogeologic unit) typically have greater fracture density and fracture permeability than nonwelded or partially welded tuffs (Montazer and Wilson, 1984, p. 14–19). Porosity is reduced greatly by the compaction and welding process such that the matrix permeability in welded tuffs is small relative to nonwelded tuffs. Nonwelded and partially welded parts of the basal Tiva Canyon Tuff and uppermost Topopah Spring Tuff have been grouped with the Yucca Mountain and Pah Canyon Tuffs and other interbedded nonwelded tuffs as the Paintbrush Tuff nonwelded (PTn) hydrogeologic unit (Montazer and Wilson, 1984; Moyer and others, 1996). Correlations among lithostratigraphic, thermal/mechanical, and hydrogeologic units have been described by Buesch and others (1996) and Rautman and Engstrom (1996a).

The potential repository horizon is located in the lower of the two welded tuffs (Topopah Spring Tuff) and is overlain by 25 to more than 100 m of non-welded tuffs of the PTn with large matrix permeabilities (Moyer and others, 1996). The potential repository horizon is 200 to 300 m above the present-day water table, which is at an elevation of 730 to 800 m beneath Yucca Mountain (Robison, 1984; Tucci and Burkhardt, 1995). Surface elevations range from 1,130 to 1,490 m above sea level resulting in total UZ thicknesses of 400 to 700 m in the vicinity of the potential repository block.

Yucca Mountain has a semiarid climate with an average annual precipitation of approximately 170 millimeters (mm) (Hevesi and others, 1992). Although precipitation is monitored at Yucca Mountain, infiltration has not been measured directly. Estimates of average infiltration in the Yucca Mountain vicinity range from less than 1 to about 6 mm per year (mm/yr) using a variety of methods including Maxey-Eakin-type or other transfer equations (Rush, 1970; Scott and others, 1983; Montazer and Wilson, 1984; Czarnecki, 1985), water balance (Winograd, 1981; Nichols, 1987), soil physics calculations (Flint and Flint, 1994), and chloride mass balance (Fabryka-Martin and others, 1994). However, translating infiltration estimates to percolation fluxes deep in the UZ at Yucca Mountain is complicated by factors such as heterogeneous fracture flow, the transfer of flow between the matrix-dominated PTn units and fracture-dominated welded tuffs, and upward water-vapor fluxes. Water that does infiltrate through the soil zone has hydrochemical compositions that are affected strongly by interactions with pedogenic calcite and silica that are present in colluvial veneers over bedrock, alluvial valley fill, and fractures in the upper 5 to 10 m of bedrock.

Tritium (^3H) and radiocarbon (^{14}C) data collected from nonwelded tuffs have been interpreted as indications of rapid percolation through the UZ, although these data have not contributed to estimates of percolation flux. Nuclear bomb-pulse (less than 50-yr travel times) tritium signatures in pore water extracted from nonwelded tuffs below the potential repository horizon indicate rapid fracture flow to depths greater than 400 to 500 m in the rock mass (Yang and others, 1996). Although indicative of rapid percolation, the resulting flux is interpreted to be low based on the erratic distribution of tritium in squeezed core and its absence in perched water (Yang and

others, 1996, p. 32). Water from perched zones in the lower part of the UZ (Patterson, 1999, p. 170) has isotopic characteristics that are consistent with longer average UZ residence times [^{14}C at 27 to 29 percent modern carbon (pmc) for aquifer-test water representative of perched reservoirs in boreholes USW UZ-14 and USW SD-7; Yang and others, 1996, table 7]. The dissolved ion compositions of perched water indicate that percolation follows interconnected fracture pathways and does not interact substantially with pore water (Yang and others, 1996, p. 34).

Fast percolation pathways also have been interpreted from elevated chlorine-36/total chloride ($^{36}\text{Cl}/\text{Cl}$) ratios found in discrete zones in the ESF (Fabryka-Martin and others, 1996, 1997). Like tritium, elevated $^{36}\text{Cl}/\text{Cl}$ ratios observed in discrete zones in the ESF are attributed to bomb-pulse ^{36}Cl components that indicate percolation travel times of less than 50 yrs to sample sites at 40-m to greater than 200-m depths (Fabryka-Martin and others, 1996, fig. 5-1). Although ^{36}Cl studies may provide information on the spatial distribution of fast percolation zones, little or no direct information on the volumes of water responsible for the elevated signatures can be inferred (Fabryka-Martin and others, 1997, p. 9-3).

Infiltration is likely to vary with time because of changes in precipitation related to shifts in Pleistocene climate (Spaulding, 1985; Winograd and others, 1992; Forester and others, 1999). Mean annual precipitation during pluvial (glacial) climates may have been 2 to 4 times greater than present-day interpluvial conditions and mean annual temperatures may have been as much as 5 and 10 degrees Celsius ($^{\circ}\text{C}$) cooler (Spaulding, 1985, table 10; Forester and Smith, 1994; Forester and others, 1999, p. 2). Consequently, conditions at the surface affecting shallow infiltration, including the amount and type of precipitation, average surface temperatures, local plant communities, evapotranspiration rates, and soil conditions at Yucca Mountain, likely were different in the past. The cumulative effect likely resulted in greater soil moisture, increased infiltration, and potentially larger percolation fluxes during pluvial conditions.

ANALYTICAL TECHNIQUES

Morphology, mineralogy, and mineral textures were determined in field and laboratory settings. Hand specimens brought back to the laboratory were

cleaned with deionized water and examined under low-power binocular magnification under both white and ultraviolet illumination. Minerals were identified by their physical appearance augmented by additional tests (hardness, fluorescence, chemical reactivity), if necessary. Small slabs of the coatings were impregnated with blue epoxy and made into thick [100- to 200-micrometer (μm)] polished sections for petrographic examination and stable isotope microsampling. Secondary electron images were taken from gold-coated fragments of mineral coatings on a Cambridge StereoScan 250 MkII scanning electron microscope (SEM) using an accelerating voltage of 20 kilovolts and a working distance of 20 mm. In this report, the term sample refers to hand specimens collected from a specific location in the ESF, whereas the term subsample refers to small parts of a sample separated in the laboratory for analysis.

Radiocarbon contents were determined on calcite subsamples prepared using routine procedures in the Isotopes Laboratory of the University of Waterloo in Ontario, Canada, and analyzed by accelerator mass spectrometry (AMS) at the IsoTrace Laboratory of the University of Toronto in Ontario, Canada. Radiocarbon ages were calculated from measured values of percent modern carbon and corrected for isotopic fractionation using measured stable carbon isotopes, on the basis of a ^{14}C half-life of 5,730 yrs. Ages were not corrected for possible variations in atmospheric ^{14}C production rates because of the lack of appropriate calibration data sets over these age ranges or for a " ^{14}C -dead" component that may have been acquired from calcrete dissolution during infiltration. All uncertainties are reported at the 95-percent confidence level. Two small fragments of marble from the Paleozoic Carrara Formation, Bare Mountain, Nevada (presumed to have 0 pmc), were washed with 0.2 normal hydrochloric acid (HCl) and submitted to the radiocarbon laboratories as procedural and instrumental blanks (Appendix 1). These blanks had measured ^{14}C contents of 0.52 and 1.17 pmc resulting in radiocarbon ages of 43.5 and 36.8 thousand radiocarbon years before present (RCYBP) uncorrected for fluctuations in the ^{14}C production rate through time. The small but finite values of ^{14}C determined in blank calcite samples presumed to have zero pmc indicate that a modern carbon contaminant either was introduced during the sampling or analytical process or that the assumption of zero pmc is incorrect. The large value of 1.17 pmc

for one of the Carrara marble blanks implies that reported ^{14}C ages older than about 36 thousand years before present (ka) may have little significance. However, uncorrected ^{14}C ages between 37.4 and 49.9 ka were obtained for 7 of the 31 calcite samples and one of the laboratory blanks. Therefore, appreciable contamination by a component with young carbon is not suspected, and the larger-than-expected value for the Carrara marble blank likely is the consequence of a subsample with non-zero pmc. If the larger value of pmc for this laboratory blank is caused by contamination during sampling or analysis, then measured ages would be skewed towards slightly younger values. However, contamination with modern carbon has a decreasing effect on analyses with larger ^{14}C contents. The addition of 1 pmc to a 40-ka calcite will result in a calculated age of about 33 ka. The same 1-pmc addition would cause a 35-ka calcite to have a calculated age of 31 ka and a 20-ka calcite to have a calculated age of about 19 ka. For samples of about 15 ka or less, this difference is within typical AMS analytical uncertainties.

Uranium and thorium isotope analyses were determined at USGS laboratories in Denver, Colorado. Subsamples of calcite and opal were digested by adding a mixture of hydrofluoric and nitric acids to the subsamples along with a mixed spike solution containing known amounts of isotopically enriched uranium-236 (^{236}U) and thorium-229 (^{229}Th) in sealed Teflon vials on a hotplate at 100°C to 200°C. Uranium and thorium were separated and purified using anion-exchange chromatographic resins (BioRadTM AG1x8) in hydrochloric and nitric acid media. Blank correction was a concern in the low-uranium calcite and smallest opal subsamples where as little as 1 to 10 nanograms (ng) of total uranium were loaded onto the filament. Total procedural blanks were between 20 and 100 picograms (pg) of ^{238}U and ^{232}Th for calcite samples and between 5 and 20 pg for the small opal samples requiring smaller volumes of resin and acid. Measured ^{230}Th blanks were typically less than 0.0004 to 0.005 pg. Abundances of ^{234}U in the blank were too low to be measured accurately; therefore, the ^{234}U is assumed to be in secular equilibrium with ^{238}U , yielding a ^{234}U blank of 0.0003 to 0.006 pg.

Isotopic measurements of $^{236}\text{U}/^{235}\text{U}$, $^{234}\text{U}/^{235}\text{U}$, $^{230}\text{Th}/^{229}\text{Th}$, and $^{232}\text{Th}/^{229}\text{Th}$ were determined on a Finnigan MAT 262 thermal ionization mass spectrometer equipped with a secondary electron multiplier operating in ion-counting mode. Uranium

was loaded as a nitrate onto the evaporation side of a double rhenium-filament assembly and measured as metal ions. Thorium was loaded onto single, center rhenium filaments along with a graphite suspension. Data were corrected for contributions from tracer solutions, procedural blank, and mass fractionation and were normalized to a constant $^{234}\text{U}/^{238}\text{U}$ value for NIST SRM 4321B uranium standard (atomic ratio of 5.29×10^{-5} or activity ratio of 0.966, National Institute of Standards and Technology, written commun. [Certificate], 1992) using the values measured in each magazine containing up to 13 filaments. Multiple analyses of a secular equilibrium standard analyzed based on the same methods result in $^{234}\text{U}/^{238}\text{U}$ and $^{230}\text{Th}/^{238}\text{U}$ ratios that are within analytical error of unity. Authigenic compositions of $^{234}\text{U}/^{238}\text{U}$ and $^{230}\text{Th}/^{238}\text{U}$ (equal to the compositions of the water) are determined by subtracting a model ^{232}Th -bearing detrital component with an atomic Th/U of 6 ± 3 (average of measured fresh and altered tuffs from Neymark and others, 1995) that is assumed to be in secular equilibrium. Measured $^{232}\text{Th}/^{238}\text{U}$ ratios were used to determine the amount of this component that must be subtracted; however, the extremely low ^{232}Th observed in most of these materials typically rendered the detrital correction insignificant. Corrected $^{234}\text{U}/^{238}\text{U}$ and $^{230}\text{Th}/^{238}\text{U}$ were used to iteratively calculate $^{230}\text{Th}/\text{U}$ age and initial $^{234}\text{U}/^{238}\text{U}$ estimates based on the standard equation relating ^{230}Th to ^{238}U as a function of time originally derived by Broecker (1963) and calculated using the program ISOPLOT (Ludwig, 1991). Decay constants used for ^{234}U and ^{230}Th were $2.8338 \times 10^{-6} \text{ yr}^{-1}$ and $9.19525 \times 10^{-6} \text{ yr}^{-1}$, respectively. All uncertainties have been propagated at the 95-percent confidence level.

Stable carbon and oxygen isotope analyses were performed at USGS laboratories in Denver, Colorado. Data used in this report for samples of calcite and silica are from Whelan and others (1998) and Moscati and Whelan (1996). Analytical techniques are described in those reports. Laboratory standards analyzed during the course of data collection (98 aliquots of NBS-19) had average values of $\delta^{13}\text{C}$ of 1.91 ± 0.02 per mil, and $\delta^{18}\text{O}$ of 28.32 ± 0.15 per mil. Accepted values for the NBS-19 standard are 1.92 per mil for $\delta^{13}\text{C}$ and 28.65 per mil for $\delta^{18}\text{O}$ (Coplen and others, 1983, tables 1 and 2). Measured $\delta^{18}\text{O}$ values reported in Whelan and others (1998) were adjusted by +0.30 per mil to account for this deviation.

Strontium isotope analyses were performed at USGS laboratories in Denver, Colorado. Strontium isotope compositions were determined on splits of the same subsamples used for carbon and oxygen isotopes. Calcite subsamples were dissolved with HCl, centrifuged, and decanted to separate the supernatant from any insoluble opal or wall rock. Residues were dried and weighed to determine the actual weights of calcite analyzed. Strontium was purified by conventional cation-exchange chromatography using an HCl medium. The purified strontium was loaded as a chloride onto the evaporation side of a double rhenium-filament assembly. The isotopic composition was determined on a Finnigan MAT 262 thermal ionization multi-collector mass spectrometer operating in a fully automatic static mode. Two samples of the USGS carbonate standard EN-1 (modern *Tridacna* shell collected from Enewetok Lagoon in the western Pacific Ocean; Ludwig and others, 1988, p. 177) were analyzed in each magazine of 13 samples. The mean strontium-87/strontium-86 ($^{87}\text{Sr}/^{86}\text{Sr}$) for EN-1 measurements was 0.709101 ± 0.00006 during the course of this study. Mass fractionation during isotopic analyses was corrected by normalizing the measured $^{86}\text{Sr}/^{88}\text{Sr}$ ratios to a value of 0.1194 and adjusting the $^{87}\text{Sr}/^{86}\text{Sr}$ ratios accordingly. The $^{87}\text{Sr}/^{86}\text{Sr}$ values corrected for mass fractionation then were adjusted to a scale on which the value for present-day ocean water, represented by standard EN-1, is 0.70920. Uncertainties in the normalized and adjusted $^{87}\text{Sr}/^{86}\text{Sr}$ ratios are less than ± 0.01 percent at the 95-percent confidence level.

MORPHOLOGY OF CALCITE AND SILICA DEPOSITS

The morphology of mineral coatings is related to mechanisms of deposition and fracture flow. Therefore, spatial relations of mineral coatings as well as their depositional settings, textures, and paragenesis preserve important geologic and hydrologic information. Interpretations of morphological observations are discussed in the Mechanisms of Unsaturated-Zone Fracture Flow and Mineral Deposition section.

Calcite and various silica phases including quartz, chalcedony, and opal are the most common low-temperature (deposited after the ash-flow tuffs cooled to below boiling temperatures of water) minerals forming coatings on fractures and in cavities.

Mineralogical studies of silica in UZ mineral coatings demonstrate the presence of both opal-A and opal-CT (Vaniman and Chipera, 1996, p. 4422). Opal fluoresces a distinctive bright green under short-wavelength ultraviolet light, a feature that was used in field and laboratory identification as well as in microsampling. Unsaturated-zone calcite fluoresces a much less intense whitish blue in contrast to saturated zone (SZ) calcite that commonly fluoresces orange-red under short-wavelength ultraviolet light (Whelan and others, 1994). Fluorite, clay minerals, zeolites, and manganese oxides also are present in mineral coatings in minor amounts. Although these minerals all are compatible with formation under present-day temperature conditions (approximately 20°C to 40°C), when present, these other minerals most commonly are observed in the earliest stages of mineral deposition.

Exposures of calcite and opal coatings in the ESF at Yucca Mountain are superior to those seen previously in drill core in terms of quantity, quality, degree of preservation of delicate textures, and the opportunity to observe larger scale physical relations. The extent and thickness of mineral coatings, the fragility of some of the calcite crystal forms, and the extensive distribution of opal were not anticipated in ESF samples based on the earlier investigations using drill core (Whelan and Stuckless, 1992; Whelan and others, 1994).

Field observations of the macroscopic features were made during numerous sample collecting and mineral surveying trips as the tunnel-boring machine excavated the ESF tunnel. About 180 samples of mineral coatings were chiseled out of fractures and lithophysal cavities throughout most of the 5,700 m of tunnel accessible by the summer of 1996; however, most analyses presented in this report are on samples from the first 4,000 m (figs. 2 and 3). Sample size generally was between 0.5 and 5 kilograms (kg) and, in all cases, attempts were made to obtain sections of the entire thickness of the mineral coatings. Observations were documented both in the ESF and from hand specimens brought back to the USGS laboratory.

Locations of Calcite and Silica in the Rock Mass

Coatings of calcite and silica are present in a small percentage of fracture cavities or on the floors of lithophysal cavities intersected by high-angle fractures or bedding-plane partings. Structures containing

coarse breccia fragments also may have coarsely crystalline calcite coatings or cements. Structures containing fine breccia fragments or clay gouge have little or no coarse calcite or opal cement and generally were not sampled for microscopic examination in this study. A relatively small proportion of the total calcite and silica is present in completely filled fractures with apertures between about 1 and 5 mm. The morphologies of mineral coatings in the shallower part of the UZ (TCw and PTn units, exposed in the first 1,200 m of the ESF) may be slightly different than those in the underlying TSw. However, deposits at shallower depths have not been studied as much as the deeper deposits. Generalized descriptions given in the following sections are based largely on mineral deposits observed in exposures of the TSw at distances between about 1,500 and 4,000 m from the north portal of the ESF (fig. 2).

Mineral coatings in the UZ consisting predominantly of calcite and opal are distinct from the vapor-phase mineral assemblage of fine tridymite/cristobalite crystals with minor alkali feldspar, hematite, and traces of garnet (Carlos, 1985, p. 12; Carlos, 1994, p. 9) that coat floors, walls, and ceilings of lithophysal cavities. This mineral assemblage formed at high temperatures during the initial cooling and degassing of the ash-flow tuffs. Relative to this vapor-phase assemblage, calcite and opal formed at temperatures in equilibrium with present-day geothermal gradients or at slightly greater temperatures associated with cooling of the tuffs or with elevated geothermal gradients caused by regional magmatic activity. Measured temperatures at or near the present-day water table range from 28°C to 39°C beneath Yucca Mountain (Sass and others, 1988, figs. 4–10; Fridrich and others, 1994, fig. 8).

Fracture Coatings

Low-temperature mineral coatings in fractures commonly are restricted to depositional sites where apertures exceed 2 to 3 mm. Fractures with apertures less than this may have vapor-phase or alteration minerals and adjacent, lighter colored bleached zones, but they generally lack calcite and opal deposits. Apertures of individual fractures exposed along the ESF walls commonly vary along their lengths. The narrow-aperture (typically less than 1 mm) portions of these fractures lack macroscopic calcite or opal deposits, whereas the same fracture may contain coarse sparry calcite and opal in wide-aperture segments (typically greater than 5 mm).

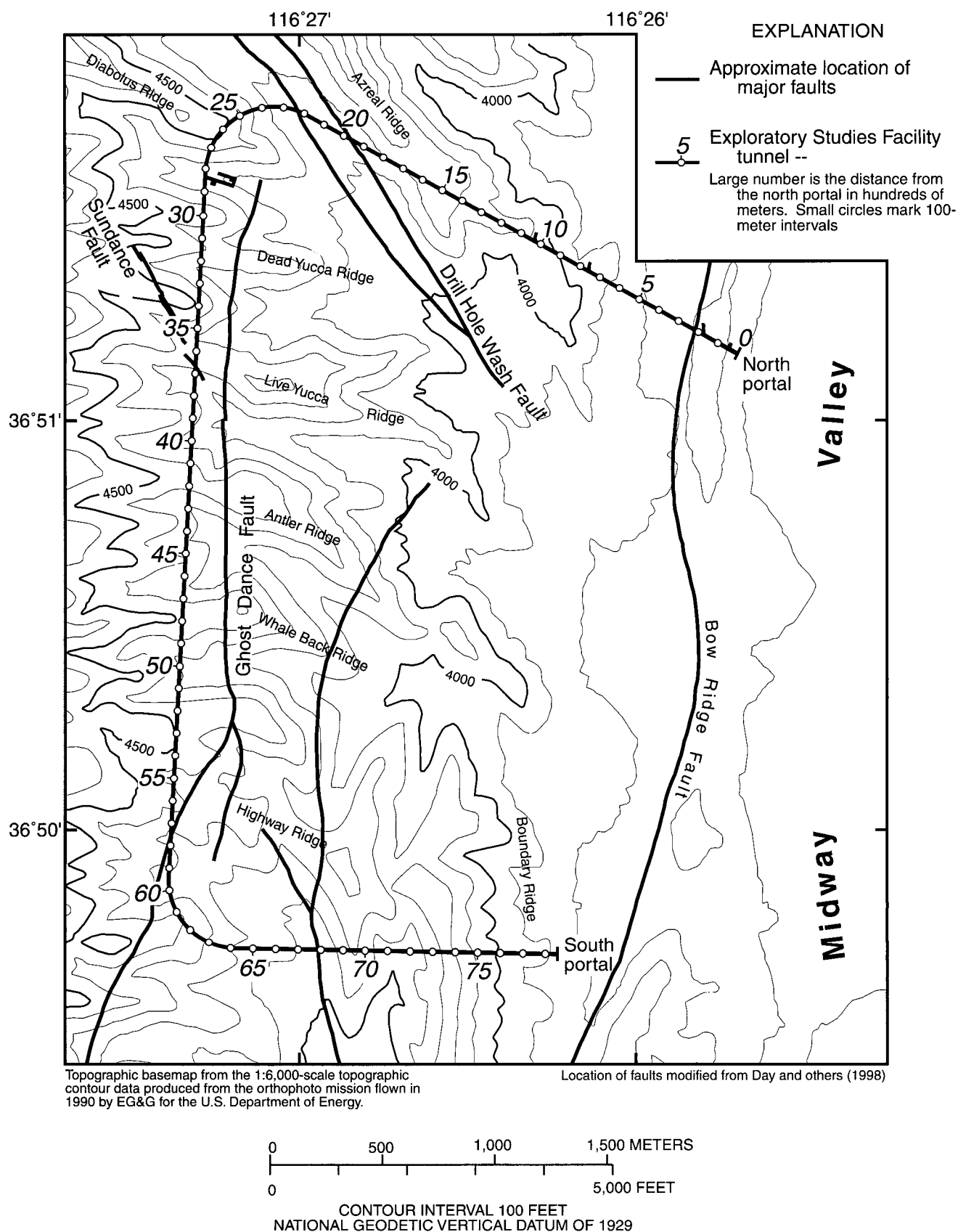


Figure 2. Location of the Exploratory Studies Facility tunnel, Yucca Mountain, Nevada.

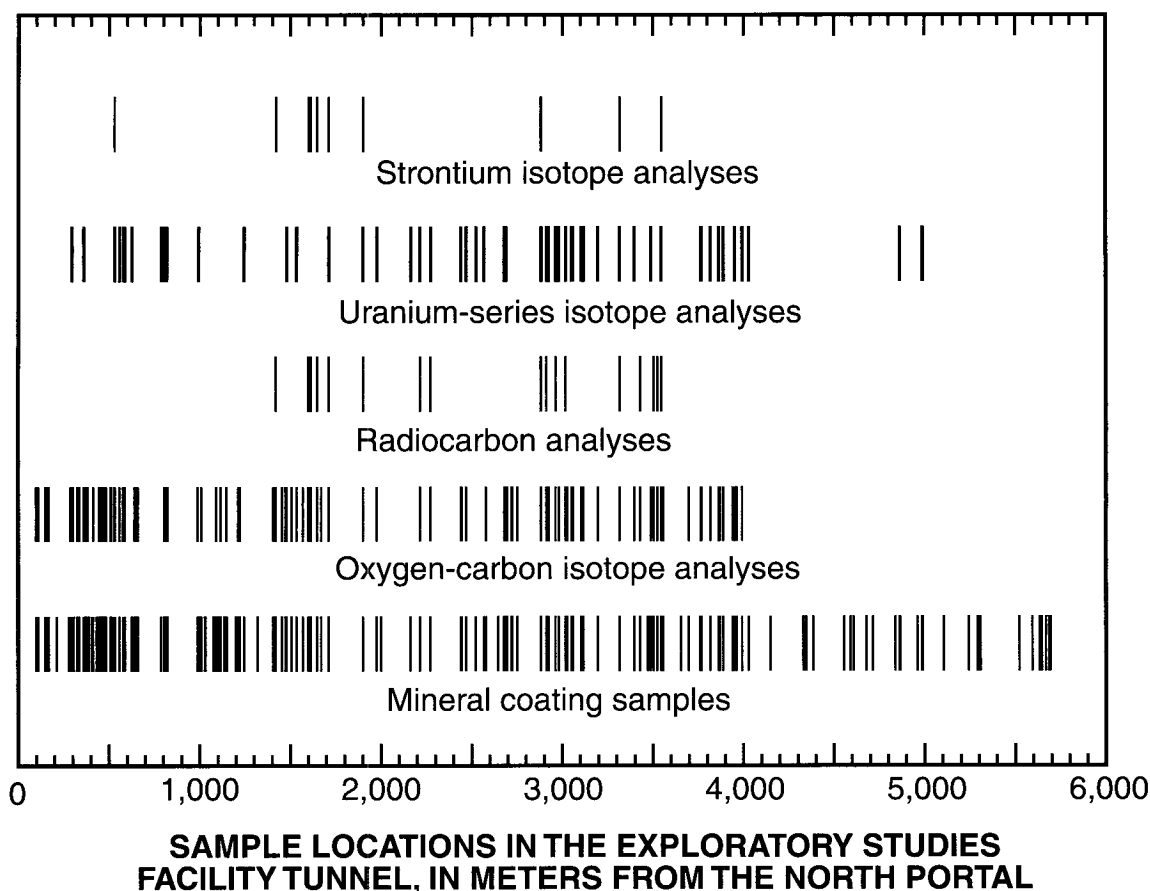


Figure 3. Location of mineral coating samples and samples used for isotopic analyses, Exploratory Studies Facility tunnel, Yucca Mountain, Nevada (see fig. 2).

Deposits of calcite and opal are present on both high-angle and low-angle fractures. Mineral coatings on high-angle fractures generally are restricted to thicknesses of 1 to 5 mm, whereas coatings on low-angle fractures may be up to 1 to 2 centimeters (cm) thick. Opal is most abundant in coatings on low-angle fractures but is rare or absent in thin deposits coating high-angle fracture surfaces. Fracture coatings are present almost exclusively on the footwalls of open-aperture fractures. Hanging-wall surfaces of the same mineralized fracture, unless near vertical, are invariably barren of mineral deposits. Mineral coatings have outer surfaces that clearly grew into the open space.

Fractures between 1 and 5 mm in width that are completely filled with calcite and, rarely, opal or

chalcedony, constitute a small volume of the mineral deposits exposed in the ESF. Only a few of these filled fractures were sampled because of the difficulty of removing the relatively soft calcite from the completely enclosing welded tuffs. Also, these samples were problematic to subsample because of the difficulty in determining the mineral paragenesis (no clear distinction of earliest or latest surfaces) and were difficult to date using $^{230}\text{Th}/\text{U}$ because of the low uranium concentration in calcite. Despite the minimal analyses of calcite from these settings, the available isotopic data appear to support an early depositional history. In contrast, data from calcite in unfilled fracture cavities are likely to represent deposition from more recent fracture flow.

Lithophysal Cavity Coatings

Floors of primary spheroidal lithophysal cavities (typically 5 to 50 cm wide) in and subjacent to the upper lithophysal unit within the TSw can contain coatings of calcite and opal up to about 4 cm thick. More commonly, coatings are between 1 and 3 cm thick. Mineral coatings are present in only a small percentage of all lithophysae. Unlike the vapor-phase minerals that cover all surfaces of these cavities, calcite and opal deposits form only on the floors of cavities; walls and ceilings are barren of calcite and opal deposits except where complex lithophysae form multichambered cavities with smaller openings above the main void. In many cases, lithophysae are flattened parallel to bedding planes, and dip gently to the east. Typically, the mineral deposits form irregular coatings, with moundlike and lumplike shapes rather than smooth, uniform layers. Nevertheless, these deposits typically follow the slope of the floor rather than accumulate at the lowest elevations in the lithophysal cavity. On the downslope end of the cavity, the coatings do not extend up the walls or ceilings to match the higher elevations of the coated floors on the upslope end of the cavity.

In most cases, lithophysae are intersected by fractures that may have served as fluid pathways. These can either be high-angle fractures cutting the cavity ceiling, or bedding-plane partings that extend short distances away from the lithophysae. In some cases, a variation in coating thickness (either greater or lesser) may correspond with the lower extension of the fracture. Connections to a fracture network are not always apparent; however, fractures may have been removed by the tunneling process or may remain unexposed.

Calcite and opal deposits do not completely fill lithophysal cavities. Typically, the thickness of the mineral coating is small relative to the height of the lithophysae. In small or flattened lithophysae with heights less than 2 to 4 cm, bladed calcite may extend from the bottom to the top of the cavity. In these instances, the voids between calcite blades remain unfilled resulting in highly porous coatings.

Textures

The textures of calcite and opal reflect the mechanisms of mineral deposition from aqueous solutions. Calcite forms large millimeter- to centimeter-

scale, clear, sparry crystals with well-formed crystal faces on outer growth surfaces. Delicate, high-relief crystal habits are common (figs. 4A and 5), especially in lithophysal cavities. Thin, tabular to bladed crystals commonly exceed 5 to 10 mm in height with widths less than 1 mm. These delicate forms were rarely observed in drill-core specimens. Latest additions of calcite commonly precipitated at the tips of these bladed crystals resulting in a distinctive upward-flaring, scepterlike cross section (fig. 4A). More massive coatings often consist of closely packed, thicker bladed crystals lacking substantial open space between blades (fig. 4B). Bladed crystal forms are less common in fractures, especially those that dip steeply. Instead, low-relief, blocky to tabular crystals are the dominant calcite form. Textures and crystal habits can be widely variable across a single mineral coating. The mammillary surfaces or banded-travertinelike textures that are common in calcite veins below the water table are not present in coatings from the UZ. Conversely, the bladed calcite forms in the UZ are not observed in SZ settings.

Opal typically forms clear to light gray hemispheres, botryoidal masses, or thin, lumpy to smooth sheets that coat calcite substrates (figs. 4, 6, and 7). Opal is most common in lithophysal cavities where it varies from thin sheets that cover much of the mineral coating surface, to patchy sheets present in only small areas, to isolated small spheroids. Opal also is present on low-angle fracture coatings; however, it is typically absent in thin coatings on high-angle fractures. Where present, opal commonly constitutes less than 1 to 10 percent of the coating by volume and often is unevenly distributed throughout the thickness of the coating (fig. 4B).

Individual opal hemispheres usually show concentric, internal layering often expressed as shelflike or skirtlike ridges around the perimeter. This layering is most obvious on opal hemispheres liberated from their calcite substrates by acid etching (fig. 8A). These skirtlike textures present below the outermost calcite surface (fig. 8B) indicate that growth of opal and calcite occurred intermittently. In addition, internal micrometer-scale layering is present in both minerals. Removal of calcite substrates by acid etching commonly reveals delicate, lacy forms of partially coalesced opal hemispheres with flat undersides reflecting the smooth, unpitted crystal faces of the underlying calcite surface. This textural relation indicates that calcite did not become chemically unstable

EXPLANATION

A

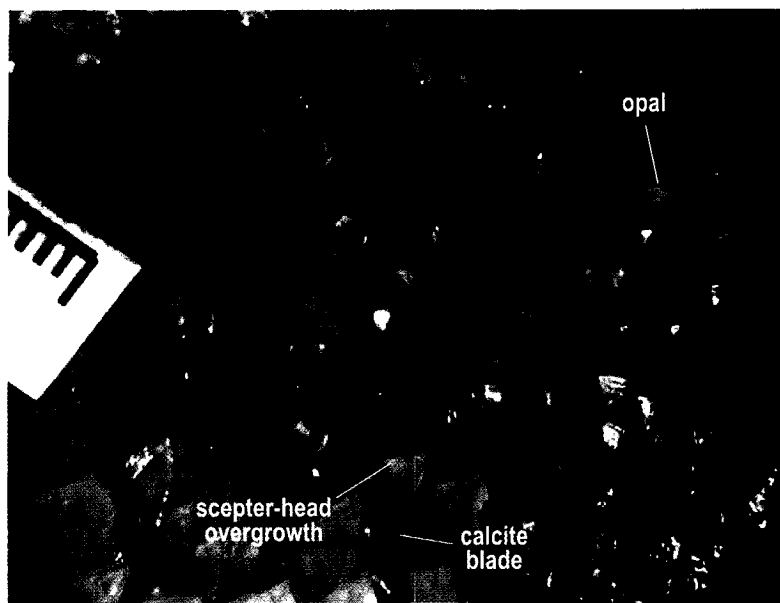
Sample - HD2059

ESF location - 3,017.8 meters from the north portal

Illumination - combination of both white and short-wave ultraviolet light

Scale - individual ticks on scale represent millimeters

Description - Oblique view of the outer surface of a lithophysal cavity coating consisting of delicate, thin (less than 0.5 millimeter thick) blades of calcite (grayish) with clear, bulbous clusters of opal (green) on top of angular, scepter-head calcite overgrowths at the tips of calcite blades



B

Sample - HD2019

ESF location - 2,881 meters from the north portal

Illumination - short-wave ultraviolet light

Description - Cross-sectional slab of a 2.5- to 3-centimeter-thick mineral coating consisting mostly of elongated calcite crystals (bluish white) growing outward from the base with multiple layers of opal (green) in the interior of the coating and small, thin layers of opal at the outer surface

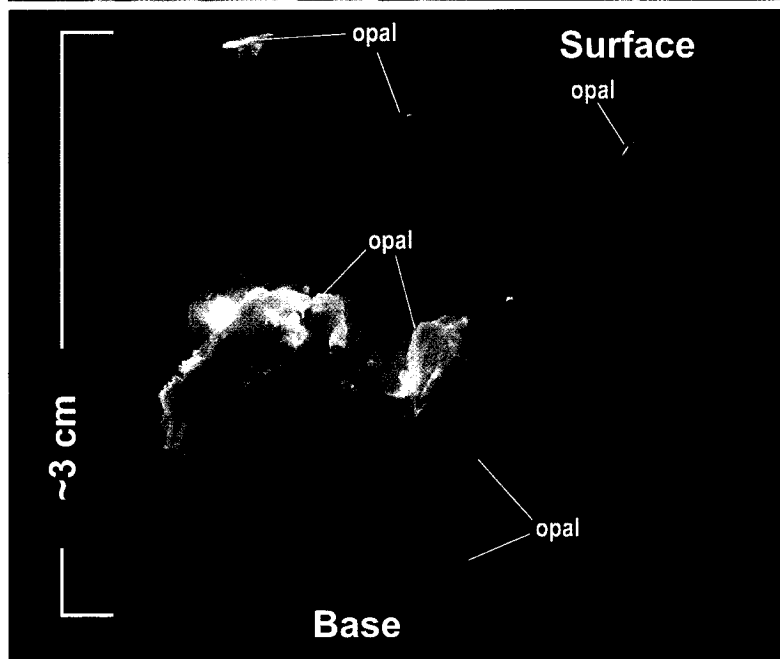


Figure 4. Calcite and opal deposits from the floors of lithophysal cavities in the Exploratory Studies Facility (ESF) tunnel, Yucca Mountain, Nevada.

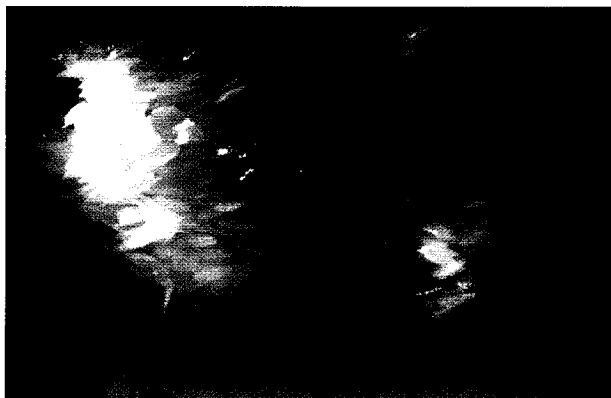
with respect to the solutions that deposited opal. Small, isolated hemispheres on well-formed calcite crystal faces have the appearance of water droplets formed by surface tension (fig. 6). In areas where opal is present in only scarce amounts on a mineral coating, it often forms at blade tips, either on top of calcite scepter heads, or between the outermost scepter-head calcite layer and the underlying, older blade (figs. 4A, 5C, and 7).

Clear evidence of corrosion or etching generally is absent on outer mineral surfaces. Crystal edges, corners, and faces of calcite crystals almost invariably appear smooth and sharp, and outer surfaces of opal hemispheres or botryoidal sheets are glassy smooth and shiny. A small number of calcite crystals may have pitted surfaces when viewed with a scanning electron microscope (Whelan and others, 1998); however, pitting also may be the result of crystal growth on a

A



B



C

Calcite blade tips:

ages of latest 1 or 2 bands

$^{14}\text{C} = 38.0 \pm 1.0 \text{ ka}$

$^{230}\text{Th}/\text{U} = 74.8 \pm 1.3 \text{ ka}$

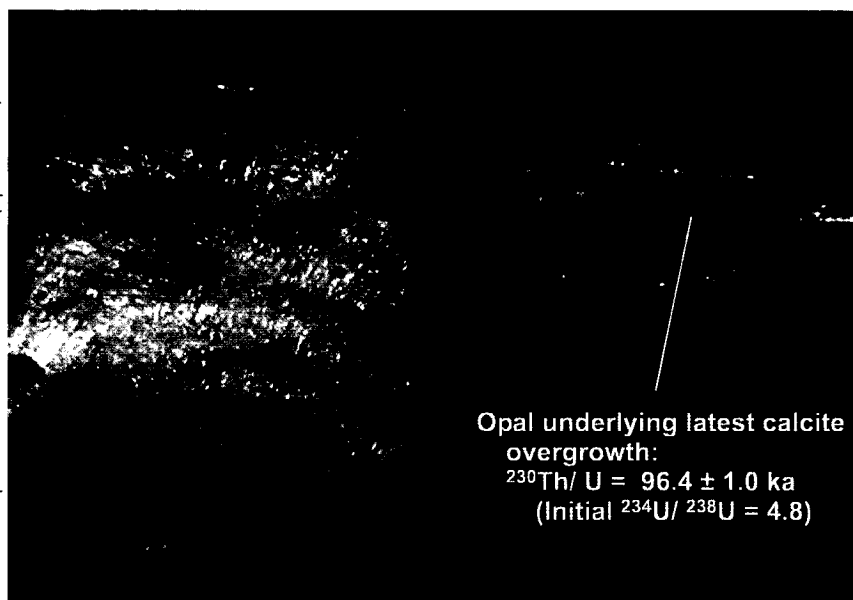
(Initial $^{234}\text{U}/^{238}\text{U} = 4.7$)

Calcite blade interiors:

composite of lower bands

$^{230}\text{Th}/\text{U} = 254 \pm 21 \text{ ka}$

(Initial $^{234}\text{U}/^{238}\text{U} = 3.6$)



Opal underlying latest calcite overgrowth:

$^{230}\text{Th}/\text{U} = 96.4 \pm 1.0 \text{ ka}$

(Initial $^{234}\text{U}/^{238}\text{U} = 4.8$)

EXPLANATION

Sample - HD2059

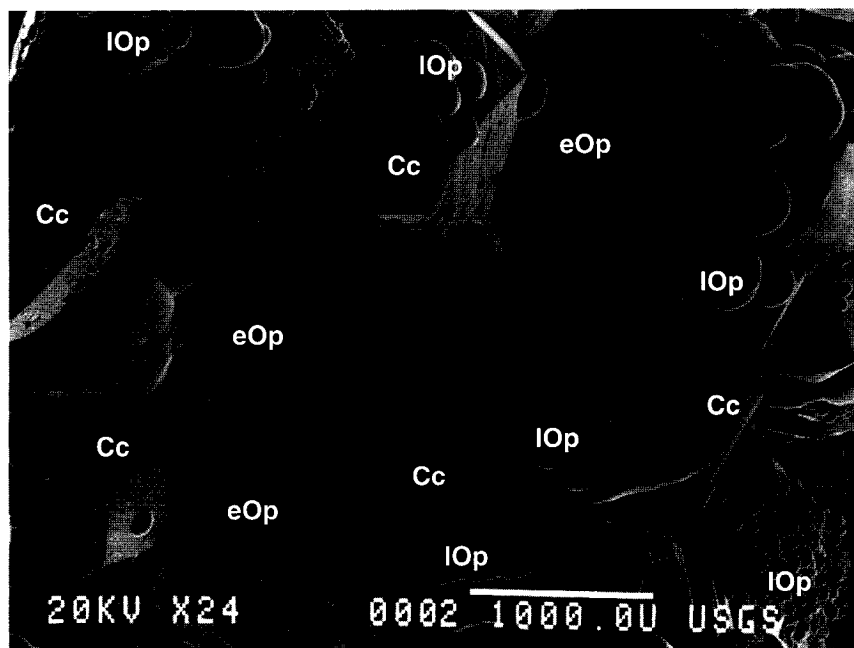
ESF location - 3,017.8 meters from the north portal

Scale - individual ticks on scale represent millimeters

Description - (A) Side view of very thin (less than 0.5 millimeter), fragile bladed calcite showing banded growth layers. Top of photo is toward the direction of outward mineral growth. (B) Top view of same specimen showing thickness of blades and scepter-head blade tops. (C) Magnification of the tips of two separate calcite blades from the same sample. Blade tip on left shows a sequence of the last 3-5 growth bands. Blade tip on right shows the latest scepter-head calcite overgrowth covering an opal hemisphere deposited on the former blade tip.

Analytical results - Ages determined using ^{14}C and $^{230}\text{Th}/\text{U}$ methods (and initial $^{234}\text{U}/^{238}\text{U}$ activity ratios) for subsamples represented by examples shown in C. Ages are given in thousands of years before present (ka).

Figure 5. Calcite blades with minor opal from the floor of a lithophysal cavity and geochronological results for calcite and opal subsamples, Exploratory Studies Facility (ESF) tunnel, Yucca Mountain, Nevada.



EXPLANATION

Sample - HD2008

ESF location - 2,272 meters from the north portal

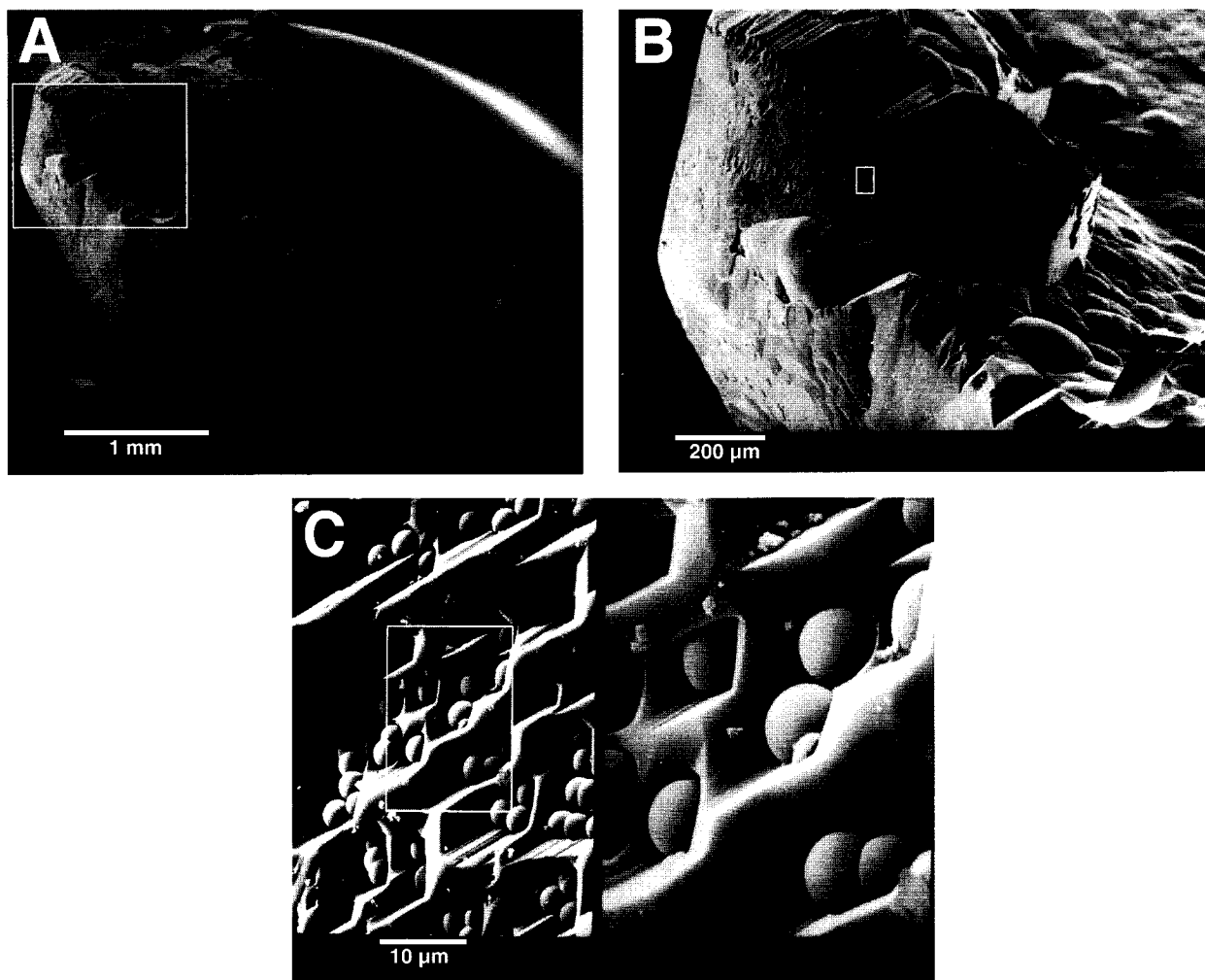
Scale - white bar represents 1 millimeter

Generalized paragenesis - earlier, botryoidal opal (eOp) followed by angular calcite (Cc) followed by small, rounded hemispheres of later opal (IOp)

Analytical results - Uranium-series disequilibrium results for seven subsamples are correlated only generally with image. In general, early opal (including single large hemispheres) shows oldest ages, calcite shows intermediate ages, and late opal shows youngest ages (smallest hemispheres represented by -U7R). Ages are given in thousands of years before present (ka).

<u>Subsample</u>	<u>Type</u>	<u>$^{230}\text{Th}/\text{U}$ Age (ka)</u>	<u>Initial $^{234}\text{U}/^{238}\text{U}$</u>
-U1	Single large hemisphere	273±9	1.51
-U2	Single large hemisphere	295±16	1.32
-U3	IOp±Cc	167±4	2.23
-U4	Cc±IOp	250±7	1.96
-U5	eOp rims	340±20	1.50
-U6R	IOp after 1N HCl	201±4	2.06
-U7R	IOp after 0.1N HCl	134±7	2.61

Figure 6. Secondary electron image of the outer growth surface from a fracture coating and geochronological results from calcite and opal subsamples, Exploratory Studies Facility (ESF) tunnel, Yucca Mountain, Nevada.



EXPLANATION

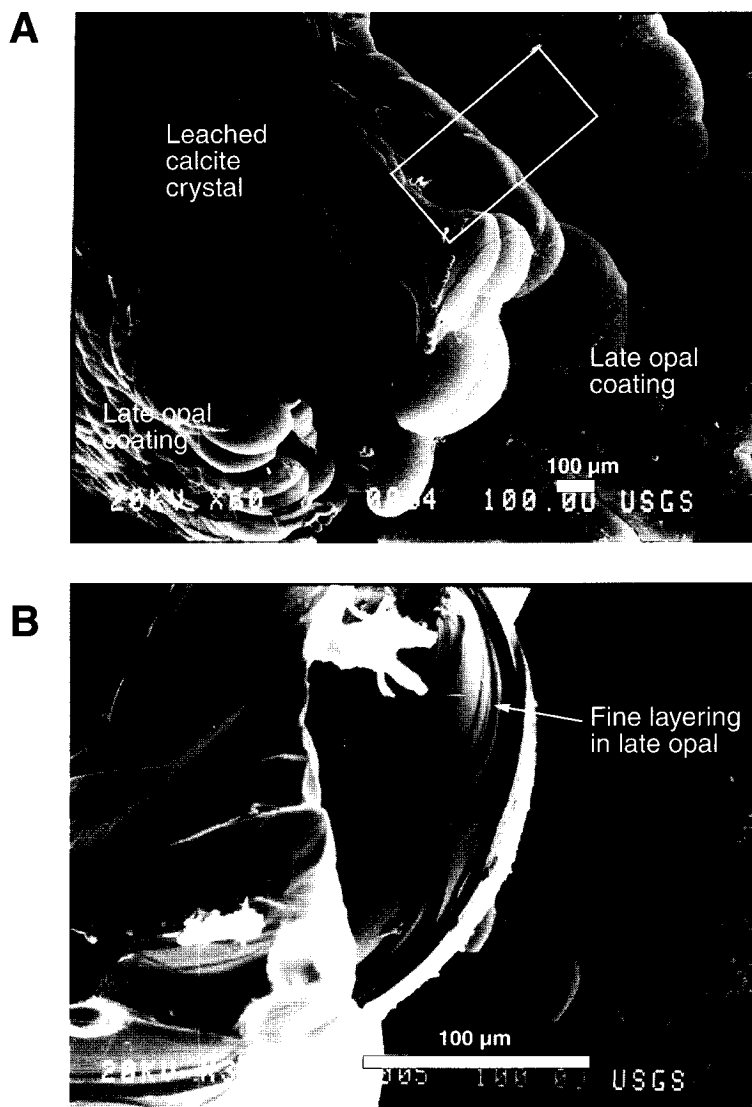
Sample - HD2057

ESF location - 2,962.2 meters from the north portal

Scale - white bars on images represent the given length in millimeters (mm) or micrometers (μm)

Description - (A) Individual narrow blade of calcite with a thin coating of botryoidal opal followed by growth of scepter-head calcite at blade tip and small euhedral calcite crystals oriented perpendicular to the blade axis. Blade is mounted on its side, but was originally in an upright position. (B) Magnified view of area in white box shown in A. Rounded surface of earlier opal-coated blade is overgrown by later calcite with patchy areas of abundant pits. (C) Magnified view of area in white box shown in B. Pits contain one or more opal hemispheres shown at greater magnification on the right side of the split image. Angular calcite has sharp corners and edges indicative of crystal growth rather than corrosion. Pits may form after deposition of 1- to 3-micrometer-diameter hemispheres of opal because calcite commonly does not grow in direct contact with preformed opal.

Figure 7. Secondary electron images of a single blade of calcite and opal at successively greater magnification, Exploratory Studies Facility (ESF) tunnel, Yucca Mountain, Nevada.



EXPLANATION

Sample - HD2008

ESF location - 2,272 meters from the north portal

Scale - white bars on images represent 100 micrometers (µm)

Description - (A) Outer mineral coating with calcite removed by acid leaching leaving opal residue. Rounded opal hemispheres in the center of the image originally projected above the surface of the outermost calcite crystal, but now show stairstep growth that extended below the latest growth surface. (B) Magnified view of the approximate area shown within the white box in A (tilted and rotated) showing fine layering of opal with individual layer thicknesses on the scale of micrometers.

Figure 8. Secondary electron image of the outer surface of a mineral coating after removal of calcite with dilute hydrochloric acid leaching, Exploratory Studies Facility (ESF) tunnel, Yucca Mountain, Nevada.

surface contaminated with impurities that inhibit calcite deposition (for instance, opal spheres at the centers of the pits shown in fig. 7C). In addition, basal porous zones may be present as scattered patches of higher porosity calcite in a narrow zone between the calcite coatings and the underlying vapor-phase minerals. These zones typically contain thin, upright blades of calcite that locally are detached from the substrate, giving the impression of being suspended. Some of these porous zones appear to host tiny calcite overgrowths that postdate the formation of the porosity. These features are most common in lithophysal cavities. Approximately 20 to 50 percent of mineralized lithophysae have porous basal zones; however, when present, these zones may occupy only a small percentage of the entire floor of an individual coating. Porous basal zones are much less common in fracture deposits, perhaps because fractures typically lack a granular vapor-phase substrate. It is unclear if these textures are related to variations in crystal growth or if they were formed by dissolution of previously formed calcite near the tuff or vapor-phase contact. Initial attempts to date the timing of porous basal zone development yielded ambiguous results (see Radiocarbon Data section).

Paragenesis

A microstratigraphic framework is useful for evaluating temporal variations in conditions of fluid flow, environmental factors, and precipitation mechanisms since tuff emplacement. Detailed reconstruction of the sequence of mineral deposition in a given sample is often difficult because of the complexities of mineral forms and small-scale variations observed in most coatings. However, petrographic examination of coating cross sections (Whelan and others, 1998) provides a generalized paragenesis that largely is consistent throughout the UZ (fig. 9).

In lithophysal cavities (fig. 9A), the sequence of post-eruptive deposition was initiated immediately after lithophysae formation resulting in high-temperature alteration of the wall rock (producing a thin bleached zone) and deposition of vapor-phase minerals covering all cavity surfaces. Liquid water could not have percolated through the rock mass until temperatures in the tuff cooled to approximately 100°C. The earliest minerals deposited from aqueous solutions commonly consist of a basal layer of massive

silica (undifferentiated quartz and chalcedony with minor opal) directly overlying the vapor-phase layer, with minor amounts of basal calcite occasionally present below the silica (Whelan and others, 1998, p. 6). Clusters of radiating quartz prisms may be present on top of the massive silica. Calcite with inter-layered opal formed on top of these earlier silica phases. Chalcedony and quartz are restricted to this early paragenesis; they do not reappear later within the thicker accumulations of calcite and opal.

Calcite deposited immediately on top of the earlier formed silica phases is dominated by blocky to tabular textures forming massive, coarsely crystalline layers. Some of this massiveness may result from infilling between tabular calcite crystals by later deposition. Cross sections often reveal internal structures indicating that contemporaneous layers follow contorted patterns. In contrast, later formed calcite has a greater tendency to form bladed crystals, although coatings often may have massive textures that extend to their outer growth surfaces. Where later formed calcite blades are present, the most recent deposition commonly is concentrated at blade tips, resulting in the scepter-head morphology. Although calcite constitutes the bulk of mineral coatings, opal often represents some of the latest deposition on outer growth surfaces. Opal sheets or strands of small hemispheres in the interior of mineral coatings commonly follow calcite crystal surfaces, marking past growth surfaces that have been covered by later deposits. The most recent depositional event on any single coating usually is identifiable only at a millimeter scale; neither calcite nor opal exclusively occupies the outermost microstratigraphic position. The complex growth sequences of a young calcite blade are illustrated by successively magnified secondary-electron SEM images (fig. 7). These SEM images also offer evidence that although calcite can appear pure on a macroscopic scale, finely disseminated opal also may be present and can contribute to the resulting chemical and isotopic characteristics of a calcite subsample.

High-angle fractures tend to have a slightly different and more simplified microstratigraphy (fig. 9B). Fractures commonly lack vapor-phase mineral assemblages, though they may have thin bleached zones and smectite-zeolite fracture coatings (Levy and others, 1996). Also, paragenetically early massive silica phases are commonly absent. The absence of these two features may be related to the possibility of creating fractures in the bedrock after the

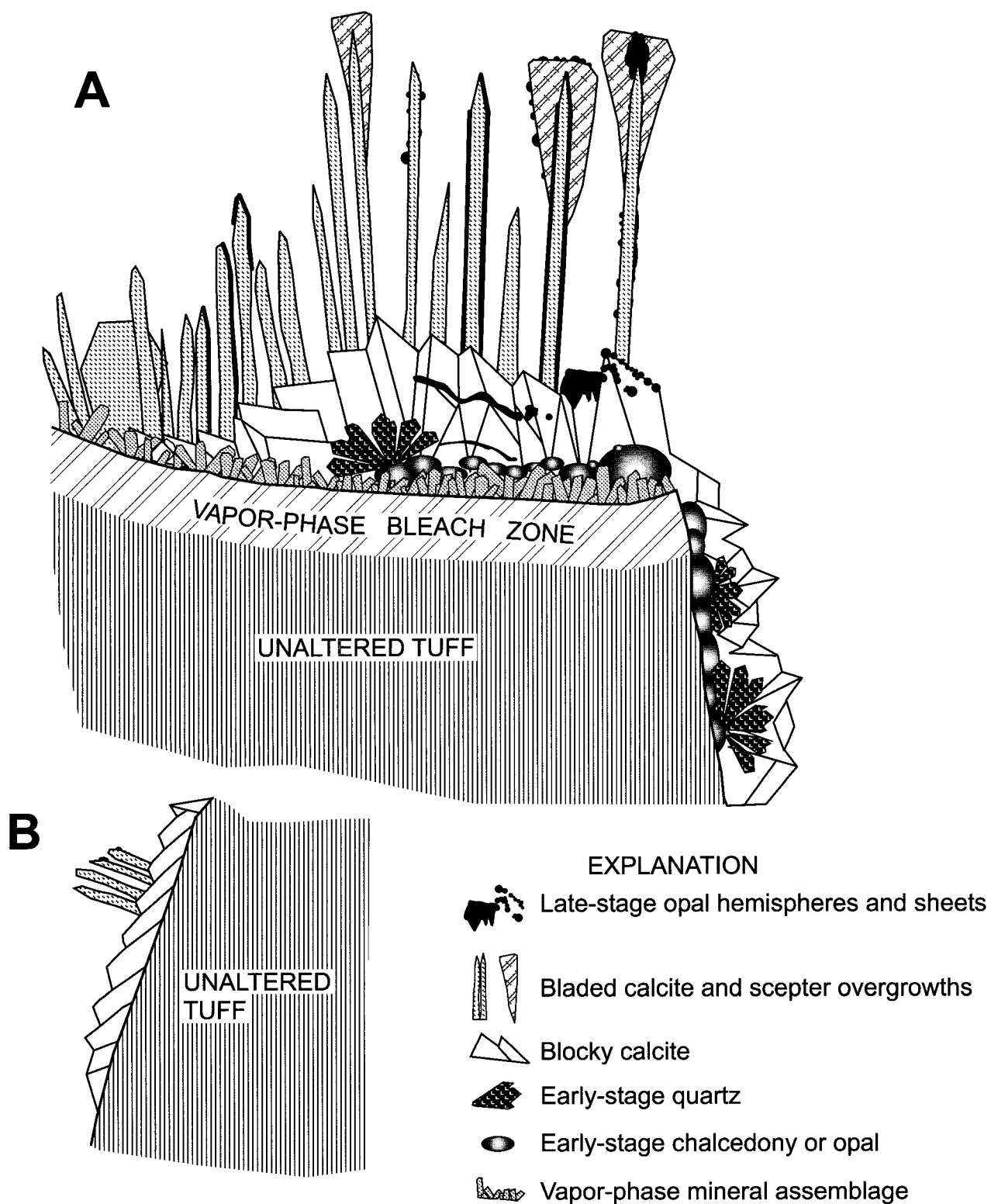


Figure 9. Typical mineral sequences coating (A) lithophysal cavity floors, and (B) steeply dipping fracture surfaces (modified from Whelan and others, 1998, fig. 3).

tuffs cooled to subboiling temperatures, compared to lithophysae that were created only during initial cooling. Coatings typically consist of blocky to tabular calcite deposited directly on the fracture wall. Calcite blades and opal are rare in these settings.

RADIOCARBON AND $^{230}\text{Th}/\text{U}$ AGES OF CALCITE AND OPAL

An understanding of mineral ages and growth histories is essential in order to use calcite and opal deposits to infer information about fracture flow in the Yucca Mountain UZ on time scales relevant to nuclear waste isolation. If UZ percolation was initiated shortly after the ash-flow tuffs cooled to less than 100°C, deposits may represent a total history of nearly 13 million years (m.y.). Because time scales of many thousands of years are required to safely isolate radioactive decay products (U.S. Department of Energy, 1998, section 2.1), sampling and analytical techniques that are most likely to yield geochronological information for the last half-million years were used in this study. Results of both radiocarbon dating of calcite and uranium-series disequilibrium dating of calcite and opal are described in this section.

Mineral textures indicate that the youngest material was added to the deposits on the outermost surfaces where crystals grew in unrestricted void space. Therefore, most subsamples analyzed in this report were obtained from outermost mineral surfaces. In addition, subsample thickness was minimized so that analyses represent materials deposited over the shortest time spans.

Radiocarbon Data

The carbon incorporated into calcite at the time of formation may include small amounts of the radioactive isotope ^{14}C , which can be used as a geochronometer for materials with ages up to 45 ka. The diversity of carbon-bearing compounds in nature has led to the wide use of the ^{14}C geochronometer on a variety of organic and inorganic materials. Radiocarbon analyses of 31 calcite subsamples from 18 sample sites in the ESF were completed for this study (fig. 3).

Calcite at Yucca Mountain acquires ^{14}C from the bicarbonate (HCO_3^-) ion dissolved in water perco-

lating through the UZ. If this water had an atmospheric ^{14}C composition at the time of deposition, the ^{14}C age of an instantaneously deposited calcite subsample would accurately reflect the true age of deposition. However, various mechanisms may cause ^{14}C contents of the fracture water to deviate from an atmospheric ^{14}C composition.

Stable carbon and oxygen isotope studies have shown that most of the calcite in the UZ precipitated from percolating meteoric water that acquired its isotopic signature from the overlying soil (Whelan and others, 1994, 1998; also see Carbon and Oxygen Isotopes in Unsaturated-Zone Calcite section). Carbon in this water is a mixture of modern carbon derived from soil carbon dioxide (CO_2) gas associated with the resident plant community and up to 50 percent inorganic carbon derived from dissolution of older calcite in calcrete (Whelan and others, 1994). Because calcrete spans a wide range of ages, its dissolution will contribute carbon ranging from 0 to 100 pmc. In theory, present-day infiltration could enter the UZ with as little as 50 pmc or, effectively, an initial age as old as one ^{14}C half-life (about 5,730 yrs). Samples of pore water from bedded tuffs in both shallower (PTn) and deeper (Calico Hills Formation) parts of the UZ commonly have ^{14}C values between 80 and 100 pmc (Yang and others, 1996, figs. 9 through 13), whereas ^{14}C in representative perched water pumped from the UZ varies from 27 to 29 pmc [samples SD-7 (3/16) through SD-7 (3/21), and UZ-14 PT-2 and UZ-14 PT-4, Yang and others, 1996, table 7].

Another reason why ^{14}C ages in UZ calcite may not accurately reflect true deposition ages is that the ^{14}C geochronometer starts at the time of infiltration rather than the time of deposition. If travel times for fracture water are greater than hundreds to thousands of years, substantial amounts of the initial ^{14}C in the dissolved HCO_3^- will have decayed prior to its incorporation into calcite. Additionally, old calcite crystal faces may be contaminated by more modern ^{14}C sources such as HCO_3^- in percolating waters or CO_2 in migrating gases. Rock gases contain CO_2 concentrations of hundredths to tenths of a percent with ^{14}C ranging from 26 to 112 pmc (Yang and others, 1996, table 9). Exchange between these gases and the calcite crystal faces could result in a thin ^{14}C -enriched layer and erroneously young ^{14}C ages.

Despite these limitations, radiocarbon data are useful to constrain ages of calcite deposited in the UZ. The resulting ^{14}C ages also were compared with those

obtained by uranium-series disequilibrium dating to help evaluate the process of mineral deposition (see Interpretation of Ages section).

Sampling Methods

Most subsamples analyzed for ^{14}C are from calcite crystal faces exposed on the outer surfaces of mineral coatings. Samples were cleaned with a fine, high-pressure stream of deionized water followed by an ultrasonic deionized water bath prior to subsampling. This treatment removed any loose or water-soluble material from the crystal faces. Secondary electron images of calcite crystal faces subjected to prolonged (more than 20 minutes) ultrasonic cleaning in deionized water revealed etched surfaces, indicating that the outermost calcite was dissolved. Although some calcite was likely removed during the routine 2.5-minute ultrasonic cleaning, secondary electron images of the cleaned calcite crystal faces are typically smooth and not pitted. Some of the samples also received a 10-second etching with 0.2 normal HCl to ensure removal of any contaminated outermost surfaces. Comparable, non-HCl-etched samples also were collected from the same site in three cases (HD2055, HD2065, and HD2067).

Subsample powders were milled from calcite crystal faces at 10x to 20x magnification with a carbide dental bur mounted in a hand-held rotary drill. Milling depths were variable. Based on the diameter of the bur, average milling depths probably ranged from 0.1 to 0.3 mm. Resulting weights for most subsamples ranged from 10 to 20 milligrams (mg). Subsamples of delicate, bladed crystals were obtained by breaking off and pulverizing one or two crystals from the coating surface.

Distribution of Radiocarbon Ages

Uncorrected ^{14}C ages for the 29 subsamples of calcite from outer coating surfaces range from 16.0 to 43.7 ka (Appendix 1). The age distribution (fig. 10) shows a prominent mode between 30 and 34 ka with values extending to both older and younger ages. Of the two attempts to date calcite from basal positions in the coatings, one analysis yielded an essentially radiocarbon "dead" age of 49.9 ka (HD2067ca), whereas the second resulted in an apparent age in the middle of the range of outermost calcite ages (33.6 ka, HD2065ca).

Radiocarbon ages are from samples more or less evenly distributed between distances of 1,400 to

3,500 m in the ESF (fig. 11). No correlation is apparent between ^{14}C age and distance in the ESF, or between ^{14}C age and lithostratigraphic depth, which increases from the north portal of the tunnel downsection to the potential repository horizon. None of the 29 subsamples of outer surfaces of calcite have "dead" radiocarbon ages. It also is clear that the outer surface of a single mineral coating was not formed during a single depositional event because multiple subsamples from the same coating can have wide ranges of apparent ^{14}C ages. Of the eight samples with multiple age determinations of outermost calcite, six subsamples have age differences that are larger than the limits of analytical error. Both samples with the youngest subsample ages (16.0 ka for 2019cc and 20.1 ka for 2006ca) also have other subsamples with much older apparent ages (up to 41.8 ka for 2019cb and 37.4 ka for 2006cb; dotted lines in fig. 11). The range of ages observed for single growth surfaces indicates that mineral coatings developed from complex growth histories rather than single depositional events.

Ten of the analyzed calcite subsamples are from two zones in the ESF containing anomalously large $^{36}\text{Cl}/\text{Cl}$ ratios (fig. 11) that have been interpreted as bomb-pulse signatures and evidence for fast (less than 50 yrs) flow through fractures to the repository horizon (Fabryka-Martin and others, 1996, fig. 5–1; Fabryka-Martin and others, 1997, fig. 6–1). These two zones are associated with the Drill Hole Wash Fault at approximately 1,931 m and the Sundance Fault at approximately 3,593 m (fig. 2). Both zones have multiple chlorine sample sites containing $^{36}\text{Cl}/\text{Cl}$ ratios greater than $1,500 \times 10^{-15}$ (Fabryka-Martin and others, 1997, fig. 6–1). Although the locations of mineral coatings in these two zones generally are not from the same fractures sampled for chlorine analyses, they are often very close [for example, 3,545.4 m from the north portal of the ESF for sample HD2071 (Appendix 1, this report) compared to 3,545 m for sample E160 of Fabryka-Martin and others, 1997, Appendix B]. In contrast to the chlorine isotope data, the range of radiocarbon ages for the 10 subsamples in these two zones is the same as the range for samples in areas containing background levels of $^{36}\text{Cl}/\text{Cl}$.

Interpretation of radiocarbon ages is complicated not only by the issues of the ^{14}C content of the infiltrating water, traveltime, and potential gas exchange, but also by depositional rates that are likely to be slow (see Interpretation of Ages section). Therefore, radiocarbon ages from these calcite subsamples are unlikely to represent discrete depositional events.

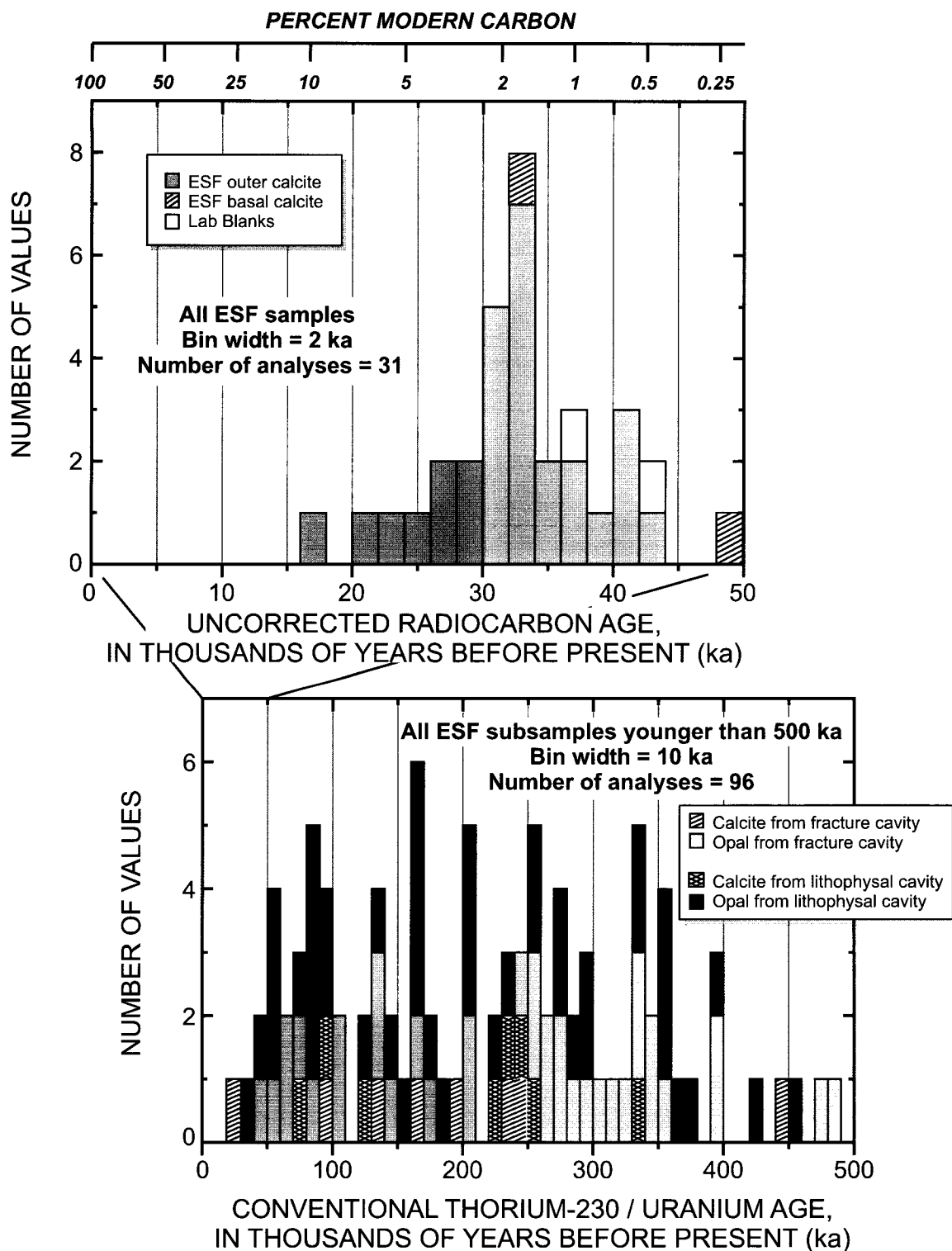


Figure 10. Distribution of radiocarbon and uranium-series disequilibrium ages for subsamples of calcite and opal from the Exploratory Studies Facility (ESF) tunnel, Yucca Mountain, Nevada.

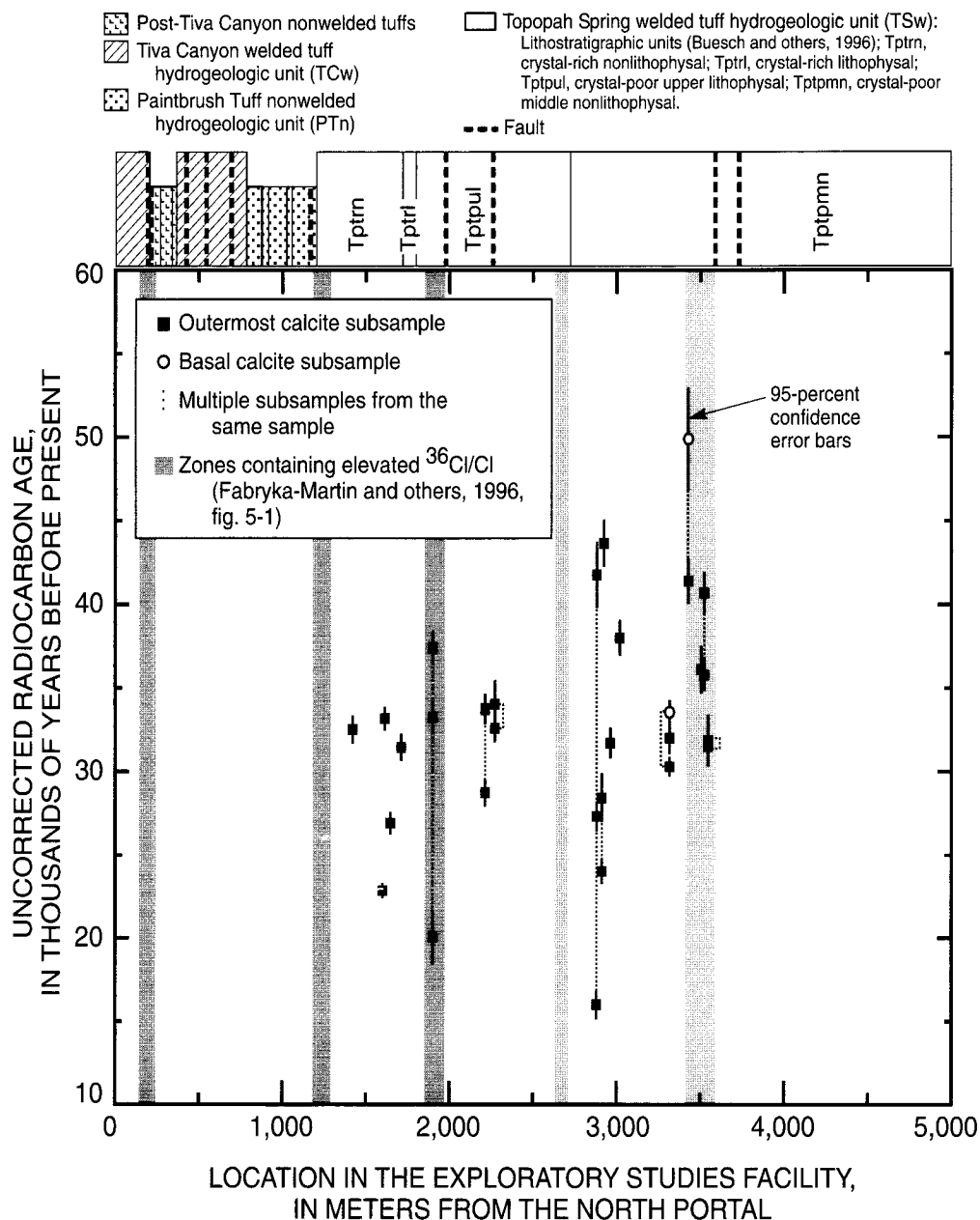


Figure 11. Uncorrected radiocarbon ages for subsamples of calcite relative to distance from the north portal of the Exploratory Studies Facility tunnel (fig. 2), Yucca Mountain, Nevada.

Evidence, including the observation of micrometer-scale growth laminae, different ^{14}C ages for multiple subsamples of the same growth surface, and much older $^{230}\text{Th}/\text{U}$ ages for the same growth surfaces dated by ^{14}C (see Uranium-Series Disequilibrium Methods and Data section), implies that simple interpretation of ^{14}C analytical results may yield erroneous conclusions concerning the history of mineral growth. An example of a simple case would be a 1-mm-thick coating consisting of two layers of calcite where the outer

layer has a modern ^{14}C age (100 pmc), and the underlying layer was deposited at 1 Ma (0 pmc). The true average age (equal to half the difference between oldest and youngest ages added to the youngest age) of the entire coating is 500 ka. However if the entire coating were analyzed for ^{14}C , a value of 50 pmc would be obtained, corresponding to an apparent ^{14}C age of 5.7 ka. The simple interpretation of the analytical results clearly misrepresents the true age relations in this coating. These issues are described more fully

in the Interpretation of Ages section along with a depositional model that simulates individual subsamples as mixtures of multiple layers with different ages.

Although inherent complexities are present, ^{14}C values indicate the presence of calcite with ages less than 44 ka at the potential repository horizon. Measured ^{14}C values greater than about 1.2 pmc (uncorrected ^{14}C age of about 37 ka) are clearly above the analytical blank value for ancient calcite measured in this study. Although ^{14}C in the gas and liquid phases may not be in equilibrium, exchange between the two phases is not likely to change the ^{14}C composition of the percolating solution. Yang and others (1996, p. 45) suggested that the mass of carbon present in HCO_3^- dissolved in the water is much larger than that in the CO_2 in the migrating gas phase, and is buffered from modification with a potentially younger carbon component through gas exchange. Therefore, the young carbon component in calcite subsamples is indicative of at least some latest Pleistocene or younger UZ water flux and calcite addition to these coatings.

The possibility of mechanically integrating younger and older layers during sampling can be addressed by experiments designed to remove the thin, outermost layers by acid etching. Comparisons of resulting ages from etched and unetched subsamples should indicate whether the thin rims of crystals contribute a distinctly younger component. Two calcite samples from the ESF were treated in this manner. Both showed resolvable older ages for the surface-etched subsample (32.0 ± 0.9 ka compared to 30.3 ± 0.5 ka for the HD2065cb-HD2065cc pair, and 28.4 ± 1.4 ka compared to 24.0 ± 0.7 ka for the HD2055cb-HD2055ca pair; Appendix 1). The amount of material removed from the outer surface during the etching process was not quantified; however, it is likely to be less than tens of micrometers.

The age of a thin, porous basal zone of calcite showing the appearance of partial dissolution was investigated to assess whether these zones represent recently active flow pathways. Macroscopically, the calcite in these dissolution zones adjacent to tuff substrates is anhedral and appears corroded. However, SEM observations show that although the calcite crystals are not euhedral, their surfaces are smooth and unpitted (Whelan and others, 1998, fig. 4e and 4f). Tiny, toothlike overgrowths of optically continuous calcite that appear newly formed also are common in these zones. Subsample HD2065ca consists of calcite

from a porous zone at the base of a thick calcite coating and had a ^{14}C age of 33.6 ± 0.7 ka. Two additional subsamples from the outermost portions of the same sample had ages of 32.0 ± 0.9 (HD2065cb) and 30.3 ± 0.5 ka (HD2065cc). Although analytically resolvable, the similarity of ages between basal and outer calcite in this coating is unexpected. Modern carbon constitutes 1.73 percent of the carbon in HD2065ca, indicating at least some component of young calcite. Therefore, the corroded-looking calcite making up the framework of this basal porous zone is either not ancient (older than 50 ka), as suggested by its position in the coating, or it contains a small amount of young calcite either as overgrowths or through exchange of carbon with younger CO_2 or HCO_3^- . Outermost opal from this same sample (HD2065-U1R) has a $^{230}\text{Th}/\text{U}$ age of 86.1 ± 1.0 ka; however, uranium-series ages for this or other basal-zone calcite are not available. Additional efforts are required to understand the timing of these porous basal zones in calcite coatings.

Uranium-Series Disequilibrium Methods and Data

Uranium-series disequilibrium dating (specifically $^{230}\text{Th}/\text{U}$ ages) was applied to a large number of calcite and opal subsamples collected from the ESF (118 analyses from 56 different sample sites, fig. 3). Determination of reliable $^{230}\text{Th}/\text{U}$ ages on these materials depends on the amount of uranium and thorium incorporated into the material at the time of formation. Ideally, the U/Th ratio should be large so that any ^{230}Th present at the time of mineral formation is small relative to that produced by in-situ decay of ^{234}U . Thorium concentrations are minimal in most calcite and opal deposits from the ESF because of the insolubility of thorium species in low-temperature, oxidizing aqueous solutions and the removal of thorium-bearing particulate matter in the upper 10 to 20 m of the UZ. In contrast, uranium concentrations differ greatly between the two phases; calcite typically contains less than 0.05 microgram/gram ($\mu\text{g}/\text{g}$) uranium whereas pure opal commonly contains more than 30 $\mu\text{g}/\text{g}$. As a consequence, the minimum amount of opal necessary for analysis by thermal ionization mass spectrometry is much smaller (less than 0.0002 g) than calcite (0.05 to 0.2 g). Therefore, a larger number of $^{230}\text{Th}/\text{U}$ age determinations are given for opal than for calcite in this report.

Sampling Procedures

Thin opal sheets or hemispheres from outermost growth surfaces were obtained by prying with a sharp needle or by liberating the opal as a residue after soaking the outer surface in dilute nitric, acetic, or hydrochloric acid. These procedures resulted in relatively pure opal without adhering calcite. Experiments were not performed to assess the possibility of adsorption of ^{230}Th onto opal surfaces from leach solutions; however, ^{230}Th adsorption is not expected to be a problem because of the low concentrations of uranium in calcite relative to opal. In addition, experiments with opal residues indicate that dilute-acid leaching does not significantly affect uranium and thorium isotope compositions of small opal fragments (Neymark and Paces, 2000, p. 150). In subsamples where calcite and opal were not separated, total digestion of the mixtures resulted in concentrations and isotopic compositions that are dominated by the opal component because of its greater uranium concentration. The thinnest subsampled opal layers are about 0.1 mm thick, which is still up to two orders of magnitude greater than the finest laminations and smallest hemispheres (figs. 6, 7, and 8). A few subsamples from more massive opal were obtained by grinding off outer surfaces using carbide or diamond dental burs to obtain a powder.

Calcite was subsampled by using carbide burs to remove a thin layer from outermost growth surfaces over a broader area (typically on the scale of square centimeters). Subsample thickness was generally limited to the outermost 0.1 to 0.5 mm; however, it is difficult to restrict powder collection to a layer of constant thickness that represents a uniform depositional episode. Calcite was dissolved completely first by using HCl, followed by removal of the supernatant and attack of any residue with concentrated hydrofluoric acid to ensure that fine opal present in the subsample was included in the analysis. The two digestions were recombined so that the analyses represent total digestions of all material present in the subsample.

Uranium and Thorium Isotopes and $^{230}\text{Th}/\text{U}$ Ages

Uranium and thorium concentrations vary by more than four orders of magnitude in ESF calcite and opal (approximately 0.001 to greater than 10 $\mu\text{g/g}$, fig. 12). Opal residues (undissolved opal after removal of adhering calcite with HCl) have uranium concentra-

tions of 10.6 to 282 $\mu\text{g/g}$ and thorium concentrations typically lower than 0.5 $\mu\text{g/g}$ resulting in large U/Th ratios. Mineral classifications used in figure 12 and Appendix 2a are based on visual examination using a low-power binocular microscope and may not identify the presence of fine inclusions of opal in calcite (for example, fig. 7C) or small amounts of calcite adhering to unleached opal. Pure calcite subsamples from mineral coatings where opal is completely absent (open circles on fig. 12) have thorium concentrations similar to opal residues but have substantially lower uranium concentrations (0.007 to 0.047 $\mu\text{g/g}$) resulting in U/Th ratios 1,000 to 100,000 times lower than those observed in opal residues. As a consequence, isotopic ratios for pure calcite subsamples typically have greater analytical uncertainty (particularly for $^{230}\text{Th}/^{238}\text{U}$) and are less likely to provide precise age determinations relative to opal or to calcite with fine opal inclusions. Calcite subsamples lacking visible opal but from deposits containing opal elsewhere on the coating (half-filled circles on fig. 12) have higher uranium concentrations (from about 0.1 to 0.7 $\mu\text{g/g}$) relative to calcite from opal-free deposits. These values overlap the uranium concentration range for calcite plus opal (filled circles on fig. 12) and most likely represent calcite that contains microscopic opal not identified under low magnification.

Most subsamples have ^{230}Th abundances that can be derived from the observed abundances of ^{234}U and ^{238}U parent isotopes allowing calculation of $^{230}\text{Th}/\text{U}$ ages (points to the left of the dashed infinite-age line on fig. 13). Very few analyses have $^{230}\text{Th}/^{238}\text{U}$ values in excess of those that define the infinite-age line, indicating that neither calcite nor opal has been strongly affected by uranium loss resulting from leaching of previously formed opal. Substantial amounts of postdepositional uranium gain affecting old opal (at or slightly above the secular equilibrium value of 1) also are unlikely because of the lack of measured isotopic compositions with low $^{234}\text{U}/^{238}\text{U}$ values and $^{230}\text{Th}/^{238}\text{U}$ values less than one. Therefore, postdepositional exchange of uranium or thorium between these minerals and migrating solutions (open-system behavior) is not obvious. However, the isotopic compositions of these subsamples do not follow conventional patterns of $^{234}\text{U}/^{238}\text{U}$ – $^{230}\text{Th}/^{238}\text{U}$ evolution. Unlike minerals formed from solutions with a narrow range of $^{234}\text{U}/^{238}\text{U}$ that then follow closed-system evolution trajectories (for example, Devils Hole calcite from Ludwig and others, 1992, shown in

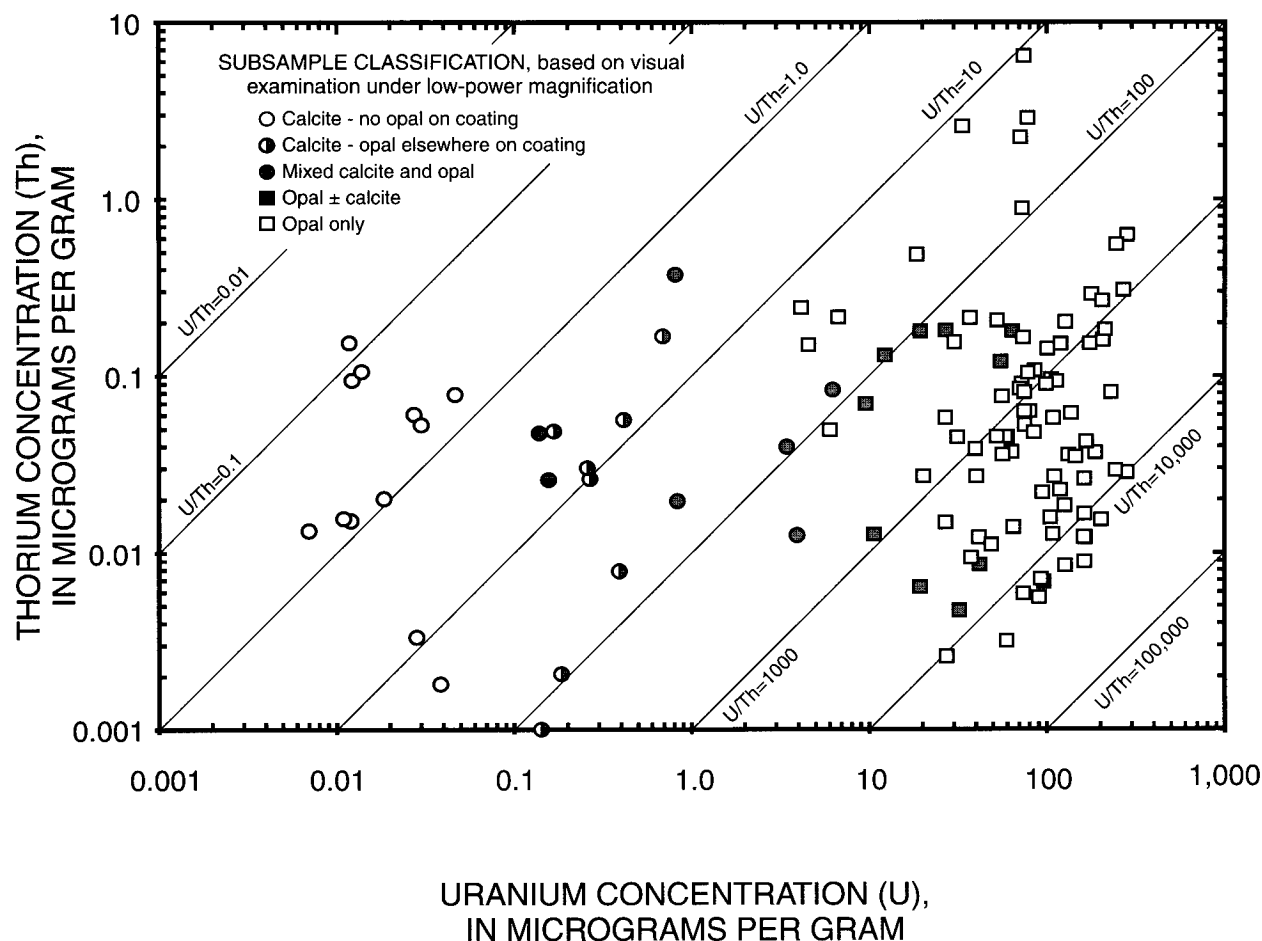


Figure 12. Uranium and thorium concentrations for subsamples of calcite and opal from the Exploratory Studies Facility tunnel, Yucca Mountain, Nevada.

fig. 13), Yucca Mountain UZ mineral data show a much wider spread in measured $^{234}\text{U}/^{238}\text{U}$ with values ranging from close to secular equilibrium (1.0) to greater than 8. In addition, although subsamples rarely contain excess ^{230}Th , analyses are displaced toward smaller values of $^{230}\text{Th}/^{238}\text{U}$ and larger values of $^{234}\text{U}/^{238}\text{U}$ relative to the expected values for materials evolving under simple closed-system conditions.

The distribution of conventional $^{230}\text{Th}/\text{U}$ ages spans a wide range from 28 to greater than 700 ka (Appendix 2b). Ninety-six of the 102 analyses from which ages can be calculated have apparent $^{230}\text{Th}/\text{U}$ ages less than 500 ka (fig. 10). Four of the six subsamples with ages greater than 500 ka are from microstratigraphic locations other than outermost growth surfaces although they still may be within the younger parts of the coatings. The bulk of the $^{230}\text{Th}/\text{U}$ ages are

fairly evenly distributed between 40 and 400 ka (fig. 10).

The youngest age reported here (28.3 ± 1.4 ka) falls within the range of two analyses (26 ± 2 and 30 ± 4 ka) reported as calcite by Szabo and Kyser (1985, table 4; and 1990, table 1), and eight analyses presented here have ages between 28 and 60 ka. However, the similarities between young ages given in this report and those in the previous studies are considered to be coincidental because of the probability that the two young "calcite" ages reported by Szabo and Kyser were affected by laboratory fractionation of uranium and thorium during chemical separation. Both young "calcite" ages of Szabo and Kyser were determined from relatively large subsamples containing mixtures of calcite and opal. The two phases were chemically separated by dilute acid leaching after heating to 900°C for 8 hours or more. Severe heating

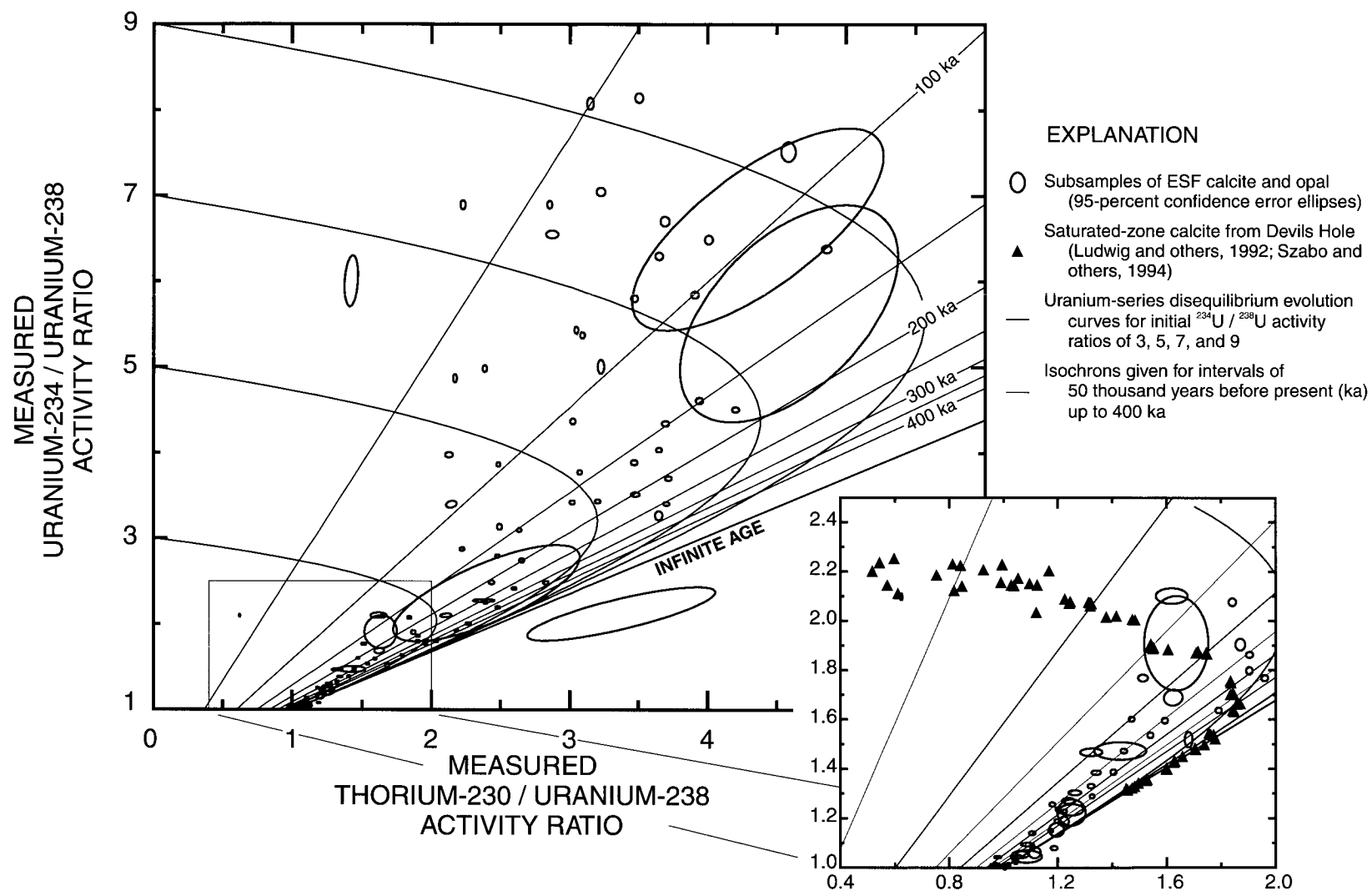


Figure 13. Uranium-series disequilibrium evolution diagram showing data for calcite and opal from the Exploratory Studies Facility (ESF) tunnel, Yucca Mountain, Nevada.

not only drives off CO_2 , converting calcite (CaCO_3) to lime (CaO), but also drives off water from hydrous phases converting opal to an anhydrous sinter or another water-free silica polymorph. Although the mineralogical consequences of this treatment were not investigated, the chemical responses of the uranium and thorium initially contained in opal are expected to be extreme. Uranium liberated from uraniferous opal in this manner would be available for mobilization during dilute acid leaching of CaO , whereas thorium would have a much greater likelihood of remaining adsorbed on the residue. Resulting concentrations of uranium in the leachate (termed "calcite" by Szabo and Kyser, 1985) would be enriched and correspondingly depleted in the residue (termed "opal" by Szabo and Kyser, 1985). Both of the leachates analyzed by Szabo and Kyser have uranium concentrations (3.02 and 0.36 $\mu\text{g/g}$, Szabo and Kyser, 1990, table 1) that are 6 to 400 times greater than concentrations determined in this study from calcite samples displaying no visible associated opal (0.007 to 0.047 $\mu\text{g/g}$, this report, Appendix 2b and fig. 12). Resulting isotopic analyses of the leachates would have erroneously low $^{230}\text{Th}/^{238}\text{U}$ and would underestimate the true $^{230}\text{Th}/\text{U}$ age. Residues would have erroneously high $^{230}\text{Th}/^{238}\text{U}$ and would overestimate the true $^{230}\text{Th}/\text{U}$ age or result in excess ^{230}Th that would clearly indicate a loss of uranium (true for both "opal" analyses by Szabo and Kyser, 1985, 1990). In addition, large samples were used for alpha counting, and the entire fracture-coating thickness (between 1 and 10 mm) was used for analysis. Ages were calculated assuming a "single generation with rapid rates of accumulation of the fracture-filling deposits" (Szabo and Kyser, 1985, p. 22). This assumption is unwarranted based on both morphological observations and interpretations of data reported here (see Interpretation of Ages section). Because of the large sample size and the likelihood that the measurements reported by Szabo and Kyser represent analytical artifacts rather than true isotopic compositions of unmodified calcite or opal, ages from their earlier study are not considered further.

Uranium-series age data are unevenly distributed in the ESF between about 2,000 to 4,000 m from the north portal (fig. 14). The uneven distribution is due, in part, to the presence or absence of mineral deposits, and in part, to focusing initial work near the potential repository horizon. Both lithophysae and fracture deposits are present in the crystal-poor upper

lithophysal zone and upper part of the underlying crystal-poor, middle nonlithophysal zone in the TSW between 2,200 and 3,400 m. Mineral deposits mostly are restricted to fracture coatings between about 3,400 and 5,000 m, although scattered lithophysae are present to about 4,000 m.

An unexpected result of this data set is the large number of young ages for outermost materials relative to the age of the host rock. No mineral coatings have outermost materials that are in secular equilibrium with respect to $^{234}\text{U}/^{238}\text{U}$ (typically established within 1,000 to 2,000 k.y.) and most are not in $^{230}\text{Th}/^{238}\text{U}$ secular equilibrium (typically established within 400 to 600 k.y.). Prior to this study, it was anticipated that mineral coatings would have formed rapidly at various times spanning the entire postdepositional history of Yucca Mountain. Therefore, less than 10 percent of the deposits were expected to have ages less than 500 ka, assuming that flux pathways would change substantially through time. Instead, ages less than 400 ka for outermost surfaces have been observed for nearly all the mineral coatings, indicating that the UZ flow paths supplied water to most sites of mineral deposition throughout the late and middle Pleistocene. Once established, connected flow pathways appear to remain stable for time periods of at least hundreds of thousands of years.

Ages show a qualitative relation to subsample size; however, this relation is difficult to quantify. The youngest ages are obtained from the thinnest opal sheets and smallest opal hemispheres or from the shallowest growth layers in calcite. Subsample weights range from 40 to 140 mg for calcite to as small as 0.2 mg for opal; however, converting this weight information into subsample thickness is inaccurate because of complex subsample morphologies. Direct measurement of thickness on a submillimeter scale also is difficult on most of these small subsample fragments or surface excavations producing powdered material. Although the thinnest subsamples tend to have the youngest ages, subsamples of similar thickness from different mineral coatings may produce ages that span most of the range observed for outermost subsamples.

Ages for subsamples from both fracture and lithophysae mineral coatings are similar in areas of the ESF that contain both types of deposits (open symbols compared to closed symbols in fig. 14). This relation implies that mineral coatings in both lithophysae and fracture settings are derived from the same fracture

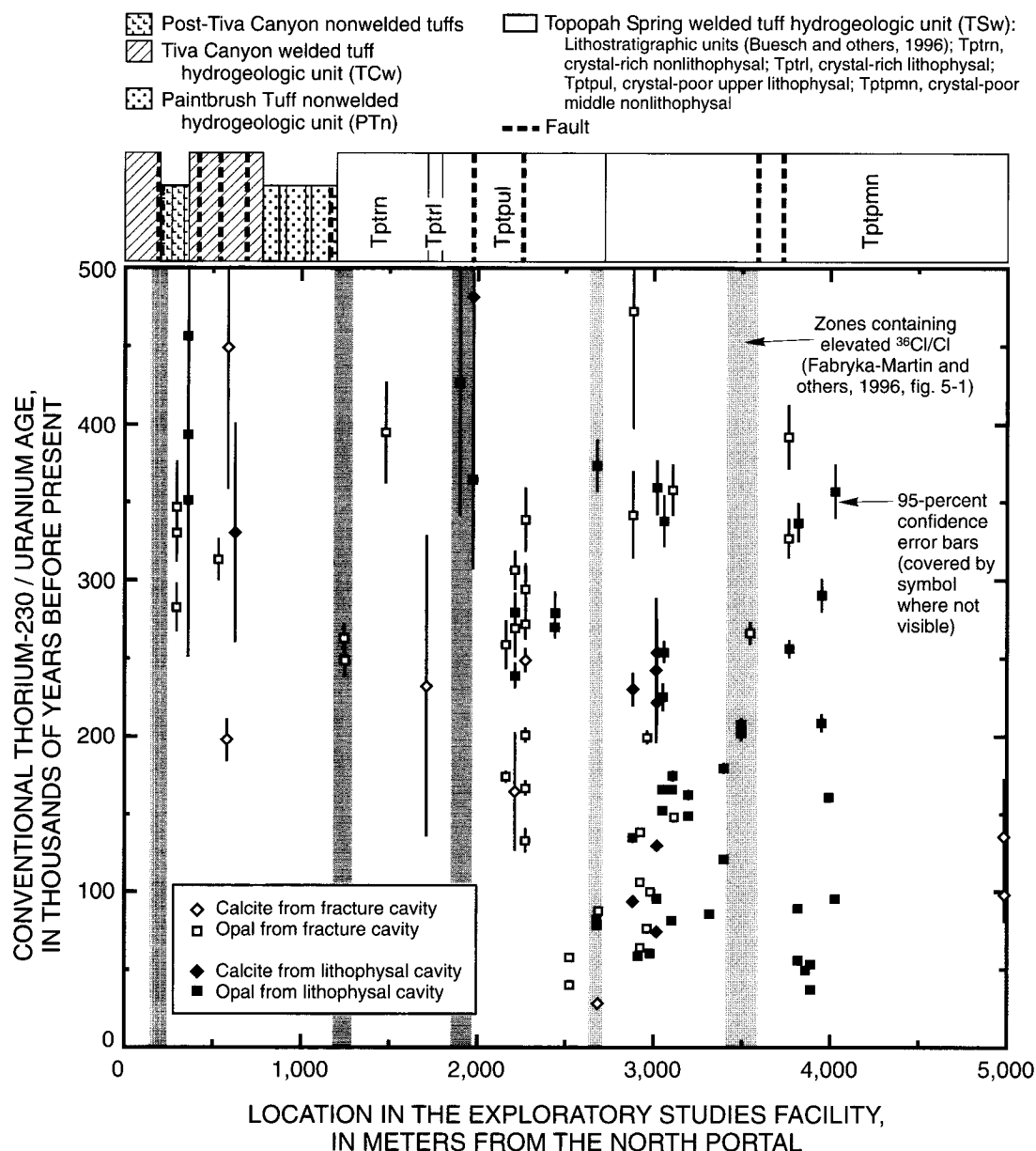


Figure 14. Conventional thorium-230/uranium ages for subsamples of calcite and opal relative to distance from the north portal of the Exploratory Studies Facility tunnel (fig. 2), Yucca Mountain, Nevada.

solutions percolating through a system of connected pathways. In addition, no systematic differences in $^{230}\text{Th}/\text{U}$ age distributions between outermost opal and calcite (square symbols compared to diamond symbols in fig. 14) are observed. This result implies either that the same solutions are capable of depositing both phases or that if two different types of solutions are responsible for the two different phases, they are present at the same depositional sites at approximately the same time periods.

There is a systematic difference between radiocarbon ages on subsamples of calcite outer layers and $^{230}\text{Th}/\text{U}$ ages for similar subsamples of calcite and opal. Although the youngest observed $^{230}\text{Th}/\text{U}$ age of 28.3 ± 1.4 ka is from a calcite with minor opal (HD2014-U2) and is within the range of observed radiocarbon ages, most calcite and opal $^{230}\text{Th}/\text{U}$ ages are substantially older than the range of measured ^{14}C ages (fig. 10). Where both age determinations are available for subsamples from the same mineral coatings (table 1), radiocarbon ages are limited to values

less than 44 ka, whereas $^{230}\text{Th}/\text{U}$ ages from similar, though not identical, subsamples of outer mineral surfaces range between 59.0 to 428 ka. This degree of discordance between the two isotopic systems is not expected if outer layers of a mineral coating were deposited rapidly during discrete percolation events.

In addition to different isotopic systems yielding discordant ages, multiple subsamples from outer surfaces of the same coating commonly have different rather than identical $^{230}\text{Th}/\text{U}$ ages (Appendix 2b) similar to radiocarbon ages discussed previously. For instance, six $^{230}\text{Th}/\text{U}$ ages for different subsamples of outer surfaces from lithophysal cavity coating HD2059 vary from 74.8 to 360 ka. Variations likely are caused by differences in subsample thickness and by complexities on individual growth surfaces, indicating that the process of mineral deposition was not uniform over small areas at a single site. Where subsamples from areas of different relief were obtained on the same sample, the subsamples from the higher-relief areas commonly have younger ages. In the few cases where older materials also were analyzed, $^{230}\text{Th}/\text{U}$ ages are consistent with microstratigraphic relations in the mineral coating (figs. 4 and 5).

Although subsample ages range widely for any particular reach of the tunnel, the distribution of $^{230}\text{Th}/\text{U}$ ages shows a gradual shift to younger values with distance in the ESF (fig. 14). Subsamples with $^{230}\text{Th}/\text{U}$ ages less than 100 ka are restricted to locations between 2,500 and 4,000 m from the north portal and represent greater lithostratigraphic depths. The youngest ages observed for subsamples from locations closer to the north portal (lesser lithostratigraphic depths) are between about 150 and 300 ka. The apparent break between younger and older $^{230}\text{Th}/\text{U}$ ages at about 2,500 m does not correspond to a major change in the lithostratigraphy. The break, however, corresponds to a shift in calculated initial $^{234}\text{U}/^{238}\text{U}$ (see the following section) observed for the same samples. Mineral coatings attain their maximum thickness (commonly between 1 and 2 cm, and rarely up to 4 cm) beyond about 2,500 m from the north portal (fig. 2). Therefore, the relation between age and location may indicate a change in depositional characteristics (for instance, growth rates) and the ability to resolve and sample fine-scale layering rather than reflecting a true age difference in the deposits.

Distribution of Initial $^{234}\text{U}/^{238}\text{U}$ and Correlation with Age

Initial $^{234}\text{U}/^{238}\text{U}$ ratios calculated from uranium and thorium isotope data provide insight into the interpretations of ages and the processes of percolation through the UZ. Most natural waters contain an excess of ^{234}U relative to secular equilibrium values of $^{234}\text{U}/^{238}\text{U}$ commonly found in rocks older than 1 to 2 Ma (Osmond and Cowart, 1992, fig. 9.1). Minerals deposited from such solutions will incorporate this elevated $^{234}\text{U}/^{238}\text{U}$ ratio at the time of formation. If there is no loss or gain of nuclides in the ^{238}U -to- ^{230}Th decay chain through time, the evolution of $^{234}\text{U}/^{238}\text{U}$ and $^{230}\text{Th}/^{238}\text{U}$ compositions in the mineral can be reconstructed, and the initial $^{234}\text{U}/^{238}\text{U}$ ratio can be calculated (y-intercept values for the curved evolution lines on a uranium-thorium isotope evolution diagram, fig. 13).

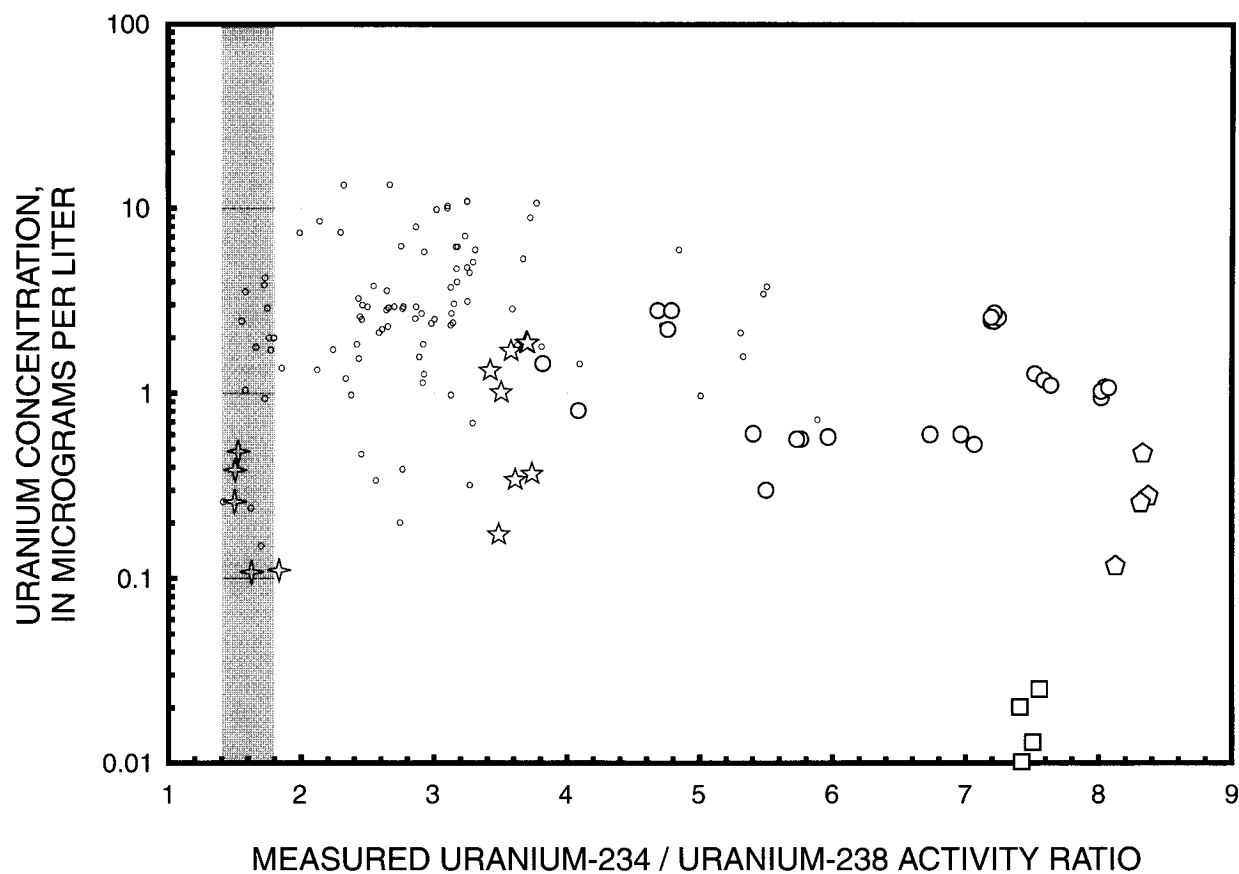
Pedogenic opal and carbonate deposits in Yucca Mountain commonly have initial $^{234}\text{U}/^{238}\text{U}$ activity ratios between 1.4 and 1.8 (shaded band in fig. 15; Szabo and others, 1981, calculated from data in table 1; Muhs and others, 1990, fig. 3; Paces and others, 1994, table 1). Most surface water from Yucca Mountain (overland flow during brief, but intense, storms) has similar values (fig. 15). Elevated $^{234}\text{U}/^{238}\text{U}$ are observed for SZ water, particularly beneath Yucca Mountain where values range from about 5 to 8 (Paces and others, 1998). Ground water perched near the base of the TSw has $^{234}\text{U}/^{238}\text{U}$ activity ratios of about 7.5 in borehole USW UZ-14 and 8.3 in borehole USW WT-24, whereas ground water perched in the Calico Hills Formation in borehole USW SD-7 has much smaller $^{234}\text{U}/^{238}\text{U}$ ratios of 3.4 to 3.7 (Paces and others, 1998, and unpublished data).

Initial $^{234}\text{U}/^{238}\text{U}$ ratios are not uniformly distributed throughout the ESF (fig. 16). Like the $^{230}\text{Th}/\text{U}$ ages, initial $^{234}\text{U}/^{238}\text{U}$ ratios show a shift in values at about 2,500 m from the north portal. Between 0 and 2,500 m, $^{234}\text{U}/^{238}\text{U}$ activity ratios range from about 1 to 3; however, beyond 2,500 m, ratios vary widely with values up to about 9.4. Initial activity ratios between 8 and 9.4 calculated for fracture minerals represent the largest activity ratios observed for water at Yucca Mountain, although present-day SZ water beneath Yucca Mountain attains $^{234}\text{U}/^{238}\text{U}$ activity ratios of just slightly greater than 8 (fig. 15). As with the age data, no obvious differences

Table 1. Comparison of carbon-14 (^{14}C) and thorium-230/uranium ($^{230}\text{Th}/\text{U}$) ages determined on outer surface subsamples from the same sample, Exploratory Studies Facility tunnel, Yucca Mountain, Nevada

[Locations in the Exploratory Studies Facility (ESF) tunnel are given in meters from the north portal. ka, thousands of years before present. Errors are given in parentheses and reported at the 95-percent confidence level]

ESF location (meters)	^{14}C		$^{230}\text{Th}/\text{U}$		
	Subsample identifier	Age (ka)	Subsample identifier	Age (ka)	Subsample type
1,710.95	HD2005ca	31.5 (0.8)	HD2005-U1	233 (96)	Calcite
1,900	HD2006ca	20.1 (1.6)	HD2006-U1	428 (+110/-59)	Opal
	HD2006cb	37.4 (0.9)			
	HD2006cc	33.3 (0.9)			
2,213	HD2007-1ca	33.7 (0.8)	HD2007-1-U2	270 (18)	Opal \pm calcite
	HD2007-1cb	33.8 (0.8)	HD2007-1-U3	165 (+44/-31)	Calcite \pm opal
	HD2007-2ca	28.8 (0.8)	HD2007-2-U1	240 (8)	Opal \pm calcite
			HD2007-2-U2	280 (12)	Opal \pm calcite
2,272	HD2008ca	32.6 (0.8)	HD2008-U3	167 (4)	Opal \pm calcite
	HD2008cb	34.0 (1.4)	HD2008-U4	250 (7)	Calcite \pm opal
			HD2008-U5	340 (20)	Opal
			HD2008-U6R	201 (4)	Opal
			HD2008-U7R	134 (7)	Opal
2,881	HD2019ca	27.3 (0.8)	HD2019-U1	135 (3)	Opal
	HD2019cb	41.8 (1.9)	HD2019-U5	94 (2)	Calcite
2,911.2	HD2055ca	24.0 (0.7)	HD2055-U1R	59.0 (0.7)	Opal
	HD2055cb	28.4 (1.4)			
2,922.9	HD2056cb	43.7 (1.4)	HD2056-U1	64.6 (0.7)	Opal
			HD2056-U2	139 (1.8)	Opal
			HD2056-U3	106.7 (1.4)	Opal
2,962.2	HD2057ca	31.7 (0.9)	HD2057-U1R	76.8 (1.0)	Opal
			HD2057-U2R	200 (4)	Opal
3,017.78	HD2059ca	38.0 (1.0)	HD2059-U1	74.8 (1.3)	Calcite
			HD2059-U3	96.4 (1.0)	Opal \pm calcite
			HD2059-U4	293 (12)	Opal
			HD2059-U5	130 (2)	Calcite \pm opal
			HD2059-U6	360 (17)	Opal
			HD2059-U7	222 (14)	Calcite
3,316.2	HD2065ca	33.6 (0.7)	HD2065-U1R	86.1 (1.0)	Opal
	HD2065cb	32.0 (0.9)			
	HD2065cc	30.3 (0.5)			
3,545.4	HD2071ca	31.9 (1.5)	HD2071-U1-UR	267 (7)	Opal
	HD2071cb	31.5 (0.7)			



EXPLANATION

- Ground-water samples from the Yucca Mountain vicinity (Ludwig and others, 1993, fig. 2)
- Yucca Mountain saturated-zone ground water
- Yucca Mountain perched ground water from boreholes:
 - USW UZ-14
 - ◑ USW WT-24
 - ☆ USW SD-7
- ✧ Runoff
- Range of $^{234}\text{U} / ^{238}\text{U}$ activity ratios in pedogenic deposits (Paces and others, 1994, table 1; and J.B. Paces and others, U.S. Geological Survey, written commun., 1995)

Figure 15. Uranium concentrations and measured uranium-234/uranium-238 activity ratios in saturated-zone ground water, perched water, and runoff in the vicinity of Yucca Mountain, Nevada.

in initial $^{234}\text{U}/^{238}\text{U}$ ratios are present between subsamples from fracture or lithophysal settings.

Calculated initial $^{234}\text{U}/^{238}\text{U}$ ratios also show a distinct negative correlation with $^{230}\text{Th}/\text{U}$ ages (fig. 17). This correlation is true for the entire data set, as well as for multiple subsamples from a single mineral coating. Minerals younger than 100 ka have a wide range of initial $^{234}\text{U}/^{238}\text{U}$ ratios between about 4 and 9.4 (only a single, 37-ka outlier with an initial

$^{234}\text{U}/^{238}\text{U}$ ratio of 2.2; HD2084-U1R). Minerals with successively older ages have increasingly smaller initial $^{234}\text{U}/^{238}\text{U}$ ratios until values decrease to near secular equilibrium (1.0) after a little more than 400 ka.

The negative correlation between age and initial $^{234}\text{U}/^{238}\text{U}$ values is not consistent with closed-system evolution of solid phases deposited from a well-mixed reservoir with temporally uniform $^{234}\text{U}/^{238}\text{U}$ values.

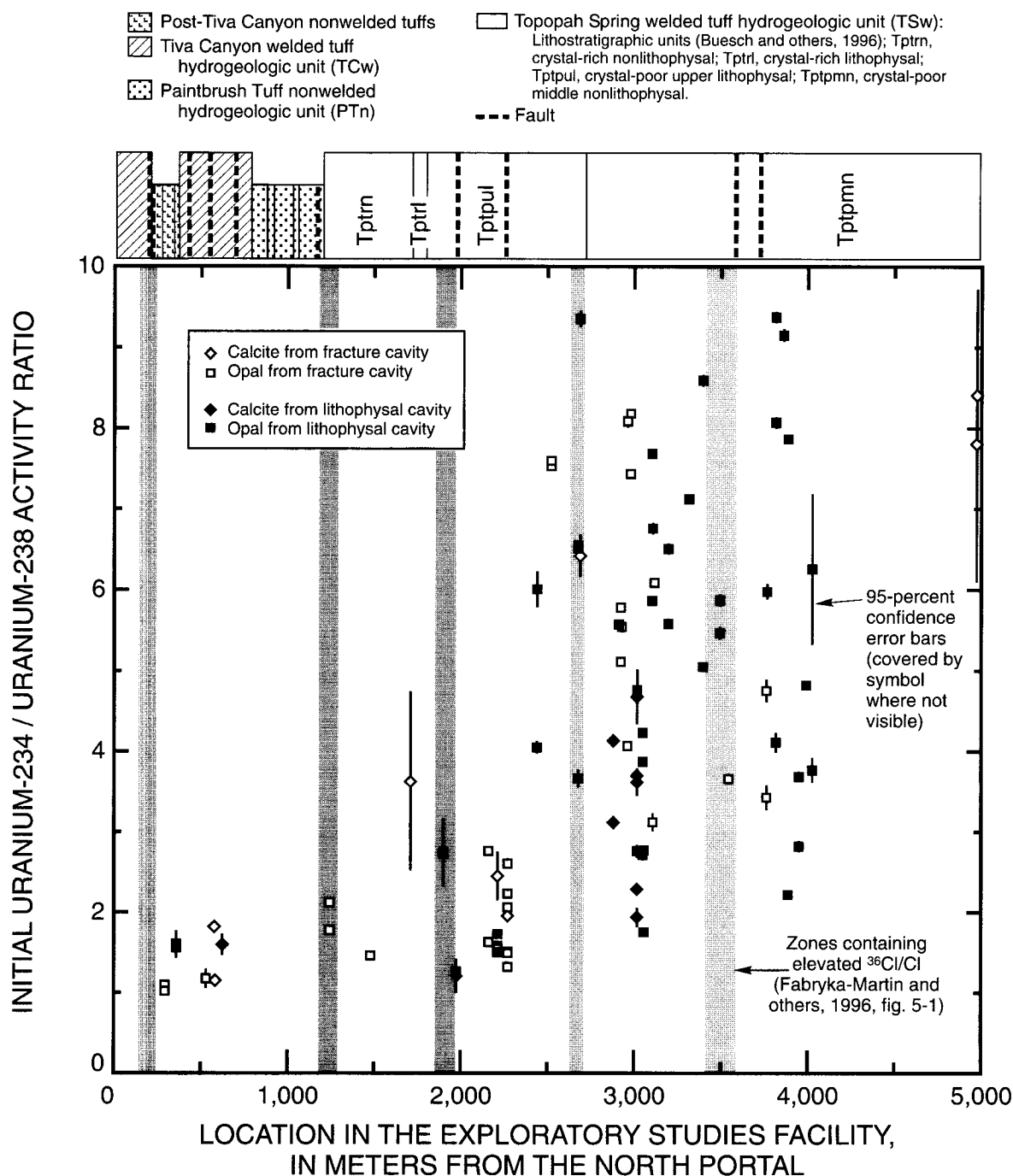


Figure 16. Initial uranium-234/uranium-238 activity ratios for subsamples of calcite and opal relative to distance from the north portal of the Exploratory Studies Facility tunnel (fig. 2), Yucca Mountain, Nevada.

This correlation cannot readily be explained by uranium mobility because of the consistent patterns of uranium and thorium isotope compositions observed in ESF subsamples (fig. 13). Recent loss or gain of uranium will result in subhorizontal arrays of data on uranium-series isotope evolution plots and the likely presence of excess ^{230}Th if uranium loss is substantial.

These correlations are absent in the ESF data set. In addition, uranium mobility will result in positive rather than negative correlations between age and initial $^{234}\text{U}/^{238}\text{U}$ ratio. Gradual changes in $^{234}\text{U}/^{238}\text{U}$ ratios of UZ percolating waters during the last 400 k.y. also is an unlikely explanation of the observed negative correlation between initial $^{234}\text{U}/^{238}\text{U}$ ratios and

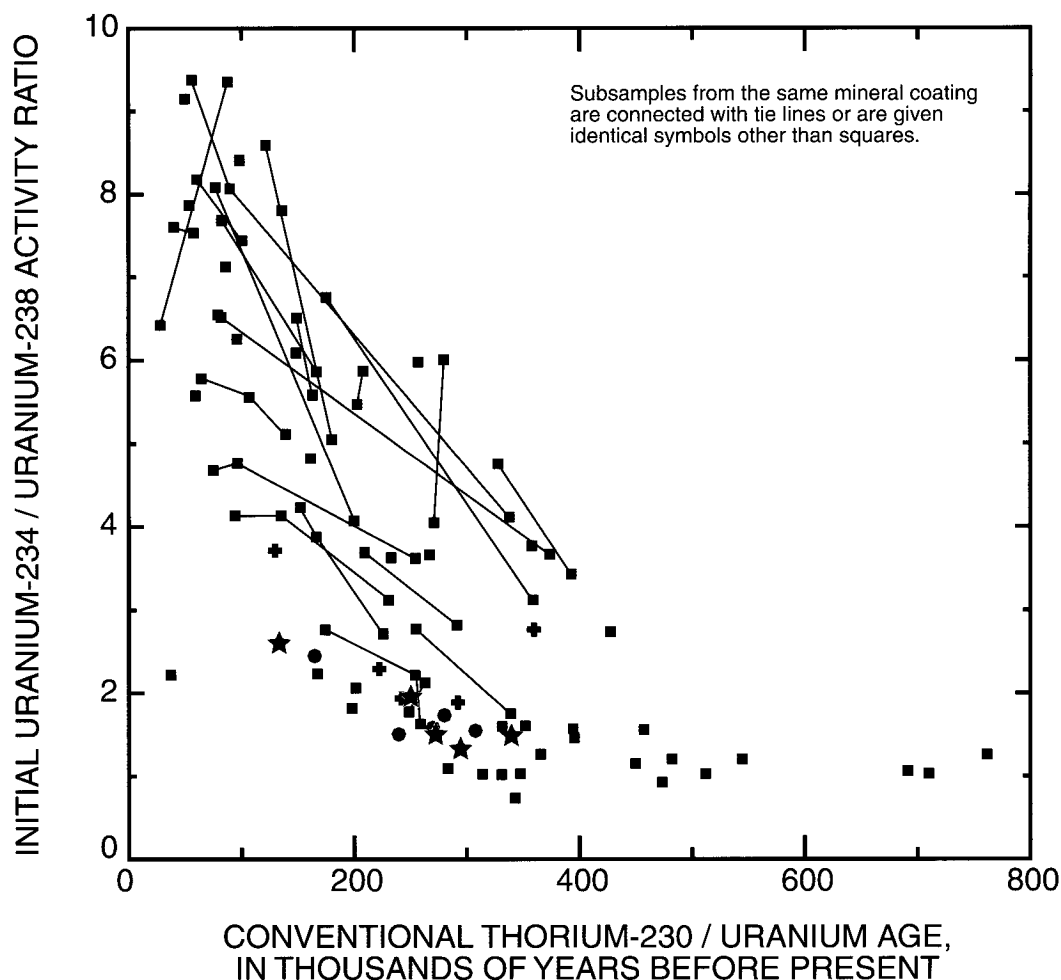


Figure 17. Initial uranium-234/uranium-238 activity ratios and conventional thorium-230/uranium ages for subsamples of calcite and opal from the Exploratory Studies Facility tunnel, Yucca Mountain, Nevada.

$^{230}\text{Th}/\text{U}$ ages. A negative correlation is not observed for either soil-zone water responsible for calcrete development or in regional SZ ground water, both of which have $^{234}\text{U}/^{238}\text{U}$ values remaining approximately constant over the last 600 k.y. (Paces and others, 1994, table 1; Ludwig and others, 1992, fig. 4). Therefore, an alternative cause, discussed in the Interpretation of Ages section, likely is responsible for the isotopic correlation observed in ESF samples.

CARBON, OXYGEN, AND STRONTIUM ISOTOPES

Calcite and opal mineral coatings in the Yucca Mountain subsurface preserve records of carbon, oxygen, and strontium isotope variations throughout

the history of deposition. Values for these isotopes and their variations through time provide information on the sources of water, carbonate, and cation components in solutions percolating through fracture pathways and on some of the changes in fracture water composition over the last 13 m.y. This section presents carbon, oxygen, and strontium isotope data from ESF calcite as well as oxygen isotope data from opal, quartz, and chalcedony. Stable isotope data were collected from both normal-sized calcite subsamples (typically 10 to 20 mg) of hand specimens and from microsamples (typically less than 0.5 mg) milled from petrographic thick-sections cut perpendicular to growth surfaces. Strontium isotope data were determined from aliquots of the same calcite subsamples analyzed for stable isotopes. Isotopic data presented in this section can be used for interpreting the sources of

fracture water, as well as the evolution of thermal conditions and isotopic compositions of fracture water percolating through the UZ at Yucca Mountain in the past.

Carbon and Oxygen Isotopes in Unsaturated-Zone Calcite

Carbon isotope compositions of calcite from mineral coatings in the ESF show a wide range of $\delta^{13}\text{C}$ values from about -8.2 to 8.5 per mil (fig. 18). The 310 subsamples analyzed by Whelan and others (1998) have $\delta^{13}\text{C}$ values that largely overlap the range of $\delta^{13}\text{C}$ previously obtained from drill core (Whelan and others, 1994; fig. 19 in this report). A large number of calcite subsamples from the ESF have $\delta^{13}\text{C}$ values between -5 and -8.5 per mil (46 percent of analyses shown in fig. 18). A similarly large proportion of calcite subsamples from drill core have $\delta^{13}\text{C}$ values less than -5 per mil. However, unlike the drill hole data set, a much larger percentage of the ESF subsamples have positive $\delta^{13}\text{C}$ values (27 percent of ESF analyses, fig. 18, compared to less than 1 percent of drill core analyses, fig. 19). This difference likely is related to differences in the quality of the mineral coatings available for subsampling between the drilling and tunneling programs. In general, the samples collected from the walls of the 7.6-m-diameter ESF tunnel tend to be thicker with delicate crystal forms that are much better preserved than those retrieved from 5- to 10-cm-diameter drill core. Most of the calcite subsamples with $\delta^{13}\text{C}$ values greater than 0 per mil are from coatings in the TSw between about 1,400 and 1,700 m, and beyond about 2,700 m from the north portal (fig. 18). In addition, where lithophysae are present in the TSw, no systematic differences appear between calcite $\delta^{13}\text{C}$ values from mineral coatings in either lithophysal or fracture settings (circles and crosses in fig. 18).

Oxygen isotope compositions of calcite from mineral coatings in the ESF have $\delta^{18}\text{O}$ values ranging from about 21 to 10 per mil (Whelan and others, 1998, Appendix 2). Maximum values of $\delta^{18}\text{O}$ tend to decrease with depth below the surface. In the shallow part of the ESF, maximum $\delta^{18}\text{O}$ values typically are 20 to 21 per mil, whereas maximum $\delta^{18}\text{O}$ values in the deeper portions of the ESF are 17 to 19 per mil (fig. 18). This relation was noted previously in calcite obtained from drill core and ascribed to increases in

temperature with depth caused by geothermal gradients similar to those measured in boreholes (Szabo and Kyser, 1990, p. 1718; Whelan and others, 1994). Calcite from depths less than about 50 m has $\delta^{18}\text{O}$ compositions of 18 to 22 per mil (fig. 19) overlapping the range of $\delta^{18}\text{O}$ values observed in pedogenic calcite (Vaniman and Whelan, 1994).

Calcite from the ESF also can show a wide range of $\delta^{18}\text{O}$ values over narrow depth intervals. Mineral coatings at locations between 1,400 and 1,700 m from the north portal have $\delta^{18}\text{O}$ values that range from about 10 to 20 per mil (fig. 18). Mineral coatings beyond about 2,700 m also show a large amount of scatter in $\delta^{18}\text{O}$ values. Both of these zones also contain calcite with a large number of $\delta^{13}\text{C}$ values greater than 0 per mil and imply that the two isotopes are correlated in calcite subsamples.

When plotted together, $\delta^{13}\text{C}$ and $\delta^{18}\text{O}$ values for calcite in the TSw show a general negative correlation (fig. 20). This correlation indicates that subsamples with large $\delta^{13}\text{C}$ values tend to have small $\delta^{18}\text{O}$ values. Subsamples shown in this plot were obtained from both outermost surfaces and from interior layers in mineral coatings. Subsamples from outermost mineral surfaces tend to plot in the dense cluster of data with $\delta^{13}\text{C}$ values less than -5 per mil. Subsamples from interior layers tend to have larger $\delta^{13}\text{C}$ values. Therefore, these data imply a general relation between age and isotopic composition of calcite forming mineral coatings in the ESF.

To further investigate the variation in isotopic compositions with microstratigraphic depth, and presumably time, subsamples across individual mineral coatings were collected and the relative microstratigraphic position of each subsample was documented. Mineral coatings are likely to contain long-term records of the isotopic compositions of fracture flow through the UZ. Uranium-lead dating on a small number of samples indicates that the basal layers of mineral coatings were deposited between 5 and 10 Ma (Neymark and others, 1998). These data indicate that coatings accumulated from their bases outward to their outer surfaces. In addition, growth rates estimated from $^{230}\text{Th}/\text{U}$ age data presented in this report are consistent with estimated ages of the lowermost layers in mineral coatings that are similar to the age of the host rocks. Therefore, the oldest materials in these mineral records likely represent periods of time extending back to the first few million years of Yucca Mountain history.

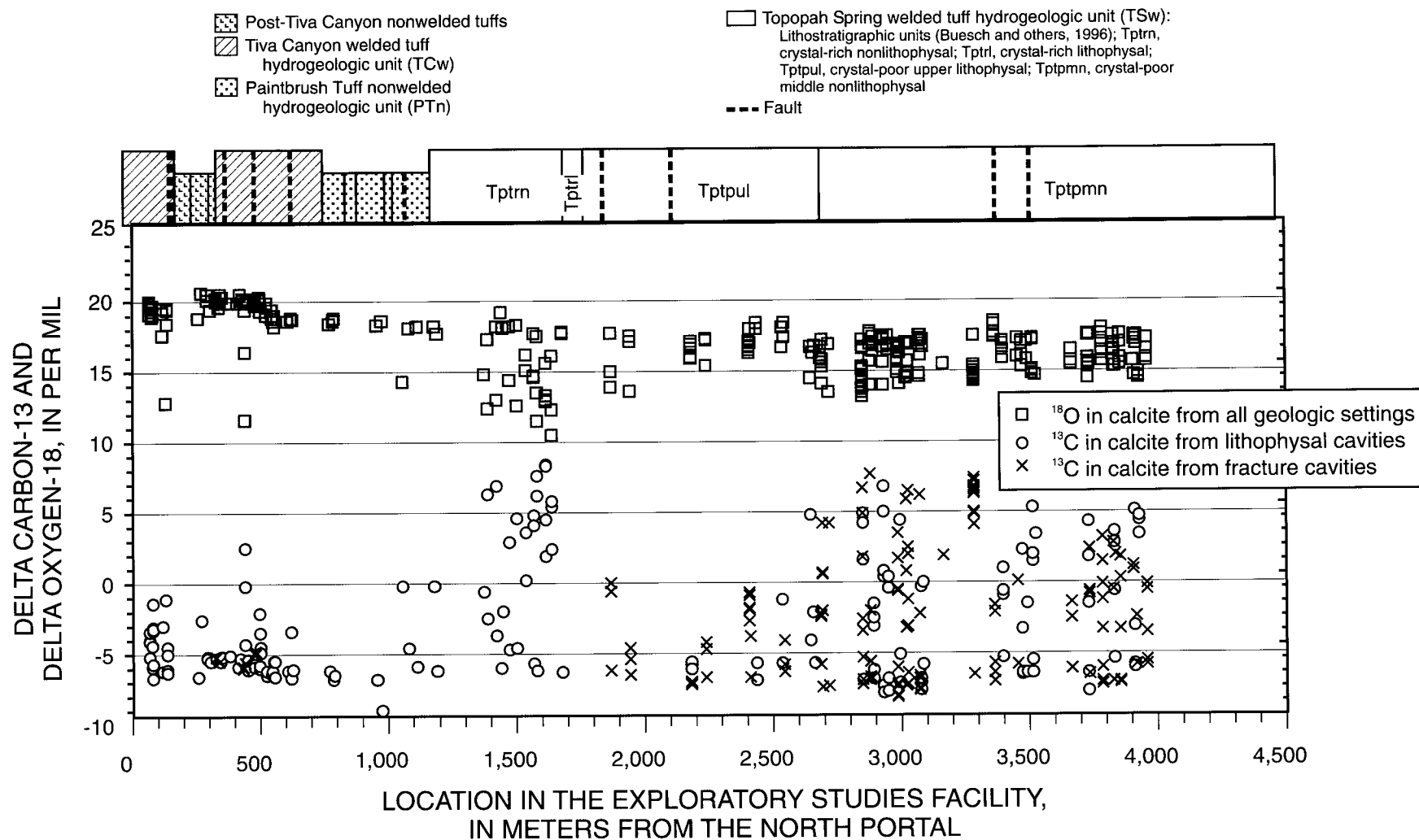
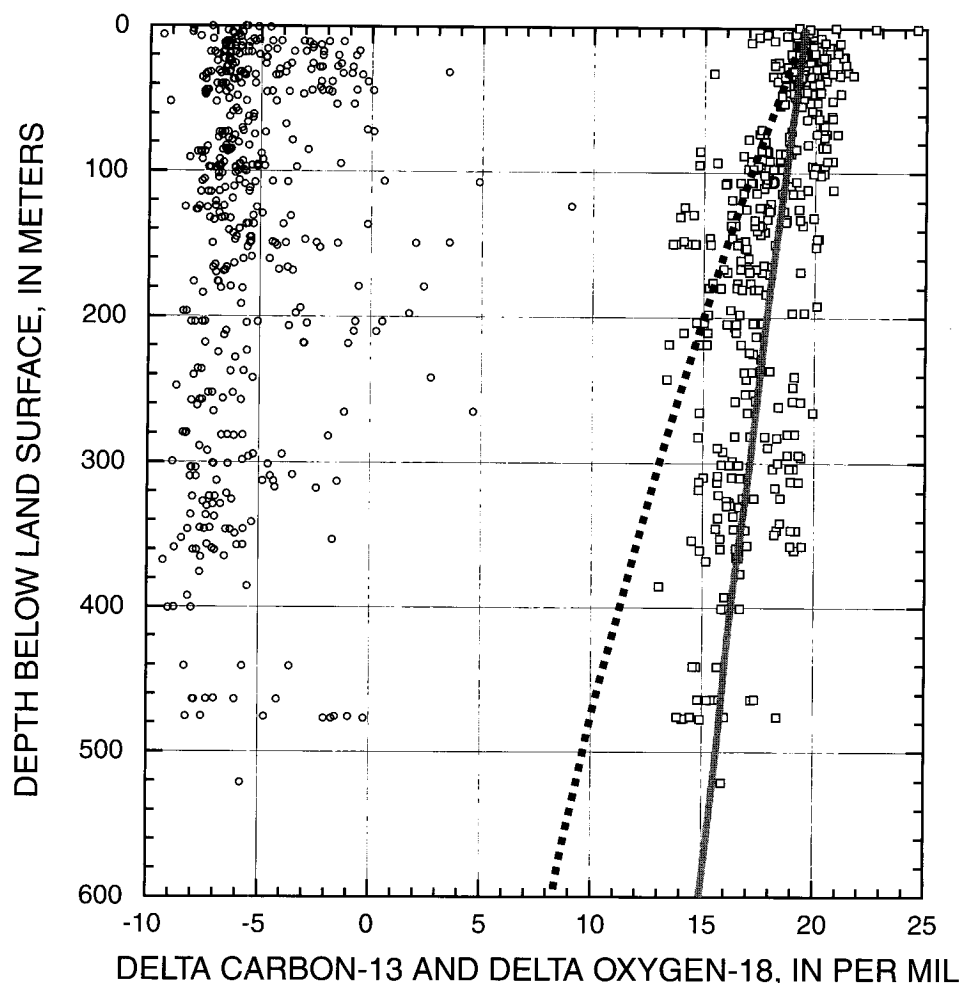


Figure 18. Carbon and oxygen isotope compositions of subsamples of calcite relative to distance from the north portal of the Exploratory Studies Facility tunnel (fig. 2), Yucca Mountain, Nevada.



EXPLANATION

- $\delta^{13}\text{C}$ values relative to Vienna Pee Dee belemnite (VPDB) carbonate standard
- $\delta^{18}\text{O}$ values relative to Vienna Standard Mean Ocean Water (VSMOW) water standard

Calculated $\delta^{18}\text{O}$ values for calcite in equilibrium with a percolation $\delta^{18}\text{O}_{\text{water}}$ of -12.5 per mil, a 10°C mean annual surface temperature, and a geothermal gradient of:

- 34°C per kilometer of depth (Szabo and Kyser, 1990, p. 1718)
- - - 100°C per kilometer of depth (using fractionation factors of Friedman and O'Neil, 1977)

Figure 19. Stable carbon and oxygen isotope compositions of subsamples of unsaturated-zone calcite from drill core at Yucca Mountain, Nevada (modified from Whelan and others, 1998, fig. 5).

Although uranium-lead ages are not available for the mineral coatings discussed in this report, it is nevertheless possible to determine the relative age in a coating by paragenetic examination. Microsamples of calcite were collected across transects of a number of mineral coatings. Microsamples were collected with a

0.3-mm-diameter carbide dental bur to excavate shallow pits or trenches on the surface of polished petrographic sections (100 to 200 μm thick) from which 0.1 to 0.5 mg of powder was retrieved (fig. 21). The microstratigraphic position of each microsample was classified as basal, intermediate, or outer on the

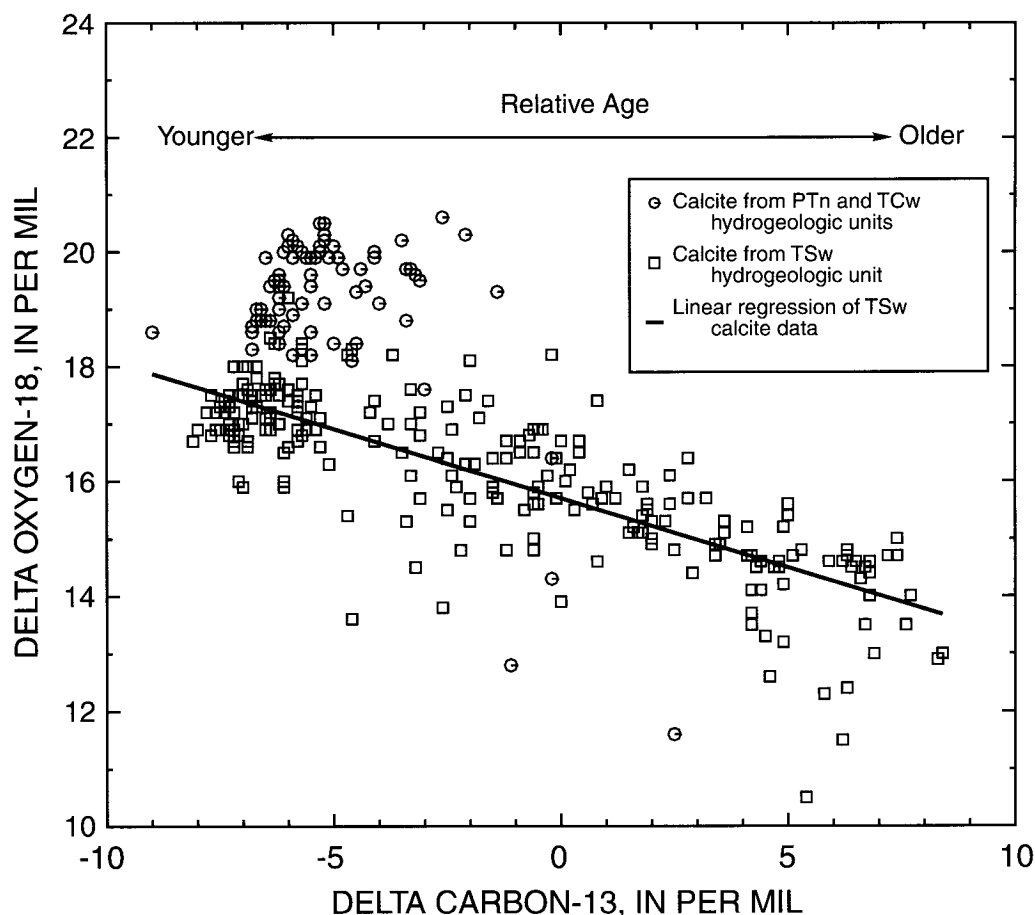


Figure 20. Isotopic compositions of carbon and oxygen in subsamples of calcite from the Exploratory Studies Facility tunnel, Yucca Mountain, Nevada (data from Whelan and others, 1998, appendix 2).

basis of relative positions in the observed microstratigraphy of each mineral coating. These classifications may misrepresent true ages of the microsample because all depositional stages may not be present in every sample, and because the boundaries between relative age classes are not uniquely defined. This simple approach was taken to maximize the objectivity of the grouping process.

Isotopic compositions of carbon and oxygen in microsamples show general variations across mineral coatings that are consistent with the data shown in figure 20. Although substantial overlap in $\delta^{13}\text{C}$ values is present between the relative age groups, microsamples of basal calcite tend to have larger $\delta^{13}\text{C}$ and smaller $\delta^{18}\text{O}$ compositions, whereas outer calcite subsamples tend to have smaller $\delta^{13}\text{C}$ and larger $\delta^{18}\text{O}$. At least some of the observed overlap may be caused by inaccuracies from estimating ages based on their relative microstratigraphic position. Microsamples

classified as outer show a tight cluster of $\delta^{13}\text{C}$ values between about -8 and -5 per mil (fig. 22); also, they almost always have $\delta^{18}\text{O}$ values greater than about 16.5 per mil. These subsamples typically were drilled from the outer layers of mineral coatings and are likely to represent deposition over the last million years based on uranium-series dating. In contrast, most of the microsamples from calcite classified as basal have $\delta^{13}\text{C}$ values that are either between -2.5 and -0.5 per mil, or greater than 2 per mil. These same basal microsamples have a wide range in $\delta^{18}\text{O}$ values from less than 10 per mil to about 17 per mil, although the smaller end of the range is more common. Microsamples classified as intermediate have a broad range of $\delta^{13}\text{C}$ values from -7 to 10 per mil as well as a range of $\delta^{18}\text{O}$ values that are similar to those in basal calcite. However, the intermediate microsamples have a slightly greater frequency of $\delta^{13}\text{C}$ values between -3 and 0 per mil. It also is possible that the smaller cluster



Sample - HD2073

ESF location - 3,103 meters from the north portal

Scale - Coating thickness is approximately 1.6 centimeters

Description - Tuff substrate is overlain by basal, ^{13}C -enriched calcite with minor chalcedony followed by intermediate dusty calcite and outer coarse, clear, sparry, ^{13}C -depleted calcite. Sample is impregnated with blue epoxy

Data - $\delta^{13}\text{C}$ (upper value) and $\delta^{18}\text{O}$ compositions in per mil



Sample - HD2065

ESF location - 3,316.2 meters from north portal

Scale - Coating thickness is approximately 2 centimeters

Description - Tuff substrate is overlain by clean, sparry calcite. Values of $\delta^{13}\text{C}$ are intermediate (0.8 to 2.4 per mil) in the basal calcite, enriched in ^{13}C in the central part of the coating ($\delta^{13}\text{C}$ 3.7 to 6.9 per mil) and depleted in ^{13}C in the outer calcite ($\delta^{13}\text{C}$ -0.6 to -6.2 per mil). Sample is impregnated with blue epoxy

Data - $\delta^{13}\text{C}$ (upper value) and $\delta^{18}\text{O}$ compositions in per mil

Figure 21. Cross sections of two mineral coatings from the Exploratory Studies Facility (ESF) tunnel, Yucca Mountain, Nevada, showing the scale of microsampling and the results of stable carbon and oxygen isotope analyses.

of basal calcite with $\delta^{13}\text{C}$ values between -2.5 and -0.5 per mil may represent intermediate calcite if mineral growth in these coatings was not initiated until after the early stages of deposition. Boundaries and more accurate age classifications may be possible if the interior portions of mineral coatings can be dated using uranium-lead methods. However, present data indicate that $\delta^{13}\text{C}$ values in calcite shifted from larger

values (2 to 9 per mil) early in the depositional history to intermediate values (-3 to 0 per mil) and finally to smaller values (-8 to -5 per mil) with time. The isotopic compositions and age relations observed in these microsample transects are consistent with the general age relations resulting in the negative correlation of $\delta^{13}\text{C}$ and $\delta^{18}\text{O}$ data observed in larger sized subsamples (fig. 20).

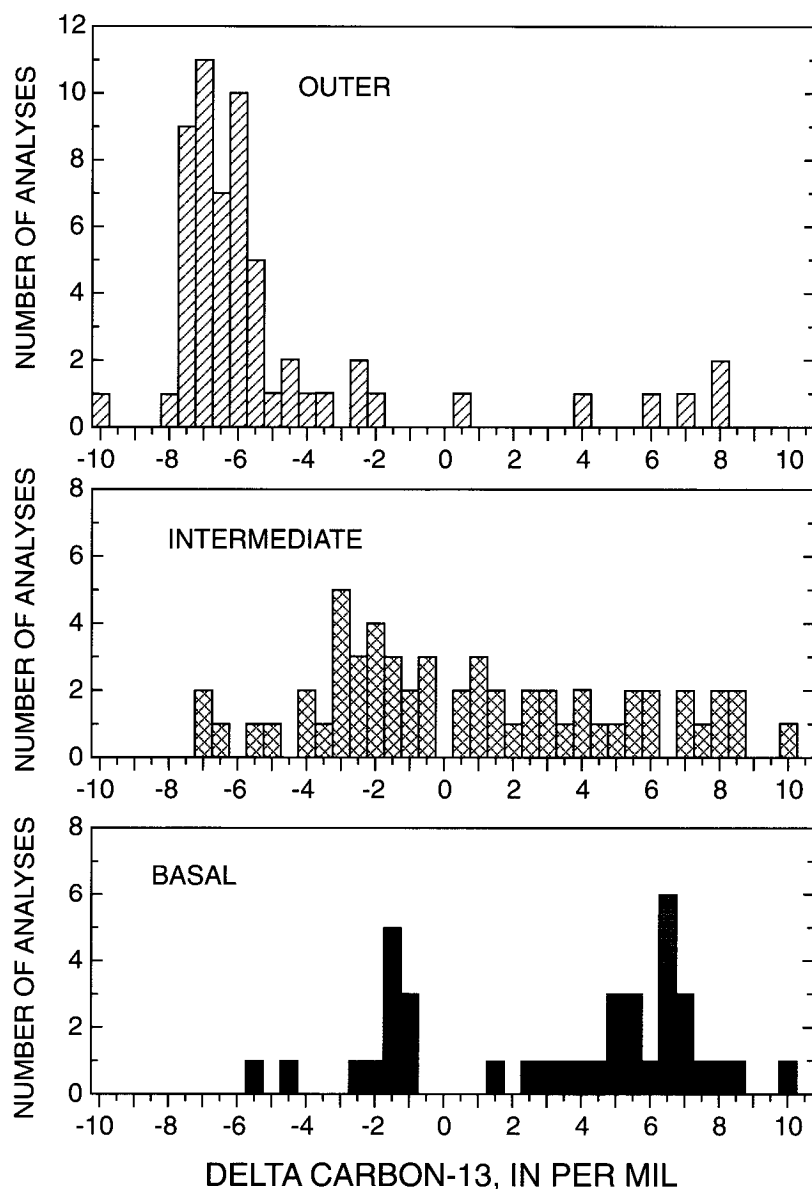


Figure 22. Distribution of delta carbon-13 values for calcite microsamples classified by relative microstratigraphic position from the Exploratory Studies Facility tunnel, Yucca Mountain, Nevada.

Oxygen Isotopes in Unsaturated-Zone Silica Phases

Opal, quartz, and chalcedony in mineral coatings contain oxygen isotope information that can be related to the conditions in the UZ at the site and time of mineral deposition. These three silica phases also show systematic paragenetic relations where chalcedony and quartz are largely restricted to early depositional stages, whereas opal is the dominant silica phase formed during intermediate and late stages (fig. 9).

Therefore, variations in $\delta^{18}\text{O}$ compositions observed in the different silica phases have the potential to provide information on the long-term evolution of the UZ flow system. Data described in this section can be used to better understand the early thermal evolution of Yucca Mountain (see Thermal Evolution section).

Oxygen isotope compositions of silica phases from both ESF and drill core samples were reported by Moscati and Whelan (1996) and Whelan and others (1998). Subsamples, typically weighing between 20 to 50 mg, were obtained by chipping or prying fragments

from hand specimens or by milling with a diamond-coated dental bur. Details of the analytical procedures used for determining stable isotope compositions of both calcite and silica phases are given in Moscati and Whelan (1996, p. 5) and Whelan and others (1998, p. 3).

Oxygen isotope compositions vary systematically in the three dominant silica phases from the smallest values observed in chalcedony through intermediate values in quartz and the largest values in opal (fig. 23). Nine subsamples of massive chalcedony from the base of mineral coatings in the UZ reported by Whelan and others (1998, appendix 3) have $\delta^{18}\text{O}$ values more or less evenly distributed between 7.9 and 17.3 per mil. The mean $\delta^{18}\text{O}$ value for this distribution is 12.4 per mil and the median value is 13.0 per mil. The two values of 7.9 and 8.4 per mil reported for UZ chalcedony are slightly larger than the smallest values reported by Whelan and others (1998, appendix 3) for quartz (5.9 per mil) and chalcedony (6.9 per mil) from deeper in the SZ.

Euhedral quartz commonly is present in the microstratigraphically lower parts of the coatings as fine prismatic layers or sprays of crystals on chalcedony. This quartz is, therefore, interpreted to be younger than the chalcedony, but still older than most of the calcite and opal. Fourteen of 17 analyses of UZ quartz published by Whelan and others (1998, appendix 3) have $\delta^{18}\text{O}$ values between 16.8 and 22.8 per mil (fig. 23). Two other subsamples have much smaller $\delta^{18}\text{O}$ values of 11.3 and 8.6 per mil. With the exception of these two values, the quartz data form an asymmetrical distribution that yields a mean value of 19.9 per mil and a median value of 20.1 per mil.

Paragenetic observations indicate that opal post-dates the deposition of quartz, but uranium-lead dating indicates that opal still can be at least as old as 8 Ma (Neymark and others, 1998). Values of $\delta^{18}\text{O}$ for opal overlap most of the range observed in quartz formed during the early stages of deposition, but tend to have larger $\delta^{18}\text{O}$ compositions with a well-defined cluster of values between 18.0 and 27.9 per mil. The mean value for this distribution is 22.1 per mil and the median is 22.6 per mil. Although opal is present throughout the long paragenetic history of many of the thick mineral coatings, information on the microstratigraphic position of opals subsampled for the earlier oxygen isotope studies is not available. Most subsamples are likely from positions near the outer surfaces of mineral coatings.

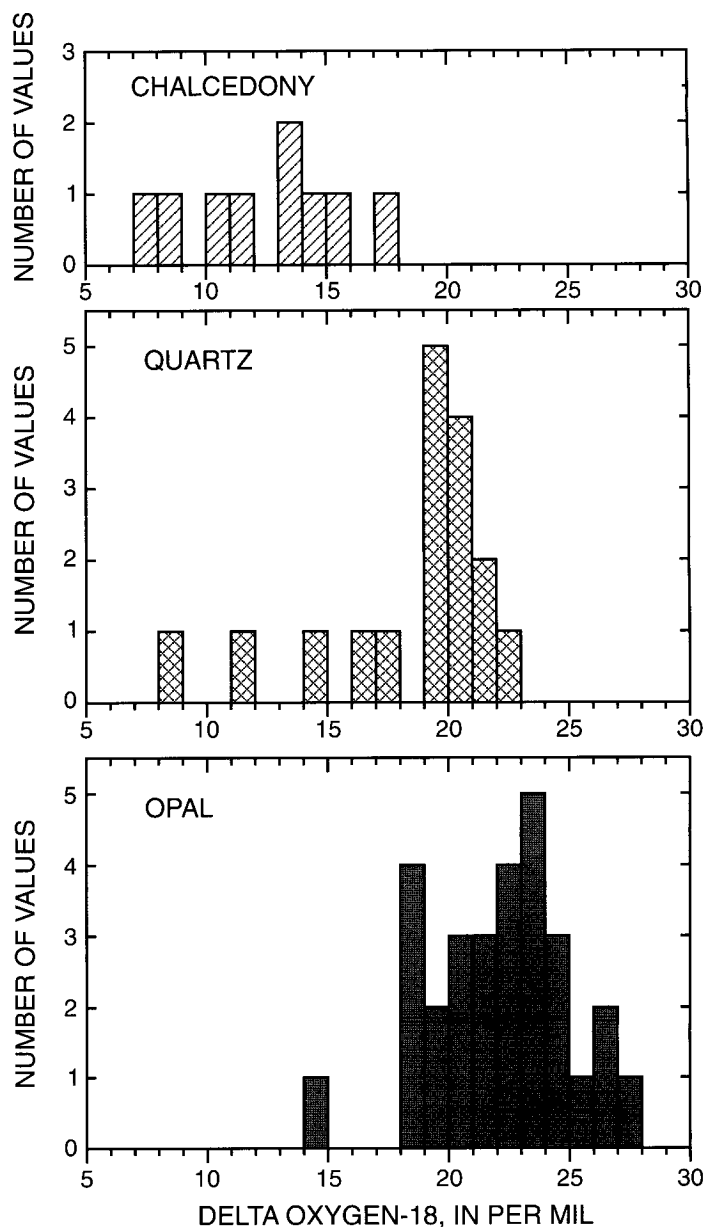


Figure 23. Distribution of delta oxygen-18 values for subsamples of unsaturated-zone chalcedony, quartz, and opal from drill core and the Exploratory Studies Facility tunnel at Yucca Mountain, Nevada (data from Moscati and Whelan, 1996, table 1; Whelan and others, 1998, appendix 3).

Strontium Isotopes in Unsaturated-Zone Calcite

Strontium isotope ratios ($^{87}\text{Sr}/^{86}\text{Sr}$) in UZ calcite are inherited directly from the $^{87}\text{Sr}/^{86}\text{Sr}$ composition of the percolating water at the time and site of mineral deposition. Although strontium typically is present only in trace amounts in most ground-water systems, it has a chemical affinity for calcium

and is incorporated readily into calcite. Unlike oxygen and carbon isotopes, the two isotopes of strontium are not appreciably fractionated between solid and liquid phases during mineral growth and are independent of temperature, pressure, or kinetic factors. Because the rubidium/strontium ratio in calcite is extremely small, and because rubidium-87 (^{87}Rb) is the parent isotope for ^{87}Sr , once calcite has formed, its $^{87}\text{Sr}/^{86}\text{Sr}$ ratio remains essentially unchanged through long periods of geologic time. Therefore, the major factors affecting $^{87}\text{Sr}/^{86}\text{Sr}$ ratios in calcite are strontium abundances and isotopic compositions in the rocks or soils that percolating water comes in contact with and the degree of interaction between these solids and the infiltrating or percolating water.

Strontium concentrations and isotope compositions have been measured on 40 splits selected from a number of ESF calcite subsamples that were analyzed for carbon and oxygen isotopes. Subsamples consisted of about 10 mg of powdered or fragmental calcite that were milled or chipped from outer surfaces or cross sections of mineral coatings. Analytical data and the microstratigraphic position of all subsamples in individual mineral coatings are listed in Appendix 3. Nearly all subsamples are from calcite deposits in the TS_w.

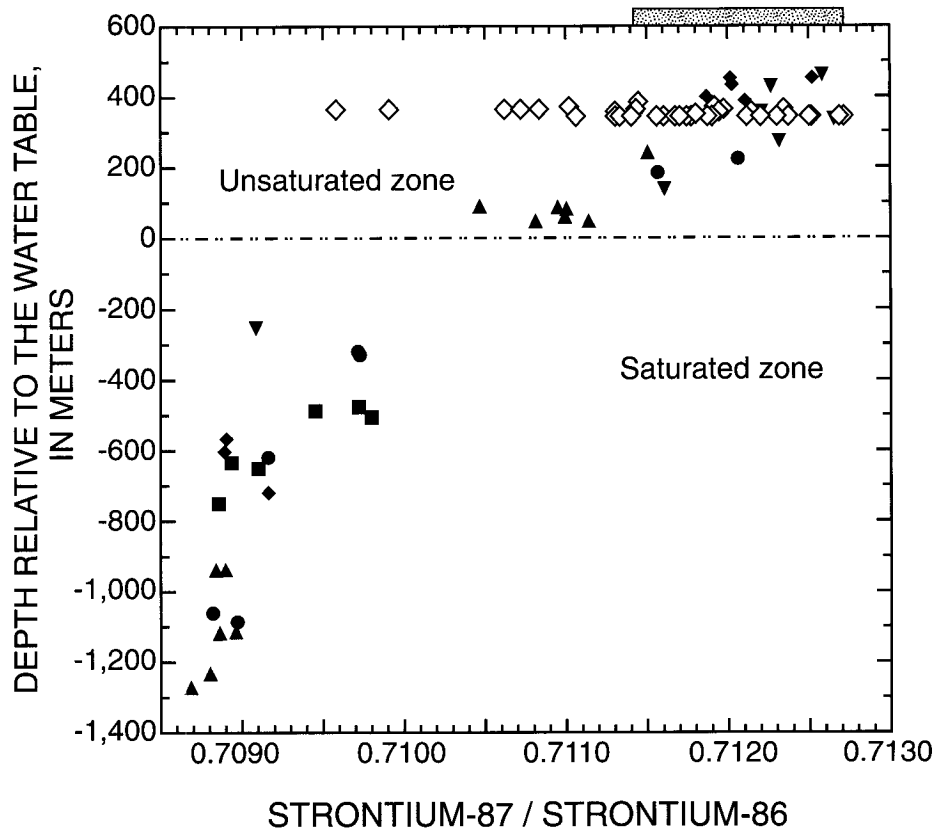
Strontium isotope compositions reported previously for calcite samples from drill core (Marshall and others, 1992) were used to distinguish UZ calcite with larger $^{87}\text{Sr}/^{86}\text{Sr}$ values (more radiogenic) from SZ calcite with smaller $^{87}\text{Sr}/^{86}\text{Sr}$ values (less radiogenic) (fig. 24). Previous data, with the exception of six subsamples from borehole USW G-2 at 85 m above the water table, also were interpreted to indicate that UZ fracture flow had a surface source because of the similarity between strontium isotopes in UZ calcite and the pervasive pedogenic calcite deposits (Marshall and others, 1993; Marshall and Mahan, 1994).

Strontium isotope ratios from ESF calcite span not only the entire range of the UZ calcite subsampled from drill core, but extend, in at least two subsamples, to lower ratios that are more typical of calcite in the upper part of the SZ (open diamonds, fig. 24). Clearly, the interpretations of the strontium data derived from the drill-core samples alone need to be revised on the basis of the data from the ESF samples. Differences between the two data sets are attributed to thicker, better quality samples obtained from the ESF as noted previously for $\delta^{13}\text{C}$ and $\delta^{18}\text{O}$ data. On the basis of textural relations and microstratigraphic positions,

most subsamples can be classified readily as either basal or outer calcite in a given sample. Subsamples between these two positions are classified as intermediate. Although this grouping is subject to the same problems relating relative ages to true depositional history, it provides a means of evaluating the general temporal variations in strontium isotope compositions in fracture fluids percolating through the UZ.

Strontium isotope compositions show a general trend of increasing ratios with time on the basis of the relative position of subsamples in a mineral coating (fig. 25A). Basal calcite deposited within the lower one-third of mineral coatings generally has the least radiogenic $^{87}\text{Sr}/^{86}\text{Sr}$ ratios between 0.7105 and 0.7120. Subsamples representing late deposition (blade tips or the outer one-third of mineral coatings) have the most radiogenic $^{87}\text{Sr}/^{86}\text{Sr}$ ratios between 0.7115 and 0.7127. With one exception, the range of $^{87}\text{Sr}/^{86}\text{Sr}$ ratios for subsamples from intermediate microstratigraphic positions lies between the ranges for basal and outer groupings. Strontium concentrations range from about 35 to 537 $\mu\text{g/g}$ and have substantial overlap among all three groups (fig. 25B). However, calcite from the basal and intermediate groups rarely has concentrations greater than about 130 $\mu\text{g/g}$, whereas calcite in the outer group commonly has concentrations greater than this value.

Two of the thicker mineral coatings subsampled in detail reflect these variations in composition with relative time across their microstratigraphy (figs. 26 and 27). Ten sequential layers were milled from sample HD2065 (distance of 3,316.2 m from the north portal) using a fine carbide bur (fig. 26). Strontium concentrations scatter around 100 $\mu\text{g/g}$ in the first seven subsamples, followed by increases to 160, 221, and finally 537 in the outer three subsamples. This last value is the largest strontium concentration so far reported for UZ calcite (Vaniman and Chipera, 1996, table 3; Denniston and others, 1997, table 1). Strontium isotope compositions in the lowermost four subsamples (HD2065sa through HD2065sd) have an average $^{87}\text{Sr}/^{86}\text{Sr}$ value of 0.7115, whereas the overlying five subsamples (HD2065se through HD2065sl) have a slightly higher average $^{87}\text{Sr}/^{86}\text{Sr}$ value of 0.7117. The $^{87}\text{Sr}/^{86}\text{Sr}$ ratio for the outermost surface (HD2065sn) shifts to a much larger value of 0.7122. Five subsamples milled from sample HD2019 (distance of 2,880 m from the north portal) have similar relations between strontium isotope compositions and relative age based on microstratigraphic



EXPLANATION

- | | |
|---|--|
| ◇ ESF calcite | Boreholes
(Data from Marshall and others, 1992, table 1) |
| ■ Calcrete (Marshall and Mahan, 1994, fig. 7) | ■ UE-25 b #1 |
| --- Water table | ● USW G-1 |
| | ▲ USW G-2 |
| | ◆ USW G-3/GU-3 |
| | ▼ USW G-4 |

Figure 24. Strontium isotope compositions of calcite subsamples from drill core and the Exploratory Studies Facility (ESF) tunnel at Yucca Mountain, Nevada, as a function of depth relative to the water table.

position (fig. 27). No clear trend in strontium concentrations is observed with microstratigraphic position across the sample, although the latest formed subsample does have the largest value. In contrast to concentrations, $^{87}\text{Sr}/^{86}\text{Sr}$ ratios show a general increase from the smallest value of 0.7111 for subsample HD2019sc near the base of the coating to 0.7125 for subsample HD2019sf at the tips of calcite blades.

The range of $^{87}\text{Sr}/^{86}\text{Sr}$ values from the outer calcite grouping (0.7115 to 0.7127) is similar to the

range of values measured in drill-core calcite from the upper part of the UZ (fig. 24). This similarity is not surprising because subsamples of fracture coatings in drill core typically were scraped from outer surfaces (Marshall and others, 1992) and thus are biased towards a characterization of the youngest materials. However, earlier interpretations of possible trends of $^{87}\text{Sr}/^{86}\text{Sr}$ with depth in the UZ based on the drill-core data are problematic now that it is clear that strontium isotope compositions from calcite at ESF depths span

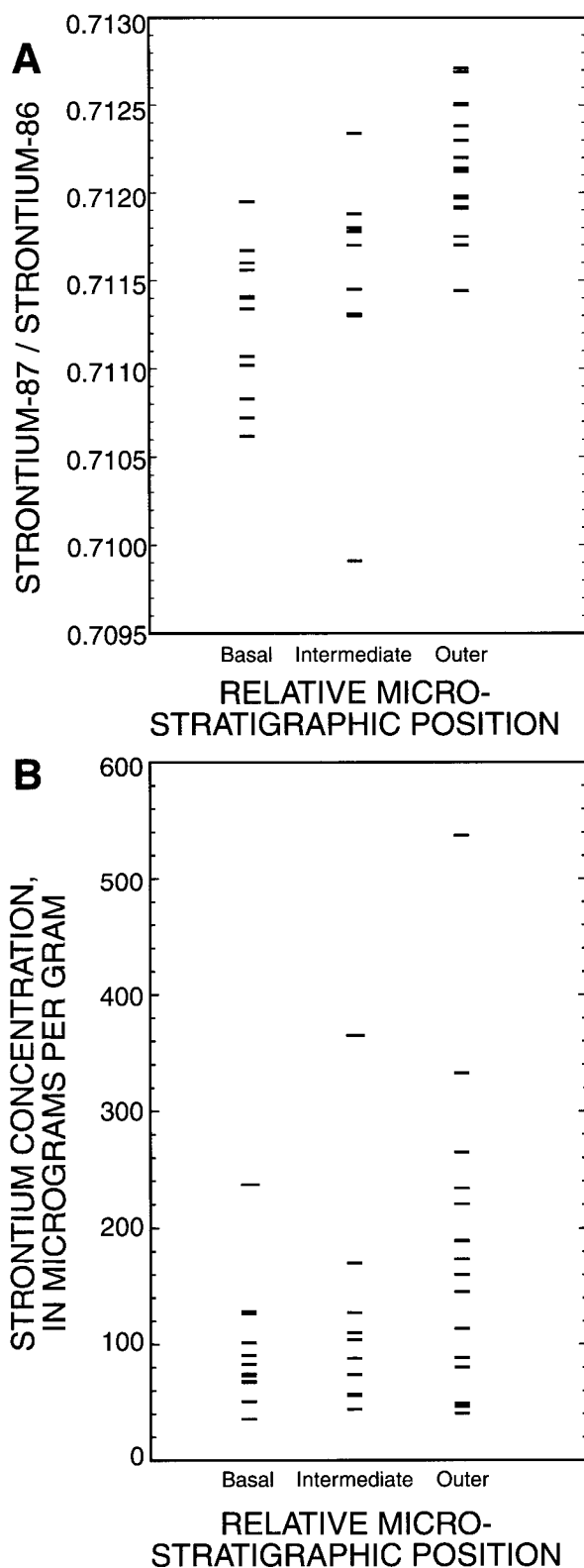


Figure 25. Strontium isotope compositions (A) and concentrations (B) for subsamples of calcite classified by relative microstratigraphic position from the Exploratory Studies Facility tunnel, Yucca Mountain, Nevada.

a much greater range. Interpretations of strontium isotope data require consideration of age in addition to position in the UZ.

Correlation Between Strontium, Carbon, and Oxygen Isotopes

Strontium isotope ratios from subsamples across mineral coatings show distinct correlations with carbon and oxygen isotopes. Carbon, oxygen, and strontium isotope data in Appendix 3 were obtained on splits of the same, relatively small subsamples. Correlations observed in these data represent a subset of the larger $\delta^{13}\text{C}$ and $\delta^{18}\text{O}$ data set plotted in figure 20. In particular, $^{87}\text{Sr}/^{86}\text{Sr}$ and $\delta^{13}\text{C}$ data for subsamples of outer calcite form a well-correlated group that mostly fall within the field defined by soil carbonate (fig. 28A). Four subsamples classified as outer calcite plot off this trend towards smaller values of $^{87}\text{Sr}/^{86}\text{Sr}$ (less than about 0.7119) and larger values of $\delta^{13}\text{C}$ (between -2.5 and 6.6 per mil). It may be that the relative microstratigraphic positions of these subsamples determined by petrographic examination are incorrect because of complex textural relations. The large $\delta^{13}\text{C}$ values above 0 per mil imply that these subsamples are more typical of either basal or intermediate calcite (fig. 22) and may have been collected from cleavage faces rather than growth surfaces, or may be from abandoned growth surfaces that lack young deposits. In contrast to the well-defined correlation between $^{87}\text{Sr}/^{86}\text{Sr}$ and $\delta^{13}\text{C}$ in outer calcite, the basal calcite group shows substantial scatter. If both basal- and intermediate-age groupings are considered together, $^{87}\text{Sr}/^{86}\text{Sr}$ and $\delta^{13}\text{C}$ data define a general negative correlation, although with a large degree of scatter. This relation and the previously described negative correlation between $\delta^{13}\text{C}$ and $\delta^{18}\text{O}$ (fig. 20) require that $^{87}\text{Sr}/^{86}\text{Sr}$ be positively correlated to $\delta^{18}\text{O}$ (fig. 28B). Although this correlation is evident for the entire data set, strontium and oxygen isotope data form poorly correlated clusters with basal and outer calcite at opposite ends of the overall trend. Oxygen-strontium relations may be complicated by the temperature dependency of equilibrium oxygen isotope fractionation, although most of the data shown in figure 28B are from a fairly restricted UZ depth interval (approximately 125- to 175-m difference estimated from bore-

HD2065 (LOCATED 3316.2 METERS FROM THE NORTH PORTAL)

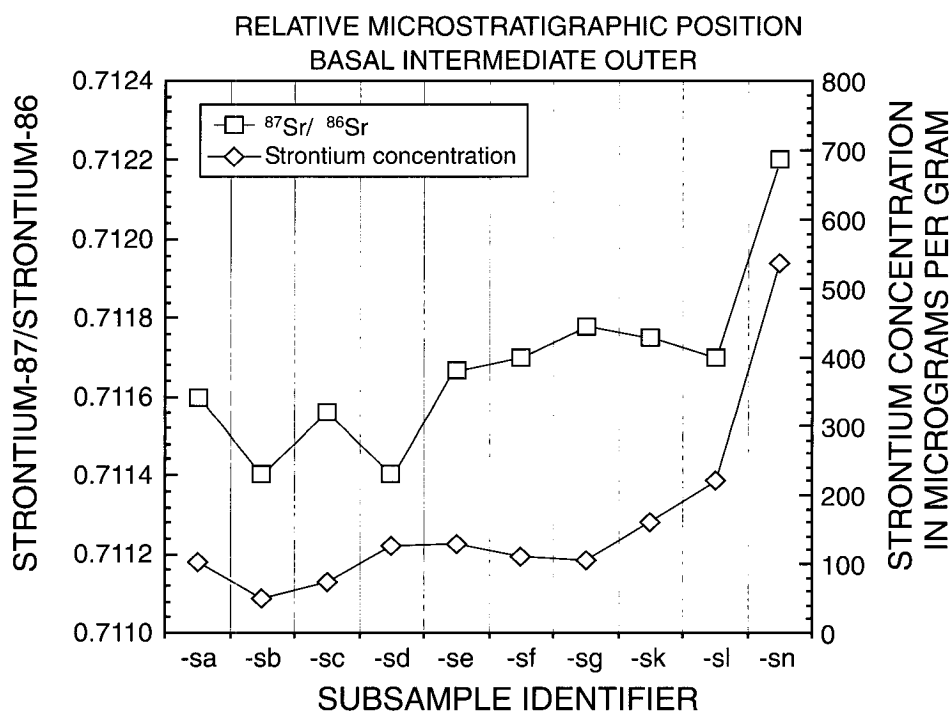
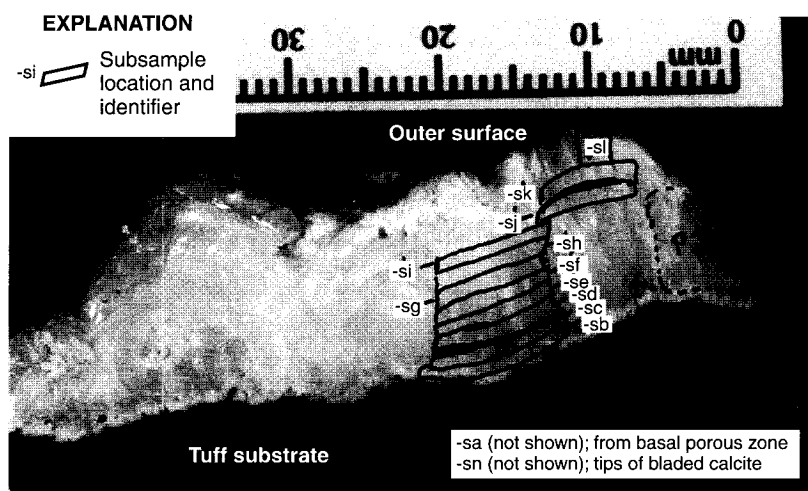


Figure 26. Photograph of sample HD2065 mineral coating from the Exploratory Studies Facility tunnel, Yucca Mountain, Nevada, showing calcite subsample locations and plot showing strontium isotope compositions and concentrations relative to microstratigraphic position.

hole data; Engstrom and Rautman, 1996, table 3; Rautman and Engstrom, 1996a, table 3, and 1996b, table 3).

The general correlations among carbon, oxygen, and strontium isotope data in UZ calcite probably are related to a gradual evolution of isotopic compositions in water percolating through fractures. The relatively

large amount of scatter observed in figure 28 indicates that the processes of evolution for each of the isotopic systems are not linked directly. Separate, time-dependent processes most likely control the resulting isotopic composition of percolating water. Alternatively, coherent trends can sometimes be attributed to mixing processes between end-member compositions,

HD2019 (LOCATED 2,880 METERS FROM THE NORTH PORTAL)

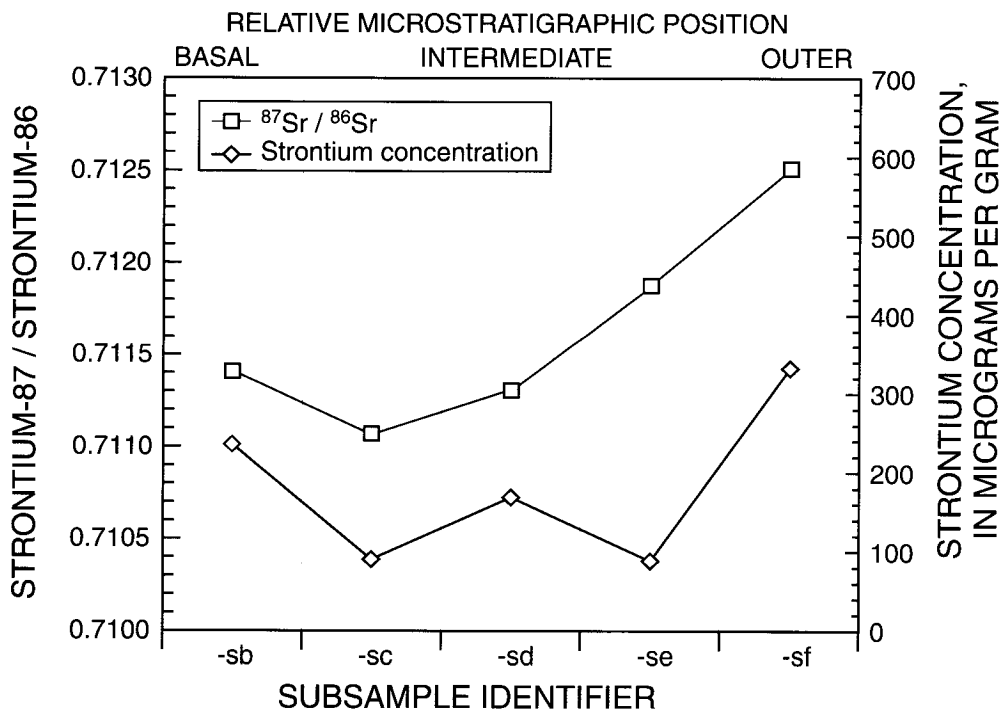
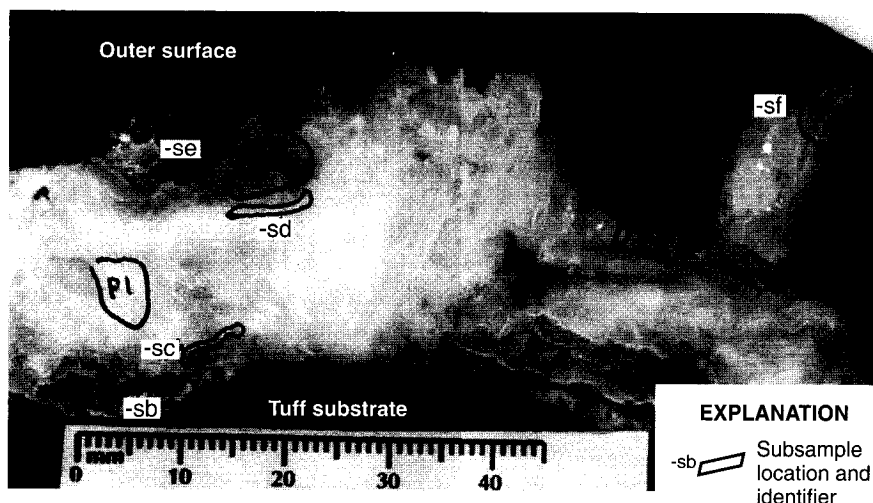


Figure 27. Photograph of sample HD2019 mineral coating from the Exploratory Studies Facility tunnel, Yucca Mountain, Nevada, showing calcite subsample locations and plot showing strontium isotope compositions and concentrations relative to microstratigraphic position.

especially when trends are highly correlated such as the outer calcite group in figure 28A. Simple binary mixing produces linear or hyperbolic trends on isotopic plots similar to those observed between $^{87}\text{Sr}/^{86}\text{Sr}$ and $\delta^{13}\text{C}$ in outer calcite subsamples (fig. 28A). However, if mixing processes were responsible for these results, strongly correlated linear trends also should be observed on other isotope plots (fig. 28B and 28C) as well as $^{87}\text{Sr}/^{86}\text{Sr}$ plotted against the recip-

rocal of strontium concentration (fig. 28D). The absence of uniformly correlated trends for outer calcite subsamples on these plots precludes mixing as an important process affecting isotopic ratios in UZ calcite. The general trends defined by basal-, intermediate-, and outer-calcite isotope compositions based on relative age observations indicate that all three isotopic systems have changed systematically since the oldest deposits were formed.

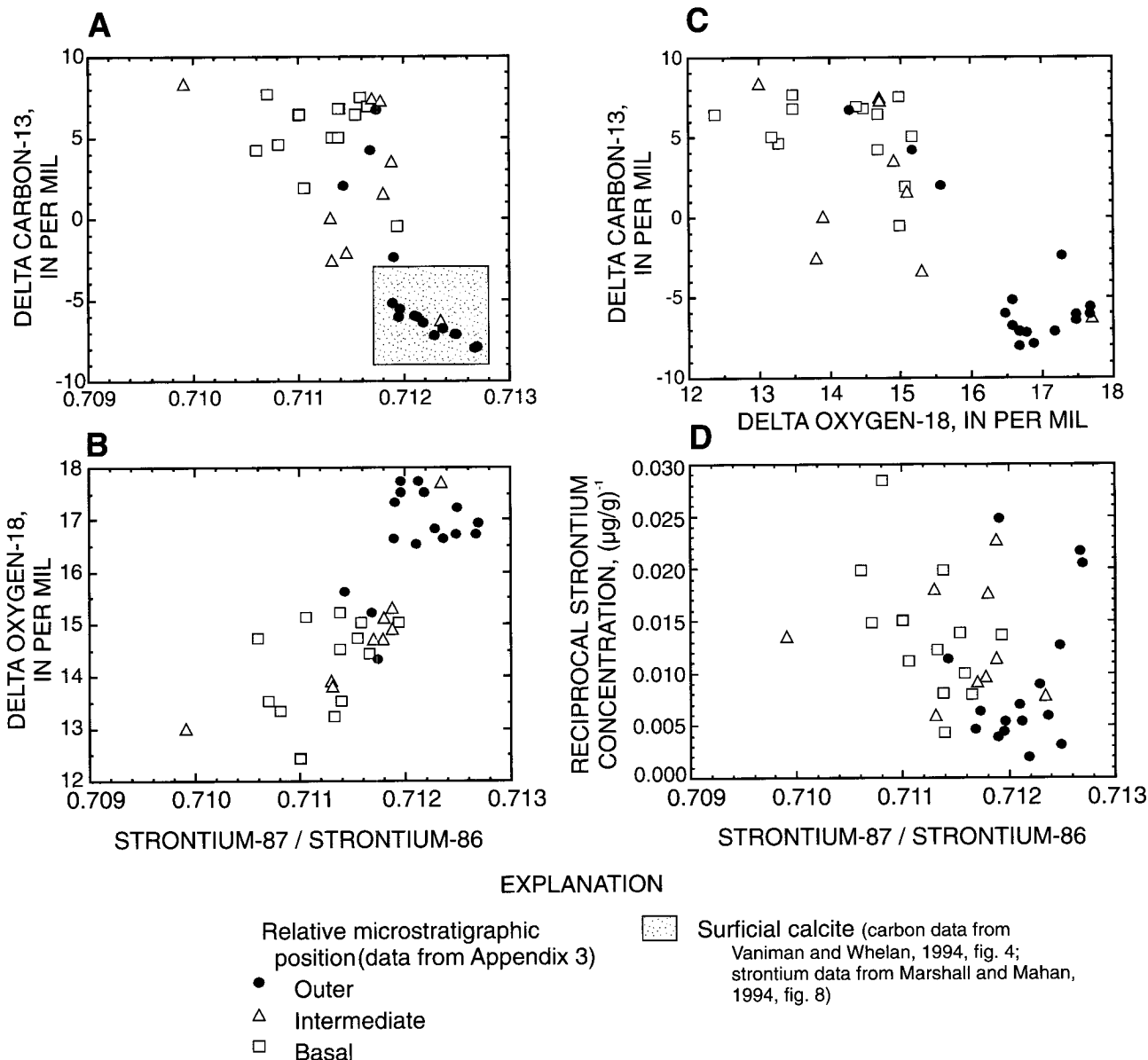


Figure 28. Relations among carbon, oxygen, and strontium isotope composition and reciprocal strontium concentration for subsamples of calcite from the Exploratory Studies Facility tunnel, Yucca Mountain, Nevada.

INTERPRETATION OF AGES

Ages based on radioactive decay are not measured directly, but are calculated from isotopic ratios on the basis of assumptions concerning the origin and subsequent behavior of the natural system. Two theoretical models can be developed to represent end-member depositional processes responsible for ESF calcite and opal. Although both models assume closed-system behavior after mineral formation, the two models have fundamental differences in the

assumptions of the initial isotopic conditions of the materials that constitute a subsample. Different numerical formulations of the temporal evolution of isotopic ratios are used in the two models, resulting in different ages and age interpretations. The two models are described conceptually and numerically.

Conceptual Models of Deposition

An episodic/instantaneous deposition model is applicable where discrete mineral layers form over

time intervals that are brief relative to the half-lives of the radioactive isotope used for age determinations. This model assumes that layers of finite thickness formed instantaneously with uniform initial isotopic compositions (fig. 29). Calculated numerical ages of an individual layer will accurately reflect the age of the discrete depositional event and will allow correlation of coeval layers on the same sample as well as between samples with similar growth histories. Because all isotopic systems in an instantaneously deposited layer are initiated at the same time, resulting ages determined from different isotopic systems must be concordant for aliquots of a single subsample.

A continuous deposition model assumes that mineral growth from percolating solutions occurs at slow, constant rates up through the present, resulting in a continuum of infinitely thin layers (fig. 29). Under these conditions, discrete layers of uniform age and initial composition cannot be defined. Subsamples of finite thickness represent mixtures of older and younger material, and apparent ages calculated from the resulting measured ratios will not represent a discrete age, but an intermediate age dependent on the thickness of a subsample and the ages of the youngest

and oldest layers. Unless deposits and subsampling techniques are remarkably uniform (or the thickness of deposits is large relative to the age span represented), calculated ages for different subsamples with similar positions in a mineral coating are not likely to correlate unambiguously. Different isotopic clocks will yield discordant calculated ages for the same materials because the ages are dependent on the half-lives of the isotope being used. If deposition has continued to the present, subsamples of outermost materials will never yield calculated ages at the upper dating limit of the isotopic system [reached at about 45 ka for ^{14}C , about 200 ka for protactinium-231/uranium-235 ($^{231}\text{Pa}/^{235}\text{U}$), and about 400 ka for $^{230}\text{Th}/\text{U}$].

Numerical Model of Continuous Deposition

The conventional numerical solution to the $^{230}\text{Th}/\text{U}$ age equation based on assumptions of instantaneous deposition yields ages and initial $^{234}\text{U}/^{238}\text{U}$ ratios that do not adequately explain many aspects of the isotopic data from the UZ at Yucca Mountain. Textural evidence of layering on a micrometer scale in

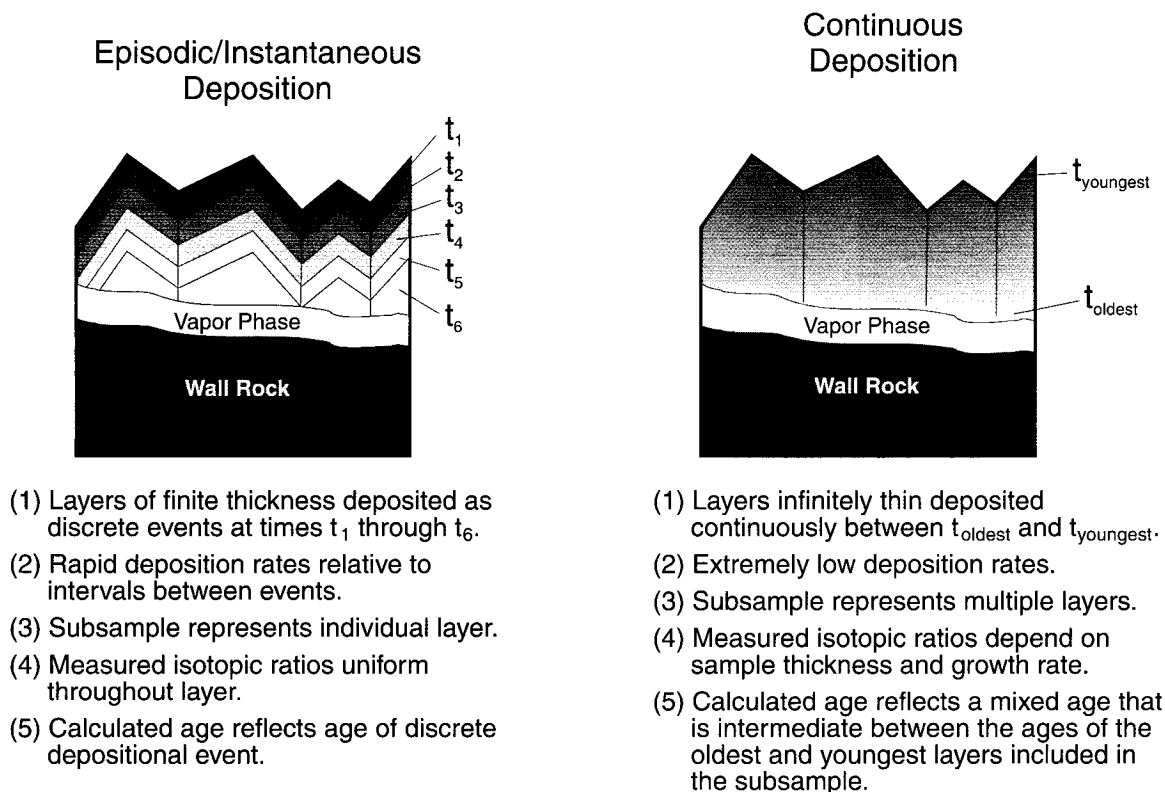


Figure 29. Conceptual models of episodic/instantaneous and continuous mineral deposition.

both opal and calcite provides a physical rationale for applying a numerical model based on assumptions of continuous deposition. In its simplest, theoretical form, the following are assumed in the model.

1. Deposition of mineral coatings started at 12 Ma (approximate age of host tuffs) and continued growing outwards until the present at a constant rate of deposition, V (in mm/yr);
2. ^{238}U is distributed uniformly through the thickness of the mineral deposits;
3. No initial ^{230}Th was inherited from the aqueous solutions carrying dissolved uranium and other cations;
4. Once formed, minerals behaved as closed systems relative to ^{238}U and its decay products through ^{230}Th ; and
5. All samples of finite size integrate multiple, infinitely thin depositional layers with continuously varying ages.

If these assumptions approximate the natural system, erroneous estimates of ages and $^{234}\text{U}/^{238}\text{U}$ initial ratios would be obtained using the conventional $^{230}\text{Th}/\text{U}$ dating equation given by Ivanovich and Harmon (1992, appendix A):

$$\frac{^{230}\text{Th}}{^{238}\text{U}} = (1 - e^{-\lambda_{230}t}) + \left(\frac{^{234}\text{U}}{^{238}\text{U}} - 1 \right) \times \left(\frac{\lambda_{230}}{\lambda_{230} - \lambda_{234}} \right) \times (1 - e^{-(\lambda_{230} - \lambda_{234})t}), \quad (1)$$

where e is the base of the natural logarithm (approximately equal to 2.71828), λ is the decay constant of the isotope given in subscript (in reciprocal years), and t is the age of the subsample.

Erroneous age estimates largely result from the fact that the analyzed material was formed over a time period that is not negligibly short relative to the half-life of ^{230}Th . The conventional $^{230}\text{Th}/\text{U}$ age equation not only would misrepresent the age spectrum within a continuously deposited subsample, but also would misrepresent the average age of the subsample because of the nonlinearity of radioactive decay equations.

In order to mathematically approximate a depositional system where material is added continuously at the same time that older material is undergoing

constant isotopic evolution, the conventional $^{230}\text{Th}/\text{U}$ age equation must be reformulated. Equations 2 and 3 describe the integrated $^{234}\text{U}/^{238}\text{U}$ and $^{230}\text{Th}/^{238}\text{U}$ compositions after a given period of time from the initial start of the system, $t=0$, to the present-day age of the subsample, t :

$$\left(\frac{^{234}\text{U}}{^{238}\text{U}} \right)_t = \frac{\int_0^t ^{234}\text{U}(t)dt}{\int_0^t ^{238}\text{U}(t)dt}, \text{ and} \quad (2)$$

$$\left(\frac{^{230}\text{Th}}{^{238}\text{U}} \right)_t = \frac{\int_0^t ^{230}\text{Th}(t)dt}{\int_0^t ^{238}\text{U}(t)dt}. \quad (3)$$

Using the simplifying assumption that $e^{-\lambda_{238}t} = 1$ because of the much longer half-life of ^{238}U relative to ^{234}U and ^{230}Th , the activities of $^{238}\text{U}(t)$, $^{234}\text{U}(t)$, and $^{230}\text{Th}(t)$ in each infinitely thin layer are defined by equations 4, 5, and 6:

$$^{238}\text{U}(t) = ^{238}\text{U}_0 e^{-\lambda_{238}t} \equiv ^{238}\text{U}_0, \quad (4)$$

$$^{234}\text{U}(t) = ^{238}\text{U}_0 \left\{ \frac{\lambda_{234}}{\lambda_{234} - \lambda_{238}} \times (1 - e^{-\lambda_{234}t}) + \left(\frac{^{234}\text{U}}{^{238}\text{U}} \right)_0 e^{-\lambda_{234}t} \right\}, \text{ and} \quad (5)$$

$$^{230}\text{Th}(t) = ^{238}\text{U}_0 \left\{ 1 - e^{-\lambda_{230}t} + \frac{\lambda_{230}}{\lambda_{230} - \lambda_{234}} \times (e^{-\lambda_{234}t} - e^{-\lambda_{230}t}) \times \left[\left(\frac{^{234}\text{U}}{^{238}\text{U}} \right)_0 - 1 \right] \right\}, \quad (6)$$

where $^{238}\text{U}_0$ and $^{234}\text{U}_0$ are the isotopic activities at $t = 0$.

Substitution of equations 4, 5, and 6 into equations 1 and 2 and integrating from 0 to t yields the

integrated isotopic composition of the subsample formed under pure, end-member continuous deposition conditions. Although the equations above are solvable analytically, solutions to the continuous deposition model mathematical expressions used in this report were derived by numerical methods using finite intervals.

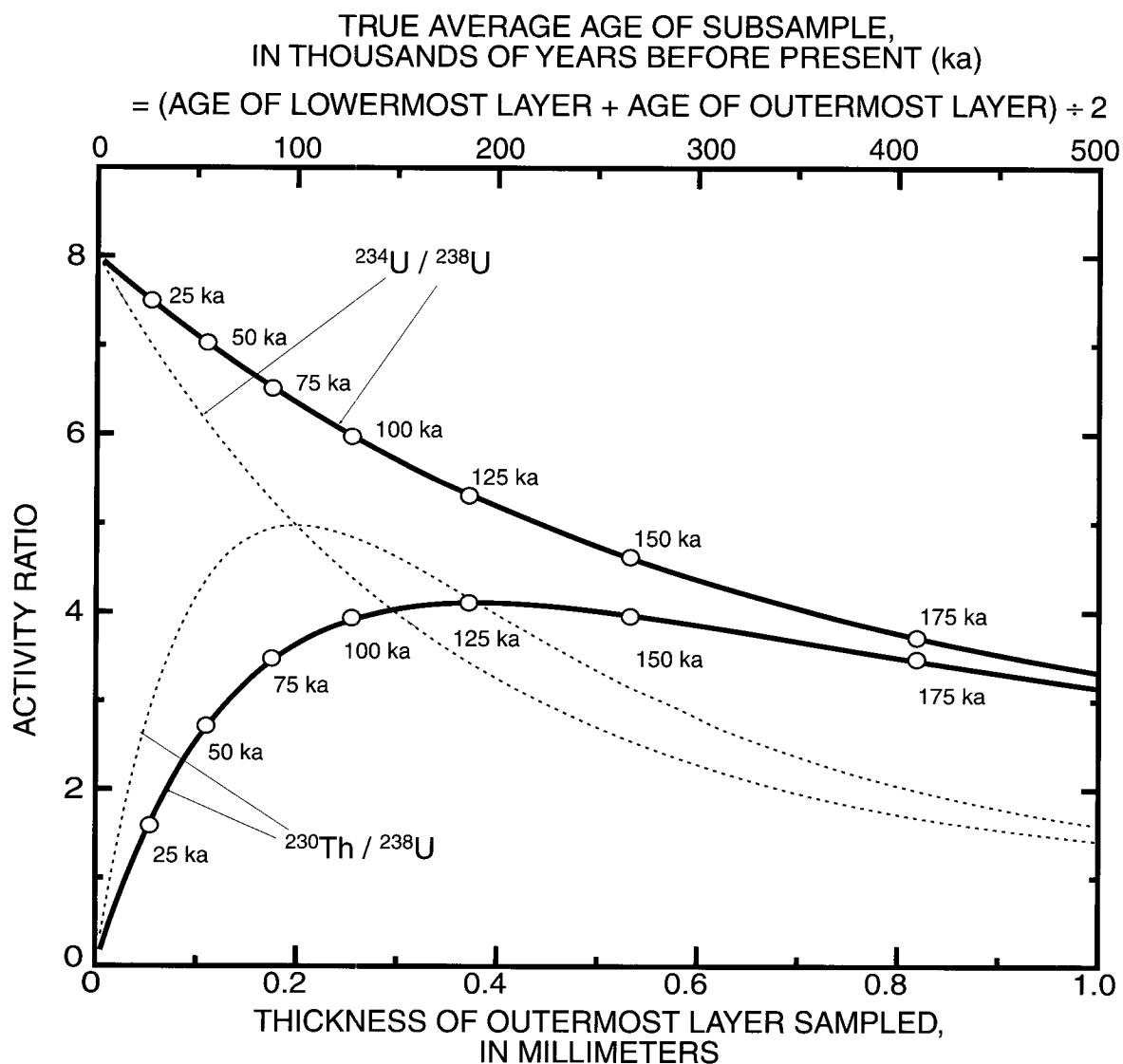
Equations 2 and 3 are applicable only where the outermost layers were included in a subsample (t is defined as growth to the present day). Layers with nonzero-aged surfaces in mineral-coating interiors can be described by changing the integration limits from 0 and t to t_1 and t_2 . The same type of equations also may be used for age calculations involving other isotopic systems with short-lived nuclides [for instance ^{231}Pa , ^{14}C , radium-226 (^{226}Ra)]. The mathematical expression of continuous deposition also may provide a good means of approximating the depositional process where numerous episodes of thin, instantaneously deposited layers (rather than an infinite number of continuously deposited layers) cannot be resolved in a single sample.

Isotopic compositions determined for a subsample that was formed under conditions of continuous deposition will be significantly different than those in a subsample formed instantaneously during a discrete depositional event. A conventional $^{230}\text{Th}/\text{U}$ age still can be calculated from the isotopic composition measured from a continuously deposited subsample, but instead of representing any single depositional event, it will represent an age intermediate between the oldest and youngest layers included in the subsample. For a hypothetical case where a 10-mm-thick mineral coating is deposited continuously at a rate of 1×10^{-6} mm/yr over a 10-m.y. period, subsamples of the outermost parts of the coating will have isotopic compositions that depend on the subsample thickness (fig. 30). Once deposited, uranium and thorium in each infinitely thin layer will start evolving isotopically at the same time that younger material is being added. A subsample of finite thickness will have $^{234}\text{U}/^{238}\text{U}$ and $^{230}\text{Th}/^{238}\text{U}$ compositions defined along the solid curves in figure 30 and will reflect a contribution from all layers younger than the age of the deepest layer sampled. Measured isotopic compositions for continuously deposited subsamples of varying thickness can be used to calculate conventional $^{230}\text{Th}/\text{U}$ ages (open circles in fig. 30); however, the resulting values will be biased toward ages younger than the true average age of the

subsample (equal to half the sum of the oldest and youngest layers present). The difference between conventionally calculated $^{230}\text{Th}/\text{U}$ ages and the true average age for continuously deposited subsamples is small for thin subsamples with true average ages less than 50 ka, but becomes greater for thicker subsamples with older true average ages (fig. 30). For instance, a 0.11-mm-thick subsample from this hypothetical, continuously deposited coating has a true average age of about 55 ka (oldest layer deposited at 110 ka), and an isotopic composition that yields a conventional $^{230}\text{Th}/\text{U}$ age of 50 ka. A 0.82-mm-thick subsample from the same coating has a true average age of about 409 ka (oldest layer deposited at 818 ka), but isotopic compositions that yield a conventionally calculated $^{230}\text{Th}/\text{U}$ age of only 175 ka. For comparison, the loci of isotopic compositions for the lowermost layers in subsamples of variable thickness from this hypothetical coating also are shown in figure 30 (dotted lines).

Isotopic compositions derived from the model of continuous deposition are strongly dependent on the rates at which minerals are deposited. If the deposition rate is fast relative to the rates of isotopic decay, the effect of sample thickness is small. At slower deposition rates, isotopic compositions can vary substantially with depth in a subsample of finite thickness. For growth rates of 5×10^{-7} to 5×10^{-6} mm/yr (fig. 31), 0.2-mm-thick subsamples deposited continuously up to the present will have isotopic compositions that yield conventional $^{230}\text{Th}/\text{U}$ ages from about 20 to 150 ka. This corresponds to true lowermost-layer ages of 40 to 400 ka (open circles in fig. 31). In addition, at growth rates as slow as 5×10^{-7} mm/yr (resulting in a total thickness of 6 mm over the last 12 m.y.), subsamples of the outermost 0.1 to 0.2 mm will have isotopic compositions that do not yield conventional $^{230}\text{Th}/\text{U}$ ages younger than about 90 to 150 ka. Younger conventional $^{230}\text{Th}/\text{U}$ ages can be calculated for the similar-sized subsamples if depositional rates are more rapid. Although subsample thickness was not measured in the current data set, values of 0.1 to 1.0 mm are typical with the thinnest subsamples yielding the youngest $^{230}\text{Th}/\text{U}$ ages. A schematic representation of this field of sample thickness and conventional $^{230}\text{Th}/\text{U}$ age is shown in figure 31 and is interpreted as evidence that deposition rates were restricted to less than about 5×10^{-6} mm/yr.

Values of $^{230}\text{Th}/^{238}\text{U}$ and $^{234}\text{U}/^{238}\text{U}$ calculated using the continuous deposition equations diverge from the isotopic compositions used to define the



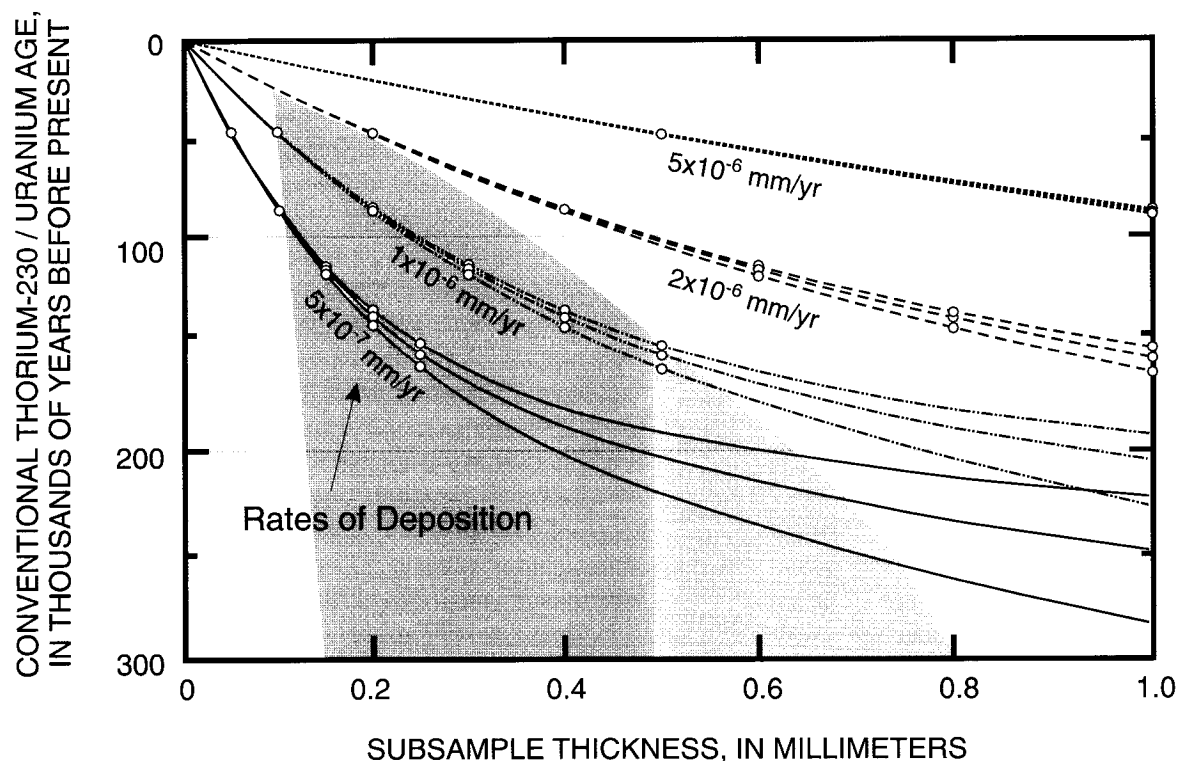
EXPLANATION

- Isotopic compositions of subsamples of variable thickness assuming ideal continuous deposition, a zero-age outermost layer, constant fluid $^{234}\text{U} / ^{238}\text{U}$ composition, and a constant rate of deposition of 1×10^{-6} millimeters per year
- Isotopic composition of the lowermost instantaneously deposited layer shown for comparison to the isotopic composition of the entire subsample
- Conventional $^{230}\text{Th}/\text{U}$ age, given in thousands of years before present (ka), calculated from the isotopic compositions of subsamples formed under conditions of continuous deposition

Figure 30. Model thorium-230/uranium-238 and uranium-234/uranium-238 activity ratios in a hypothetical 1-millimeter-thick mineral coating formed under conditions of continuous deposition over the last million years.

conventional uranium-series disequilibrium evolution curves (fig. 32). Differences between the models are small for materials younger than 50 to 100 ka; however, as material in continuously deposited subsamples becomes older, isotopic compositions shift to smaller values of $^{230}\text{Th}/^{238}\text{U}$ at a given value of $^{234}\text{U}/^{238}\text{U}$. For example, a coating deposited continuously over the last 500 k.y. from percolating solutions with a constant $^{234}\text{U}/^{238}\text{U}$ ratio of 6 may yield subsamples of varying thickness that yield conventionally calculated $^{230}\text{Th}/\text{U}$ ages up to 150 ka with a range of initial ratios between about 5.2 and 6. As subsample thicknesses and true average ages become greater, continuous deposition evolution curves start to become nearly parallel to conventionally calculated isochrons

greater than about 150 ka. Consequently, isotopic data from continuously deposited subsamples representing a long history of deposition may appear to have relatively minor variations in age accompanied by large variations of $^{234}\text{U}/^{238}\text{U}$ initial ratios in spite of the fact that percolating solutions had constant $^{234}\text{U}/^{238}\text{U}$ ratios. These theoretical tendencies roughly coincide with observed data (fig. 32). In contrast, trends expected for mixtures of older (secular equilibrium) material and material formed during a relatively young depositional event would fall along straight mixing lines such as the dashed line shown in figure 32. These mixing trends would tend to populate the uranium-series isotope evolution plot with points



EXPLANATION

- Loci of conventional $^{230}\text{Th}/\text{U}$ ages calculated for ideal continuous deposition at different growth rates, given in millimeters per year (mm/yr). All models assume a zero-age outermost layer and constant initial $^{234}\text{U}/^{238}\text{U}$ activity ratios of 1.6 (lowermost of each set of curves), 3.0, and 6.0 (uppermost of each set of curves)
- True age of the lowermost layer within a subsample given for 100,000 year intervals up to 500,000 years (to 200,000 years for the 5×10^{-6} mm/yr curves)
- Generalized range observed for subsamples of calcite and opal from the Exploratory Studies Facility, Yucca Mountain, Nevada

Figure 31. Relation between subsample thickness and conventional thorium-230/uranium calculated from isotopic ratios in hypothetical minerals formed under conditions of continuous deposition at slow growth rates.

above and to the left of secular equilibrium $^{234}\text{U}/^{238}\text{U}$ and $^{230}\text{Th}/^{238}\text{U}$ values.

Conventional $^{230}\text{Th}/\text{U}$ ages and initial $^{234}\text{U}/^{238}\text{U}$ ratios can be calculated from uranium and thorium isotope compositions simulated by simple continuous deposition models. These model ages and initial ratios compare favorably with the general negative correlation observed in the ESF data (fig. 33). In addition, multiple subsamples from single mineral coatings commonly mimic patterns of variation predicted for continuously deposited layers of variable thickness from solutions with uniform $^{234}\text{U}/^{238}\text{U}$ ratios. In contrast, mixing of old and young materials would fail to produce the observed relations between ages and initial ratios. For example, a mixture of modern material having a $^{234}\text{U}/^{238}\text{U}$ ratio of 10 with material in secular equilibrium ($^{234}\text{U}/^{238}\text{U}$ equal to unity) results in a hyperbolic curve (fig. 33) defining rapidly decreasing $^{234}\text{U}/^{238}\text{U}$ ratios and slowly increasing apparent ages as more of the older material is added (dash-dot line in fig. 33). If mixing of this type were a controlling process, data would populate the lower left corner of figure 33 instead of the present distribution. Although the age-initial ratio relation calculated for isotopic compositions in continuously deposited subsamples mimic much of the observed data, a simple model cannot simulate all of the data shown in figure 33. In order to explain data simultaneously showing old apparent ages and high initial $^{234}\text{U}/^{238}\text{U}$ ratios (points to the right of the dashed curves in fig. 33), the simple model of continuous deposition could be modified to include a nonzero age of the outermost layer, implying that deposition at a given site terminated in the past.

Discordance Between Isotopic Systems

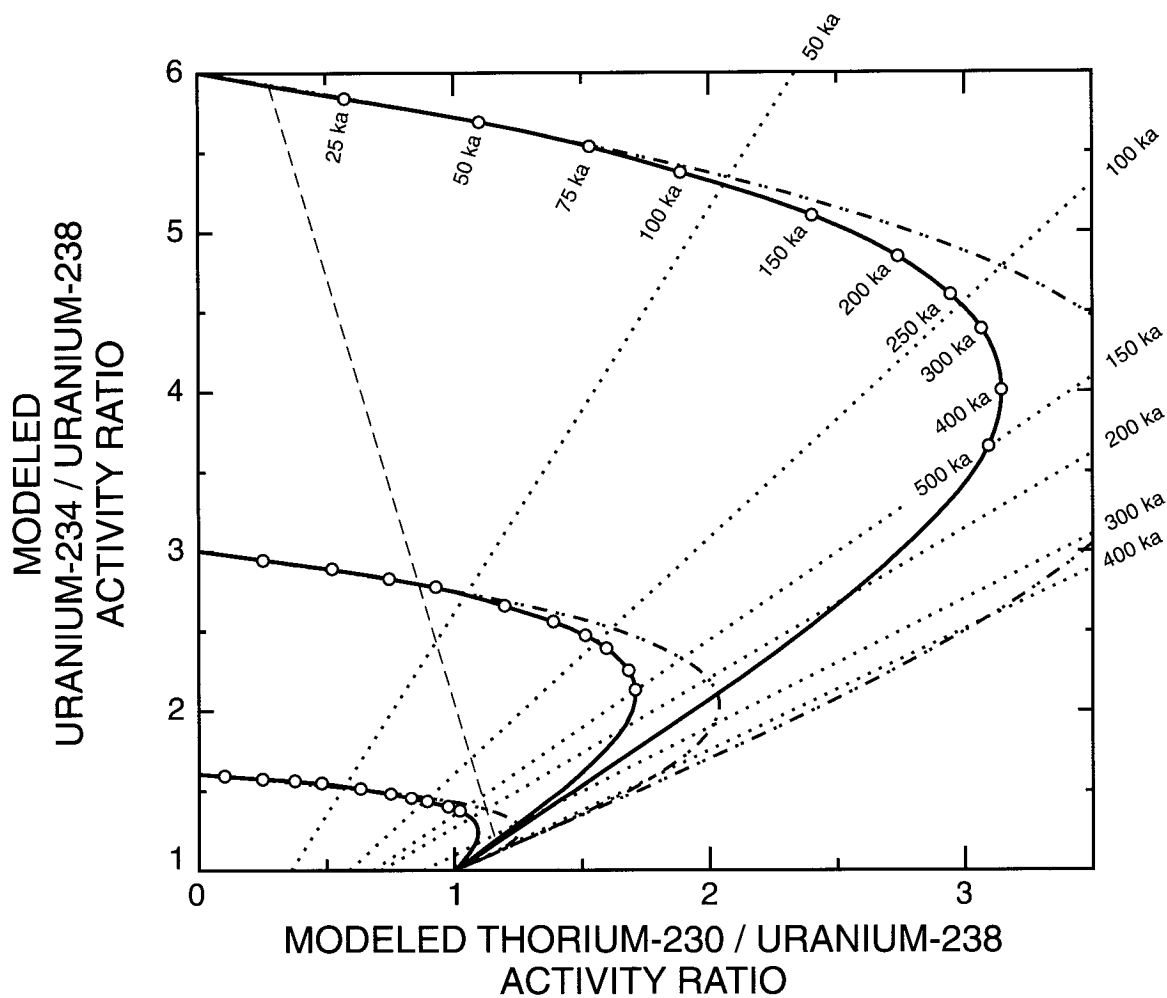
The equations for continuous deposition also can explain the observed discordance between radiocarbon and $^{230}\text{Th}/\text{U}$ ages (fig. 10). Because radioactive decay involves exponential terms, the addition of young material on outer mineral surfaces will result in subsamples with mixed isotopic compositions that never reach the older age limits of the radioactive systems being used for dating. As a result, conventional $^{230}\text{Th}/\text{U}$, $^{231}\text{Pa}/^{235}\text{U}$, ^{14}C , and $^{226}\text{Ra}/^{230}\text{Th}$ ages calculated from continuously deposited materials increasingly deviate from the true average ages in older subsamples (fig. 34).

Therefore, conventionally calculated ages near the older end of the working range may substantially misrepresent the true average age of the subsample. For example, calcite with a conventionally calculated ^{14}C age of about 30 ka actually may represent deposition over the last 600 k.y. (true average age of 300 ka on fig. 34). The same material would have a conventionally calculated $^{230}\text{Th}/\text{U}$ age of about 160 to 175 ka (depending on $^{234}\text{U}/^{238}\text{U}$ initial activity ratio), which is still little more than half of the true average age. Therefore, discordance between ages determined by different isotopic systems is expected for subsamples formed under conditions approximating the continuous deposition model. Comparisons between the observed distribution of $^{230}\text{Th}/\text{U}$ ages (28 to greater than 500 ka) and radiocarbon ages (16 to 44 ka) for subsamples from the ESF calcite and opal (fig. 10) are consistent with the general concepts described by a continuous deposition model.

Constraints on Depositional Processes from Geochronology

Geochronological data from mineral deposits deep in the Yucca Mountain UZ support the concept of slow, more or less continuous deposition over the past 500 k.y. or more, in contrast to rapid, episodic growth during a limited number of discrete depositional events. Aspects of both of these contrasting depositional models are summarized in table 2. Radiocarbon and uranium-thorium isotope data from the ESF subsamples are consistent with many of the features listed under the continuous deposition model. A simplistic mathematical model of pure continuous deposition simulates many of the observations that are difficult to explain if subsamples are considered to be the result of instantaneous deposition. In particular, wide variations in ages for subsamples from a single mineral coating, the negative correlation between conventional $^{230}\text{Th}/\text{U}$ ages and initial $^{234}\text{U}/^{238}\text{U}$ ratios, and the discordance between different isotopic systems for subsamples from outer sample surfaces are difficult to reconcile if mineral deposits are assumed to form under conditions of instantaneous deposition. These aspects are all expected if mineral coatings were deposited more or less continuously.

Slow rates of mineral deposition over the last 500 k.y. are inferred from the geochronological data set for minerals collected from the deep UZ at Yucca



EXPLANATION

- Loci of model isotopic compositions for a hypothetical mineral formed under conditions of continuous deposition assuming constant growth rates, constant initial $^{234}\text{U}/^{238}\text{U}$ ratios, and a zero-age outermost layer
- True ages of the lowermost layer in subsamples of varying thickness deposited under conditions of continuous deposition, in thousands of years before present (ka)
- - - Loci of model isotopic compositions for a hypothetical mineral deposited instantaneously
- Isochrons for instantaneously deposited minerals, in ka
- · - Two-component mixing trend between older and younger components

Figure 32. Uranium-series disequilibrium evolution diagram showing comparisons between isotopic compositions of hypothetical minerals formed under conditions of continuous and instantaneous deposition.

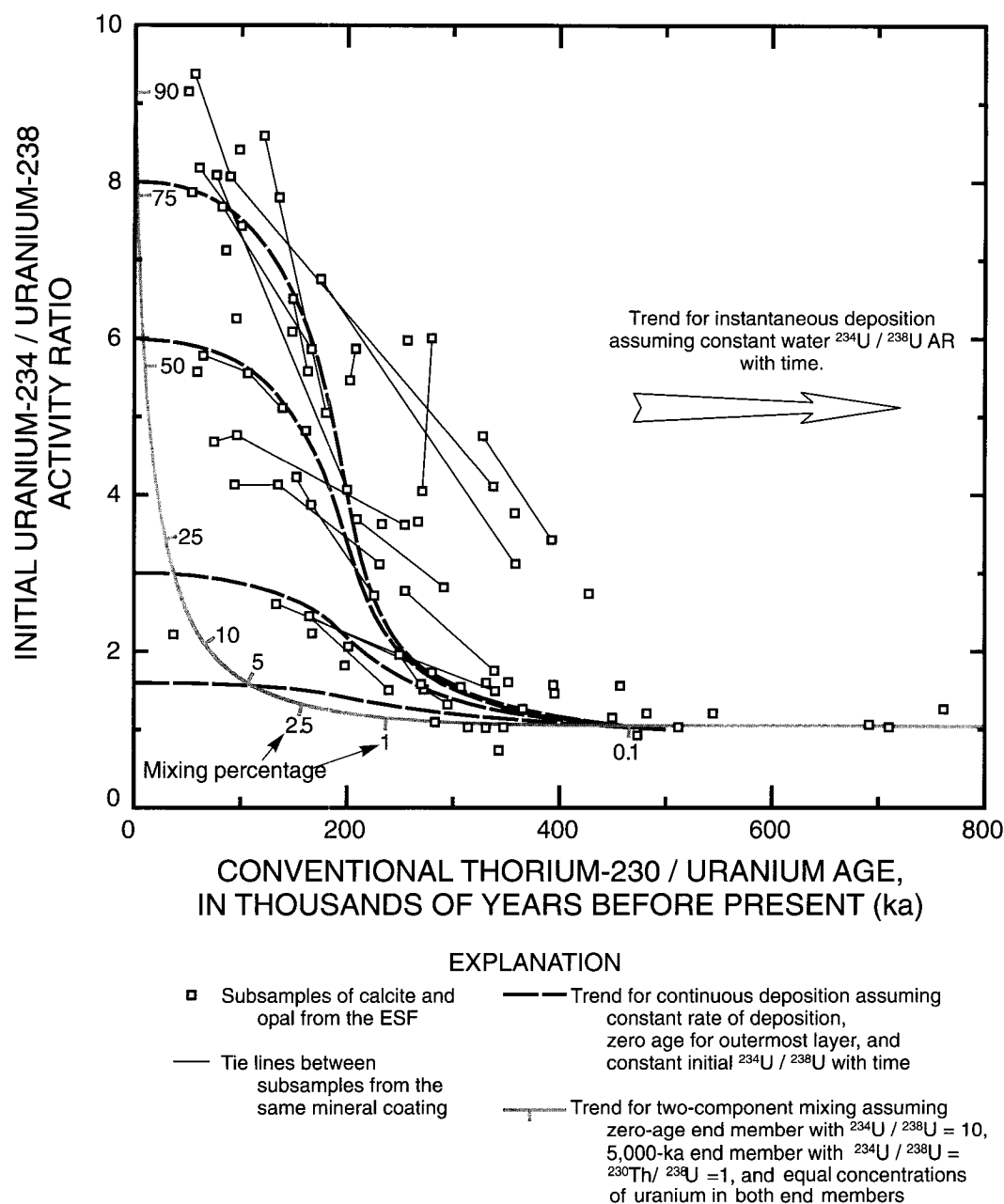


Figure 33. Conventional thorium-230/uranium age and initial uranium-234/uranium-238 activity ratios for subsamples of calcite and opal from the Exploratory Studies Facility (ESF) tunnel, Yucca Mountain, Nevada, along with trends expected for continuous deposition, instantaneous deposition, and mixing between two components with different ages.

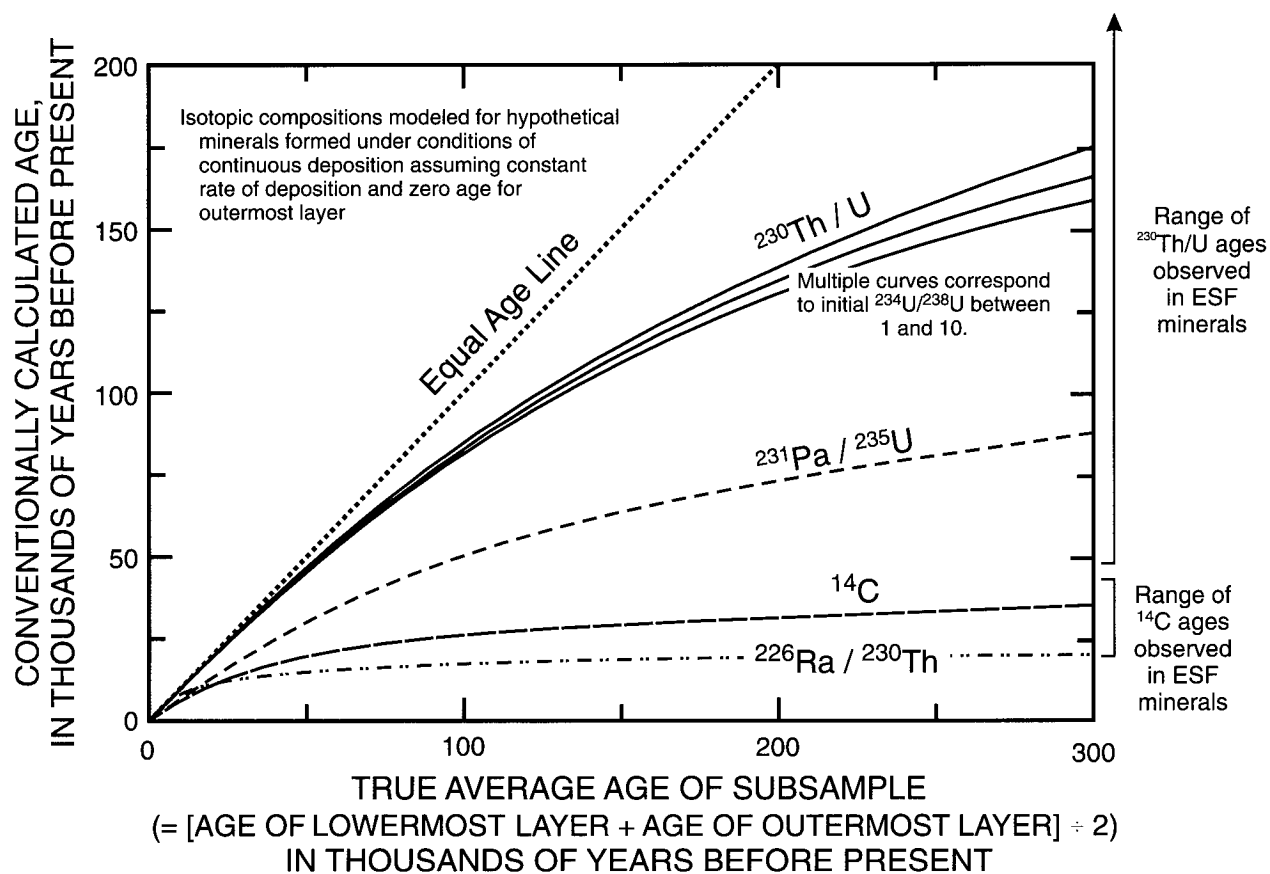


Figure 34. Relations between the true average ages of hypothetical minerals formed under conditions of continuous deposition and the conventionally calculated ages based on the isotopic compositions of oldest to youngest materials within a subsample for geochronometers with different decay constants.

Mountain. Probable long-term growth rates are on the order of 1 to 5 mm of mineral per million years (fig. 31) with the more rapid rates possible over shorter periods of time. These rates are consistent with observed coating thicknesses (from about 5 to 40 mm) assuming that deposition was continuous over the past 10 to 13 m.y. Preliminary uranium-lead dating of interior layers of chalcedony and opal in individual mineral coatings indicates that these deposition rates are reasonable (Neymark and others, 1998).

Under these types of slow, continuous growth conditions, isotopic compositions of a subsample represent an integration of new layers added sequentially at the same time radioactive decay is taking place in older layers. As a result, measured isotopic ratios for subsamples of finite thickness will be intermediate between those for the oldest and youngest materials in a subsample. Ages calculated from these isotopic compositions using conventional decay equa-

tions therefore may misrepresent the true distribution of ages in a subsample. Because of the longer half-life of ^{230}Th relative to ^{14}C and the presence of young, but very thin, material on outer surfaces, conventionally calculated $^{230}\text{Th}/\text{U}$ ages given in this report represent closer approximations of the true average ages for subsamples, especially for materials younger than 100 ka (fig. 34). Nevertheless, the presence of ^{14}C in all samples indicates that outermost layers of calcite were deposited after 16 to 44 ka. Identification of the youngest components in these mineral coatings is not possible until micrometer-scale subsampling becomes available or isotopic systems with half-lives younger than ^{14}C ($^{226}\text{Ra}/^{230}\text{Th}$, for instance) are used.

The model of continuous deposition presented above is a simple mathematical representation of an end-member depositional process possible in the Yucca Mountain UZ environment. The actual process of secondary mineral deposition probably lies between

Table 2. Comparison of effects for instantaneous and continuous depositional models

Instantaneous deposition	Continuous deposition
1. A single depositional event can be represented in a subsample of finite thickness.	1. Multiple depositional events are present in a subsample of finite thickness.
2. Ages determined on a single subsample using different isotopic systems with different half-lives should be concordant.	2. Ages determined on a single subsample using isotopic systems with different half-lives are likely to be discordant.
3. Ages of subsamples from the outermost materials may be greater than the dating limit of a given geochronometer if the outermost layer is older than about 5 half-lives of the parent isotope.	3. Ages of subsamples from the outermost materials are likely to be younger than the dating limit of a given geochronometer as long as only small amounts of recently deposited material are present on outer surfaces.
4. Ages from a given layer are independent of subsample thickness.	4. Ages depend on subsample thickness: thinner subsamples incorporate less older material, resulting in younger ages.
5. Ages are not affected by growth rate.	5. Ages of subsamples of uniform thickness are dependent on mineral growth rates.

the purely continuous and instantaneous extremes. Slow rates of deposition probably do occur over long time periods. However, these rates probably are not constant, and they are likely to be disrupted by at least short episodes of nondeposition. The presence of a zero-age, or even uniform-age (for instance, last glacial maximum) outer layer may not be a realistic assumption for the continuous deposition model. These issues can be better refined only by increasing the level of subsample resolution.

ORIGIN AND COMPOSITION OF FRACTURE WATER AND MECHANISMS OF MINERAL DEPOSITION

Tracer-isotope data (carbon, oxygen, strontium, and uranium) from UZ calcite and opal at Yucca Mountain provide information on the origins of these elements in percolating water in the past, as well as constraints on depositional processes. Previous studies of samples collected from drill cores and trenches at Yucca Mountain have demonstrated that UZ calcite formed from downward-percolating meteoric water containing isotopic and chemical signatures characteristic of the soil zone (Stuckless and others, 1991; Marshall and others, 1992, 1993; Peterman and others, 1992; Whelan and Stuckless, 1992; Whelan and others, 1994). Alternatively, Hill and others (1995) have proposed, based on earlier speculations (J.S. Szymanski, 1989, Department of Energy unpublished report), that ground water from the SZ is introduced into the UZ through a seismic pumping mechanism forcing ground water to heights greater than 500 m above the present-day water table. Both UZ and

pedogenic calcite deposits have been attributed to this SZ hydrogenic source (Hill and others, 1995; Dublyansky and others, 1996; Dublyansky, 1998; Dublyansky and Reutsky, 1998). This interpretation has been strongly rebutted on the basis of a preponderance of evidence in support of a descending meteoric water source (Stuckless, 1991; Stuckless and others, 1991; National Research Council, 1992; Vaniman and others, 1994; Monger and Adams, 1996; Stuckless and others, 1998) and by the absence of credible driving mechanisms for large vertical fluctuations of the water table (Carrigan and others, 1991; Bredehoeft, 1992; Rojstaczer, 1999). The calcite textures and isotopic data from UZ calcite and opal presented in this report further support a descending meteoric water source for mineral formation in a UZ environment. In this section, isotopic data are used to further constrain the sources and mechanisms of mineral deposition in the UZ and, by inference, processes of fracture flow.

Origins of Fracture Water

Calcite textures and isotopic compositions from UZ calcite and opal provide evidence for the origins of fracture water. A gradation of calcite textures in the upper 10 to 30 m of the UZ provides a genetic link between fine-grained, detritus-rich pedogenic deposits, and the detritus-free, coarse calcite and opal present deeper in the UZ. Authigenic minerals in the soil zone (calcite, opal, and smectitic or sepiolitic clays) have microcrystalline textures and are mixed with both coarse and fine detrital materials (Vaniman and others, 1994; Vaniman and Whelan, 1994). In the upper parts of the bedrock fracture network, the clays

and fine detritus are successively filtered out with increasing depth. Calcite gradually becomes coarser grained in this zone, and the amorphous, opaque, cream- to tan-colored opal/calcite mixtures common in pedogenic deposits change to translucent, milky-white opal at shallow levels and finally the transparent, botryoidal opal typical of the deeper UZ. A decrease in abundance of insoluble ^{232}Th in opal from surface to deeper UZ deposits accompanies this morphological change and further supports the effectiveness of filtering the suspended solid components (for instance, soil-zone clay) from percolating fracture water. Carbon, oxygen, strontium, and uranium isotope characteristics provide further evidence of a strong connection between meteoric water, infiltration through calcite-rich soils at the surface, and downward percolation into the UZ.

Isotopic Compositions Associated with a Meteoric Water Source

Meteoric precipitation that infiltrates into the UZ is modified substantially by both solid-liquid and gas-liquid chemical reactions that take place in the soil zone. Soils at Yucca Mountain contain evidence of these reactions in the form of an abundance of pedogenic calcite, opal, and clays (Vaniman and others, 1994; Taylor and Huckins, 1995). Cations in these pedogenic minerals are derived from eolian sources or through weathering of soil components, whereas the anions come from meteoric water (for oxygen) or the transpiration of plants and oxidation of organic matter (for carbon).

Oxygen and carbon isotope compositions of soil water are dependent on weather patterns, environmental conditions, and soil biological activity. Oxygen isotope compositions of soil water have a meteoric origin and thus are dependent on the $\delta^{18}\text{O}$ values of the rainwater and snowmelt. Seasonal weather fluctuations cause substantial variations in the $\delta^{18}\text{O}$ between individual precipitation events (Benson and Klieforth, 1989); however, increasing residence time, mixing of water in the soil zone, and reaction with soil constituents tend to average these fluctuations. Although soil-zone water from Yucca Mountain has not been analyzed, the $\delta^{18}\text{O}$ of pedogenic calcite can be used as a proxy over much of the Pleistocene. The range of $\delta^{18}\text{O}$ values in pedogenic calcite is much narrower (about 3 per mil, Quade and Cerling, 1990; Vaniman and Whelan, 1994, fig. 4) than that for individual

precipitation events at Yucca Mountain (about 17 per mil, Benson and Klieforth, 1989, fig. 16), reflecting these mixing processes. Because evapotranspiration does not fractionate oxygen isotopes substantially (Förstel, 1982), except in extreme arid environments (Allison and others, 1984; Quade and others, 1989), water that infiltrates through the lower part of the soil zone at Yucca Mountain is assumed to have $\delta^{18}\text{O}$ compositions close to the values for long-term average precipitation at a given site.

Infiltrating water acquires a dissolved inorganic carbon component (HCO_3^-) from incorporation of CO_2 from soil gas, the oxidation of organic matter, and dissolution of previously formed pedogenic calcite. Respiration of CO_2 from plants most likely dominates the carbon mass balance from these sources. Pedogenic calcite, therefore, inherits a carbon signature related to the composition of the local plant community at the time of mineral formation. Respired soil gas $\delta^{13}\text{C}$ depends on the ratio of C3 to C4 photosynthetic biomass (Quade and others, 1989, p. 464). Plants that use the C3 photosynthetic pathway tend to produce CO_2 with smaller $\delta^{13}\text{C}$ values compared to plants that use the C4 photosynthetic pathway. Pedogenic calcite in equilibrium with soil CO_2 in these two environments will have $\delta^{13}\text{C}$ values of about -12 to -17 per mil for C3 vegetation, and -1 to -5 per mil for C4 vegetation (Clark and Fritz, 1997, fig. 5-6). Plant communities, in turn, will vary because of local and regional climate variations. Quade and others (1989) documented these climate effects on $\delta^{13}\text{C}$ and $\delta^{18}\text{O}$ in pedogenic calcite at different elevations. In addition to elevation and climate effects, pedogenic calcite formed at a single site can record $\delta^{13}\text{C}$ and $\delta^{18}\text{O}$ variations that reflect shifting past climate patterns. Therefore, if calcite in the UZ can be tied to a pedogenic infiltration source (Whelan and Stuckless, 1992; Whelan and others, 1994; Stuckless and others, 1998), then variations in $\delta^{13}\text{C}$ and $\delta^{18}\text{O}$ values provide a link between the hydrologic response of UZ percolation and past climate changes.

Most pedogenic calcite at Yucca Mountain has $\delta^{18}\text{O}$ values between about 19 and 22 per mil (Vaniman and Whelan, 1994). Soil-zone water in equilibrium with these calcite $\delta^{18}\text{O}$ values (using fractionation equation of Friedman and O'Neil, 1977) will have $\delta^{18}\text{O}$ values of -12 to -9 per mil at 15°C (modern mean annual air temperature) or -13 to -10 per mil at 10°C (reflecting cooler annual air temperatures under past pluvial climates). Modern

precipitation has a wide range of $\delta^{18}\text{O}$ values. Individual rain events of more than 0.25 cm and snowfalls at Yucca Mountain typically have $\delta^{18}\text{O}$ values between about -1 and -18 per mil (Benson and Klieforth, 1989, figs. 14 and 16) with mean $\delta^{18}\text{O}$ values of -8 to -11 per mil for different collection stations. Mean $\delta^{18}\text{O}$ values were likely somewhat more negative for precipitation during the cooler pluvial conditions of the Pleistocene.

Pedogenic calcite at Yucca Mountain has $\delta^{13}\text{C}$ values between -3 and -9 per mil (Vaniman and Whelan, 1994). Values of $\delta^{13}\text{C}$ in soil CO_2 gas in equilibrium with this calcite should be between -11 to -17 per mil, which is consistent with a mixture of contributions from both C3 and C4 plants in the Yucca Mountain soils. The $\delta^{13}\text{C}$ in modern soil gas measured in the Yucca Mountain vicinity ranges from about -22 to -8 per mil and largely depends on the elevation and the associated vegetation at a given site (McConaughy and others, 1994).

Values of $\delta^{18}\text{O}$ and $\delta^{13}\text{C}$ in calcite from the shallowest parts of the ESF and in pedogenic calcite of similar age overlap and indicate a descending meteoric source of percolating water at Yucca Mountain (Whelan and Stuckless, 1992; Whelan and others, 1994; Stuckless and others, 1998). The stable isotope data from Whelan and others (1998, appendix 2) described in this report indicate that only samples of outer calcite with $\delta^{13}\text{C}$ values of about -5 per mil or less (figs. 22 and 28) closely match the range of $\delta^{13}\text{C}$ in pedogenic calcite (Vaniman and Whelan, 1994). It also is likely that this outer calcite is the only material in the UZ mineral coatings that is comparable in age with the surface deposits. The $^{230}\text{Th}/\text{U}$ ages for outer mineral surfaces of UZ mineral coatings and the slow rates of mineral growth interpreted above indicate that the ages of calcite classified as outer in this report are likely to be less than 1 to 2 Ma. Pedogenic calcite from surface exposures and trenches typically has $^{230}\text{Th}/\text{U}$ ages less than 500 ka (Szabo and others, 1981; Szabo and O'Malley, 1985; Muhs and others, 1990; Paces and others, 1994), although buried soils sometimes have $^{234}\text{U}/^{238}\text{U}$ model ages (based on an assumed initial $^{234}\text{U}/^{238}\text{U}$ activity ratio) of up to 1 Ma (J.B. Paces and others, U.S. Geological Survey, written commun., 1995). An older history of pedogenic calcite is possible but has not been specifically identified. The four sites used by Vaniman and Whelan (1994) for characterizing the $\delta^{13}\text{C}$ and $\delta^{18}\text{O}$ compositions of pedogenic calcite are dominated by surface deposits

with ages less than 500 ka (Muhs and others, 1990; Paces and others, 1994; J.B. Paces and others, U.S. Geological Survey, written commun., 1995). In contrast, oxygen and carbon isotope compositions for basal and intermediate UZ calcite most likely have no equivalent-aged pedogenic calcite preserved at the surface. Isotopic compositions from these subsamples should not be compared to the younger pedogenic materials. In addition, samples of outer calcite from greater depths in the UZ (analyses labeled as TSw in fig. 20) have $\delta^{18}\text{O}$ values less than the 18 to 22 per mil range that is observed in either outer calcite from the shallow UZ (TCw in fig. 20) or in pedogenic calcite (Vaniman and Whelan, 1994). The smaller $\delta^{18}\text{O}$ values for deeper UZ calcite are attributed to deposition at the higher temperatures expected along typical geothermal gradients. Values of $\delta^{18}\text{O}$ for both pedogenic and UZ calcite in the shallow subsurface are consistent with equilibrium fractionation between calcite and meteoric water with $\delta^{18}\text{O}$ between -13 and -8 per mil at temperatures between 10°C and 25°C during the last 500 k.y. (fig. 35A).

Strontium isotope compositions in pedogenic calcite are derived from eolian carbonate sources from both local fluvial systems as well as more distant playas (Marshall and Mahan, 1994). Strontium derived from bedrock or silicate detritus also may contribute to the composition of pedogenic calcite, but the contributions are likely to be small because of the slow rates of silicate weathering in the semiarid environment at Yucca Mountain and the small concentrations of strontium in the felsic tuffs. Values of $^{87}\text{Sr}/^{86}\text{Sr}$ reported for calcrete at Yucca Mountain range from about 0.7117 to 0.7128 (fig. 7 of Marshall and Mahan, 1994). Precipitation with very small dissolved ion contents and relatively small pH values in equilibrium with atmospheric CO_2 will dissolve small amounts of pedogenic calcite as water infiltrates through the soil and will rapidly acquire a $^{87}\text{Sr}/^{86}\text{Sr}$ composition identical to pedogenic calcite values.

Strontium isotope ratios from outer UZ calcite overlap the range observed for pedogenic calcite in calcrete deposits (fig. 28A). The range of $^{87}\text{Sr}/^{86}\text{Sr}$ for basal and intermediate calcite extends to substantially smaller values, but, as described earlier, the older UZ calcite deposits most likely have no surface equivalent. It is unclear whether or not pedogenic carbonate was abundant in the soils during the early history of Yucca Mountain. Arid-land soils may have developed only as climates shifted to drier, more seasonal conditions

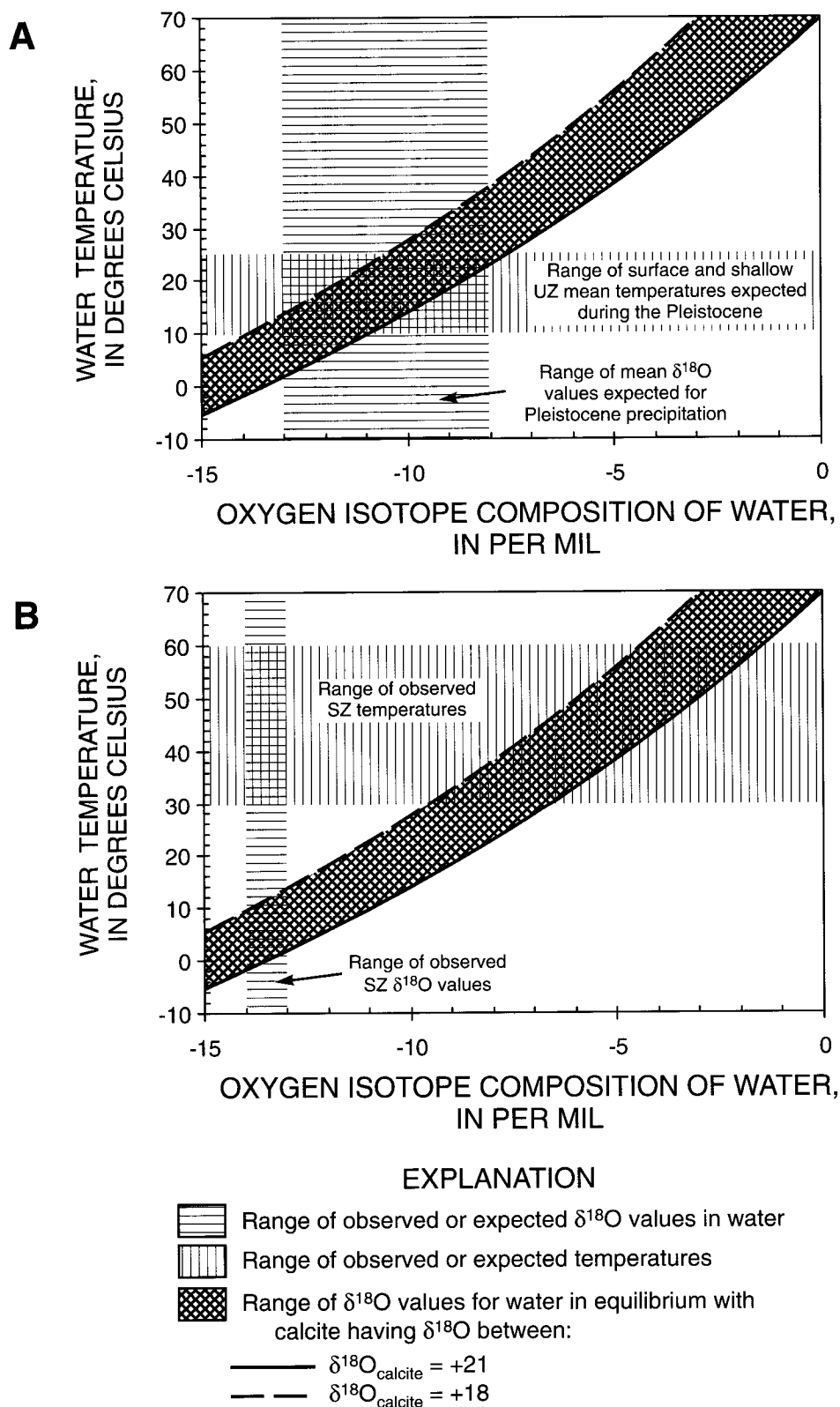


Figure 35. Oxygen isotope composition of water in equilibrium with calcite at various temperatures compared to (A) the ranges of surface and shallow unsaturated-zone (UZ) temperatures and oxygen isotope compositions of precipitation expected during the Pleistocene, and (B) the ranges of present-day ground-water temperatures and oxygen isotope compositions.

during the Quaternary (Thompson, 1991, p. 126–127). Therefore, the large strontium reservoir represented by pedogenic calcite may have become available to infiltrating fluids only in the last 1 to 2 m.y. Basal and intermediate UZ calcite may have had an $^{87}\text{Sr}/^{86}\text{Sr}$ source more directly linked to the tuffs, in which $^{87}\text{Sr}/^{86}\text{Sr}$ ratios gradually increased with time because of the decay of ^{87}Rb .

Isotopic Compositions Associated with a Saturated-Zone Water Source

Carbon, oxygen, and strontium isotope values in UZ calcite are difficult to reconcile with a water source from the SZ. Ground water sampled from shallower parts of the SZ beneath Yucca Mountain has dissolved inorganic carbon $\delta^{13}\text{C}$ values of about –11 to –7 per mil, and $\delta^{18}\text{O}$ values of –14 to –13 per mil (Claassen, 1985, table 6; Benson and Klieforth, 1989, table 1a). Calcite precipitating from this SZ water would have $\delta^{13}\text{C}$ values of –10.5 to –6.5 per mil—similar to the range observed for both UZ and pedogenic calcite. It is not surprising that shallow ground water has a $\delta^{13}\text{C}$ signature similar to soil $\delta^{13}\text{C}$ values because the volcanic-rock aquifer contains little carbon to modify the HCO_3^- of soil-zone infiltration and recharge. Therefore, carbon isotopes do not readily allow discrimination between a descending meteoric or ascending SZ water source. In contrast, deeper water from the underlying Paleozoic carbonate aquifer has substantially larger $\delta^{13}\text{C}$ values. Ground water from the only deep well at Yucca Mountain, borehole UE-25 p#1, sampled between 1,300 to 1,800 m in depth and open to the Paleozoic carbonate aquifer, has a HCO_3^- $\delta^{13}\text{C}$ value of –2.2 per mil (Craig and Robison, 1984, table 4). Calcite precipitated from this water would have a $\delta^{13}\text{C}$ of greater than –2 per mil, at least 3 to 6 per mil larger than values observed for outer UZ calcite or in pedogenic calcite. Calcite deposits obtained from drill core from depths below the water table have $\delta^{13}\text{C}$ values that are substantially larger (–3 to 3 per mil) than those observed in outer UZ calcite (fig. 3 of Whelan and others, 1994). The age of most SZ calcite is unknown, but it is likely to be older than about 10 Ma (Broxton and others, 1987; Bish and Aronson, 1993; Neymark and others, 2000) and is not likely in equilibrium with modern ground water in the volcanic-rock aquifer. Regardless of the age of SZ calcite, ground water from the regional Paleozoic carbonate aquifer cannot represent a source for

the more negative $\delta^{13}\text{C}$ values observed in outer UZ calcite.

Oxygen isotope ratios also are inconsistent with formation of UZ calcite from SZ water beneath Yucca Mountain. The modern SZ water with $\delta^{18}\text{O}$ values of –13 to –14 per mil (Benson and Klieforth, 1989, table 1a) and temperatures of about 30°C would precipitate calcite with $\delta^{18}\text{O}$ values from 13 to 14 per mil assuming the equilibrium fractionation equation of Friedman and O'Neil (1977). Calcite precipitation at warmer temperatures results in even smaller calcite $\delta^{18}\text{O}$ values than those listed above. Ground water from the Paleozoic carbonate aquifer sampled in UE-25 p#1 has a similar $\delta^{18}\text{O}$ value of –13.8 per mil but a warmer temperature of about 56°C (Craig and Robison, 1984, table 4). Calcite precipitated from this deeper water would have $\delta^{18}\text{O}$ values of about 9 per mil. If ground water similar to the modern ground water in the SZ was the source of the UZ calcite, UZ temperatures of less than 0°C to about 14°C are required to explain the $\delta^{18}\text{O}$ compositions of 18 to 21 per mil for outer calcite deposited in the TCw (figs. 20 and 35B). These UZ temperatures would require surface temperatures at or below 0°C to be maintained over the last several million years. Studies of past vegetation in the region indicate that mean annual temperatures typically were less than 5°C cooler than present, and were at most only 5°C to 7°C cooler than present during the relatively short periods associated with Pleistocene maximum glacial climates (Spaulding, 1985; Forester and others, 1999). Conversely, if more reasonable UZ temperatures are assumed (20°C to 25°C), larger SZ ground water $\delta^{18}\text{O}$ values between about –11.5 and –7.5 per mil are required. These large $\delta^{18}\text{O}$ values have not been observed in the volcanic-rock, carbonate-rock, or alluvial aquifers in the Yucca Mountain vicinity (Claassen, 1985, table 6; Benson and Klieforth, 1989, table 1a; Thomas and others, 1996, appendix A and B; Davisson and others, 1999, fig. 2). Therefore, although $\delta^{18}\text{O}$ values cannot be determined directly for water from which UZ calcite formed, restrictions based on equilibrium temperatures and observed $\delta^{18}\text{O}$ values do not support a SZ ground-water source.

Ground water from the shallower part of the SZ beneath Yucca Mountain has $^{87}\text{Sr}/^{86}\text{Sr}$ ratios between 0.7093 and 0.7116 (Peterman and Stuckless, 1993; Patterson and others, 1998; Peterman and Patterson, 1998). These values are less radiogenic than either outer UZ calcite or pedogenic calcite. Deeper ground

water from the Paleozoic carbonate aquifer sampled in UE-25 p#1 has a slightly larger $^{87}\text{Sr}/^{86}\text{Sr}$ ratio of 0.7118 (Peterman and Stuckless, 1993, fig. 2).

Although this value just overlaps the range observed for pedogenic calcite, it is substantially smaller than most pedogenic and outer UZ calcite (0.7117 to 0.7128, Marshall and Mahan, 1994; Appendix 3 of this report). If SZ water were to ascend into the UZ, reaction with the ^{87}Sr -enriched tuffs could result in an increase of the water $^{87}\text{Sr}/^{86}\text{Sr}$ ratios. Johnson and DePaolo (1994, p. 1579) proposed a model describing evolution of $^{87}\text{Sr}/^{86}\text{Sr}$ ratios in calcite from Yucca Mountain drill core in response to solute transport and water/rock reaction. Although this model was able to simulate some of the UZ calcite $^{87}\text{Sr}/^{86}\text{Sr}$ data starting with a water $^{87}\text{Sr}/^{86}\text{Sr}$ ratio of 0.7090, Johnson and DePaolo (1994, p. 1585) concluded that the calcite $^{87}\text{Sr}/^{86}\text{Sr}$ data are not diagnostic of either an upwelling or downward percolation model. Injection of ground water into the UZ through seismic pumping (Hill and others, 1995, p. 69) would take place over time scales too short to allow significant water/rock interaction in welded tuffs at temperature conditions observed in the SZ environment (that is, less than 100°C). Therefore, it is considered unlikely that the larger $^{87}\text{Sr}/^{86}\text{Sr}$ ratios measured for outer UZ and pedogenic calcite could be derived from either a Tertiary volcanic or a Paleozoic carbonate SZ ground-water source beneath Yucca Mountain.

Cumulatively, oxygen, strontium, and to at least some degree, carbon isotope data in UZ calcite deposited over the last million years are difficult to reconcile with a SZ source similar to ground water sampled in the Yucca Mountain vicinity. In contrast, data from all three isotopic systems are compatible with the formation of paragenetically late calcite in the UZ from solutions containing isotopic compositions very similar to those that also formed pedogenic calcite in Yucca Mountain soils. Other field, morphologic, chemical, and isotopic evidence have been used to refute a SZ water source for pedogenic calcite deposits (Muhs and others, 1990; Stuckless and others, 1991; Stuckless, 1991; National Research Council, 1992, p. 54; Whelan and Stuckless, 1992; Vaniman and others, 1994; Vaniman and Whelan, 1994; Marshall and Mahan, 1994; Taylor and Huckins, 1995, p. 36; Stuckless and others, 1998). Isotopic compositions in UZ mineral coatings presented in this report are comparable to values in pedogenic calcite and are consistent with a meteoric water source that is modified by chem-

ical interactions in the soil zone during infiltration and by subsequent conditions associated with slow, downward percolation through the UZ.

Hydrochemistry of Fracture Water

Mineral deposition in the UZ at Yucca Mountain is dependent on the chemistry of water percolating through the fracture network; however, natural fracture flow has not been observed or sampled at the level of the potential repository. Perched water bodies observed at Yucca Mountain are presumed to be recharged by fracture flow, although the relatively small ^{14}C contents (approximately 30 pmc, Yang and others, 1996, table 7) indicate long enough average residence times to allow water/rock reactions to take place in the perching horizon. Therefore, the chemical composition of fracture water likely is intermediate between surface runoff and perched water pumped from boreholes deep in the UZ. Chemical analyses of these waters are used to estimate the level of mineral saturation expected in the UZ fracture network.

The water compositions used in this section are from perched water bodies (Yang and others, 1996, table 6), runoff (L. Benson, U.S. Geological Survey, written commun., 1990; Savard, 1996, table 10), and SZ ground water (Benson and Klieforth, 1989, table 1b). Analyses of soil-zone water are not available. Only chemical analyses with charge imbalances less than 10 percent were used for calculation of mineral saturation. The resulting analyses were used as input to the PHREEQC hydrochemical model (Parkhurst, 1995) to calculate the calcite and silica saturation indices. The saturation index (Drever, 1997; Langmuir, 1997) is a measure of how far a chemical system is out of equilibrium and normally is expressed as a log scale such that when a given dissolution-precipitation reaction is at equilibrium the saturation index is zero. Undersaturated waters have negative saturation indices and oversaturated waters have positive indices. Because no thermodynamic data are available for opal in the PHREEQC database, the silica phase is assumed to be chalcedony.

Saturation indices of calcite and chalcedony calculated from analyses of runoff, perched water, and SZ ground water show a wide range in calcite saturation levels and a more restricted range for chalcedony (fig. 36). Many of the runoff analyses have calculated calcite saturation indices between -0.5 and 0.5, implying that meteoric precipitation rapidly interacts

with surface deposits and becomes saturated, or nearly so, with pedogenic calcite. Perched water from boreholes at Yucca Mountain plots closer to calcite saturation between -0.3 and 0.15 . In contrast, most SZ water analyses have calcite saturation indices between -0.45 and -1.4 , indicating a strong potential for calcite dissolution rather than precipitation. Calculated chalcedony saturation indices typically are greater than zero, reflecting the abundance of silica in the volcanic host rocks. Most runoff samples have chalcedony saturation indices between 0 and 0.3 , whereas perched and SZ water samples typically have slightly higher values between 0.3 and 0.6 . Runoff samples with negative calcite saturation indices form a well-defined positive trend with perched water plotting as one end member containing calcite saturation indices of about 0 and chalcedony saturation indices of about 0.5 . The composition of this end member, and the band of chalcedony saturation indices defined by the SZ samples, most likely reflects conditions of true silica saturation in Yucca Mountain ground water. The displacement of the indices to nonzero values is probably an artifact of the uncertainties in the thermodynamic data used.

Fracture water in the Yucca Mountain UZ is likely to have compositions that are somewhat more chemically evolved than runoff samples considering the interactions between infiltration and the calcite- and opal-rich soils. Concentrations of about 15 to 25 milligrams per liter (mg/L) calcium and 25 to 35 mg/L silica are present in runoff samples with the largest dissolved-solids concentrations. Pore water extracted from nonwelded tuff of the PTn by uniaxial compression has similar or somewhat greater calcium concentrations (Yang and others, 1996, tables 2, 3, and 4). Perched water pumped from borehole USW UZ-14 is likely to be most representative of fracture water in the TSw in the potential repository horizon because pumped samples are more representative of the water in the aquifer than bailed samples, and because the water has not been modified by chemical changes caused by interactions with the zeolitized units of the Calico Hills Formation. Perched water from USW UZ-14 has calcium and silica concentrations (23 to 30 mg/L for calcium and 26 to 36 mg/L for silica; Yang and others, 1996, table 6) that are similar to or slightly greater than the concentrations in runoff.

Therefore, water infiltrating into the fracture network is expected to be close to or at saturation with respect to calcite and opal. Calcite saturation probably

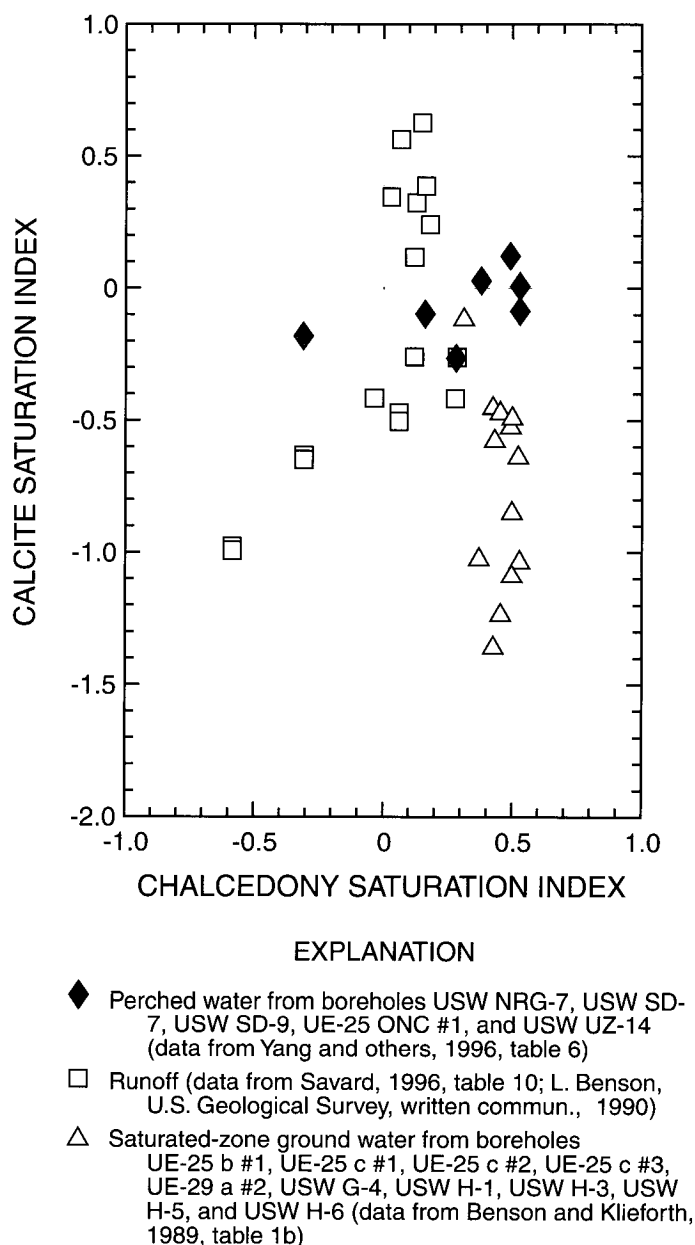


Figure 36. Calcite and chalcedony saturation indices for perched water, runoff, and saturated-zone ground water from Yucca Mountain, Nevada.

is maintained as water percolates to the potential repository horizon because of the decrease in calcite solubility with increasing temperature. Although calcite precipitation will result in increased pH values favoring opal dissolution, neither calcite nor opal formed during the late stages of deposition shows widespread dissolution textures, and both phases are intergrown on very fine scales. These textural features

imply that the composition of fracture water remained at or very near the levels of mineral saturation as solutions descended through the UZ.

Modification of $^{234}\text{U}/^{238}\text{U}$ Activity Ratios in Fracture Water

Initial $^{234}\text{U}/^{238}\text{U}$ activity ratios of minerals and measured $^{234}\text{U}/^{238}\text{U}$ of perched and SZ water show progressive changes with depth in Yucca Mountain (fig. 37). Initially, meteoric water interacts with soil-zone minerals and acquires a pedogenic dissolved uranium isotope composition. However, as percolation descends through the bedrock fracture network, ^{234}U is incorporated preferentially relative to ^{238}U . In addition, elevated $^{234}\text{U}/^{238}\text{U}$ ratios are characteristic of perched and SZ water beneath Yucca Mountain and are consistent with a local recharge source for these waters by downward percolation through fractures. In the following discussion on the evolution of $^{234}\text{U}/^{238}\text{U}$ ratios in fracture minerals, the effects on calculated initial $^{234}\text{U}/^{238}\text{U}$ of mixing older and younger layers during calcite and opal subsampling (see Interpretation of Ages section) are minimized by considering only the ESF subsamples with $^{230}\text{Th}/\text{U}$ ages less than 100 ka.

Meteoric water is dilute and mildly acidic, resulting in solutions that have small uranium concentrations and are highly reactive with readily soluble minerals in the soil zone. Runoff and infiltration rapidly acquire the isotopic signature of the most reactive components in the soil zone. Authigenic carbonate and opal are abundant in soil at Yucca Mountain and readily react with meteoric water. These minerals have a narrow range of $^{234}\text{U}/^{238}\text{U}$ activity ratios between about 1.4 and 1.8 (Muhs and others, 1990, fig. 3; Paces and others, 1994, table 1) and reflect the isotopic composition of the water from which they formed. Although samples of natural infiltration have not been collected for isotopic analysis, shallow percolating water is expected to have $^{234}\text{U}/^{238}\text{U}$ ratios that are similar to those observed in Yucca Mountain soils.

As water percolates downward along fracture surfaces, its $^{234}\text{U}/^{238}\text{U}$ ratio increases by mechanisms that preferentially incorporate ^{234}U into solution relative to ^{238}U . These mechanisms are related to alpha-recoil processes (the physical displacement of ^{238}U daughter products as a result of spontaneous ejection of $^4\text{He}^{+2}$ particles) and the interactions of percolating water with thin selvages (nanometer scale) of mineral

grains along fracture-flow-path surfaces. Various mechanisms may contribute to this effect including preferential leaching of ^{234}U from radiation-damaged lattice sites (Szilard-Chalmers effect), radiation-induced oxidation of ^{234}U leading to a more soluble ^{234}U -uranyl ion, and alpha-recoil of ^{234}Th from crystal surfaces (Gascoyne, 1992, p. 56–58). As a result, the $^{234}\text{U}/^{238}\text{U}$ ratio in percolating water evolves to larger values as long as bulk dissolution of rock with uranium isotope compositions of secular equilibrium remains minimal. The amount of excess ^{234}U preferentially incorporated into migrating solutions is dependent on the mass of uranium available along flow paths, water/rock ratios, flow-path length, and time between flow events in the UZ, as well as the amount of bulk-rock dissolution. Both high-silica rhyolite wall rock (uranium concentrations typically 3 to 5 $\mu\text{g/g}$, Neymark and others, 1995, tables 1 and 2) and previously deposited opal lining fracture surfaces (uranium concentrations of 50 to 300 $\mu\text{g/g}$) represent potential sources of ^{234}U .

Available data from subsurface mineral coatings indicate that fracture water acquires progressively larger $^{234}\text{U}/^{238}\text{U}$ ratios with depth below the base of the PTn. Limited data from mineral coatings in the TCw imply that the fracture water above the PTn is similar to soil water and runoff, although this part of the lithostratigraphic section is poorly characterized. Below the PTn, maximum values for the initial $^{234}\text{U}/^{238}\text{U}$ ratios increase with depth to activity ratios of greater than four to nine (fig. 16). The largest initial $^{234}\text{U}/^{238}\text{U}$ ratios (up to 9.38 ± 0.06) observed in the ESF are from opals in the lower portion of the upper lithophysal and upper portion of the middle nonlithophysal units of the TSw. The large range of initial $^{234}\text{U}/^{238}\text{U}$ activity ratios for young materials (figs. 17 and 37) is interpreted to reflect the differences in flow velocities, volumes, and path lengths associated with different percolation pathways through the UZ.

Of the perched water bodies identified at Yucca Mountain, only three were pumped sufficiently to obtain water samples with reliable uranium isotope data. Perched water in boreholes USW UZ-14 and USW WT-24 are largely confined to the TSw, whereas water in borehole USW SD-7 is perched in the nonwelded units of the Calico Hills Formation. Perched water bodies in the two different reservoirs have very different uranium characteristics (figs. 15 and 37); water from USW UZ-14 and USW WT-24 has $^{234}\text{U}/^{238}\text{U}$ activity ratios of about 7.5 and 8.3 and

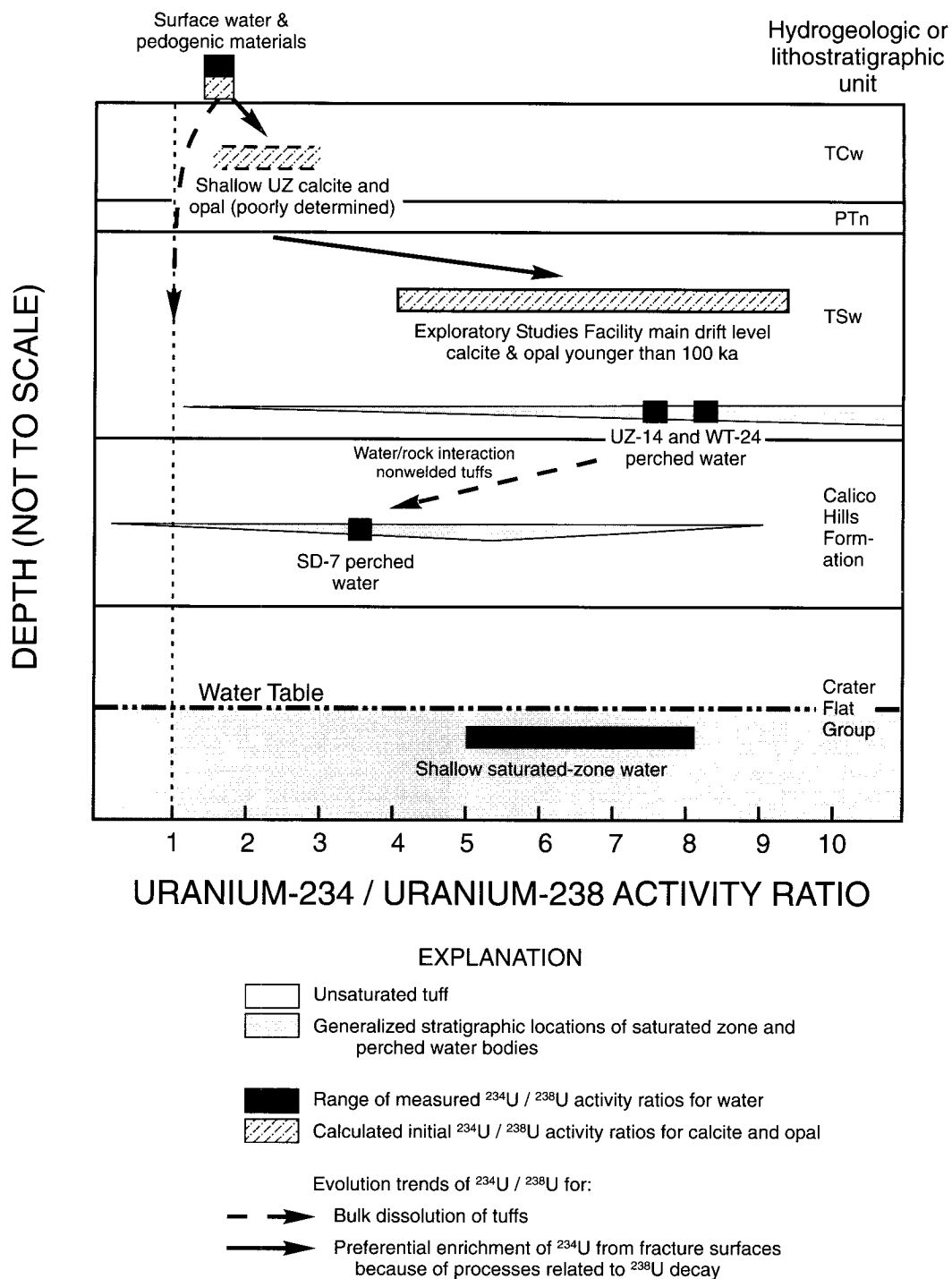


Figure 37. Uranium isotope compositions of water, calcite, and opal, Yucca Mountain, Nevada.

uranium concentrations of about 0.01 to 0.48 microgram per liter ($\mu\text{g/L}$), whereas USW SD-7 water has $^{234}\text{U}/^{238}\text{U}$ activity ratios of 3.4 to 3.7 and concentrations between 0.17 to 1.9 $\mu\text{g/L}$. The larger uranium concentrations and smaller $^{234}\text{U}/^{238}\text{U}$ ratios in the USW SD-7 water likely reflect a greater degree of water/rock interaction with the porous vitric or zeolitized matrix of the nonwelded tuffs of the Calico Hills Formation relative to water perched in the devitrified, densely welded tuffs in USW UZ-14 and WT-24. Therefore, water from the perched bodies sampled at USW UZ-14 and WT-24 is considered to have uranium that is more representative of fracture water percolating through the potential repository horizon. The $^{234}\text{U}/^{238}\text{U}$ activity ratio observed in these perched water bodies is within the range of initial $^{234}\text{U}/^{238}\text{U}$ ratios calculated for young fracture-lining opal and calcite. These uranium data may indicate that the USW UZ-14 perched water body may represent a mixture of fracture water from numerous pathways characterized by a variety of $^{234}\text{U}/^{238}\text{U}$ compositions weighted by the relative volumes and uranium concentrations contributed from each flow path. The elevated $^{234}\text{U}/^{238}\text{U}$ ratio of the USW UZ-14 and USW WT-24 water body also indicates that the fracture paths contributing recharge are similar to those containing fracture minerals rather than pathways that may circumvent the processes of $^{234}\text{U}/^{238}\text{U}$ modification by rapid, frequent, or large-volume flow.

Water in the upper part of the SZ beneath Yucca Mountain also has elevated $^{234}\text{U}/^{238}\text{U}$, typically between about 5 and 8 (figs. 15 and 37). These values are higher than most regional ground water in the vicinity, which typically is less than 4 (Ludwig and others, 1993; Paces and others, 1998). The elevated $^{234}\text{U}/^{238}\text{U}$ compositions of SZ water are consistent with uranium isotope compositions of fracture minerals and perched water, implying that UZ percolation may form a substantial percentage of the recharge to the shallow SZ beneath Yucca Mountain. Most of the recharge to the SZ has been attributed to higher elevation areas in the Timber Mountain Caldera to the north (Waddell, 1982; Waddell and others, 1984; Czarnecki, 1985; White and Chuma, 1987). However, uranium data from regional SZ samples imply that the SZ beneath Yucca Mountain is isolated from much of the regional flow pattern (Paces and others, 1998). Chemical and stable isotope data also may indicate that the SZ beneath Yucca Mountain is not well

connected to ground water flowing in adjacent areas (Peterman and Patterson, 1998).

Mechanisms of Unsaturated-Zone Fracture Flow and Mineral Deposition

Isotopic data presented in this report require that calcite and opal mineral coatings in the Yucca Mountain UZ formed from solutions that percolated through a network of connected fractures to appropriate depositional sites, became saturated or oversaturated with respect to calcite or opal, and precipitated those minerals at extremely slow rates of deposition. The process starts at the surface where meteoric water reacts with soil-zone materials (carbonates, opal, organic carbon) and dissolves readily soluble cations and anions. The isotopic compositions of carbon, oxygen, strontium, and uranium acquired at this time reflect the pedogenic source of solutes. Water that infiltrates to the soil/bedrock interface is likely to have calcium, HCO_3^- , and silica concentrations such that they are nearly saturated with respect to calcite and opal at surface conditions. However, it is conceivable that larger volumes of infiltrating solutions associated with past periods of greater effective surface moisture may have remained undersaturated with respect to calcite and opal.

Once water reaches the soil/bedrock interface (typically the fractured, welded tuffs of the Paintbrush Group), it will either be diverted downslope in the porous surface deposits or enter the tuff through open pores or fractures. Evidence of downslope diversion is apparent as thick, massive calcrete deposits located at buried fault scarps where the surface deposits thicken abruptly and the water-storage capacity is increased substantially. Many fractures in the welded tuffs near the soil/bedrock interface also are filled with micritic calcite or opal similar in appearance and composition to calcrete. These fillings, though porous, may diminish the capability of water to readily percolate into the bedrock fracture network and may tend to enhance downslope diversion in the colluvium. Infiltration that does enter open fractures is then distributed through connected fracture pathways in response to gravity-controlled downward percolation. Fracture flow probably occurs mostly as thin films that do not require complete water saturation of the welded tuff matrix (Tokunaga and Wan, 1997, p. 1294). Flow velocity will depend on a variety of factors including

the volume of water, film thickness, and the aperture, surface characteristics, dip, and connectivity of fractures.

Inferences regarding deposition mechanisms and the hydrologic environment of fracture flow can be made from the mineral morphology. Textural evidence indicates that calcite and opal were deposited in open cavities under unsaturated hydrologic conditions. Mineral coatings lack the types of features commonly observed in SZ mineral deposits, such as banded travertine textures, mammillary calcite textures, deposits coating cavity walls and roofs, or completely filled void space. The bright orange-red fluorescence that is common in SZ calcite is absent in calcite from the ESF. The presence of calcite and opal coatings in only a small percentage of the total number of lithophysal cavities and fractures is inconsistent with a mechanism whereby SZ water invades the ESF horizon. The lack of planar high-water marks in lithophysal cavities, including calcite and opal coatings covering a sloping cavity floor, refutes mineral deposition under conditions of even localized saturation. In addition, open space appears to be required for calcite and opal deposits. The presence of mineral coatings only on fracture footwalls and cavity floors indicates that water only flowed downward on the lower surfaces and never filled the open space. Even the earliest mineral deposits consisting of massive silica and quartz largely are restricted to the same sites that continued to accumulate younger deposits, indicating that the welded tuffs exposed in the ESF have never been saturated with water.

The textures of Yucca Mountain UZ calcite and opal deposits indicate that mineral growth commonly takes place preferentially on crystal tips and edges rather than on faces. Because deposits formed in open space in the UZ rock mass, some mechanism is required to transport dissolved ions to the crystal tips and then provide a means to reach mineral saturation or supersaturation. The presence of thick coatings containing bladed calcite crystals on near-horizontal substrates and thin coatings of blocky calcite on high-angle fractures indicates that slowing of downward-migrating water may be an important factor.

The bladed calcite textures along with the presence of opal on crystal extremities observed in many lithophysae and low-angle fracture-cavity coatings are uncommon with respect to UZ calcite deposits in other environments. Speleothems in karst environments more typically consist of laminated flowstone and

dripstone composed of aggregates of fine-grained crystals (Hill and Forti, 1997). Coarse, sparry calcite crystals can occur in karst speleothems; however, in their extensive inventory of cave minerals and mineral textures, Hill and Forti (1997) do not document calcite with narrow, bladed textures and scepterlike overgrowths commonly observed in the Yucca Mountain UZ. In addition, rates of mineral growth are very different between deposits in the UZ environment at Yucca Mountain and in karst environments. The growth rates reported by Hill and Forti (1997, p. 286) commonly range from millimeters to centimeters of mineral per year. The slowest reported karst growth rates ranged from 0.007 to 0.042 mm/yr, which are more than three orders of magnitude greater than growth rates estimated from UZ calcite at Yucca Mountain. This fundamental difference would imply that textures observed in speleothem deposits are not good examples for understanding the processes of mineral deposition in the UZ at Yucca Mountain.

Deposition of calcite and opal will occur at favorable locations along fracture pathways as the percolating solutions reach or exceed mineral saturation levels. The presence of mineral coatings in open cavities and their general absence in narrow-aperture fractures indicates a need for liquid/gas exchange. Solubilities of both CO_2 and calcite decrease in percolating water as it descends through the UZ and gradually warms. However, in order to allow calcite precipitation, the solution must be transported to sites with lower CO_2 contents, implying the presence of an independently migrating gas phase. Although increasing temperature promotes calcite deposition by lowering CO_2 solubility, an increase in temperature will not cause opal precipitation. In contrast, loss of water vapor from percolation that enters open cavity space will result in precipitation of both opal and calcite. Although humidity in the rock cavities is close to water-vapor saturation (Thorstenson and others, 1990), gas convection may permit water transport upward and out of Yucca Mountain (Montazer and Wilson, 1984). The rates of mass transfer of water vapor and CO_2 in deeper parts of the UZ are likely to be very small. However, these processes operating over long time periods (thousands to millions of years) are responsible for the observed slow growth rates of UZ secondary mineral deposits. Physical and chemical evidence from calcite and opal coatings is consistent with mineral formation from thin sheets or films of water that migrate downward along a small number of

fracture pathways into open cavities where the water interacts with an independently migrating gas phase.

Once water has been transported into a cavity, it then must reach the actual sites of mineral precipitation. In the case of the elongated calcite blades, water must be transported to crystal extremities up to 1 to 2 cm above the base of the blades. Because the cavities show no evidence of local water ponding, water films likely reach the blade tips by capillary forces up their outer surfaces. Similar capillary mechanisms are proposed to explain anthodite and frostwork speleothems that form radiating clusters of crystals with no central capillary channels supplying solutions to crystal tips (Hill and Forti, 1997, p. 47). Thinning of water films around the edges of crystal tips may result in larger free energies favoring increased liquid/gas reactions and greater loss of water vapor or CO₂ at these sites relative to other areas on the water film. Preferential addition of calcite or opal at crystal extremities eventually results in the bladed calcite forms as well as the scepter-head overgrowths on calcite and opal hemispheres concentrated at calcite blade tips. Alternatively, the bladed forms may be a result of preferential incorporation of minor or trace elements on selected crystal faces (Paquette and Reeder, 1995, p. 747) that then inhibit further growth on those faces. Although this mechanism may result in the bladed calcite forms, it cannot readily explain the scepter-head overgrowths or common occurrence of opal hemispheres at blade tips (figs. 4A, 5, 7, and 9). In either case, water must be transported to the tips of minerals by thin films.

Mineral precipitation leaves water at near-equilibrium chemical conditions with respect to calcite and opal, although further loss of CO₂ or water vapor can cause additional mineral precipitation as water continues to percolate downward. Once solutions reach mineral saturation, returning them to undersaturated conditions is difficult. Only a few discontinuities in the depositional sequence are present in the interiors of individual coatings; they generally are not observed in the outer parts of the mineral coatings. Therefore, percolating solutions most likely remain saturated with respect to calcite and opal and may continue to precipitate these minerals at suitable sites until the water film either dissipates and evaporates completely or reaches the water table.

LONG-TERM THERMAL AND ISOTOPIC EVOLUTION OF FRACTURE WATER

Changes in thermal and climate conditions at Yucca Mountain have resulted in systematic variations in the isotopic composition of UZ fracture water and associated minerals. Thermal conditions in the UZ evolved most rapidly during the first several million years in response to the local and regional magmatic activity. Relative to this period, subsequent thermal evolution has been minor, responding to gradual changes in crustal heat flow and average surface temperatures. Oxygen isotope compositions of both calcite and the various silica phases are not only dependent on the $\delta^{18}\text{O}$ values in the solutions from which they formed, but also on the temperature of mineral formation (Clayton and others, 1972). Therefore, oxygen isotope data from basal, intermediate, and outer parts of mineral coatings can be used to evaluate thermal conditions at the time of mineral deposition. Oxygen isotopes from both calcite and silica phases shift systematically to larger values with time and do not support the claim of recent ascending warm SZ water (greater than 40°C) into the UZ proposed by Dublyansky and others (1996), Dublyansky (1998), and Dublyansky and Reutsky (1998) based on fluid inclusions in calcite.

Isotopic compositions of fracture water also varied with time because of changes in climate conditions between Tertiary and Quaternary periods as well as pluvial-interpluvial fluctuations in the Quaternary. Oxygen, carbon, and strontium isotopes show systematic shifts in calcite of different ages, and these long-term changes and their causes are discussed below. In addition to the longer term variations, increased mean annual precipitation during wetter Pleistocene climate conditions likely would have had a direct impact on the amount of fracture water percolating through the potential repository block. Geochronological, textural, and isotopic data are used to constrain the impacts that increased amounts of surface water may have had on percolation through fractures at the repository horizon.

Thermal Evolution

The pattern of increasing $\delta^{18}\text{O}$ values in silica phases from chalcedony to quartz to opal has been interpreted as an indication of progressive cooling of the UZ during the early history of mineral deposition

(Whelan and others, 1998, p. 18). Chalcedony and quartz from the lower parts of the mineral coatings have the smallest $\delta^{18}\text{O}$ values between 7.9 and 8.6 per mil. These values imply formation temperatures between 77°C and 115°C assuming water $\delta^{18}\text{O}$ compositions similar to modern precipitation of -12.5 to -8 per mil (equilibrium fractionation factors for quartz and water given by Kawabe, 1978). Temperatures similar to those measured at the present-day water table cannot be calculated from these small chalcedony $\delta^{18}\text{O}$ values unless unreasonably small water $\delta^{18}\text{O}$ values (less than -20 per mil) are assumed. Intermediate $\delta^{18}\text{O}$ values for chalcedony and quartz of 10 to 15 per mil indicate slightly cooler conditions of between about 43°C to 99°C assuming a water composition between -12.5 and -8 per mil. Smaller $\delta^{18}\text{O}$ values in the water also may explain the larger $\delta^{18}\text{O}$ values in chalcedony but require $\delta^{18}\text{O}$ compositions of -19 to -14 per mil in the water to produce chalcedony $\delta^{18}\text{O}$ values of 10 to 15 per mil at a temperature of about 35°C. In contrast, most of the quartz and opal data are broadly consistent with temperatures approximating present-day geothermal gradients and water compositions. Assuming water $\delta^{18}\text{O}$ compositions between -12.5 and -8 per mil, the median quartz value of 20.1 per mil indicates formation temperatures between 21°C and 40°C. The median opal value of 22.6 per mil indicates formation temperatures between 26°C and 45°C using the same range in water compositions (equilibrium fractionation factors between water and amorphous silica from Kita and others, 1985). Temperatures calculated from these silica phases are considered to be only approximations of true temperatures because of the unknown isotopic compositions in associated water, the difficulty of calibrating accurate fractionation factors at low temperatures, and the possibility of nonequilibrium mineral formation. However, the general trend of increasing $\delta^{18}\text{O}$ from older chalcedony to younger quartz and finally to opal is considered reliable evidence that temperatures were highest during the earliest mineral formation but decreased to near modern geothermal conditions prior to deposition of most of the calcite and opal coatings.

Systematic changes in older to younger calcite $\delta^{18}\text{O}$ also are consistent with interpretations based on $\delta^{18}\text{O}$ in silica phases. Basal calcite from the TSw typically has $\delta^{18}\text{O}$ values less than 16 per mil, whereas outer calcite from the same lithostratigraphic unit typically has $\delta^{18}\text{O}$ values greater than 16 per mil. A

temperature of about 45°C is calculated for calcite with a $\delta^{18}\text{O}$ value of 12 per mil in equilibrium with water having a $\delta^{18}\text{O}$ value of -12.6 per mil (fractionation equation of Friedman and O'Neil, 1977). The same calcite would have a calculated temperature of 76°C if the water had a $\delta^{18}\text{O}$ composition of -8 per mil. In order to replicate present-day temperatures at the water table, calcite with a $\delta^{18}\text{O}$ value of 12 per mil would have to be in equilibrium with water containing $\delta^{18}\text{O}$ values between -15 to -14 per mil. In contrast, outer calcite with $\delta^{18}\text{O}$ values between 16 and 18 per mil has a calculated temperature between about 25°C and 16°C if they formed from water with a -12.5 per mil $\delta^{18}\text{O}$ composition. Depth/temperature relations for basal calcite sampled from drill core also are consistent with a larger geothermal gradient during the early history of mineral deposition (Whelan and others, 1998). Oxygen isotope compositions corresponding to calcite analyses with $\delta^{13}\text{C}$ values greater than -1 per mil were interpreted by Whelan and others (1998, p. 15) to be consistent with a geothermal gradient of approximately 100°C/km (dotted line in fig. 19).

Variations in $\delta^{18}\text{O}$ of both silica phases and calcite record the evolution of thermal conditions during the postdepositional history of the UZ at Yucca Mountain. The felsic ash-flow tuffs were emplaced at temperatures above 500°C; however, water could not have effectively percolated into the hot volcanic rocks until the tuffs cooled to less than 100°C. This initial cooling phase probably was rapid, on the order of thousands of years or less rather than hundreds of thousands of years or more. Temperatures close to boiling conditions may have been present during the earliest stages of chalcedony deposition. In addition to heat from the volcanic eruptions, large bodies of magma associated with caldera complexes to the north of Yucca Mountain were emplaced at shallow crustal levels and also may have contributed to steeper regional geothermal gradients. Large-scale magmatic activity in this area ceased between 9 and 11 Ma (Sawyer and others, 1994, p. 1312) such that, by the time of initial quartz and calcite formation, crustal heat flow in the Yucca Mountain UZ probably resulted in temperatures between 45°C and 100°C. Oxygen isotope data for main-stage calcite and opal indicate that temperatures present during formation of the bulk of the mineral coatings probably were reduced further to values less than 45°C resulting in UZ conditions consistent with measured geothermal gradients (Szabo and Kyser, 1990; fig. 19 of this report).

Fluid inclusion studies of calcite from the ESF and interpretations of trapping temperatures have yielded controversial results. As minerals grow, they can trap small bubbles of gas or liquid representing the fluids present at crystal surfaces. Roedder and others (1994) observed that the vast majority of fluid inclusions in drill-core calcite at Yucca Mountain are small (from about 2 to less than 100 μm) and are mostly all-liquid-filled or, less frequently, all-gas-filled. Primary fluid inclusions containing both liquid and gas that can be used to determine trapping temperatures were found to be extremely rare. Arguments based on gas-bubble nucleation and crushing experiments led Roedder and others (1994) to infer that calcite crystallization temperatures were well below 100°C (equal to or less than 40°C in Roedder and Whelan, 1998) and that the minerals formed under atmospheric pressure conditions in the UZ. In contrast, elevated trapping temperatures between 30°C and 130°C for rare, gas-liquid fluid inclusions in calcite from shallow depths (about 50 m) in the ESF have been reported (Dublyansky and others, 1996; Dublyansky, 1998; Dublyansky and Reutsky, 1998). These data have been used along with seven fluid-inclusion trapping temperatures obtained from deeper calcite from older studies of drill core to construct a model geothermal gradient of about 160°C/km (Dublyansky, 1998). Microstratigraphic positions in mineral coatings of the individual fluid inclusions used in these studies are not documented so the relative age of the host calcite is unknown. Trapping temperatures greater than 30°C are consistent with the interpretation of thermal evolution based on $\delta^{18}\text{O}$ data presented herein and by Whelan and others (1998) if the two-phase fluid inclusions are restricted to basal calcite. If these two-phase fluid inclusions are present in calcite formed during late stages of deposition, they contradict the simple thermal evolution interpretation discussed above and require additional heating events throughout the late Tertiary and Quaternary. Additional characterizations of both trapping temperatures as well as the ages of calcite hosting the two-phase inclusions are required to resolve this issue.

Long-Term Isotopic Variations

Carbon and strontium isotope compositions in fracture water continued to evolve after a reduced geothermal gradient was established at Yucca Mountain. Carbon isotope compositions changed from $\delta^{13}\text{C}$

values of about -3 to 0 per mil in intermediate calcite to values of about -9 to -5 per mil in outer calcite. Strontium isotope compositions evolved over a similar time period from intermediate $^{87}\text{Sr}/^{86}\text{Sr}$ ratios (0.711 to 0.712) to more radiogenic values (0.7115 to 0.7127). These variations are directly related to changes in isotopic compositions of the fracture water caused by a shift in the pedogenic environment around the Pliocene-Pleistocene boundary and the gradual evolution of $^{87}\text{Sr}/^{86}\text{Sr}$ in the volcanic rocks.

Changes in carbon isotope signatures likely represent shifts in the mixture of C3 and C4 plants present at the surface over time. The data indicate that Yucca Mountain plant communities were dominated by C4 species earlier in its history with more recent climates favoring a greater proportion of C3 plants. Whelan and Moscati (1998) suggested that this shift in carbon sources occurred within the Pliocene as the regional climate shifted from milder, wetter conditions in the Tertiary to the more severe, semiarid conditions characteristic of the Quaternary based on paleobotanical, paleosol, and paleolimnological data (Axelrod, 1979; Thompson, 1991). A shift to increased aridity in the Yucca Mountain vicinity between about 1 and 2 Ma also was inferred from changes in hydrogen isotope compositions of fluid inclusions in calcite veins of Pliocene and Pleistocene age (Winograd and others, 1985). Outer calcite $\delta^{13}\text{C}$ values of -8 to -5 per mil are consistent with the observed mixed C3 and C4 semiarid plant community forming pedogenic calcite under Pleistocene climate conditions. In contrast, modern grasslands and savannas in North America and Africa are dominated by C4 plant communities and contain soil calcite with $\delta^{13}\text{C}$ values of -5 to 2 per mil (Cerling and Quade, 1993). Similar conditions may have been present in the Yucca Mountain region during the Pliocene and Tertiary and may have been the source of carbon for intermediate calcite sampled from mineral coatings in the ESF.

Strontium isotope compositions in older calcite are substantially less radiogenic than those in younger calcite. The tuffs themselves provided a likely source of $^{87}\text{Sr}/^{86}\text{Sr}$ in the basal calcite. Initial $^{87}\text{Sr}/^{86}\text{Sr}$ ratios (measured $^{87}\text{Sr}/^{86}\text{Sr}$ corrected for radiogenic strontium produced from the measured $^{87}\text{Rb}/^{86}\text{Sr}$ over the last 12.8 m.y.) in the high-silica rhyolite parts of the TSw are too radiogenic (0.7124 to 0.7129, Peterman and others, 1991, table II and fig. 6) to account for the $^{87}\text{Sr}/^{86}\text{Sr}$ values observed in basal calcite (approximately 0.710 to 0.712, Appendix 3). However, other

lithostratigraphic units, including the quartz latite parts of the TSw and nonwelded tuffs in the PTn, have initial $^{87}\text{Sr}/^{86}\text{Sr}$ ratios between 0.709 and 0.710 with relatively large strontium concentrations up to about 400 $\mu\text{g/g}$ (Peterman and others, 1991, table II and fig. 6). Some of these units are vitric tuffs that are much more reactive than the devitrified nonwelded tuffs. Therefore, strontium in these volcanic units may have provided a reasonable source of strontium for basal calcite and may continue to provide at least some of the strontium in outer calcite.

In addition to the volcanic rock strontium whose $^{87}\text{Sr}/^{86}\text{Sr}$ ratios gradually increased with time by the in-situ decay of ^{87}Rb to ^{87}Sr , calcite-rich soils began to develop at some point in the history of Yucca Mountain. Outer calcite in the UZ generally contains greater strontium concentrations and more-radiogenic $^{87}\text{Sr}/^{86}\text{Sr}$ ratios than intermediate calcite. Greater strontium concentrations in the calcite indicate that percolating solutions also became more enriched in strontium. Higher strontium concentrations of percolating solutions may be explained if calcic soils were developed after the climate shifted to more arid conditions over the last 2 m.y. Little is known about the long-term history of surface deposits. Winograd and others (1985) hypothesized that renewed uplift in the Sierra Nevada and Transverse mountain ranges over the last 2 m.y. caused a change in regional climate in southern Nevada to more arid conditions. Development of strontium-rich calcrete at Yucca Mountain may have been initiated or accelerated as a response to the increasing aridity in the rain shadow of the newly uplifted mountains. The resulting increased pedogenic calcite formed a large chemical reservoir of strontium at the surface that may have changed the dominant source of strontium in UZ calcite from the volcanic rocks to the overlying soils.

Variations in Quaternary Moisture

The record of percolation over the past 500 k.y. can be used to evaluate the relative amounts of UZ flux on time scales relevant to long-term isolation of radioactive waste at the potential repository. Modern conditions are typical of relatively warm and dry interpluvial episodes; however, 100-k.y. cycles of glaciation in the Northern Hemisphere resulted in episodes of transitional and pluvial climate conditions at Yucca Mountain (Forester and others, 1999). Some

records of regional climate variation indicate that up to 80 percent of the last million years may have been characterized by cooler, wetter conditions relative to the present climate (Forester and others, 1999, p. 21). Greater effective moisture during pluvial conditions may have translated into higher volumes of infiltrating water during the past. Examination of UZ mineral records for evidence of variations that correlate with past surface-moisture records is one means of assessing the UZ hydrologic response to climate change.

Data presented in this report indicate that mineral coatings formed at slow rates over long time periods. Although subsampling effects complicate the interpretation of older ages, $^{230}\text{Th}/\text{U}$ ages of less than 100 to 200 ka from the outer surfaces of thicker coatings at the potential repository horizon should reflect average ages of depositional episodes at least on the scale of major climate change. These data preserve information pertinent to the last two to four climate cycles and corresponding mineral deposition in the UZ.

Although evidence for the last two pluvial climate cycles (last 180 k.y.) is abundant in surface records (Bischoff and others, 1997; Bradbury, 1997; Smith and others, 1997; Forester and others, 1999), UZ mineral data show no evidence of increased deposition during this same interval. Effective moisture levels estimated from surface records were substantially greater between about 10 and 60 ka than the presently observed values at Yucca Mountain (Spaulding, 1985, table 10; Forester and others, 1999, p. 57). Greater effective moisture levels in recharge areas during this time translated to a SZ hydrologic response in the form of regional and local water tables that were tens of meters higher than their present elevations (Paces and others, 1993; Szabo and others, 1994; Quade and others, 1995). However, it is not apparent that greater moisture levels at the surface affected rates of UZ mineral deposition at the potential repository horizon.

No evidence for substantial dissolution of calcite or opal forming outer surfaces has been observed. Greater effective moisture levels and amounts of shallow infiltration might be expected to result in percolation that is more dilute than present surface and UZ water. Substantial percolation that is undersaturated with respect to calcite and opal might be expected to dissolve the minerals. If dissolution had occurred during the latest pluvial episode, it is likely

that it would have been well preserved because only minute amounts of new material would have been deposited during the last 15 k.y.

If pluvial percolation remained saturated with respect to calcite and opal, or if the kinetics of the reaction between UZ minerals and undersaturated solutions were sluggish, dissolution of outer surfaces may not have occurred. Although these undersaturated solutions may not have dissolved calcite or opal present on fracture surfaces, they still would have percolated through the potential repository block without leaving a mineral record. If so, pluvial episodes should be marked by nondeposition and the history of mineral deposition should favor periods of lower flux during the drier climates of the Pleistocene interglacial periods. Instead, observed $^{230}\text{Th}/\text{U}$ ages are more or less evenly distributed throughout the last 400 k.y. (fig. 10). Even though individual ages do not represent discrete depositional events, the distribution of average $^{230}\text{Th}/\text{U}$ ages should be different if depositional histories were punctuated by substantial pluvial hiatuses. Therefore, the distribution of available data supports a more or less uniform growth history on pluvial time scales rather than one of cyclic growth.

Current data do not provide definitive evidence for the presence or absence of deposition in the Holocene (last 10 k.y.). Results of radiocarbon dating indicate that, although the true average age is much older than the percentage of modern carbon measured in an individual subsample indicates, layers younger than 30 ka are present on all growth surfaces. Subsamples with the youngest ^{14}C ages (16 to 25 ka) contain larger proportions of recently deposited material and are less sensitive to the deviation between apparent and true average ages (fig. 34). However, it is not clear whether these four samples contain large proportions of late Pleistocene calcite or only small amounts of Holocene material mixed in with older materials. Finer sample resolution or dating using an isotopic system with a shorter half-life (for instance, ^{226}Ra with a half-life of 1,600 yrs) is required to determine whether or not deposition continued throughout the last 10 k.y. of relatively arid climate conditions.

Stable carbon isotopes also may preserve information on the relation between climate and percolation. Data for microsamples of outer calcite span a $\delta^{13}\text{C}$ range of about 3 per mil between -8 and -5 per mil (fig. 22). This range is slightly greater than that observed in the 500-k.y. Devils Hole calcite record (Coplen and others, 1994), which was directly related

to variations observed in the climate-induced $\delta^{18}\text{O}$ record (Winograd and others, 1992). If calcite deposition was favored in either pluvial or interpluvial climate episodes, a narrower range in $\delta^{13}\text{C}$ values might be expected. Similar arguments can be made for the cluster of $\delta^{18}\text{O}$ data between about $+16$ and $+18$ per mil for outer calcite from the Yucca Mountain UZ. Winograd and others (1992) documented a similar total $\delta^{18}\text{O}$ range of about 2 per mil between pluvial and interpluvial climate cycles in the Devils Hole calcite record. Therefore, current data support calcite deposition from fracture water with a wide range of $\delta^{13}\text{C}$ and $\delta^{18}\text{O}$ values consistent with formation during interpluvial, transitional, and pluvial climate episodes. Future data collection at scales of resolution of less than 0.1 mm may provide a record of cyclic stable isotope variation that can be related to climate-induced changes in plant communities and meteoric water signatures throughout the last one to four pluvial cycles.

Data presented in this report indicate that UZ calcite and opal preserve no clear geochronological or isotopic evidence that can be related to climate variations observed at the surface. This conclusion, although based on a limited amount of data, is consistent with the concept that the rate of deposition of UZ opal and calcite at the potential repository horizon was relatively constant over long periods of time, including the last 500 k.y. If mineral deposition is closely linked to percolation flux, these conclusions imply that the deep UZ may be buffered from the wide variations in potential infiltration expected between pluvial and interpluvial climates.

IMPLICATIONS FOR PERCOLATION FLUX

Data and interpretations from calcite and opal coatings in the ESF can be used to constrain variations in percolation flux through fractures in the Yucca Mountain UZ. Although relating the mineral record to specific flux values is difficult, the depositional histories and changes in isotopic compositions can be used to infer relative differences in fluxes at different times in the past. These data imply that percolation through the deep UZ at Yucca Mountain was buffered from large changes in flux in the past, and that the hydrogeology at the site is capable of providing long-term fracture-flow stability in the deep UZ.

The processes of liquid and gas flow through fractures and lithophysae in the TSw at Yucca Mountain have resulted in UZ calcite and opal growth at extremely slow rates on the order of millimeters per million years. These rates are consistent with the cumulative thickness of 1 to 2 cm observed for many coatings assuming a total duration of deposition of about 10 to 13 m.y. Initiation of mineral deposition shortly after tuff emplacement is supported by the elevated depositional temperatures inferred from observed $\delta^{18}\text{O}$ values of stable isotopes in silica and calcite formed during early stages of deposition and by similarities between $^{87}\text{Sr}/^{86}\text{Sr}$ ratios in basal calcite and initial ratios in the 12.7- to 12.8-Ma strontium-enriched quartz latitic tuffs. Once established, transmissive fracture pathways appear to have been maintained for very long time periods, based on the cumulative thickness of the mineral coatings and the common observation of relatively young ages (compared to the age of the tuffs) for most outer surfaces. These interpretations of slow, uniform growth rates at the same depositional sites over long periods indicate that a large degree of hydrologic stability has been maintained in the UZ fracture network.

Another indicator of hydrologic stability in the deep UZ is the apparent lack of correlation between UZ opal and calcite growth histories and other indicators of climate variation. Large variations in mean annual precipitation probably existed between pluvial and interpluvial conditions throughout the Quaternary. However, these variations are not apparent in young mineral records at the 100- to 200- μm scale of subsample resolution. In addition, differences in $\delta^{13}\text{C}$ compositions among subsamples from intermediate to outer portions of individual mineral coatings record a gradual shift in plant communities that may correspond to the onset of the cooler, drier conditions of the Quaternary (Whelan and Moscati, 1998). A major shift in surface moisture between pluvial and interpluvial climates should translate into large differences in growth rates and textures between mineral coatings formed during intermediate and late depositional stages unless percolation flux in the deep UZ was somehow buffered from change. Geochronological data for opal and chalcedony in interior positions within mineral coatings indicate that long-term average deposition rates of mineral coatings from welded tuffs below the PTn are similar to those calculated from $^{230}\text{Th}/\text{U}$ dating of outer surfaces, and have

been uniform over the past 8 to 10 m.y. (Neymark and others, 1998). The major shift in climate implied by the changing carbon sources does not appear to be accompanied by a substantial change in mineral deposition rates in the deep UZ.

These observations are best explained if UZ percolation flux at the potential repository level is buffered relative to variations in precipitation, infiltration, or shallow percolation. This may be accomplished, in part, by limiting the amount of net infiltration during wetter periods through an increase in the plant biomass and associated evapotranspiration rates. Downslope diversion of soil water along the tuff/colluvium interface into thicker alluvium also may be an important mechanism during wetter periods by focusing net infiltration into valleys with larger storage capacities and greater evapotranspiration potentials. In addition, the highly porous nonwelded units of the PTn represent a large reservoir for shallow percolation (Montazer and Wilson, 1984). Water saturation levels in the PTn matrix are likely to fluctuate on seasonal to millennial time scales in response to short-term variations in net infiltration. However, percolating water transmitted through the base of the PTn into the fracture network of the underlying welded tuffs may occur at a relatively uniform rate. As a result, outermost calcite and opal subsamples from deposits in the TSw appear to be buffered from substantial variations in percolation flux despite the fluctuating conditions documented by studies of Pleistocene climate change.

Uranium isotope compositions observed in young ESF opal and calcite also provide a qualitative limit on amount of percolation flux transmitted through fracture pathways. Large $^{234}\text{U}/^{238}\text{U}$ ratios similar to those observed in the deep UZ minerals are uncommon in oxidizing ground waters (Osmond and Cowart, 1992, fig. 9.1) and probably are obtained only under conditions of relatively low flux and minimal bulk-rock dissolution. Small reaction rates between devitrified tuff and low-temperature percolating water limit the amount of bulk dissolution of fracture surfaces to negligible amounts. Instead, surfaces along fracture pathways will tend to provide ^{234}U to passing solutions preferentially to ^{238}U because of decay-related processes. However, these processes produce available ^{234}U only in small amounts generated over long periods of time. The uranium isotope budget in surface water and infiltration is dominated by ^{238}U , resulting in relatively low $^{234}\text{U}/^{238}\text{U}$ activity ratios. Therefore, uranium with isotopic compositions domi-

nated by ^{238}U is characteristic of large percolation fluxes and will tend to overwhelm the relatively small contributions of ^{234}U available from fracture surfaces. A consequence of large amounts of percolation is that relatively low $^{234}\text{U}/^{238}\text{U}$ will be maintained in solutions percolating through the UZ. However, if the volume of fracture water, and, thus, the mass of uranium from pedogenic sources, is limited, the uranium isotope budget in fracture water can be affected by the small amounts of ^{234}U that are incorporated preferentially during percolation. Therefore, the largest $^{234}\text{U}/^{238}\text{U}$ ratios are expected in percolation that has the smallest volumes and the longest path lengths. Although these relations have not been quantified, the large $^{234}\text{U}/^{238}\text{U}$ ratios characteristic of the Yucca Mountain UZ are not observed in other volcanic-rock perched flow systems elsewhere at the Nevada Test Site that have smaller $^{234}\text{U}/^{238}\text{U}$ ratios and represent greater total recharge flux (Paces and others, 1998).

SUMMARY AND CONCLUSIONS

Calcite and opal were deposited from water percolating through the thick UZ at Yucca Mountain, Nevada, and provide a record of past water percolation through fractures at the level of the potential high-level nuclear waste repository. The compositions and textures of these secondary minerals can be related to the source of percolating water and the hydrologic conditions under which they formed. An evaluation of the composition and growth history of these deposits is especially important because examples of present-day fracture water have not been observed. In addition, the growth histories of the mineral coatings provide an indication of how the Yucca Mountain UZ has responded to changes in climate conditions in the past.

Secondary mineral coatings from 0.1 to 4 cm thick are present in high- to low-angle fractures where apertures exceed 2 to 3 mm and on floors of lithophysal cavities. A small proportion of the calcite and opal deposits are present as cements coating breccia fragments in narrow rubble zones, or as thin (1- to 5-mm-thick), filled veins. Mineral coatings are restricted to fracture footwalls or cavity floors, reflecting the effect of gravity on downward-percolating solutions. Calcite forms coarse, sparry crystals ranging from equant prisms to thin, upright blades commonly having flaring-upward overgrowths at the

blade tips (scepter-head overgrowths). Opal is present as thin sheets or lacey patchworks veneering calcite crystals or as small hemispheres on calcite surfaces. Both opal and calcite are finely layered (micrometer or finer) and often are intimately intergrown. These features contrast markedly with occurrences in the SZ where large-aperture fractures commonly are filled completely with coarse, banded calcite, and opal is rare. The sequence of mineralization commonly includes early-stage deposits of silica with or without calcite and fluorite followed by main-stage deposits consisting of older calcite with blocky to tabular textures and younger calcite with delicate thin-bladed textures. Opal is present throughout this main-stage sequence but commonly is concentrated near outer surfaces.

Outermost growth surfaces have been dated using radiocarbon (calcite) and $^{230}\text{Th}/\text{U}$ (calcite and opal) methods. Radiocarbon ages range from 16 to 44 ka, whereas $^{230}\text{Th}/\text{U}$ ages range from 28 to greater than 500 ka. No systematic age differences are present between calcite and opal regardless of depositional setting. Mineral coatings from both lithophysal and fracture cavities have outer surfaces with ages that are young (typically less than 500 ka) compared to the age of the host rocks (13 Ma). Radiocarbon ages are systematically younger than $^{230}\text{Th}/\text{U}$ ages determined from outer surfaces of the same sample. Even when a single method is used, multiple subsamples from the same outer surfaces commonly have different rather than similar ages. Typically, the thinnest subsamples from a given surface tend to have the youngest ages. Initial $^{234}\text{U}/^{238}\text{U}$ activity ratios representing the isotopic composition of fracture water at the time of mineral deposition range from 4 to 9.5 for samples younger than 100 ka. A distinct negative correlation between age and initial $^{234}\text{U}/^{238}\text{U}$ ratios is observed.

A common assumption in conventional geochronological models is that mineral deposition occurs instantaneously and that the resulting deposit consists of a layer of finite thickness, constant age, and uniform initial isotopic compositions. In contrast, data from Yucca Mountain UZ mineral coatings are more consistent with a depositional model where very thin layers are added more or less continuously on a scale finer than sampling techniques can resolve. Therefore, subsamples represent mixtures of both younger and older layers and the resulting isotopic measurements are intermediate between values present in the end members. The model simulates the correlation

between ages and subsample thickness, wide-ranging ages from a single outer surface, the discordance between isotopic systems with different half-lives, the negative correlation between $^{230}\text{Th}/\text{U}$ age and initial $^{234}\text{U}/^{238}\text{U}$ ratios, and ages that are less than those at which secular equilibrium or complete decay is attained. The slow, long-term rates of deposition inferred from subsamples of outermost calcite and opal (less than about 5 mm per m.y.) are similar to those calculated by assuming that the total thickness of mineral coatings accumulated over 12 m.y.

Calcite from mineral coatings in the ESF shows a wide range of $\delta^{13}\text{C}$ values from about -8.2 to 8.5 per mil with corresponding $\delta^{18}\text{O}$ values of about 21 to 10 per mil. Both $\delta^{13}\text{C}$ and $\delta^{18}\text{O}$ in calcite are negatively correlated such that subsamples with large $\delta^{13}\text{C}$ values tend to have small $\delta^{18}\text{O}$ values. Systematic microsampling across individual mineral coatings indicates that $\delta^{13}\text{C}$ values in calcite shifted from larger values (2 to 9 per mil) early in the depositional history to intermediate values (-3 to 0 per mil) and finally to smaller values (-8 to -5 per mil) with time. Also, systematic $\delta^{18}\text{O}$ differences are observed with the largest values from outer calcite and smallest values from basal calcite.

Opal, quartz, and chalcedony also show shifts in both abundance and $\delta^{18}\text{O}$ compositions with time. The paragenesis of chalcedony followed by quartz is restricted to early depositional stages, whereas opal is most common in intermediate and late stages of deposition. Massive chalcedony has the smallest $\delta^{18}\text{O}$ values (7.9 to 17.3 per mil), whereas quartz $\delta^{18}\text{O}$ values are substantially larger (16.8 to 22.8 per mil). Opal deposited throughout most of the depositional history of the mineral coatings has a larger range of $\delta^{18}\text{O}$ values overlapping those for quartz and extending to much larger values (18.0 to 27.9 per mil).

Strontium isotope ratios of calcite correlate with microstratigraphic positions in individual mineral coatings and show a general trend of increasing $^{87}\text{Sr}/^{86}\text{Sr}$ ratios with time. Outer calcite $^{87}\text{Sr}/^{86}\text{Sr}$ ratios of 0.7115 to 0.7127 overlap values observed in the local pedogenic calcite deposits. Basal calcite has the least radiogenic $^{87}\text{Sr}/^{86}\text{Sr}$ ratios between 0.7105 and 0.7120. Temporal variations in strontium concentrations are less well defined than $^{87}\text{Sr}/^{86}\text{Sr}$ ratios; however, basal and intermediate calcite typically has concentrations less than about $130\text{ }\mu\text{g/g}$, whereas outer calcite commonly has larger concentrations. Strontium isotope ratios from subsamples across mineral coat-

ings show distinct correlations with carbon and oxygen isotopes that probably are related to a gradual evolution of isotopic compositions in water percolating through fractures. The relatively large amount of scatter observed in these correlations indicates that separate, time-dependent processes most likely control the resulting isotopic composition of fracture water.

Isotopic data from UZ minerals support a descending meteoric water source that has interacted with soil at Yucca Mountain. Textural gradations in the upper 10 to 30 m of the UZ provide a link between fine-grained, detritus-rich pedogenic deposits, and the detritus-free, coarse-grained calcite and opal present in the deeper UZ. Isotopic compositions of oxygen, carbon, and strontium in outer UZ calcite also overlap the isotopic compositions of pedogenic calcite. In contrast, ground water from shallower parts of the SZ has isotopic compositions that would result in much smaller $\delta^{18}\text{O}$ values and less radiogenic $^{87}\text{Sr}/^{86}\text{Sr}$ than those observed in outer UZ calcite. Ground water from the deeper Paleozoic carbonate aquifer is similarly incompatible with the $\delta^{18}\text{O}$ and $^{87}\text{Sr}/^{86}\text{Sr}$ compositions observed in UZ calcite but also has a carbon isotope composition that would result in $\delta^{13}\text{C}$ values larger than those observed in the outer UZ calcite. The isotopic data from UZ calcite presented in this report are inconsistent with a SZ source of water, but are compatible with a surface source.

Fracture water percolating through the UZ most likely has a major element composition that is intermediate between runoff and perched water. Precipitation rapidly interacts with calcite- and opal-rich materials in surface deposits. Fracture water is likely to have compositions that are even more chemically evolved than runoff considering the interactions that take place during infiltration through calcite- and opal-rich soils. Therefore, descending fracture water is likely to be saturated with respect to both calcite and opal. Chemical and textural arguments imply that once fracture water reaches mineral saturation, it is not likely to become undersaturated later during further descent through the UZ.

The process of UZ mineral deposition is initiated during infiltration where meteoric water interacts with materials in the soil after which a small portion may enter the bedrock fracture network. Fracture water is distributed into connected pathways in response to gravity-controlled downward percolation as thin films. Physical and textural evidence indicates calcite and opal coatings formed in fracture or litho-

physal cavities that were never filled with water. Textures indicate that mineral growth commonly occurs on crystal tips, requiring capillary flow up outer mineral surfaces. Differences in textures between near-horizontal substrates and high-angle fractures indicate that slowing of downward-migrating water is an important factor in influencing mineral growth. The presence of mineral coatings in open cavities implies a need for liquid/gas exchange. An independently migrating gas phase capable of transporting both CO₂ gas and water vapor away from cavities containing seepage provides a depositional mechanism. Rates of water vapor and CO₂ transfer from deeper parts of the UZ are likely to be small; however, operation of these processes over long periods of time results in the very slow growth rates observed for calcite and opal in the UZ.

Patterns of $\delta^{18}\text{O}$ variations in both silica phases and calcite preserve a record of decreasing temperatures in the welded tuffs through time. Chalcedony and quartz formed during the early depositional stages have $\delta^{18}\text{O}$ values indicating elevated UZ temperatures (as high as about 80°C) relative to the present-day geothermal gradient. Heat sources include the cooling tuffs themselves but more likely are related to magmatic intrusions into the upper crust that caused steeper geothermal gradients. Much of the quartz as well as the subsequent calcite and opal have larger $\delta^{18}\text{O}$ values, indicating that UZ temperatures cooled to less than about 45°C prior to deposition of most of the mineral coatings.

Isotopic compositions of fluids continued to evolve after the early cooling stage at Yucca Mountain. Carbon isotope compositions shift from $\delta^{13}\text{C}$ values of about -3 to 0 per mil in intermediate calcite to values of about -9 to -5 per mil in outer calcite. This shift likely is caused by changes in the local plant community associated with a major shift in climate from milder, wetter conditions during the Tertiary to the more severe, semiarid conditions of the Quaternary. The observed shift in strontium isotope compositions in basal calcite ($^{87}\text{Sr}/^{86}\text{Sr}$ ratios of about 0.7105 to 0.7120) to more radiogenic values (0.7118 to 0.7127) in outer calcite likely is related to the evolving isotopic compositions of the felsic tuffs as well as the development of calcite-rich soils during the Quaternary.

Geochronological and isotopic data show no strong evidence of the effects of pluvial-interpluvial climate variations associated with Pleistocene glacial cycles. Although evidence throughout the Great Basin implies that cooler conditions and greater amounts of precipitation were common during pluvial episodes,

$^{230}\text{Th}/\text{U}$ ages of calcite and opal show neither an increase nor decrease in frequency during these intervals. Calcite and opal formed during the late stages of deposition show no obvious evidence of dissolution corresponding to periods of greater precipitation at the surface. Carbon and oxygen isotopes show a range of 2 to 3 per mil in outer calcite, similar to the entire range of pluvial and interpluvial variation in SZ calcite at nearby Devils Hole. If deposition of UZ calcite were restricted to specific climate conditions, a more restricted range of $\delta^{13}\text{C}$ and $\delta^{18}\text{O}$ values would be expected. These observations are consistent with the concept that the rate of deposition of UZ opal and calcite at the potential repository horizon may be relatively constant over long time periods.

Slow, uniform growth rates over long periods imply that the UZ fracture network has maintained a large degree of hydrologic stability over time. Evidence from mineral coatings indicates that fracture flow in the deep UZ is buffered from climate-induced variations in precipitation and infiltration. This buffering may have been accomplished, in part, by increasing the plant biomass and associated evapotranspiration rates during wetter periods, by effective downslope diversion of soil water along the tuff/colluvium interface, and by buffering long-term flux through the highly porous nonwelded units of the PTn. Large $^{234}\text{U}/^{238}\text{U}$ ratios in fracture flow also may indicate that amounts of percolation in the deep UZ are small.

REFERENCES

- Allison, G.B., Barnes, C.J., Hughes, M.W., and Leany, F.W.J., 1984, The effect of climate and vegetation on the oxygen-18 and deuterium profiles in soils, *in* Isotope Hydrology 1983: Vienna, International Atomic Energy Agency, p. 105-123.
- Axelrod, D.I., 1979, Age and origin of Sonoran Desert vegetation: California Academy of Sciences, Occasional Papers, no. 132, 74 p.
- Benson L., and Klieforth, H., 1989, Stable isotopes in precipitation and ground water in the Yucca Mountain region, southern Nevada—Paleoclimatic implications, *in* Peterson, D.H., ed., Aspects of climate variability in the Pacific and the Western Americas: American Geophysical Union, Geophysical Monograph 55, p. 41-59.
- Bischoff, J.L., Fitts, J.P., and Fitzpatrick, J.A., 1997, Responses of sediment geochemistry to climate change in Owens Lake sediment—An 800-k.y. record of saline/fresh cycles in core OL-92, *in* Smith, G.I., and

- Bischoff, J.L., eds., An 800,000-year paleoclimate record from core OL-92, Owens Lake, southeast California: Geological Society of America Special Paper 317, p. 37-47.
- Bish, D.L., and Aronson, J.L., 1993, Paleogeothermal and paleohydrologic conditions in silicic tuff from Yucca Mountain, Nevada: *Clays and clay minerals*, v. 41, no. 2, p. 148-161.
- Bish, D.L., and Chipera, S.J., 1989, Revised mineralogic summary of Yucca Mountain, Nevada: Los Alamos National Laboratory Report LA-11497-MS, 68 p.
- Bradbury, J.P., 1997, A diatom-based paleohydrologic record of climate change for the past 800 k.y. from Owens Lake, California, in Smith, G.I., and Bischoff, J.L., eds., An 800,000-year paleoclimate record from core OL-92, Owens Lake, southeast California: Geological Society of America Special Paper 317, p. 99-112.
- Bredehoeft, J.D., 1992, Response of the ground-water system at Yucca Mountain to an earthquake, in National Research Council, Ground water at Yucca Mountain, how high can it rise? Final report of the Panel on Coupled Hydrologic/Tectonic/Hydrothermal Systems at Yucca Mountain: Washington, D.C., National Academy Press, p. 212-222.
- Broecker, W.S., 1963, A preliminary evaluation of uranium-series inequilibrium as a tool for absolute age measurement on marine carbonates: *Journal of Geophysical Research*, v. 68, p. 2817-2834.
- Broxton, D.E., Bish, D.L., and Warren, R.G., 1987, Distribution and chemistry of diagenetic minerals at Yucca Mountain, Nye County, Nevada: *Clays and Clay Minerals*, v. 35, p. 89-110.
- Broxton, D.E., Chipera, S.J., Byers, F.M., Jr., and Rautman, C.A., 1993, Geologic evaluation of six nonwelded tuff sites in the vicinity of Yucca Mountain, Nevada, for a surface-based test facility for the Yucca Mountain Project: Los Alamos National Laboratory Report LA-12542-MS, 83 p.
- Buesch, D.C., Spengler, R.W., Moyer, T.C., and Geslin, J.K., 1996, Proposed stratigraphic nomenclature and macroscopic identification of lithostratigraphic units of the Paintbrush Group exposed at Yucca Mountain, Nevada: U.S. Geological Survey Open-File Report 94-469, 45 p.
- Carlos, B.A., 1985, Minerals in fractures of the unsaturated zone from drill core USW G-4, Yucca Mountain, Nye County, Nevada: Los Alamos National Laboratory Report LA-10415-MS, 55 p.
- Carlos, B.A., 1994, Field guide to fracture-lining minerals at Yucca Mountain, Nevada: Los Alamos National Laboratory Report LA-12803-MS, 12 p.
- Carr, W.J., Byers, F.M., Jr., and Orkild, P.P., 1986, Stratigraphic and volcano-tectonic relations of the Crater Flat Tuff and some older volcanic units, Nye County, Nevada: U.S. Geological Survey Professional Paper 1323, 28 p.
- Carrigan, C.R., King, G.C.P., Barr, G.E., and Bixler, N.E., 1991, Potential for water table excursions induced by seismic events at Yucca Mountain, Nevada: *Geology*, v. 19, p. 1157-1160.
- Cerling, T.E., and Quade, J., 1993, Stable carbon and oxygen isotopes in soil carbonates, in Swart, P.K., Lohmann, K.C., McKenzie, J., and Savin, S., eds., *Climate change in continental isotopic records: Geophysical Monograph*, v. 78, Washington, D.C., American Geophysical Union, p. 217-231.
- Christiansen, R.L., Lipman, P.W., Carr, M.J., Byers, F.M., Jr., Orkild, P.P., and Sargent, K.A., 1977, The Timber Mountain - Oasis Valley caldera complex of southern Nevada: Geological Society of America Bulletin, v. 88, p. 943-959.
- Claassen, H.C., 1985, Sources and mechanisms of recharge for ground water in the west-central Amargosa Desert, Nevada—A geochemical interpretation: U.S. Geological Survey Professional Paper 712-F, 31 p.
- Clark, I., and Fritz, P., 1997, *Environmental isotopes in hydrogeology*: New York, Lewis Publishers, 328 p.
- Clayton, R.N., O'Neil, J.R., and Mayeda, K., 1972, Oxygen isotope exchange between quartz and water: *Journal of Geophysical Research*, v. 77, p. 3057-3067.
- Coplen, T.B., Kendall, Carol, and Hopple, Jessica, 1983, Comparison of stable isotope reference samples: *Nature*, v. 302, p. 236-238.
- Coplen, T.B., Winograd, I.J., Landwehr, J.M., and Riggs, A.C., 1994, 500,000-year stable carbon isotopic record from Devils Hole, Nevada: *Science*, v. 263, p. 361-365.
- Craig, R.W., and Robison, J.H., 1984, Geohydrology of rocks penetrated by test well UE-25p#1, Yucca Mountain area, Nye County, Nevada: U.S. Geological Survey Water-Resources Investigations Report 84-4248, 57 p.
- Czarnecki, J.B., 1985, Simulated effects of increased recharge on the ground-water flow system of Yucca Mountain and vicinity, Nevada-California: U.S. Geological Survey Water-Resources Investigations Report 84-4344, 33 p.
- Davisson, M.L., Smith, D.K., Kenneally, J., and Rose, T.P., 1999, Isotope hydrology of southern Nevada ground-water—Stable isotopes and radiocarbon: *Water Resources Research*, v. 35, p. 279-294.
- Day, W.C., Potter, C.J., Sweetkind, D., Dickerson, R.P., and San Juan, C.A., 1998, Bedrock geologic map of the central block area, Yucca Mountain, Nye County, Nevada: U.S. Geological Survey Miscellaneous Investigations Series Map I-2601, 15 p., 2 sheets.

- Denniston, R.F., Shearer, C.K., Layne, G.D., and Vaniman, D.T., 1997, SIMS analyses of minor and trace element distributions in fracture calcite from Yucca Mountain, Nevada, USA: *Geochimica et Cosmochimica Acta*, v. 61, p. 1803–1818.
- Drever, J.I., 1997, *The geochemistry of natural waters: Upper Saddle River, New Jersey*, Prentice-Hall, 436 p.
- Dublyansky, Y.V., 1998, Traces of epigenetic hydrothermal activity in the Yucca Mountain volcanic tuffs—Fluid inclusions and gas chemistry evidence, *in* Vanko, D.A., and Cline, J.S., eds., *Program and Abstracts, Seventh Biennial Pan-American Conference on Research on Fluid Inclusions*, June 1–4, 1998: Nevada Bureau of Mines and Geology Open-File Report 98–4.
- Dublyansky, Y.V., and Reutsky, V.N., 1998, Epigenetic quartz-opal-calcite crusts in the Yucca Mountain subsurface—Fluid inclusion and stable isotopic evidence of hydrothermal origin: *Geological Society of America, Abstracts with Programs*, v. 30, no. 7, p. A–79.
- Dublyansky, Y.V., Reutsky, V.N., and Shugurova, N., 1996, Fluid inclusions in calcite from the Yucca Mountain exploratory tunnel, *in* Brown, P.E., and Hagemann, S.G., eds., *Program and Abstracts, Sixth Biennial Pan-American Conference on Research on Fluid Inclusions*, May 30–June 1, 1996: Madison, Wisc., University of Wisconsin Department of Geology, p. 38–39.
- Engstrom D.A., and Rautman, C.A., 1996, *Geology of the USW SD-9 drill hole, Yucca Mountain, Nevada: Sandia Report SAND96–2030*, Albuquerque, New Mexico, Sandia National Laboratories, 128 p.
- Fabryka-Martin, J.T., Flint, A.L., Sweetkind, D.S., Wolfsberg, A.V., Levy, S.S., Roemer, G.J.C., Roach, J.L., Wolfsberg, L.E., and Duff, M.C., 1997, Evaluation of flow and transport models of Yucca Mountain, based on chlorine-36 studies for FY97: Los Alamos National Laboratory Report LA–CST–TIP–97–010.
- Fabryka-Martin, J.T., Wightman, S.J., Robinson, B.A., and Vestal, E.W., 1994, Infiltration processes at Yucca Mountain inferred from chloride and chlorine-36 distributions: Los Alamos National Laboratory Report LA–CST–TIP–94–022, 37 p.
- Fabryka-Martin, J.T., Wolfsberg, A.V., Dixon, P.R., Levy, S., Musgrave, J., and Turin, H.J., 1996, Summary report of chlorine-36 studies—Systematic sampling for chlorine-36 in the Exploratory Studies Facility: Los Alamos National Laboratory Report LA–CST–TIP–96–002.
- Flint, A.L., and Flint, L.E., 1994, Spatial distribution of potential near surface moisture flux at Yucca Mountain, *in* High Level Radioactive Waste Management, Proceedings of the Fifth Annual International Conference, Las Vegas, Nevada, May 22–26, 1994: La Grange Park, Illinois, American Nuclear Society, p. 2352–2358.
- Forester, R.M., Bradbury, J.P., Carter, C., Elvidge, A., Hemphill, M., Lundstrom, S.C., Mahan, S.A., Marshall, B.D., Neymark, L.A., Paces, J.B., Sharpe, S., Whelan, J.F., and Wigand, P., 1999, The climatic and hydrologic history of southern Nevada during the late Quaternary: U.S. Geological Survey Open-File Report 98–635, 63 p.
- Forester, R.M., and Smith, A.J., 1994, Late glacial climate estimates for southern Nevada: the ostracode fossil record, *in* High Level Radioactive Waste Management, Proceedings of the Fifth Annual International Conference, Las Vegas, Nevada, May 22–26, 1994: La Grange Park, Illinois, American Nuclear Society, p. 2553–2561.
- Förstel, H., 1982, $^{18}\text{O}/^{16}\text{O}$ ratio of water in plants and their environment, *in* Schmidt, H.L., Förstel, H., and Heinsinger, K., eds., *Stable isotopes*: Amsterdam, The Netherlands, Elsevier, p. 503–516.
- Fridrich, C.J., Dudley, W.W., Jr., and Stuckless, J.S., 1994, Hydrogeologic analysis of the saturated-zone groundwater system, under Yucca Mountain, Nevada: *Journal of Hydrology*, v. 154, p. 133–168.
- Friedman, Irving, and O'Neil, J.R., 1977, Compilation of stable isotope fractionation factors of geochemical interest, *in* Fleischer, M., ed., *Data of geochemistry*: U.S. Geological Survey Professional Paper 440–KK, 6th ed., fig. 13.
- Frizzell, V.A., Jr., and Shulters, Jacqueline, 1990, *Geologic map of the Nevada Test Site, southern Nevada*: U.S. Geological Survey Miscellaneous Investigations Series Map I–2046, scale 1:100,000.
- Gascoyne, M., 1992, Geochemistry of the actinides and their daughters, *in* Ivanovich, M., and Harmon, R.S., eds., *Uranium-series disequilibrium: Applications to earth, marine, and environmental sciences* (2d ed.): Oxford, U.K., Clarendon Press, p. 34–61.
- Hanks, T.C., Winograd, I.J., Anderson, R.E., Reilly, T.E., and Weeks, E.P., 1999, Yucca Mountain as a radioactive-waste repository: U.S. Geological Survey Circular 1184, 19 p.
- Hevesi, J.A., Flint, A.L., and Istok, J.D., 1992, Precipitation estimation in mountainous terrain using multivariate geostatistics: II. Isohyetal maps: *Journal of Applied Meteorology*, v. 31, no. 7, p. 677–678.
- Hill, C.A., Dublyansky, Y.V., Harmon, R.S., and Schluter, C.M., 1995, Overview of calcite/opal deposits at or near the proposed high-level nuclear waste site, Yucca Mountain, Nevada, USA—Pedogenic, hypogene or both?: *Environmental Geology*, v. 26, p. 69–88.

- Hill, C.A., and Forti, Paolo, 1997, Cave minerals of the world: Huntsville, Alabama, National Speleological Society, Inc., 463 p.
- Ivanovich, M., and Harmon, R.S., eds., 1992, Uranium-series disequilibrium—Applications to earth, marine, and environmental sciences (2d ed.): Oxford, U.K., Clarendon Press, 910 p.
- Johnson, T.M., and DePaolo, D.J., 1994, Interpretation of isotopic data in groundwater-rock systems—Model development and application to Sr isotope data from Yucca Mountain: *Water Resources Research*, v. 30, p. 1571–1587.
- Kawabe, I., 1978, Calculation of oxygen isotope fractionation in quartz-water system with special reference to the low temperature fractionation: *Geochimica et Cosmochimica Acta*, v. 42, p. 613–621.
- Kita, I., Taguchi, S., and Matsubaya, O., 1985, Oxygen isotope fractionation between amorphous silica and water at 34–93°C: *Nature*, v. 314, p. 83–84.
- Langmuir, Donald, 1997, Aqueous environmental geochemistry: Upper Saddle River, New Jersey, Prentice-Hall, 600 p.
- Levy, S.S., 1991, Mineralogic alteration history and paleohydrology at Yucca Mountain, Nevada, in *High Level Radioactive Waste Management, Proceedings of the Second Annual International Conference*, Las Vegas, Nevada, April 28–May 3, 1991: La Grange Park, Illinois, American Nuclear Society, p. 477–485.
- Levy, S.S., Norman, D.I., and Chipera, S.J., 1996, Alteration history studies in the Exploratory Studies Facility, Yucca Mountain, Nevada, USA: *Proceedings of the Materials Research Society*, v. 412, p. 783–790.
- Ludwig, K.R., 1991, ISOPLOT: A plotting and regression program for radiogenic-isotope data; Version 2.71: U.S. Geological Survey Open-File Report 91–445 (June 9, 1993 revision), 42 p.
- Ludwig, K.R., Halley, R.B., Simmons, K.R., and Peterman, Z.E., 1988, Strontium-isotope stratigraphy of Enewetak Atoll: *Geology*, v. 16, p. 173–177.
- Ludwig, K.R., Peterman, Z.E., Simmons, K.R., and Gutentag, E.D., 1993, $^{234}\text{U}/^{238}\text{U}$ ratios as a groundwater flow tracer, SW Nevada-SE California, in *High Level Radioactive Waste Management, Proceedings of the Fourth Annual International Conference*, Las Vegas, Nevada, April 26–30, 1993: La Grange Park, Illinois, American Nuclear Society, p. 1567–1572.
- Ludwig, K.R., Simmons, K.R., Szabo, B.J., Winograd, I.J., Landwehr, J.M., Riggs, A.C., and Hoffman, R.J., 1992, Mass-spectrometric ^{230}Th - ^{234}U - ^{238}U dating of the Devils Hole calcite vein: *Science*, v. 258, p. 284–287.
- Marshall, B.D., and Mahan, S.A., 1994, Strontium isotope geochemistry of soil and playa deposits near Yucca Mountain, Nevada, in *High Level Radioactive Waste Management, Proceedings of the Fifth Annual International Conference*, Las Vegas, Nevada, May 22–26, 1994: La Grange Park, Illinois, American Nuclear Society, p. 2685–2691.
- Marshall, B.D., Peterman, Z.E., and Stuckless, J.S., 1993, Strontium isotopic evidence for a higher water table at Yucca Mountain, in *High Level Radioactive Waste Management, Proceedings of the Fourth Annual International Conference*, Las Vegas, Nevada, April 26–30, 1993: La Grange Park, Illinois, American Nuclear Society, p. 1948–1952.
- Marshall, B.D., Whelan, J.F., Peterman, Z.E., Futa, K., Mahan, S.A., and Stuckless, J.S., 1992, Isotopic studies of fracture coatings at Yucca Mountain, Nevada: *Proceedings of the Seventh International Symposium on Water-Rock Interaction*, v. 1, p. 737–740.
- McConnaughey, T.A., Whelan, J.F., Wickland, K.P., and Moscati, R.J., 1994, Isotopic studies of Yucca Mountain soil fluids and carbonate pedogenesis, in *High Level Radioactive Waste Management, Proceedings of the Fifth Annual International Conference*, Las Vegas, Nevada, May 22–26, 1994: La Grange Park, Illinois, American Nuclear Society, p. 2584–2589.
- Monger, H.C., and Adams, H.P., 1996, Micromorphology of calcite-silica deposits, Yucca Mountain, Nevada: *Soil Science Society of America Journal*, v. 60, p. 519–530.
- Montazer, Parviz, and Wilson, W.E., 1984, Conceptual hydrological model of flow in the unsaturated zone, Yucca Mountain, Nevada: U.S. Geological Survey Water-Resources Investigations Report 84–4345, 55 p.
- Moscati, R.J., and Whelan, J.F., 1996, Origin of secondary silica within Yucca Mountain, Nye County, southwestern Nevada: U.S. Geological Survey Open-File Report 95–289, 14 p.
- Moyer, T.C., Geslin, J.K., and Flint, L.E., 1996, Stratigraphic relations and hydrologic properties of the Paintbrush Tuff nonwelded (PTn) hydrologic unit, Yucca Mountain, Nevada: U.S. Geological Survey Open-File Report 95–397, 151 p.
- Muhs, D.R., Whitney, J.W., Shroba, R.R., Taylor, E.M., and Bush, C.A., 1990, Uranium-series dating of secondary carbonates near Yucca Mountain, Nevada—Applications to tectonic, paleomagnetic, and paleohydrologic problems, in *High Level Radioactive Waste Management, Proceedings of the International Conference*, Las Vegas, Nevada, April 8–12, 1990: La Grange Park, Illinois, American Nuclear Society, p. 924–929.

- National Research Council, 1992, Ground water at Yucca Mountain, how high can it rise?: Final report of the Panel on Coupled Hydrologic/Tectonic/Hydrothermal Systems at Yucca Mountain: Washington, D.C., National Academy Press, 231 p.
- Neymark, L.A., Amelin, Y.V., Paces, J.B., and Peterman, Z.E., 1998, U-Pb age evidence for long-term stability of the unsaturated zone at Yucca Mountain, *in* High-Level Radioactive Waste Management, Proceedings of the Eighth International Conference, Las Vegas, Nevada, May 11–14, 1998: La Grange Park, Illinois, American Nuclear Society, p. 85–87.
- Neymark, L.A., Amelin, Y.V., Paces, J.B., Whelan, J.F., and Peterman, Z.E., 2000, U-Pb dating of opal and chalcedony above and below the modern water table at Yucca Mountain, southern Nevada (abs.): Geological Society of America Abstracts with Programs, v. 32, p. A–259.
- Neymark, L.A., Marshall, B.D., Kwak, L.M., Futa, K., and Mahan, S.A., 1995, Geochemical and Pb, Sr, and O isotopic study of the Tiva Canyon Tuff and Topopah Spring Tuff, Yucca Mountain, Nye County, Nevada: U.S. Geological Survey Open-File Report 95–134, 17 p.
- Neymark, L.A., and Paces, J.B., 2000, Consequences of slow growth for $^{230}\text{Th}/\text{U}$ dating of Quaternary opals, Yucca Mountain, NV, USA: Chemical Geology, v. 164, p. 143–160.
- Nichols, W.D., 1987, Geohydrology of the unsaturated zone at the burial site for low level radioactive waste near Beatty, Nye County, Nevada: U.S. Geological Survey Water-Supply Paper 2312, 52 p.
- Office of Civilian Radioactive Waste Management, 2000, Yucca Mountain site description: prepared for the U.S. Department of Energy, Yucca Mountain Site Characterization Office, North Las Vegas, Nevada, TDR-CRW-GS-000001 Rev 01 ICN 01 (September 2000), 3 books.
- O'Neil, J.R., Clayton, R.N., and Mayeda, T.K., 1969, Oxygen isotope fractionation in divalent metal carbonates: Journal of Chemistry and Physics, v. 51, p. 5547–5558.
- Ortiz, T.S., Williams, R.L., Nimick, F.B., Whittet, B.C., and South, D.L., 1985, A three-dimensional model of reference thermal/mechanical and hydrological stratigraphy at Yucca Mountain, southern Nevada: Sandia Report SAND84–1076, Albuquerque, New Mexico, Sandia National Laboratories, 76 p.
- Osmond, J.K., and Cowart, J.B., 1992, Ground water, *in* Ivanovich, M., and Harmon, R.S., eds., Uranium-series disequilibrium—Applications to earth, marine, and environmental sciences (2d ed.): Oxford, U.K., Clarendon Press, p. 290–333.
- Paces, J.B., Ludwig, K.R., Peterman, Z.E., Neymark, L.A., and Kenneally, J.M., 1998, Anomalous groundwater $^{234}\text{U}/^{238}\text{U}$ beneath Yucca Mountain—Evidence for local recharge?, *in* High-Level Radioactive Waste Management, Proceedings of the Eighth International Conference, Las Vegas, Nevada, May 11–14, 1998: La Grange Park, Illinois, American Nuclear Society, p. 185–188.
- Paces, J.B., Menges, C.M., Widmann, B., Wesling, J.R., Bush, C.A., Futa, K., Millard, H.T., Maat, P.B., and Whitney, J.W., 1994, Preliminary U-series disequilibrium and thermoluminescence ages of surficial deposits and paleosols associated with Quaternary faults, eastern Yucca Mountain, *in* High Level Radioactive Waste Management, Proceedings of the Fifth Annual International Conference, Las Vegas, Nevada, May 22–26, 1994: La Grange Park, Illinois, American Nuclear Society, p. 2391–2401.
- Paces, J.B., Taylor, E.M., and Bush, C., 1993, Late Quaternary history and uranium isotopic compositions of ground-water discharge deposits, Crater Flat, Nevada, *in* High Level Radioactive Waste Management, Proceedings of the Fourth Annual International Conference, Las Vegas, Nevada, April 26–30, 1993: La Grange Park, Illinois, American Nuclear Society, p. 1573–1580.
- Paquette, Jeanne, and Reeder, R.J., 1995, Relationship between surface structure, growth mechanism, and trace element incorporation in calcite: *Geochimica et Cosmochimica Acta*, v. 59, p. 735–749.
- Parkhurst, D.L., 1995, User's guide to PHREEQC—A computer program for speciation, reaction-path, advective-transport, and inverse geochemical calculations: U.S. Geological Survey Water-Resources Investigations Report 95–4227, 143 p.
- Patterson, G.L., 1999, Occurrences of perched water in the vicinity of the Exploratory Studies Facility north ramp, *in* Rousseau, J.P., Kwicklis, E.M., and Gillies, D.C., eds., Hydrogeology of the unsaturated zone, north ramp area of the Exploratory Studies Facility, Yucca Mountain, Nevada: U.S. Geological Survey Water-Resources Investigations Report 98–4050, p. 170.
- Patterson, G.L., Peterman, Z.E., and Paces, J.B., 1998, Hydrochemical evidence for the existence of perched water at USW WT-24, Yucca Mountain, Nevada, *in* High-Level Radioactive Waste Management, Proceedings of the Eighth International Conference, Las Vegas, Nevada, May 11–14, 1998: La Grange Park, Illinois, American Nuclear Society, p. 277–278.

- Peterman, Z.E., and Patterson, G.L., 1998, Isotopes aid in understanding the Yucca Mountain flow system, *in* High-Level Radioactive Waste Management, Proceedings of the Eighth International Conference, Las Vegas, Nevada, May 11–14, 1998: La Grange Park, Illinois, American Nuclear Society, p. 182–184.
- Peterman, Z.E., Spengler, R.W., Futa, K., Marshall, B.D., and Mahan, S.A., 1991, Assessing the natural performance of felsic tuffs using Rb-Sr and Sm-Nd systems—A study of the altered zone in the Topopah Spring member, Paintbrush Tuff, Yucca Mountain, Nevada: Materials Research Society Symposium Proceedings, v. 212, p. 687–694.
- Peterman, Z.E., and Stuckless, J.S., 1993, Isotopic evidence of complex ground-water flow at Yucca Mountain, Nevada, USA, *in* High Level Radioactive Waste Management, Proceedings of the Fourth Annual International Conference, Las Vegas, Nevada, April 26–30, 1993: La Grange Park, Illinois, American Nuclear Society, p. 1559–1566.
- Peterman, Z.E., Stuckless, J.S., Marshall, B.D., Mahan, S.A., and Futa, K., 1992, Strontium isotope geochemistry of calcite fracture fillings in deep core, Yucca Mountain, Nevada – A progress report, *in* High Level Radioactive Waste Management, Proceedings of the Third Annual International Conference, Las Vegas, Nevada, April 12–16, 1992: La Grange Park, Illinois, American Nuclear Society, p. 1582–1586.
- Quade, Jay, and Cerling, T.E., 1990, Stable isotopic evidence for a pedogenic origin of carbonates in Trench 14 near Yucca Mountain, Nevada: *Science*, v. 250, p. 1549–1552.
- Quade, Jay, Cerling, T.E., and Bowman, J.R., 1989, Systematic variations in the carbon and oxygen isotopic composition of pedogenic carbonate along elevation transects in the southern Great Basin, United States: *Geological Society of America Bulletin*, v. 101, p. 464–475.
- Quade, Jay, Mifflin, M.D., Pratt, W.L., McCoy, W., and Burckle, L., 1995, Spring deposits and water table levels in the southern Great Basin during the late Quaternary: *Geological Society of America Bulletin*, v. 107, p. 213–230.
- Rautman, C.A., and Engstrom D.A., 1996a, Geology of the USW SD-7 drill hole, Yucca Mountain, Nevada: Sandia Report SAND96–1474, Albuquerque, New Mexico, Sandia National Laboratories, 164 p.
- Rautman, C.A., and Engstrom, D.A., 1996b, Geology of the USW SD-12 drill hole, Yucca Mountain, Nevada: Sandia Report SAND96–1368, Albuquerque, New Mexico, Sandia National Laboratories, 131 p.
- Robison, J.H., 1984, Ground water level data and preliminary potentiometric-surface maps, Yucca Mountain and vicinity, Nye County, Nevada: U.S. Geological Survey Water-Resources Investigations Report 84–4197, 8 p.
- Roedder, Edwin, and Whelan, J.F., 1998, Ascending or descending water flow through Yucca Mountain tuffs? —Fluid inclusion evidence, *in* Vanko, D.A., and Cline, J.S., eds., Program and Abstracts, Seventh Biennial Pan-American Conference on Research on Fluid Inclusions, June 1–4, 1998: Nevada Bureau of Mines and Geology Open-File Report 98–4, p. 56.
- Roedder, Edwin, Whelan, J.F., and Vaniman, D.T., 1994, Fluid inclusion homogenization and crushing studies of calcite veins from Yucca Mountain, Nevada, tuffs—Environment of formation, *in* High Level Radioactive Waste Management, Proceedings of the Fifth Annual International Conference, Las Vegas, Nevada, May 22–26, 1994: La Grange Park, Illinois, American Nuclear Society, p. 1854–1860.
- Rojstaczer, Stuart, 1999, Stress dependent permeability and its political consequences at Yucca Mountain (abs.): Eos, Transactions, American Geophysical Union, 1999 Spring Meeting, Boston, Massachusetts, June 1–4, 1999, v. 80, p. S4.
- Rush, F.E., 1970, Regional ground-water system in the Nevada Test Site area, Nye, Lincoln, and Clark Counties, Nevada: Nevada Department of Conservation and Natural Resources Reconnaissance Series Report 54, 25 p.
- Sass, J.H., Lachenbruch, A.H., Dudley, W.W., Jr., Priest, S.S., Munroe, R.J., 1988, Temperature, thermal conductivity, and heat flow near Yucca Mountain, Nevada—Some tectonic and hydrologic implications: U.S. Geological Survey Open-File Report 87–649, 118 p.
- Savard, C.S., 1996, Selected hydrologic data from Fortymile Wash in the Yucca Mountain area, Nevada, water years 1993–94: U.S. Geological Survey Open-File Report 95–709, 30 p.
- Sawyer, D.A., Fleck, R.J., Lanphere, M.A., Warren, R.G., and Broxton, D.E., 1994, Episodic volcanism in the Miocene southwest Nevada volcanic field—Stratigraphic revisions, $^{40}\text{Ar}/^{39}\text{Ar}$ geochronologic framework, and implications for magmatic evolution: *Geological Society of America Bulletin*, v. 106, no. 10, p. 1304–1318.
- Scott, R.B., and Bonk, Jerry, 1984, Preliminary geologic map of Yucca Mountain, Nye County, Nevada, *with geologic sections*: U.S. Geological Survey Open-File Report 84–494, 9 p., map scale 1:12,000.
- Scott, R.B., Spengler, R.W., Diehl, S., Lappin, A.R., and Chornack, M.P., 1983, Geologic character of tuffs in the unsaturated zone at Yucca Mountain, southern Nevada, *in* Mercer, J.W., Rao, P.S.C., and Marine, I.W., eds., Role of the unsaturated zone in radioactive and hazardous waste disposal: Ann Arbor, Mich., Ann Arbor Science, p. 289–335.

- Smith, G.I., Bischoff, J.L., and Bradbury, J.P., 1997, Synthesis of the paleoclimatic record from Owens Lake core OL-92, *in* Smith, G.I., and Bischoff, J.L., eds., An 800,000-year paleoclimate record from core OL-92, Owens Lake, southeast California: Geological Society of America Special Paper 317, p. 143–160.
- Spaulding, W.G., 1985, Vegetation and climates of the last 45,000 years in the vicinity of the Nevada Test Site, south-central Nevada: U.S. Geological Survey Professional Paper 1329, 83 p.
- Stuckless, J.S., 1991, An evaluation of evidence pertaining to the origin of vein deposits exposed in Trench 14, Nevada Test Site, Nevada Formation, *in* High Level Radioactive Waste Management, Proceedings of the Second Annual International Conference, Las Vegas, Nevada, April 28–May 3, 1991: La Grange Park, Illinois, American Nuclear Society, p. 1429–1437.
- Stuckless, J.S., Marshall, B.D., Vaniman, D.T., Dudley, W.W., Peterman, Z.E., Paces, J.B., Whelan, J.F., Taylor, E.M., Forester, R.M., and O'Leary, D.W., 1998, Comments on "Overview of calcite/opal deposits at or near the proposed high-level nuclear waste site, Yucca Mountain, Nevada, USA: Pedogenic, hypogene or both?" by C.A. Hill, Y.V. Dublyansky, R.S. Harmon, and C.M. Schluter: *Environmental Geology*, v. 34, p. 70–78.
- Stuckless, J.S., Peterman, Z.E., and Muhs, D.R., 1991, U and Sr isotopes in ground water and calcite, Yucca Mountain, Nevada—Evidence against upwelling water: *Science*, v. 254, p. 551–554.
- Szabo, B.J., Carr, W.J., and Gottschall, W.C., 1981, Uranium-thorium dating of Quaternary carbonate accumulations in the Nevada Test Site region, southern Nevada: U.S. Geological Survey Open-File Report 81–119, 35 p.
- Szabo, B.J., Kolesar, P.T., Riggs A.C., Winograd, I.J., and Ludwig K.R., 1994, Paleoclimatic inferences from a 120,000-yr calcite record of water-table fluctuation in Browns Room of Devils Hole, Nevada: *Quaternary Research*, v. 41, p. 59–69.
- Szabo, B.J., and Kyser, T.K., 1985, Uranium, thorium isotopic analyses and uranium-series ages of calcite and opal, and stable isotopic compositions of calcite from drill cores UE25a#1, USW G-2 and USW G-3/GU-3, Yucca Mountain, Nevada: U.S. Geological Survey Open-File Report 85–224, 25 p.
- , 1990, Ages and stable-isotope compositions of secondary calcite and opal in drill cores from Tertiary volcanic rocks of the Yucca Mountain area, Nevada: *Geological Society of America Bulletin*, v. 102, p. 1714–1719.
- Szabo, B.J., and O'Malley, P.A., 1985, Uranium-series dating of secondary carbonate and silica precipitates relating to fault movements in the Nevada Test Site Region and of caliche and travertine samples from the Amargosa Desert: U.S. Geological Survey Open-File Report 85–47, 12 p.
- Taylor, E.M., and Huckins, H.E., 1995, Lithology, fault displacement and origin of secondary calcium carbonate and opaline silica at Trenches 14 and 14D on the Bow Ridge Fault at Exile Hill, Nye County, Nevada: U.S. Geological Survey Open-File Report 93–477, 38 p.
- Thomas, J.M., Welch, A.H., and Dettinger, M.D., 1996, Geochemistry and isotope hydrology of representative aquifers in the Great Basin region of Nevada, Utah and adjacent States: U.S. Geological Survey Professional Paper 1409–C, 100 p.
- Thompson, R.S., 1991, Pliocene environments and climates in the western United States: *Quaternary Science Reviews*, v. 10, p. 115–132.
- Thorstenson, D.C., Weeks, E.P., Haas, H., and Woodward, J.C., 1990, Physical and chemical characteristics of topographically affected airflow in an open borehole at Yucca Mountain, Nevada, *in* Proceedings of the Topical Meeting on Nuclear Waste Isolation in the Unsaturated Zone; Focus '89, Las Vegas, Nevada, Sept. 17–21, 1989: La Grange Park, Illinois, American Nuclear Society, p. 256–270.
- Tokunaga, T.K., and Wan, J., 1997, Water film flow along fracture surfaces of porous rock: *Water Resources Research*, v. 33, p. 1287–1295.
- Tucci, Patrick, and Burkhardt, D.J., 1995, Potentiometric-surface map, 1993, Yucca Mountain and vicinity, Nevada: U.S. Geological Survey Water-Resources Investigations Report 95–4149, 15 p.
- U.S. Department of Energy, 1998, Viability assessment of a repository at Yucca Mountain: U.S. Department of Energy, Office of Civilian Radioactive Waste Management, 5 v. and overview.
- Vaniman, D.T., and Chipera, S.J., 1996, Geochemical stratigraphy of secondary calcites in the tuffs of Yucca Mountain, Nevada: *Geochimica et Cosmochimica Acta*, v. 60, p. 4417–4433.
- Vaniman, D.T., Chipera, S.J., and Bish, D.L., 1994, Pedogenesis of siliceous calcretes at Yucca Mountain: *Geoderma*, v. 63, p. 1–17.
- Vaniman, D.T., and Whelan, J.F., 1994, Inferences of paleoenvironments from petrographic, chemical and stable-isotope studies of calcretes and fracture calcites, *in* High Level Radioactive Waste Management, Proceedings of the Fifth Annual International Conference, Las Vegas, Nevada, May 22–26, 1994: La Grange Park, Illinois, American Nuclear Society, p. 2730–2737.

- Waddell, R.K., 1982, Two dimensional, steady-state model of ground-water flow, Nevada Test Site and vicinity, Nevada-California: U.S. Geological Survey Water-Resources Investigations Report 82-4085, 72 p.
- Waddell, R.K., Robison, J.H., and Blankennagel, R.K., 1984, Hydrology of Yucca Mountain and vicinity, Nevada-California—Investigative results through mid-1983: U.S. Geological Survey Water-Resources Investigations Report 84-4267, 72 p.
- Whelan, J.F., and Moscati, R.F., 1998, 9 m.y. record of southern Nevada climate from Yucca Mountain secondary minerals, *in* High-Level Radioactive Waste Management, Proceedings of the Eighth International Conference, Las Vegas, Nevada, May 11-14, 1998: La Grange Park, Illinois, American Nuclear Society, p. 12-15.
- Whelan, J.F., Moscati, R.J., Allerton, S.B.M., and Marshall, B.D., 1998, Applications of isotope geochemistry to the reconstruction of Yucca Mountain paleohydrology - Status of investigations: June 1996: U.S. Geological Survey Open-File Report 98-83, 41 p.
- Whelan, J.F., and Stuckless, J.S., 1992, Paleohydrologic implications of the stable isotopic composition of secondary calcite within the Tertiary volcanic rocks of Yucca Mountain, Nevada, *in* High Level Radioactive Waste Management, Proceedings of the Third Annual International Conference, Las Vegas, Nevada, April 12-16, 1992: La Grange Park, Illinois, American Nuclear Society, p. 1572-1581.
- Whelan, J.F., Vaniman, D.T., Stuckless, J.S., and Moscati, R.J., 1994, Paleoclimatic and paleohydrologic records from secondary calcite: Yucca Mountain, Nevada, *in* High Level Radioactive Waste Management, Proceedings of the Fifth Annual International Conference, Las Vegas, Nevada, May 22-26, 1994: La Grange Park, Illinois, American Nuclear Society, p. 2738-2745.
- White, A.T., and Chuma, N.J., 1987, Carbon and isotope mass balance models of Oasis Valley-Fortymile Canyon groundwater basin, southern Nevada: *Water Resources Research*, v. 23, p. 571-582.
- Winograd, I.J., 1981, Radioactive waste disposal in thick unsaturated zones: *Science*, v. 212, no. 4502, p. 1457-1464.
- Winograd, I.J., Coplen, T.B., Landwehr, J.M., Riggs, A.C., Ludwig, K.R., Szabo, B.J., Kolesar, P.T., and Revesz, K.M., 1992, Continuous 500,000-year climate record from vein calcite in Devils Hole, Nevada: *Science*, v. 258, p. 255-260.
- Winograd, I.J., Szabo, B.J., Coplen, T.B., Riggs, A.C., and Kolesar, P.T., 1985, Two-million-year record of deuterium depletion in Great Basin ground waters: *Science*, v. 227, p. 519-522.
- Yang, I.C., Rattray, G.W., and Yu, P., 1996, Chemical and isotopic data and interpretations, unsaturated-zone boreholes, Yucca Mountain, Nevada: U.S. Geological Survey Water-Resources Investigations Report 96-4058, 58 p.

APPENDIX

The page intentionally
left blank

Appendix 1. Radiocarbon data for subsamples of unsaturated-zone calcite from the Exploratory Studies Facility tunnel, Yucca Mountain, Nevada, and procedural blanks

[Locations in the Exploratory Studies Facility (ESF) tunnel are given in meters from the north portal. Delta carbon-13 isotope values are calculated relative to the Vienna Pee Dee belemnite (VPDB) carbon isotope standard and are used to adjust radiocarbon contents relative to normalized delta carbon-13 values of -25 per mil. Radiocarbon content in percent modern carbon (pmc) was determined by accelerator mass spectrometry at the IsoTrace Laboratory, University of Toronto. Uncorrected radiocarbon ages, in thousands of years before present (ka), are calculated using the equation $t = -8.270 \times \ln(\text{pmc} \times 0.01)$, without correction for variations in radiocarbon production rates or incorporation of dead carbon from soil calcite. Errors in radiocarbon contents and age are given in parentheses and are reported at the 95-percent confidence level. HCl, hydrochloric acid; ---, not applicable]

Subsample identifier	ESF location (meters)	Delta carbon-13 (per mil)	Radiocarbon content (pmc)	Uncorrected radiocarbon age (ka)	Subsample description
HD2001ca	1420	-2.4	1.96 (0.18)	32.5 (0.8)	Top edges of late, matted calcite blades.
HD2002ca	1599.95	-4.5	6.31 (0.30)	22.9 (0.4)	Top edges of squat calcite blades.
HD2003ca	1612.38	-6.2	1.81 (0.14)	33.2 (0.7)	Tiny calcite crystals adjacent to tuff formed late after vein reopened.
HD2004ca	1646.6	0.0	3.86 (0.28)	26.9 (0.6)	Two areas of tiny calcite blades (may include some subjacent calcite).
HD2005ca	1710.95	-6.5	2.23 (0.20)	31.5 (0.8)	Edges of hexagonal calcite plates from fracture coating.
HD2006ca	1900	-5.7	8.8 (1.6)	20.1 (1.6)	Whole, thin calcite blades from fracture intersecting lithophysal cavity.
HD2006cb	1900	-2.9	1.09 (0.12)	37.4 (0.9)	Whole, thin calcite blades shingling floor of lithophysal cavity.
HD2006cc	1900	-6.9	1.79 (0.18)	33.3 (0.9)	Tips of thin and thick calcite blades; should be younger than HD2006ca and HD2006cb.
HD2007-1ca	2213	-10.7	1.70 (0.16)	33.7 (0.8)	Calcite overgrowths on blade tips (paint removed with acetone).
HD2007-1cb	2213	-6.9	1.68 (0.16)	33.8 (0.8)	Calcite blades without overgrowths (paint removed with acetone).
HD2007-2ca	2213	-5.9	3.09 (0.28)	28.8 (0.8)	Blocky calcite crystal faces from fracture intersecting lithophysal cavity.
HD2008ca	2272	-6.2	1.94 (0.18)	32.6 (0.8)	Front and leading edges of a partial calcite coating on a fracture surface.
HD2008cb	2272	-6.6	1.63 (0.26)	34.0 (1.4)	"Ridge crest" formed of stacked tabular hexagonal calcite plates.
HD2019cc	2880	-7.2	14.4 (1.4)	16.0 (0.8)	Top edges of scalloped calcite blades coated with late opal hemispheres.
HD2019ca	2881	-7.6	3.67 (0.36)	27.3 (0.8)	Faces of scepter terminations of calcite blades.
HD2019cb	2881	-7.2	0.64 (0.14)	41.8 (1.9)	Outer halves of two very thin blades in a lithophysal cavity.
HD2055ca	2911.2	-7.8	5.48 (0.44)	24.0 (0.7)	Coxcomb calcite crystals on opal that coats older, thick calcite blades; not HCl washed.
HD2055cb	2911.2	-6.8	3.21 (0.52)	28.4 (1.4)	Thin layer from faces of free-growth calcite; HCl washed.
HD2056cb	2922.9	-6.3	0.51 (0.08)	43.7 (1.4)	Top faces of thick calcite blades; not HCl washed.

Appendix 1. Radiocarbon data for subsamples of unsaturated-zone calcite from the Exploratory Studies Facility tunnel, Yucca Mountain, Nevada, and procedural blanks – Continued

Subsample identifier	ESF location (meters)	Delta carbon-13 (per mil)	Radio-carbon content (pmc)	Uncorrected radiocarbon age (ka)	Subsample description
HD2057ca	2962.2	-7.4	2.16 (0.22)	31.7(0.9)	Top faces of broad scepter calcite crystals; HCl washed.
HD2059ca	3017.78	-7.7	1.01 (0.12)	38.0 (1.0)	Outermost one or two "growth" bands of delicate thin, elongated calcite blades.
HD2065ca	3316.2	7.6	1.73 (0.14)	33.6 (0.7)	Irregular calcite blades from a basal porous zone containing 5 to10 percent tiny pyramidal calcite crystals.
HD2065cb	3316.2	-6.9	2.08 (0.22)	32.0 (0.9)	Tips of bladed scepter-head calcite crystals; HCl washed.
HD2065cc	3316.2	-6.2	2.56 (0.16)	30.3 (0.5)	Tips of bladed scepter-head calcite crystals; not HCl washed.
HD2067ca	3428.18	-2.7	0.02 (0.08)	49.9 (3.0)	Basal calcite, partly detached from fracture surface; not HCl washed.
HD2067cb	3428.18	-7.5	0.67 (0.10)	41.4 (1.3)	Top and faces of tabular calcite crystals; HCl washed.
HD2069ca	3503.78	-7.7	1.27 (0.20)	36.1 (1.4)	Faces (mostly large flats) of thick tabular calcite; HCl washed.
HD2070ca	3523.63	-8.4	1.32 (0.14)	35.8 (0.9)	Faces (mostly large flats) of tabular calcite; HCl washed.
HD2070cb	3523.63	-7.2	0.73 (0.10)	40.7 (1.2)	Single, small scepter-head calcite crystal broken off; HCl washed.
HD2071ca	3545.4	-6.0	2.12 (0.36)	31.9 (1.5)	Leading edges from group of small bladed calcite crystals; HCl washed.
HD2071cb	3545.4	-6.0	2.21 (0.18)	31.5 (0.7)	Top faces of scepter-head calcite crystals; HCl washed.
Blank	---	-0.6	1.17 (0.26)	36.8 (1.9)	Paleozoic limestone (Cararra Formation, west side, Bare Mountain, Nevada) assumed to contain no ^{14}C ; HCl washed.
Blank	---	-0.8	0.52 (0.14)	43.5 (2.4)	Paleozoic limestone (Cararra Formation, west side, Bare Mountain, Nevada) assumed to contain no ^{14}C ; HCl washed.

Appendix 2a. Description of subsamples of unsaturated-zone calcite and opal analyzed for uranium and thorium isotopes from the Exploratory Studies Facility tunnel, Yucca Mountain, Nevada

[Locations in the Exploratory Studies Facility (ESF) tunnel are given in meters from the north portal. Geologic settings include fracture cavities, lithophysal cavities, altered pumice clasts, or settings that are unclear and probably are related to early fractures formed during initial cooling of the ash-flow sheet. N, normal]

Subsample identifier	ESF location (meters)	Geologic setting	Subsample description
HD1846-U1	293.96	Fracture	Chalcedony/opal: massive botryoidal silica.
HD1846-U2	293.96	Fracture	Chalcedony/opal: massive botryoidal silica.
HD1845-U1	295.1	Fracture	Chalcedony/opal: outer layers.
HD1848-U1	358.95	Pumice	Chalcedony/opal: outermost layer of free-face hemisphere.
HD1848-U2	358.95	Pumice	Chalcedony/opal: interior layers of free-face hemisphere.
HD1848-U3	358.95	Pumice	Chalcedony/opal: interior layers of free-face hemisphere.
HD1865-U1	531.25	Fracture	Calcite \pm opal: free-face crystals.
HD1865-U2	531.25	Fracture	Chalcedony/opal: mixed older and younger silica.
HD1865-U3	531.25	Fracture	Chalcedony/opal: massive, milky silica.
HD1865-U4	531.25	Fracture	Chalcedony/opal: interior horizon in coating with diffuse layers.
SPC00504275-U1	556.95	Fracture	Chalcedony/opal: 1-millimeter-thick layer of coarse, botryoidal material.
SPC00504305-U1	579.15	Fracture	Calcite: outermost blade surfaces.
SPC00509026-U1	584.75	Fracture	Calcite \pm opal: white sparry calcite with minor opal.
SPC00509037-U1	625.18	Unclear	Calcite: outermost calcite blade tips and surfaces.
SPC00509072-U1	787.3	Unclear	Chalcedony/opal: massive silica from interior of coating.
SPC00509088-U1	803.8	Fracture	Chalcedony/opal: small fragment of older silica.
SPC00509098-U1	818.2	Fracture	Opal + calcite: whole 2- to 3-millimeter-thick mineral coating.
SPC00509108-U1	993.88	Unclear	Chalcedony/opal: older-looking botryoidal silica.
HD2094-U1	1,244	Fracture	Opal: individual botryoidal cluster on free-face surface.
HD2094-U3	1,244	Fracture	Opal: thin botryoidal film directly on fracture surface.
HD2027-U1	1,479.55	Fracture	Opal: outermost botryoidal clusters/sheets on blocky calcite crystals.
HD2027-U2	1,479.55	Fracture	Opal: outermost botryoidal clusters/sheets on blocky calcite crystals.
HD2029-U1	1,533.25	Fracture	Opal \pm calcite: outermost botryoidal cluster.
HD2029-U2	1,533.25	Fracture	Opal \pm calcite: basal massive chalcedony.
HD2005-U1	1,710.95	Fracture	Calcite: outermost low-relief, imbricated, tabular crystals.
HD2006-U1	1,900	Lithophysae	Opal: individual small hemisphere on free-face calcite surface.
ESF1975-U1	1,975	Unclear	Calcite: free-face crystal surfaces.
ESF1975-U2	1,975	Unclear	Calcite + opal: free-face crystal surfaces.
HD2094-U2	2,161.78	Fracture	Opal: outer coating on quartz prisms.
HD2095-U1R	2,161.78	Fracture	Opal: thin sheets coating thin, spiny calcite blades.
HD2095-U2	2,161.78	Fracture	Opal; individual botryoidal cluster from free-face growth surface.
HD2007-1-U1	2,213	Fracture	Opal: interior layer.
HD2007-1-U2	2,213	Fracture	Opal + calcite: botryoidal cluster on outermost surface along with adhering calcite.
HD2007-1-U3	2,213	Fracture	Calcite + opal: outermost calcite blades with adhering opal hemispheres.
HD2007-2-U1	2,213	Lithophysae	Opal + calcite: outermost opal sheets on calcite blades.
HD2007-2-U2	2,213	Lithophysae	Opal \pm calcite: outermost botryoidal clusters on calcite blades.
HD2008-U1	2,272	Fracture	Opal: older, large, individual opal hemisphere.
HD2008-U2	2,272	Fracture	Opal: older, large, individual opal hemisphere.
HD2008-U3	2,272	Fracture	Opal \pm calcite: mixture of small hemispheres and sheets on top of calcite prisms.
HD2008-U4	2,272	Fracture	Calcite \pm opal: surfaces of blocky prisms with minor, small opal hemispheres.
HD2008-U5	2,272	Fracture	Opal: outer layers from broad, undulating mammillary surface.
HD2008-U6R	2,272	Fracture	Opal: outermost intermediate-sized hemispheres after 1N hydrochloric acid leach.
HD2008-U7R	2,272	Fracture	Opal: outermost smallest-sized hemispheres after 0.1N hydrochloric acid leach.

Appendix 2a. Description of subsamples of unsaturated-zone calcite and opal analyzed for uranium and thorium isotopes from the Exploratory Studies Facility tunnel, Yucca Mountain, Nevada – Continued

Subsample identifier	ESF location (meters)	Geologic setting	Subsample description
HD2020-U1	2,439.58	Lithophysae	Opal: small hemispheres from outer crystal surfaces.
HD2020-U2	2,439.58	Lithophysae	Opal: small hemispheres from outer crystal surface.
HD2010-U1	2,468.2	Fracture	Calcite: tips from elongated blades.
HD2096-U1R	2,523	Fracture	Opal: outermost thin sheets on calcite crystal surfaces.
HD2096-U2R	2,523	Fracture	Opal: outermost thin sheets on calcite crystal surfaces.
HD2096-U3	2,523	Fracture	Calcite: irregular-shaped calcite from basal porous zone.
HD2011-U1	2,568	Fracture	Calcite: outer surface of blocky prisms.
HD2011-U2	2,568	Fracture	Calcite: tips from elongated blades.
HD2098-U1R	2,678.1	Lithophysae	Opal: very thin sheet on outermost coarse calcite crystal surfaces.
HD2098-U2R	2,678.1	Lithophysae	Opal: outermost thin sheets on calcite crystals.
HD2098-U3R	2,678.1	Lithophysae	Opal: outermost thin sheets on calcite crystals.
HD2014-U1R	2,688	Fracture	Opal; outermost thin sheets on calcite crystals.
HD2014-U2	2,688	Fracture	Calcite ± opal; outermost growth surfaces.
HD2019-U1	2,881	Lithophysae	Opal: thin sheet on outer calcite blade surface.
HD2019-U2	2,881	Lithophysae	Opal ± calcite: interior layer of thick calcite coating.
HD2019-U3	2,881	Lithophysae	Calcite: interior layer of thick calcite coating.
HD2019-U4	2,881	Lithophysae	Calcite: mixture of both growth (outer) and cleavage (interior) surfaces.
HD2019-U5	2,881	Lithophysae	Calcite: outermost crystal surfaces.
HD2054-U1R	2,881.6	Fracture	Opal(?): outermost 0.1-millimeter-thick milky sheet coating calcite blade.
HD2054-U2R	2,881.6	Fracture	Opal(?): botryoidal sheet coating three sides of a small calcite blade.
HD2055-U1R	2,911.2	Lithophysae	Opal: outermost hemispheres completely coating calcite surface.
HD2056-U1	2,922.9	Fracture	Opal: outermost, very thin sheet on calcite prism face.
HD2056-U2	2,922.9	Fracture	Opal: outermost, thin sheet on calcite prism face.
HD2056-U3	2,922.9	Fracture	Opal: outermost, uniform sheet on blocky calcite prism.
HD2057-U1R	2,962.2	Fracture	Opal: opal on high-relief calcite blade below outermost calcite layer.
HD2057-U2R	2,962.2	Fracture	Opal: outermost, botryoidal sheet on thin calcite blade.
HD2058b-U1R	2,979.98	Fracture	Opal: outermost, thin opal sheet coating outer calcite surface.
HD2058b-U2R	2,979.98	Fracture	Opal: tiny opal hemispheres from outermost calcite surface after acid leach.
HD2059-U1	3,017.78	Lithophysae	Calcite: outermost layer on tips of very thin calcite blades.
HD2059-U2	3,017.78	Lithophysae	Calcite: interior layers (composite) from thin calcite blades.
HD2059-U3	3,017.78	Lithophysae	Opal ± calcite (64:36): outermost opal overgrown by calcite at blade tip.
HD2059-U4	3,017.78	Lithophysae	Opal: outer bands of large, watery bubbles on free-face surface.
HD2059-U5	3,017.78	Lithophysae	Calcite + opal: outermost botryoidal cluster.
HD2059-U6	3,017.78	Lithophysae	Opal: whole, large bubble on calcite blade tip.
HD2059-U7	3,017.78	Lithophysae	Calcite: scepter-head blade tips.
HD2059-U8	3,017.78	Lithophysae	Calcite: lower, "corroded" portions of thin blades.
HD2074-U1R	3,050.7	Lithophysae	Opal: outermost hemisphere about 1-millimeter diameter on calcite prism.
HD2074-U3R	3,050.7	Lithophysae	Opal: outermost opal-covered calcite blade.
HD2074-U4R	3,050.7	Lithophysae	Opal: outermost botryoidal sheet coating thin calcite blade.
HD2061-U1R	3,057.68	Lithophysae	Opal: outermost thin coating on delicate calcite blades.
HD2061-U2R	3,057.68	Lithophysae	Opal: outermost thin coating on delicate calcite blades.
HD2073-U1R	3,103	Lithophysae	Opal: opal coating thin, elongated calcite blade about 10x5x0.2 millimeter.
HD2073-U2R	3103	Lithophysae	Opal: opal coating thin, elongated calcite blade about 5x4x0.1 millimeter.
HD2062-U1	3107.4	Fracture	Opal: outermost opal on tip of single, high-relief calcite blade.
HD2062-U2R	3107.4	Fracture	Opal: outermost opal coating low-relief rib of calcite.
HD2063-U1R	3116.1	Fracture	Opal: outermost botryoidal opal sheet coating three sides of a calcite blade.
HD2063-U2R	3116.1	Fracture	Opal: lowermost botryoidal coating on a small tuff fragment near base.
HD2064-U1	3196.7	Lithophysae	Opal: outermost coatings on calcite blades.
HD2064-U2	3196.7	Lithophysae	Opal + Calcite: outermost opal films + calcite overgrowths.

Appendix 2. Description of subsamples of unsaturated-zone calcite and opal analyzed for uranium and thorium isotopes from the Exploratory Studies Facility tunnel, Yucca Mountain, Nevada – Continued

Subsample identifier	ESF location (meters)	Geologic setting	Subsample description
HD2065-U1R	3,316.2	Lithophysae	Opal: outermost, very thin coating on blocky calcite blades.
HD2066-U1R	3,395.78	Lithophysae	Opal: outermost sheets on calcite blades from area of low relief.
HD2066-U2R	3,395.78	Lithophysae	Opal: outermost sheets on calcite blades from area of high relief.
HD2068-U1R	3,495.49	Lithophysae	Opal: outermost, coalescing hemispheres after 0.2N hydrochloric acid leach.
HD2068-U2R	3,495.49	Lithophysae	Opal: outermost, tiniest hemispheres after 0.2N hydrochloric acid leach.
HD2071-U1R	3,545.4	Fracture	Opal: outermost botryoidal sheet on low, blocky calcite crystal.
HD2077-U1R	3,762.9	Fracture	Opal: outermost coatings on delicate, thin calcite blades.
HD2077-U2R	3,762.9	Fracture	Opal: outermost thin botryoidal sheets on calcite prisms.
HD2078-U1R	3,767	Lithophysae	Opal: outermost thin botryoidal sheet on calcite blade.
HD2078-U2R	3,767	Lithophysae	Opal: outermost botryoidal sheet on bladed calcite.
HD2079C-U1R	3,817.2	Lithophysae	Opal: outermost smallest/thinnest hemispheres and sheets.
HD2079C-U2R	3,817.2	Lithophysae	Opal: fragments of outermost botryoidal sheet on calcite crystals.
HD2079C-U3R	3,817.2	Lithophysae	Opal: outermost sheet on calcite blade.
HD2081-U1R	3,861	Lithophysae	Opal: outermost thin botryoidal sheets on blocky calcite prisms.
HD2084-U1R	3,887.8	Lithophysae	Opal: outermost thin sheets on thin calcite blades.
HD2084-U2R	3,887.8	Lithophysae	Opal: outermost botryoidal sheet on thin calcite blades.
HD2087-U1R	3,950.7	Lithophysae	Opal: outermost thin, uniform coating on low-relief calcite prism.
HD2087-U2R	3,950.7	Lithophysae	Opal: outermost tiny botryoidal clusters.
HD2089-U1R	3,991.4	Lithophysae	Opal + calcite: outermost coating of opal plus underlying prismatic calcite.
HD2100-U1R	4,026.9	Lithophysae	Opal: outermost botryoidal sheet on calcite crystal surface.
HD2100-U2R	4,026.9	Lithophysae	Opal: outermost botryoidal sheet on calcite crystal surface.
HD2100-U3	4,026.9	Lithophysae	Calcite: outermost crystal faces in sub-vertical fracture cutting lithophysae.
HD2111-U1	4,861.4	Fracture	Calcite: outermost crystal faces on thin fracture coating.
HD2111-U2	4,861.4	Fracture	Calcite: outermost crystal faces on thin fracture coating.
HD2114-U1	4,986.5	Fracture	Calcite: outermost crystal faces on thin fracture coating.
HD2115-U1	4,988.9	Fracture	Calcite: outermost crystal faces on thin fracture coating.

Appendix 2b. Uranium-series disequilibrium data for subsamples of unsaturated-zone calcite and opal from the Exploratory Studies Facility tunnel, Yucca Mountain, Nevada

[Locations in the Exploratory Studies Facility (ESF) tunnel are given in meters from the north portal. All uranium and thorium isotope data were obtained by mass spectrometry at the U.S. Geological Survey, Denver, Colorado. Uncertainties for uranium and thorium concentrations are not given but typically are less than 5 percent (95-percent confidence limit) of the reported value except for thorium values less than about 0.1 microgram per gram ($\mu\text{g/g}$) where uncertainties may be as large as 50 percent of the reported value. Measured activity ratios are corrected for the addition of spike solutions, mass discrimination, and procedural blank. Errors are given in parentheses and reported at the 95-percent confidence level. Reported $^{230}\text{Th}/\text{U}$ ages and initial $^{234}\text{U}/^{238}\text{U}$ activity ratios are calculated using conventional $^{234}\text{U}/^{238}\text{U}$ - $^{230}\text{Th}/^{238}\text{U}$ age equations (equation 1, Interpretation of Ages section). ka, thousands of years before present]

Sub-sample identifier	ESF location (meters)	Subsample weight (grams)	Uranium concentration ($\mu\text{g/g}$)	Thorium concentration ($\mu\text{g/g}$)	Measured activity ratios				$^{230}\text{Th}/\text{U}$ age (ka)	Initial $^{234}\text{U}/^{238}\text{U}$ activity
					$^{234}\text{U}/^{238}\text{U}$	$^{230}\text{Th}/^{238}\text{U}$	$^{232}\text{Th}/^{238}\text{U}$	$^{230}\text{Th}/^{232}\text{Th}$		
HD1846-U1	293.96	0.01043	70.9	2.24	1.0428 (0.0037)	0.978 (0.010)	0.01039 (0.00004)	94.1	283 (15)	1.096 (0.010)
HD1846-U2	293.96	0.00863	106	0.0961	1.0085 (0.0032)	0.9631 (0.0069)	0.00029 (0.00002)	3,272	331 (18)	1.022 (0.008)
HD1845-U1	295.1	0.00941	74.2	6.47	1.0116 (0.0044)	0.9745 (0.0047)	0.02873 (0.00012)	33.9	348 (29)	1.031 (0.015)
HD1848-U1	358.95	0.01015	18.5	0.488	1.2228 (0.0042)	1.249 (0.042)	0.00867 (0.00009)	144	352 (+110/-58)	1.61 (0.15)
HD1848-U2	358.95	0.03141	4.57	0.151	1.187 (0.016)	1.221 (0.014)	0.01086 (0.00013)	112	394 (+89/-55)	1.57 (0.13)
HD1848-U3	358.95	0.03634	4.15	0.245	1.152 (0.022)	1.193 (0.022)	0.01942 (0.00020)	61.4	457 (+ ∞ /-130)	1.56 (0.12)
HD1865-U1	531.25	0.22047	0.807	0.382	1.0420 (0.0087)	1.077 (0.012)	0.1561 (0.0012)	6.90	Excess ^{230}Th	Undefined
HD1865-U2	531.25	0.21682	20.3	0.0271	1.0124 (0.0057)	1.0177 (0.0052)	0.000436 (0.000004)	2,333	939 (+ ∞ /-460)	1.18 (0.11)
HD1865-U3	531.25	0.07909	202	0.0154	1.0113 (0.0033)	0.9584 (0.0055)	0.000020 (0.000001)	48,091	314 (13)	1.028 (0.008)
HD1865-U4	531.25	0.00338	6.71	0.216	1.061 (0.018)	1.114 (0.018)	0.01060 (0.00068)	105	Excess ^{230}Th	Undefined
SPC00504275-U1	556.95	0.09880	37.0	0.214	1.0301 (0.0048)	1.0424 (0.0043)	0.001896 (0.000010)	550	762 (+ ∞ /-264)	1.26 (0.12)
SPC00504305-U1	579.15	0.37819	0.420	0.0561	1.457 (0.010)	1.315 (0.030)	0.04402 (0.00032)	29.9	198 (13)	1.820 (0.038)
SPC00509026-U1	584.75	0.47464	0.826	0.0196	1.0421 (0.0060)	1.0416 (0.0083)	0.00780 (0.00005)	133	450 (+93/-57)	1.152 (0.039)
SPC00509037-U1	625.18	0.26603	0.166	0.0493	1.222 (0.013)	1.237 (0.021)	0.09771 (0.00071)	12.7	331 (+78/-52)	1.60 (0.12)
SPC00509072-U1	787.3	0.06137	79.9	0.0632	1.0223 (0.0058)	1.0452 (0.0050)	0.000255 (0.000003)	4,094	Excess ^{230}Th	Undefined
SPC00509088-U1	803.8	0.02594	33.4	2.59	0.9853 (0.0055)	1.0110 (0.0069)	0.02555 (0.00020)	39.6	Undefined	Depleted ^{234}U
SPC00509098-U1	818.2	0.01624	30.2	0.156	1.0070 (0.0049)	1.001 (0.019)	0.00169 (0.00003)	591	512 (+ ∞ /-130)	1.030 (0.022)
SPC00509108-U1	993.88	0.14297	75.1	0.0529	1.0092 (0.0047)	1.0114 (0.0044)	0.000227 (0.000002)	4,458	691 (+ ∞ /-212)	1.065 (0.010)
HD2094-U1	1,244	0.00205	63.6	0.0373	1.5361 (0.0092)	1.5400 (0.0090)	0.00019 (0.00005)	8,323	263 (8)	2.129 (0.016)
HD2094-U3	1,244	0.00663	73.5	0.165	1.3847 (0.0074)	1.340 (0.014)	0.000734 (0.000014)	1,827	249 (10)	1.779 (0.020)
HD2027-U1	1,479.55	0.00535	55.0	0.121	1.1505 (0.0062)	1.1735 (0.0076)	0.00072 (0.00005)	1,638	395 (32)	1.462 (0.046)
HD2027-U2	1,479.55	0.01032	59.8	0.0455	1.0041 (0.0093)	1.0044 (0.0062)	0.00025 (0.00002)	4,093	710 (+ ∞ /-280)	1.031 (0.020)
HD2029-U1	1,533.25	0.00808	58.7	0.0454	1.0447 (0.0054)	1.0558 (0.0066)	0.00025 (0.00003)	4,235	545 (+320/-98)	1.21 (0.13)
HD2029-U2	1,533.25	0.01010	19.4	0.179	1.0267 (0.0054)	1.0431 (0.0090)	0.00303 (0.00008)	344	Excess ^{230}Th	Undefined
HD2005-U1	1,710.95	0.06656	0.0271	0.0607	1.832 (0.059)	1.857 (0.056)	0.737 (0.014)	2.52	233 (96)	3.63 (1.10)

Appendix 2b. Uranium-series disequilibrium data for subsamples of unsaturated-zone calcite and opal from the Exploratory Studies Facility tunnel, Yucca Mountain, Nevada – Continued

Sub-sample identifier	ESF location (meters)	Subsample weight (grams)	Uranium concentration (µg/g)	Thorium concentration (µg/g)	Measured activity ratios				²³⁰ Th/U age (ka)	Initial ²³⁴ U/ ²³⁸ U activity
					²³⁴ U/ ²³⁸ U	²³⁰ Th/ ²³⁸ U	²³² Th/ ²³⁸ U	²³⁰ Th/ ²³² Th		
HD2006-U1	1,900	0.00273	52.6	0.207	1.518 (0.026)	1.679 (0.012)	0.00129 (0.00011)	1,306	428 (+110/-59)	2.74 (0.41)
ESF1975-U1	1,975	0.51416	0.692	0.170	1.0510 (0.0071)	1.0590 (0.0098)	0.08092 (0.00050)	13.1	482 (+∞/-97)	1.21 (0.20)
ESF1975-U2	1,975	0.24574	6.20	0.0830	1.0942 (0.0056)	1.088 (0.020)	0.00441 (0.00003)	247	366 (+69/-45)	1.266 (0.046)
HD2094-U2	2,161.78	0.00295	41.6	0.0123	1.5951 (0.0096)	1.5927 (0.0093)	0.00009 (0.00005)	17,913	254 (7)	2.223 (0.016)
HD2095-U1R	2,161.78	0.00133	52.2	0.0454	2.076 (0.013)	1.841 (0.012)	0.00028 (0.00009)	6,648	174 (3)	2.764 (0.014)
HD2095-U2	2,161.78	0.00164	77.9	2.89	1.3017 (0.0080)	1.260 (0.019)	0.01221 (0.00009)	103	259 (15)	1.632 (0.025)
HD2007-1-U1	2,213	0.03730	27.0	0.181	1.2288 (0.0064)	1.2246 (0.0065)	0.00220 (0.00002)	555	307 (12)	1.547 (0.024)
HD2007-1-U2	2,213	0.00294	9.56	0.0698	1.2708 (0.0097)	1.238 (0.018)	0.00240 (0.00054)	516	270 (18)	1.583 (0.036)
HD2007-1-U3	2,213	0.03756	0.155	0.0257	1.88 (0.15)	1.616 (0.092)	0.0548 (0.0026)	29.5	165 (+44/-31)	2.45 (0.29)
HD2007-2-U1	2,213	0.00432	48.8	0.0112	1.2566 (0.0068)	1.1796 (0.0088)	0.00007 (0.00007)	17,023	240 (8)	1.506 (0.017)
HD2007-2-U2	2,213	0.00386	64.0	0.180	1.3305 (0.0077)	1.321 (0.011)	0.00092 (0.00006)	1,440	280 (12)	1.731 (0.029)
HD2008-U1	2,272	0.01452	40.1	0.0270	1.2369 (0.0065)	1.2003 (0.0071)	0.00022 (0.00003)	5,582	273 (9)	1.513 (0.019)
HD2008-U2	2,272	0.00146	84.9	0.0482	1.1402 (0.0065)	1.105 (0.010)	0.00018 (0.00012)	6,103	295 (16)	1.323 (0.021)
HD2008-U3	2,272	0.00362	12.3	0.131	1.767 (0.011)	1.512 (0.015)	0.00351 (0.00034)	430.2	167 (4)	2.234 (0.023)
HD2008-U4	2,272	0.06914	3.49	0.0398	1.4715 (0.0077)	1.4416 (0.0098)	0.00375 (0.00007)	384	250 (7)	1.958 (0.025)
HD2008-U5	2,272	0.00530	26.8	0.0581	1.1890 (0.0066)	1.1977 (0.0086)	0.00071 (0.00011)	1,693	340 (20)	1.495 (0.033)
HD2008-U6R	2,272	0.00286	72.5	0.0908	1.6014 (0.0084)	1.4709 (0.0085)	0.00040 (0.00007)	3,633	201 (4)	2.064 (0.019)
HD2008-U7R	2,272	0.00020	39.6	0.0388	2.101 (0.026)	1.618 (0.048)	0.00031 (0.00087)	5,159	134 (7)	2.608 (0.051)
HD2020-U1	2,439.58	0.00194	127	0.203	2.415 (0.013)	2.598 (0.014)	0.00051 (0.00006)	5,092	271 (7)	4.051 (0.066)
HD2020-U2	2,439.58	0.00194	72.5	0.889	3.261 (0.043)	3.641 (0.022)	0.00403 (0.00011)	905	280 (13)	6.01 (0.21)
HD2010-U1	2,468.2	0.05544	0.0301	0.0528	1.404 (0.025)	40.40 (1.19)	0.578 (0.016)	69.8	Excess ²³⁰ Th	Undefined
HD2096-U1R	2,523	0.00087	207	0.160	6.547 (0.037)	2.874 (0.038)	0.00024 (0.00003)	11,973	57.7 (1.0)	7.533 (0.040)
HD2096-U2R	2,523	0.00030	178	0.291	6.892 (0.043)	2.227 (0.015)	0.00053 (0.00011)	4,241	40.1 (0.4)	7.603 (0.043)
HD2096-U3	2,523	0.19706	0.0138	0.105	1.193 (0.014)	4.142 (0.074)	2.506 (0.034)	1.65	Undefined	Undefined
HD2011-U1	2,568	0.04223	0.0070	0.0132	1.73 (0.14)	5.69 (0.46)	0.622 (0.066)	9.15	Excess ²³⁰ Th	Undefined
HD2011-U2	2,568	0.03699	0.0466	0.0792	1.790 (0.043)	2.67 (0.10)	0.560 (0.011)	4.77	Excess ²³⁰ Th	Undefined
HD2098-U1R	2,678.1	0.00254	162	0.0262	5.433 (0.031)	3.049 (0.014)	0.000037 (0.000014)	82,744	79.1 (0.8)	6.546 (0.030)
HD2098-U2R	2,678.1	0.00127	205	0.267	5.370 (0.030)	3.097 (0.015)	0.00041 (0.00002)	7,501	82.0 (0.8)	6.515 (0.029)
HD2098-U3R	2,678.1	0.00294	174	0.153	1.925 (0.011)	2.181 (0.011)	0.000278 (0.000012)	7,839	374 (16)	3.67 (0.10)
HD2014-U1R	2,688	0.00090	120	0.152	7.512 (0.093)	4.584 (0.042)	0.00039 (0.00006)	11,605	88 (2)	9.354 (0.088)
HD2014-U2	2,688	0.13853	0.137	0.0474	5.70 (0.17)	1.397 (0.019)	0.1140 (0.0016)	12.3	28.3 (1.4)	6.42 (0.25)

Appendix 2b. Uranium-series disequilibrium data for subsamples of unsaturated-zone calcite and opal from the Exploratory Studies Facility tunnel, Yucca Mountain, Nevada – Continued

Sub-sample identifier	ESF location (meters)	Subsample weight (grams)	Uranium concentration ($\mu\text{g/g}$)	Thorium concentration ($\mu\text{g/g}$)	Measured activity ratios				$^{230}\text{Th}/\text{U}$ age (ka)	Initial $^{234}\text{U}/^{238}\text{U}$ activity
					$^{234}\text{U}/^{238}\text{U}$	$^{230}\text{Th}/^{238}\text{U}$	$^{232}\text{Th}/^{238}\text{U}$	$^{230}\text{Th}/^{232}\text{Th}$		
HD2019-U1	2,881	0.00580	6.02	0.0496	3.132 (0.028)	2.491 (0.015)	0.00270 (0.00043)	922	135 (3)	4.133 (0.047)
HD2019-U2	2,881	0.00980	85.5	0.108	0.9583 (0.0056)	0.9953 (0.0052)	0.000409 (0.000018)	2,431	Undefined	Depleted ^{234}U
HD2019-U3	2,881	0.12232	0.395	0.0079	1.0797 (0.0067)	1.186 (0.011)	0.00661 (0.00042)	179	Excess ^{230}Th	Undefined
HD2019-U4	2,881	0.08503	0.260	0.0307	2.079 (0.012)	2.082 (0.028)	0.03888 (0.00073)	53.6	231 (10)	3.117 (0.069)
HD2019-U5	2,881	0.10512	0.266	0.0262	3.356 (0.024)	2.124 (0.029)	0.03257 (0.00059)	65.2	94 (2)	4.132 (0.047)
HD2054-U1R	2,881.6	0.00340	282	0.0285	0.8999 (0.0049)	0.8289 (0.0046)	0.000029 (0.000006)	28,689	343 (+31/-24)	0.736 (0.025)
HD2054-U2R	2,881.6	0.00082	282	0.628	0.9810 (0.0057)	0.9610 (0.0076)	0.00073 (0.00003)	1,320	473 (+170/-75)	0.927 (0.033)
HD2055-U1R	2,911.2	0.00417	108	0.0128	4.868 (0.039)	2.170 (0.012)	0.000028 (0.000013)	78,894	59.0 (0.7)	5.573 (0.047)
HD2056-U1	2,922.9	0.00027	108	0.0580	4.982 (0.032)	2.386 (0.014)	0.00016 (0.00020)	14,586	64.6 (0.7)	5.781 (0.039)
HD2056-U2	2,922.9	0.00456	104	0.0158	3.773 (0.020)	3.076 (0.016)	0.000034 (0.000012)	91,618	139 (1.8)	5.113 (0.037)
HD2056-U3	2,922.9	0.00188	132	0.0359	4.367 (0.028)	3.022 (0.018)	0.00007 (0.00002)	41,178	106.7 (1.4)	5.555 (0.042)
HD2057-U1R	2,962.2	0.00199	37.5	0.0094	6.700 (0.047)	3.691 (0.026)	0.00006 (0.00008)	58,286	76.8 (1.0)	8.086 (0.062)
HD2057-U2R	2,962.2	0.00161	163	0.0166	2.742 (0.019)	2.654 (0.015)	0.00002 (0.00002)	136,237	200 (4)	4.071 (0.049)
HD2058b-U1R	2,979.98	0.00269	27.2	0.0026	5.843 (0.033)	3.909 (0.023)	0.00001 (0.00008)	370,087	100.5 (1.2)	7.438 (0.049)
HD2058b-U2R	2,979.98	0.00067	31.4	0.0452	7.043 (0.040)	3.229 (0.026)	0.00046 (0.00028)	7,064	60.8 (0.7)	8.181 (0.050)
HD2059-U1	3,017.78	0.08866	0.185	0.0020	3.970 (0.024)	2.125 (0.024)	0.00362 (0.00092)	586	74.8 (1.3)	4.68 (0.33)
HD2059-U2	3,017.78	0.13757	0.142	0.0010	2.273 (0.014)	2.379 (0.065)	0.00234 (0.00078)	1,018	254 (21)	3.62 (0.16)
HD2059-U3	3,017.78	0.00832	32.1	0.0047	3.864 (0.021)	2.485 (0.012)	0.000035 (0.000001)	70,304	96.4 (1.0)	4.763 (0.029)
HD2059-U4	3,017.78	0.00186	26.9	0.0148	1.3867 (0.0092)	1.4041 (0.0092)	0.00017 (0.00012)	8,045	293 (12)	1.886 (0.020)
HD2059-U5	3,017.78	0.02739	3.85	0.0125	2.875 (0.016)	2.221 (0.014)	0.00105 (0.00014)	2,107	130 (2)	3.710 (0.017)
HD2059-U6	3,017.78	0.00399	70.3	0.0849	1.6367 (0.0094)	1.7901 (0.0098)	0.00039 (0.00002)	4,607	360 (17)	2.764 (0.066)
HD2059-U7	3,017.78	0.10683	0.0280	0.0033	1.674 (0.024)	1.610 (0.025)	0.0394 (0.0051)	40.9	222 (14)	2.292 (0.040)
HD2059-U8	3,017.78	0.06517	0.0378	0.0018	1.469 (0.029)	1.425 (0.078)	0.0160 (0.0062)	89.2	242 (+53/-39)	1.94 (0.11)
HD2074-U1R	3,050.7	0.00287	163	0.0090	3.097 (0.017)	2.636 (0.013)	0.000004 (0.000013)	643,399	152 (2)	4.230 (0.033)
HD2074-U3R	3,050.7	0.01009	127	0.0085	2.795 (0.015)	2.477 (0.013)	0.000009 (0.000005)	280,167	166 (3)	3.876 (0.032)
HD2074-U4R	3,050.7	0.00912	96.3	0.0069	1.904 (0.020)	1.870 (0.015)	0.000014 (0.000007)	138,240	226 (8)	2.714 (0.055)
HD2061-U1R	3,057.68	0.01430	59.3	0.0032	1.8622 (0.0098)	1.904 (0.011)	0.000007 (0.000007)	254,176	255 (6)	2.775 (0.038)
HD2061-U2R	3,057.68	0.00762	42.0	0.0086	1.2891 (0.0070)	1.3251 (0.0071)	0.000061 (0.000019)	21,889	339 (16)	1.755 (0.039)
HD2073-U1R	3,103	0.00415	126	0.0185	4.034 (0.021)	3.649 (0.018)	0.000029 (0.000011)	125,801	167 (2)	5.864 (0.047)
HD2073-U2R	3,103	0.00084	78.4	0.105	6.293 (0.036)	3.649 (0.023)	0.00042 (0.00009)	8,679	82.3 (1)	7.684 (0.049)
HD2062-U1	3,107.4	0.00243	94.5	0.0219	4.504 (0.024)	4.203 (0.021)	0.00005 (0.00003)	77,746	175 (3)	6.757 (0.058)
HD2062-U2R	3,107.4	0.00247	92.2	0.0071	1.768 (0.010)	1.960 (0.010)	0.00002 (0.00003)	130,143	359 (16)	3.122 (0.099)
HD2063-U1R	3,116.1	0.00086	110	0.0270	4.341 (0.025)	3.695 (0.022)	0.00006 (0.00006)	60,662	148 (2)	6.088 (0.049)
HD2063-U2R	3,116.1	0.00120	270	0.306	0.9696 (0.0052)	0.9500 (0.0057)	0.000369 (0.000018)	2,572	Undefined	Depleted ^{234}U

Appendix 2b. Uranium-series disequilibrium data for subsamples of unsaturated zone calcite and opal from the Exploratory Studies Facility tunnel, Yucca Mountain, Nevada – Continued

Sub-sample identifier	ESF location (meters)	Subsample weight (grams)	Uranium concentration (µg/g)	Thorium concentration (µg/g)	Measured activity ratios				²³⁰ Th/U age (ka)	Initial ²³⁴ U/ ²³⁸ U activity
					²³⁴ U/ ²³⁸ U	²³⁰ Th/ ²³⁸ U	²³² Th/ ²³⁸ U	²³⁰ Th/ ²³² Th		
HD2064-U1	3,196.7	0.00110	73.6	0.0059	3.887 (0.024)	3.470 (0.021)	0.00001 (0.00019)	434,064	163 (3)	5.581 (0.051)
HD2064-U2	3,196.7	0.01407	19.4	0.0064	4.608 (0.030)	3.942 (0.022)	0.00009 (0.00002)	44,488	149 (2)	6.506 (0.058)
HD2065-U1R	3,316.2	0.00111	188	0.0371	5.800 (0.033)	3.472 (0.021)	0.0000466 (0.0000004)	74,427	86.1 (1.0)	7.126 (0.046)
HD2066-U1R	3,395.78	0.00228	243	0.0294	3.433 (0.019)	3.206 (0.017)	0.000023 (0.000011)	141,112	180 (3)	5.051 (0.045)
HD2066-U2R	3,395.78	0.00057	229	0.0809	6.377 (0.036)	4.860 (0.029)	0.00009 (0.00005)	53,729	122 (2)	8.590 (0.061)
HD2068-U1R	3,495.49	0.00257	113	0.0938	3.515 (0.020)	3.479 (0.027)	0.00025 (0.00005)	13,692	203 (4)	5.467 (0.065)
HD2068-U2R	3,495.49	0.00594	90.6	0.0056	3.702 (0.021)	3.717 (0.020)	0.00000 (0.00003)	6,169,563	208 (4)	5.870 (0.063)
HD2071-U1R	3,545.4	0.00639	165	0.0123	2.250 (0.012)	2.390 (0.012)	0.000012 (0.000006)	202,031	267 (7)	3.664 (0.055)
HD2077-U1R	3,762.9	0.00103	74.7	0.0813	2.483 (0.015)	2.828 (0.017)	0.00034 (0.00008)	8,230	328 (12)	4.76 (0.13)
HD2077-U2R	3,762.9	0.00455	56.1	0.0767	1.7976 (0.0095)	2.031 (0.012)	0.00044 (0.00002)	4,617	393 (20)	3.43 (0.14)
HD2078-U1R	3,767	0.00337	56.5	0.0359	6.514 (0.041)	10.932 (0.068)	0.00015 (0.00003)	72,196	Excess ²³⁰ Th	Undefined
HD2078-U2R	3,767	0.00654	64.7	0.0140	3.404 (0.018)	3.702 (0.018)	0.000052 (0.000014)	71,723	257 (5)	5.977 (0.084)
HD2079C-U1R	3,817.2	0.00050	167	0.0426	8.142 (0.046)	3.505 (0.023)	0.00007 (0.00007)	53,363	56.2 (0.6)	9.375 (0.056)
HD2079C-U2R	3,817.2	0.00059	119	0.0227	6.484 (0.042)	4.009 (0.024)	0.00004 (0.00009)	96,286	89.7 (1.1)	8.071 (0.058)
HD2079C-U3R	3,817.2	0.00173	161	0.0123	2.195 (0.012)	2.481 (0.015)	0.00001 (0.00002)	209,028	338 (12)	4.11 (0.11)
HD2081-U1R	3,861	0.00111	74.9	0.0633	8.074 (0.057)	3.153 (0.020)	0.00026 (0.00007)	12,033	50.0 (0.6)	9.151 (0.067)
HD2084-U1R	3,887.8	0.00359	246	0.557	2.098 (0.011)	0.6226 (0.0033)	0.000744 (0.000008)	837	37.1 (0.3)	2.220 (0.012)
HD2084-U2R	3,887.8	0.00274	101	0.143	6.896 (0.037)	2.856 (0.016)	0.00045 (0.00002)	6,300	53.7 (0.5)	7.866 (0.044)
HD2087-U1R	3,950.7	0.00030	212	0.184	2.487 (0.018)	2.435 (0.017)	0.00027 (0.00009)	8,960	209 (5)	3.690 (0.052)
HD2087-U2R	3,950.7	0.00111	99.2	0.0901	1.797 (0.012)	1.9030 (0.0098)	0.00029 (0.00005)	6,581	291 (10)	2.820 (0.059)
HD2089-U1R	3,991.4	0.03216	10.6	0.0128	3.420 (0.018)	3.017 (0.017)	0.000380 (0.000018)	7,945	161 (2)	4.823 (0.039)
HD2100-U1R	4,026.9	0.00050	145	0.0351	5.006 (0.066)	3.229 (0.019)	0.000063 (0.000001)	51,666	96 (2)	6.26 (0.92)
HD2100-U2R	4,026.9	0.00023	137	0.0616	2.006 (0.013)	2.267 (0.016)	0.000136 (0.000007)	16,706	358 (17)	3.77 (0.14)
HD2100-U3	4,026.9	0.06874	0.0119	0.156	2.55 (0.54)	31.01 (5.31)	4.31 (0.42)	7.19	Undefined	Undefined
HD2111-U1	4,861.4	0.06691	0.0186	0.0203		3.011 (0.093)	0.359 (0.014)	8.40	No ²³⁴ U data	No ²³⁴ U data
HD2111-U2	4,861.4	0.08128	0.0126	0.0952	52.22 (4.63)		2.503 (0.076)		No ²³⁰ Th data	Undefined
HD2114-U1	4,986.5	0.08240	0.0119	0.0154	4.59 (0.61)	3.78 (0.27)	0.427 (0.018)	8.86	136 (37)	7.8 (1.7)
HD2115-U1	4,988.9	0.06343	0.0109	0.0156	5.22 (0.19)	3.53 (0.34)	0.471 (0.026)	7.49	98 (17)	8.4 (1.3)

Appendix 3. Strontium, carbon, and oxygen isotope data for subsamples of unsaturated-zone calcite from the Exploratory Studies Facility tunnel, Yucca Mountain, Nevada

[Locations in the Exploratory Studies Facility (ESF) tunnel are given in meters from the north portal. Geologic settings include fracture cavities or lithophysal cavities. Strontium concentrations are determined by isotope dilution and are reported in micrograms per gram ($\mu\text{g/g}$). All isotopic measurements were made at the U.S. Geological Survey in Denver, Colorado. Values of $^{87}\text{Sr}/^{86}\text{Sr}$ are normalized to 0.70920 for present-day ocean water based on laboratory standard EN-1. Uncertainties in $^{87}\text{Sr}/^{86}\text{Sr}$ measurements are ± 0.00005 at the 95-percent confidence level. Stable isotope measurements are relative to carbonate standard Vienna Pee Dee belemnite (VPDB) for carbon and Vienna Standard Mean Ocean Water (VSMOW) for oxygen. Microstratigraphic positions are determined by visual examination under low-power binocular magnification. Lithostratigraphic units follow the nomenclature given in Buesch and others (1996): Tpcpul, Tiva Canyon crystal-poor upper lithophysal zone; Tptrn, Topopah Spring crystal-rich nonlithophysal zone; Tptpul, Topopah Spring crystal-poor upper lithophysal zone; and Tptpmn, Topopah Spring crystal-poor middle nonlithophysal zone]

Sub-sample identifier	ESF location (meters)	Geologic setting	Strontium concentration ($\mu\text{g/g}$)	$^{87}\text{Sr}/^{86}\text{Sr}$	Delta carbon-13 (per mil)	Delta oxygen-18 (per mil)	Subsample description	Microstratigraphic position	Lithostratigraphic unit
HD1941a	529.4	Fracture	364.7	0.71146	-2.1	20.3	Calcite crystals coated with quartz	Intermediate	Tpcpul
HD2001sa	1,420.0	Fracture	40.51	0.71192	-2.5	17.3	Tips of calcite blades	Outer	Tptrn
HD2001sb	1,420.0	Fracture	67.22	0.71102	6.3	12.4	Basal sparry calcite	Basal	Tptrn
HD2002sa	1,599.5	Fracture	50.80	0.71060	4.1	14.7	Basal banded white calcite	Basal	Tptrn
HD2002sc	1,599.5	Fracture	188.9	0.71198	-5.7	17.7	Late calcite blades	Outer	Tptrn
HD2003sa	1,612.4	Fracture	256.4	0.70958	6.2	11.5	Largely filled vein	Not classified	Tptrn
HD2003sb	1,612.4	Fracture	68.31	0.71070	7.6	13.5	Inner portion of vein	Basal	Tptrn
HD2003sc	1,612.4	Fracture	233.71	0.71197	-6.2	17.5	Later calcite blades	Outer	Tptrn
HD2004sa	1,646.6	Fracture	35.49	0.71081	4.5	13.3	Early calcite	Basal	Tptrn
HD2004sb	1,646.6	Fracture	73.97	0.70991	8.3	13.0	Middle third of coating	Intermediate	Tptrn
HD2004sc	1,646.6	Fracture	88.47	0.71144	1.9	15.6	Late calcite blades	Outer	Tptrn
HD2005sa	1,711.0	Fracture	127.3	0.71234	-6.3	17.7	Whole calcite coating	Intermediate	Tptrn
HD2006sa	1,900.0	Lithophysae	74.25	0.71195	-0.6	15.0	Early calcite on vapor phase	Basal	Tptpul
HD2006sb	1,900.0	Lithophysae	55.86	0.71127	0.0	13.9	Base of bladed calcite	Intermediate	Tptpul
HD2006sc	1,900.0	Lithophysae	189.4	0.71214	-6.2	17.7	Tips of bladed calcite	Outer	Tptpul
HD2019sb	2,880.0	Lithophysae	236.8	0.71141	6.7	13.5	Earliest calcite	Basal	Tptpmn
HD2019sc	2,880.0	Lithophysae	90.48	0.71107	1.8	15.1	Lower third of coating	Basal	Tptpmn
HD2019sd	2,880.0	Lithophysae	169.8	0.71131	-2.6	13.8	Middle third of coating	Intermediate	Tptpmn
HD2019se	2,880.0	Lithophysae	87.85	0.71188	-3.4	15.3	Middle third of coating	Intermediate	Tptpmn
HD2019sf	2,880.0	Lithophysae	332.5	0.71251	-7.2	17.2	Latest calcite blade tips	Outer	Tptpmn
HD2019sa	2,881.0	Lithophysae	265.0	0.71191	-5.3	16.6	Calcite scepter terminations	Outer	Tptpmn
HD2019sg	2,881.0	Lithophysae	82.60	0.71134	4.9	13.2	Earliest calcite	Basal	Tptpmn
HD2019sh	2,881.0	Lithophysae	173.5	0.71238	-6.9	16.6	Latest calcite blade tips	Outer	Tptpmn

Appendix 3. Strontium, carbon, and oxygen isotope data for subsamples of unsaturated-zone calcite from the Exploratory Studies Facility (ESF) tunnel, Yucca Mountain, Nevada – Continued

Sub-sample identifier	ESF location (meters)	Geologic setting	Strontium concentration (µg/g)	⁸⁷ Sr/ ⁸⁶ Sr	Delta carbon-13 (per mil)	Delta oxygen-18 (per mil)	Subsample description	Microstratigraphic position	Lithostratigraphic unit
HD2059sa	3,017.8	Lithophysae	49.55	0.71265	-8.0	16.9	Last two bands of calcite blade	Outer	Tptpmn
HD2059sb	3,017.8	Lithophysae	46.90	0.71260	-8.1	16.7	Last two bands of calcite blade	Outer	Tptpmn
HD2059sc	3,017.8	Lithophysae	79.93	0.71250	-7.2	16.7	Calcite blade tips - exterior bands	Outer	Tptpmn
HD2059sd	3,017.8	Lithophysae	145.3	0.71212	-6.1	16.5	Calcite blade tips - interior bands	Outer	Tptpmn
HD2059se	3,017.8	Lithophysae	113.6	0.71230	-7.3	16.8	Calcite blade tips - exterior bands	Outer	Tptpmn
HD2059sf	3,017.8	Lithophysae	44.08	0.71188	3.5	14.9	Base of bladed calcite	Intermediate	Tptpmn
HD2065sa	3,316.2	Lithophysae	101.3	0.71160	7.4	15.0	Basal porous zone calcite	Basal	Tptpmn
HD2065sb	3,316.2	Lithophysae	51.03	0.71136	4.9	15.2	Lower third of coating	Basal	Tptpmn
HD2065sc	3,316.2	Lithophysae	73.10	0.71153	6.3	14.7	Lower third of coating	Basal	Tptpmn
HD2065sd	3,316.2	Lithophysae	126.4	0.71140	6.7	14.5	Lower third of coating	Basal	Tptpmn
HD2065se	3,316.2	Lithophysae	128.2	0.71167	6.8	14.4	Lower third of coating	Basal	Tptpmn
HD2065sf	3,316.2	Lithophysae	110.0	0.71170	7.4	14.7	Middle third of coating	Intermediate	Tptpmn
HD2065sg	3,316.2	Lithophysae	104.0	0.71178	7.2	14.7	Middle third of coating	Intermediate	Tptpmn
HD2065sk	3,316.2	Lithophysae	160.2	0.71175	6.6	14.3	Outer third of coating	Outer	Tptpmn
HD2065sl	3,316.2	Lithophysae	220.5	0.71170	4.1	15.2	Outer third of coating	Outer	Tptpmn
HD2065sn	3,316.2	Lithophysae	537.3	0.71220	-6.5	17.5	Calcite blade tips	Outer	Tptpmn
HD2071sa	3,545.4	Fracture	56.83	0.71180	1.5	15.1	Thin coating of calcite crystals	Intermediate	Tptpmn